

# Lifetime Measurements in Neutron-rich Isotopes close to $N = 40$ and Development of a Simulation Tool for RDDS Spectra

Inaugural-Dissertation  
zur  
Erlangung des Doktorgrades  
der Mathematisch-Naturwissenschaftlichen Fakultät  
der Universität zu Köln

vorgelegt von

Thomas Christian Braunroth

aus Frechen

Hundt Druck GmbH, Köln  
2017

**Berichtersteller:**  
**(Gutachter)**

Prof. Dr. Alfred Dewald  
Prof. Dr. Jan Jolie

**Tag der mündlichen Prüfung:** 10. Oktober 2017

## Abstract

The main topic of the present work is the experimental determination of level lifetimes in  $^{58,60,62}_{24}\text{Cr}$  by means of the recoil distance Doppler-shift technique. The corresponding experiment was performed at the National Superconducting Cyclotron Laboratory at Michigan State University (USA). Excited states in  $^{58,60,62}\text{Cr}$  were populated by one-proton knockout reactions from fast radioactive  $^{59,61,63}\text{Mn}$  beams.

Level lifetimes were determined for the  $2_1^+$  and  $4_1^+$  states as well as – in case of  $^{58,60}\text{Cr}$  – for the  $6_1^+$  states. The determined  $B(\text{E}2; 2_1^+ \rightarrow 0_{\text{gs}}^+)$  values in  $^{58,60,62}\text{Cr}$  are in reasonable agreement with previous results from intermediate Coulomb-excitation experiments, although the present data suggests slightly enhanced collectivity. In  $^{58}\text{Cr}$ , the  $B(\text{E}2)$  values of the  $4_1^+ \rightarrow 2_1^+$  and  $6_1^+ \rightarrow 4_1^+$  transitions are comparable to the  $B(\text{E}2; 2_1^+ \rightarrow 0_{\text{gs}}^+)$  value. From  $^{58}\text{Cr}$  to  $^{60,62}\text{Cr}$ , the  $B(\text{E}2; 4_1^+ \rightarrow 2_1^+)$  values evolve more rapidly compared to the  $B(\text{E}2; 2_1^+ \rightarrow 0_{\text{gs}}^+)$  values which suggests rotor-like behaviour with pronounced quadrupole deformations  $\sim 0.3$ .

Compared to the neighbouring iron isotones, the evolution of  $B(\text{E}2)$  values along the chromium isotopes toward  $N = 40$  indicates a comparable trend, although the collectivity in chromium appears to be mildly enhanced.

The experimental results are discussed in the shell-model framework using the effective interaction LNPS. The comparison shows a pleasant agreement, although the experimental data suggests a slightly stronger enhancement of collectivity toward  $N = 40$ .

Calculations with the interacting boson model were performed for  $^{56,58,60,62}\text{Cr}$ . They are able to reproduce the experimental excitation energies and transition strengths with reasonable accuracy but do not indicate a significant degree of quadrupole deformation. Other isotopes that were produced in the experiment were investigated with respect to the identification of  $\gamma$ -ray transitions and level lifetimes. Of particular interest are the neutron-rich  $^{59,61}\text{Mn}$  isotopes ( $Z = 25$ ), for which level lifetimes of the  $7/2_1^-$ ,  $9/2_1^-$  and  $11/2_1^-$  states were determined (in  $^{61}\text{Mn}$  the assignment is only tentative). In addition, level lifetimes in  $^{63}\text{Mn}$  of the tentatively assigned ( $7/2_1^-$ ) and ( $9/2_1^-$ ) states were evaluated. The results are compared to shell-model calculations using the  $fp$  interaction KB3G as well as the state-of-the-art interaction LNPS- $m$ . The present data indicates a structural change close to  $N = 36$ . The experimental data for  $^{61}\text{Mn}$  suggests that the  $B(\text{M}1)$  value for the  $7/2_1^- \rightarrow 5/2_{\text{gs}}^-$  is underestimated by the LNPS- $m$  interaction when free  $g$  factors are used.

In the second part of this thesis, a tool is presented which allows to generate  $\gamma$ -ray spectra of lifetime studies based on the electromagnetic Doppler-shift using empirical parameters. The tool is highly flexible which enables the incorporation of various experimental bounding conditions. It is applied to investigate the influence of velocity distributions on the lifetime analysis and results indicate that systematic deviations are minimized if distance-dependent mean recoil velocities are taken into account.

---

## Zusammenfassung

Kernziel dieser Arbeit ist die experimentelle Bestimmung der Lebensdauer angeregter Kernzustände in  $^{58,60,62}\text{Cr}$  unter Verwendung der etablierten Recoil Distance Doppler-shift Methode, aus denen modellunabhängige Übergangswahrscheinlichkeiten gewonnen werden können.

Das dazugehörige Experiment wurde am National Superconducting Cyclotron Laboratory an der Michigan State University (USA) durchgeführt. Hierbei wurden angeregte Kernzustände in  $^{58,60,62}\text{Cr}$  durch Protonen-Knockout an schnellen  $^{59,61,63}\text{Mn}$ -Isotopen bevölkert. Im Rahmen dieser Arbeit konnten Lebensdauern der Zustände  $2_1^+$ ,  $4_1^+$  sowie – im Falle von  $^{58,60}\text{Cr}$  – der  $6_1^+$  Zustände bestimmt werden. In  $^{58,60,62}\text{Cr}$  sind die experimentellen reduzierten Übergangswahrscheinlichkeiten des  $2_1^+ \rightarrow 0_{\text{gs}}^+$  Übergangs in Einklang mit bereits bekannten Übergangsstärken, die aus Experimenten unter Verwendung der Coulomb-Anregung gewonnen wurden, obschon die vorliegenden Werte ein höheres Maß an Kollektivität vermuten lassen. Die  $4_1^+$ - und  $6_1^+$ -Zustände in  $^{58}\text{Cr}$  zeigen ein dem  $2_1^+$  Zustand ähnliches kollektives Verhalten, während aus den Übergangsstärken bestimmte Verhältnisse in  $^{60,62}\text{Cr}$  eher auf Rotor-artiges Verhalten mit ausgeprägten Quadrupoldeformationen  $\beta_2 \sim 0.3$  hinweisen. Verglichen mit den benachbarten Eisen-Isotopen zeigen die Chrom-Isotope eine ähnliche kollektive Entwicklung hin zu  $N = 40$ , obschon diese in Chrom leicht erhöht erscheint.

Die Ergebnisse werden im Rahmen des Schalenmodells unter Verwendung der modernen Wechselwirkung LNPS in einem erweiterten Modellraum diskutiert. Dabei wird eine gute Übereinstimmung beobachtet, wobei die LNPS-Rechnungen den experimentell beobachteten Anstieg der Kollektivität hin zu  $N = 40$  tendenziell unterschätzen.

Für neutronenreiche Chrom-Isotope wurden Rechnungen im IBM durchgeführt. Diese reproduzieren die experimentellen Daten mit zufriedenstellender Genauigkeit, bedingen allerdings kein hohes Maß an Quadrupoldeformation.

Weitere im Rahmen dieses Experiments bevölkerte Isotope wurden untersucht. Hervorzuheben sind hierbei die neutronenreichen  $^{59,61}\text{Mn}$  Isotope, für die Lebensdauerinformationen der angeregten  $7/2_1^-$ ,  $9/2_1^-$  und  $11/2_1^-$  Zustände (die Zuordnung in  $^{61}\text{Mn}$  ist bis dato nur vorläufig) extrahiert werden konnten. Ferner konnten in  $^{63}\text{Mn}$  die Lebensdauer zweier angeregter Zustände bestimmt werden, deren Zuordnung zu  $7/2_1^-$  und  $9/2_1^-$  noch bestätigt werden muss. Die Diskussion dieser Ergebnisse im Rahmen des Schalenmodells geschieht durch Vergleich mit der KB3G Wechselwirkung sowie der weiterentwickelten LNPS- $m$  Wechselwirkung. Dabei wird eine strukturelle Veränderung in unmittelbarer Nähe zu  $N = 36$  beobachtet. Dies ähnelt dem Verhalten der benachbarten Eisen-Isotope. Zum Abschluss wird eine Simulation vorgestellt, mit der – unter Berücksichtigung rein empirischer Parameter – Simulationen von Lebensdauer-messungen im Pikosekunden-Bereich durchgeführt werden können. Das Programm zeichnet sich durch ein hohes Maß an Flexibilität aus, sodass unterschiedliche experimentelle Randbedingungen berücksichtigt werden können. Im Rahmen dieser Arbeit wird die Anwendung dieses Programms auf die Untersuchung von Geschwindigkeitsverteilungen mit relativen Breiten bis zu  $\sim 30\%$  diskutiert. Die Ergebnisse erlauben den Rückschluss, dass die Annahme von abstandsabhängigen mittleren Rückstoßgeschwindigkeiten in der Lebensdaueranalyse systematische Abweichungen minimieren.



---

# Contents

<b>I. Lifetime Measurements in Neutron-rich Isotopes close to <math>N = 40</math></b>	<b>1</b>
<b>1. Introduction</b>	<b>2</b>
1.1. The Recoil Distance Doppler-Shift Technique and its Application at NSCL	4
<b>2. Experimental Setup</b>	<b>7</b>
2.1. Development and Purification of the Cocktail Beam	7
2.2. The Spectrograph S800	9
2.3. The Plunger Device TRIPLEX	11
2.4. The Segmented Germanium Array	13
<b>3. Data Preparation</b>	<b>15</b>
3.1. The SeGA in Plunger Configuration	15
3.1.1. Geometry of the SeGA Detectors	15
3.1.2. Data Taken with a Standard $^{152}\text{Eu}$ Source	17
3.1.3. Background Measurement	22
3.1.4. Doppler Reconstruction	23
3.2. Plunger Device	25
3.2.1. Calculation of Zero Offsets	25
3.2.2. Calculation of Absolute Foil Separations	28
3.2.3. Plunger Foil Thicknesses	28
3.3. S800 Calibration	30
3.3.1. Calibration of the CRDC Detectors	30
3.3.2. Calibration of the Ionisation Chamber	31
3.3.3. Correction of Time-of-Flight Signals	32
3.4. Particle Identification and Gate Conditions	36
<b>4. Analysis</b>	<b>39</b>
4.1. Determination of Transition Energies	39
4.2. Lifetime Estimates from Decay Curves	39
4.3. Determination of Level Lifetimes Using a Realistic Monte Carlo Simulation	40
4.3.1. Relativistic effects	41
4.3.2. Effect of the Level Lifetime on the Line Shape	42
4.3.3. Changes to the Code G4LifeTimeG	42
4.4. Error Estimates	43
4.5. Calculation of Transition Strengths and Related Signatures	47
<b>5. Results</b>	<b>49</b>
5.1. Composition of the Cocktail Beams	49
5.2. $^{58}\text{Cr}_{34}$ - Measurement of $\gamma$ -Ray Transition Energies and Level Lifetimes	53

5.3.	$^{60}\text{Cr}_{36}$ - Measurement of $\gamma$ -Ray Transition Energies and Level Lifetimes . . . . .	59
5.4.	$^{62}\text{Cr}_{38}$ - Measurement of $\gamma$ -Ray Transition Energies and Level Lifetimes . . . . .	64
5.5.	Vanadium Isotopes . . . . .	69
5.5.1.	$^{56}\text{V}_{33}$ - Measurement of $\gamma$ -Ray Transition Energies . . . . .	69
5.5.2.	$^{55}\text{V}_{32}$ - Measurement of $\gamma$ -Ray Transition Energies and Level Lifetimes . . . . .	70
5.6.	Other Chromium Isotopes . . . . .	73
5.6.1.	$^{57}\text{Cr}_{33}$ - Measurement of Level Lifetimes . . . . .	73
5.7.	Manganese Isotopes . . . . .	76
5.7.1.	$^{59}\text{Mn}_{34}$ - Measurement of Level Lifetimes . . . . .	76
5.7.2.	$^{61}\text{Mn}_{36}$ - Measurement of Level Lifetimes . . . . .	80
5.7.3.	$^{63}\text{Mn}_{38}$ - Measurement of Level Lifetimes . . . . .	83
5.8.	$^{64}\text{Fe}_{38}$ - Measurement of Level Lifetimes . . . . .	87
5.9.	Summary . . . . .	90
<b>6.</b>	<b>Discussion</b> . . . . .	<b>91</b>
6.1.	Qualitative Discussion for Even-Even Nuclei . . . . .	91
6.2.	The Interacting Boson Approximation . . . . .	95
6.2.1.	Choice of the IBM-1 Hamiltonian . . . . .	95
6.2.2.	IBM-1 Calculations for Neutron-Rich Cr Isotopes . . . . .	97
6.2.3.	Comparison of $^{58,60,62}\text{Cr}$ with the Critical Point Symmetry E(5) . . . . .	100
6.3.	Shell Model Framework . . . . .	102
6.3.1.	Comparison of $^{58,60,62}\text{Cr}$ with the LNPS Interaction . . . . .	102
6.3.2.	Comparison of $^{59,61,63}\text{Mn}$ with the KB3G and LNPS- <i>m</i> Interactions . . . . .	106
<b>7.</b>	<b>Summary</b> . . . . .	<b>112</b>
<b>II.</b>	<b>Development of a Simulation Tool for RDDS Spectra</b> . . . . .	<b>113</b>
<b>8.</b>	<b>Motivation</b> . . . . .	<b>114</b>
<b>9.</b>	<b>Basic Properties</b> . . . . .	<b>116</b>
9.1.	Sketch of an Iteration . . . . .	117
9.2.	Tracking of Events . . . . .	118
9.3.	Limitations . . . . .	119
<b>10.</b>	<b>Proof of Principles</b> . . . . .	<b>120</b>
10.1.	Simulation of $^{58}\text{Cr}$ . . . . .	120
10.2.	Determination of Absolute Foil Separations in a Multi-Nucleon Transfer Experiment . . . . .	122
10.3.	The Impact of Velocity Distributions on RDDS Spectra . . . . .	124
<b>11.</b>	<b>Summary</b> . . . . .	<b>130</b>
<b>A.</b>	<b>Considered Transitions in <math>^{152}\text{Eu}</math> Data</b> . . . . .	<b>131</b>

<b>B. Decay Curves in <math>^{58,60,62}\text{Cr}</math></b>	<b>132</b>
<b>C. Reacted Beam Cuts</b>	<b>134</b>
<b>D. Experimental Data - Systematics</b>	<b>138</b>
<b>E. Theoretical Calculations</b>	<b>142</b>
E.1. Shell-Model Calculations for $^{56,58,60,62,64}\text{Cr}$ . . . . .	142
E.2. Shell-Model Calculations for $^{59,61,63}\text{Mn}$ . . . . .	144
<b>F. Input Parameters for the Monte Carlo Simulation</b>	<b>146</b>
<b>Bibliography</b>	<b>152</b>

---

Part I.

Lifetime Measurements in  
Neutron-rich Isotopes close to  
 $N = 40$

---

# 1. Introduction

The atomic nucleus is a many-body system consisting of interacting fermions, represented by the neutrons and the protons. The fermionic nature of the nucleons in combination with the attractive nuclear potential leads directly to inherent shell-like configurations.

From an experimental perspective, Kurt Guggenheimer in 1933 was among the first to link discontinuities in the (neutron/proton) separation energies at certain neutron/proton numbers to such a shell structure, which have been called *magic numbers* later on. However, model-based theoretical calculations performed in the 1930's were able to reproduce only part of these numbers. It took over fifteen years till the crucial role of the spin-orbit coupling for the nuclear structure was fully realized. Calculations within a mean-field (shell) model performed by Maria Goeppert-Mayer and Hans Jensen showed that such a term in the Hamiltonian is mandatory to reproduce these *magic numbers*. In 1963, their efforts were rewarded with the Noble prize in physics and the nuclear shell model with its various derivatives can safely be considered as one of the corner stones in modern nuclear physics.

In recent years it was found that the magic numbers cannot retain their universal character when leaving the valley of  $\beta$  stability toward nuclei with extreme isospins as a result of residual nucleon-nucleon interactions. Examples for collapsing shell closures, e.g. in  $^{32}_{12}\text{Mg}_{20}$  [Dét79; Mot95] and  $^{42}_{14}\text{Si}_{28}$  [Bas07], as well as emerging shell gaps, e.g. in  $^{24}_8\text{O}_{16}$  [Hof09; Kan09] and  $^{54}_{20}\text{Ca}_{34}$  [Ste13], were found in the light to medium mass region of the nuclear landscape. Many of these observations were enabled by the advent of Radioactive Ion Beam (RIB) facilities in conjunction with efficient (and segmented) High-Purity Germanium (HPGe) arrays and highly efficient spectrometers for particle-identification purposes, which have allowed to expand the borders of experimentally accessible nuclei step by step toward the proton and neutron drip lines. Many efforts were also invested to understand the *shell evolution*, i.e. the evolution of single-particle energies as a function of neutron and proton numbers ( $N$  and  $Z$ ), in regions characterized by rapidly changing structures, e.g. in the vicinity of emerging/collapsing shell closures.

One example is the so-called *island of inversion* around  $^{32}\text{Mg}$ , where deformed  $2p-2h$  intruder configurations are energetically favoured compared to canonic  $0p-0h$  structures. Another interesting region of the nuclear landscape is given by the neutron-rich isotopes around  $^{68}\text{Ni}$  ( $N = 40$ ), where the emergence of another island of inversion around  $^{64}\text{Cr}$  was suggested [Len10].

In  $^{68}\text{Ni}$ , the high  $2^+_1$  state energy of 2033 keV [Bro95] as well as the small reduced transition strength of  $B(E2; 2^+_1 \rightarrow 0^+_{\text{gs}}) = 51(12) e^2\text{fm}^4$  [Sor02; Bre08] are substantial signatures expected for a nucleus at a (sub-)shell closure. In addition, the existence of low-lying  $0^+$  states is interpreted due to  $n$ -particle  $n$ -hole excitations related to shape coexistence (see, e.g., Ref. [Tsu14]), which is believed to act as a doorway toward the island of inversion (see, e.g., Ref. [Now16]). The interpretation of  $N = 40$  as a (sub-)shell closure is questioned by the fact that only a weak and very localized closure in  $^{68}\text{Ni}$  was observed

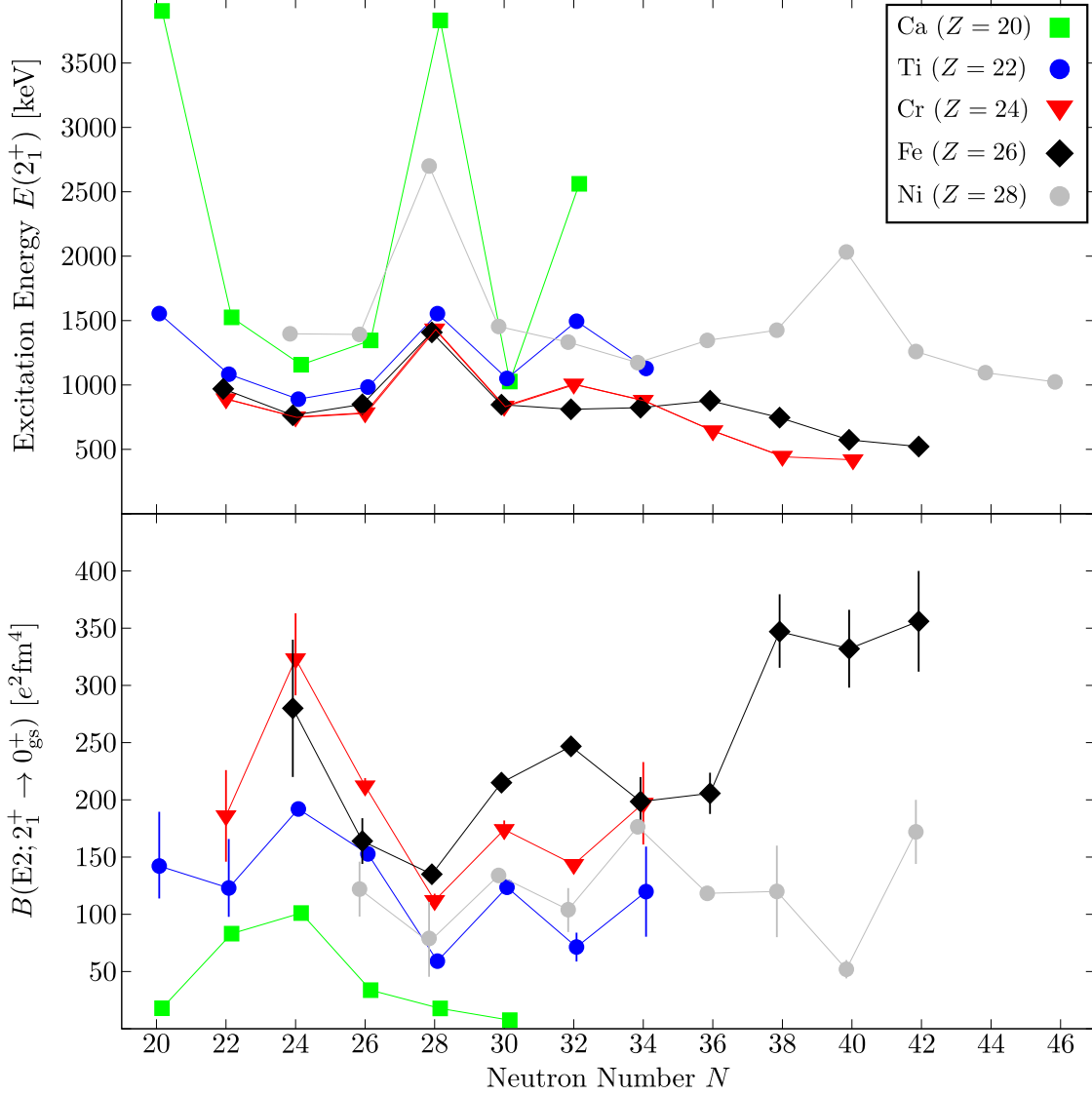


Figure 1.1.: Systematics of excitation energies for the first  $2^+$  state ( $E(2_1^+)$ ) (*top*) and  $B(E2; 2_1^+ \rightarrow 0_{gs}^+)$  values (*bottom*) for even-even nuclei with  $20 \leq Z \leq 28$ . Shown are experimental data published till the beginning of 2012.

[Gué07] and by a theoretical study of Langanke and colleagues [Lan03], which concludes that the calculated transition strength to the first  $2_1^+$  state in  $^{68}\text{Ni}$  exhausts only a fraction of the low-lying  $B(E2)$  strength and that a significant part of the experimental  $B(E2)$  strength resides in excited states above 4 MeV.

Reducing the number of protons by two, the even-even iron isotopes show rapidly decreasing  $E(2_1^+)$  energies [ENSDF; Lid13] and increasing  $B(E2; 2_1^+ \rightarrow 0_{gs}^+)$  values [Lju10; Rot11; Cra13] toward  $N = 40$ . Within the shell model, this onset of quadrupole collectivity is only reproduced if the neutron valence space is expanded with the  $g_{9/2}$  and  $d_{5/2}$  orbitals. One interaction tailored to such an enlarged model space is the effective interac-

tion LNPS [Len10], which has been applied successfully to various isotopes in the  $N = 40$  region [Rec12; Cra13; Lou13; Rec13]. Shell-model calculations using the LNPS interaction were performed for chromium isotopes and predict a rapid increase in quadrupole collectivity toward  $N = 40$  which is associated with a pronounced quadrupole deformation ( $\beta_2 \sim 0.3$ ) as a result of significant contributions from neutron  $2p - 2h$  and  $4p - 4h$  excitations [Len10]. In fact, the experimental  $E(2_1^+)$  values in  $^{60,62,64}\text{Cr}_{36,38,40}$  depicted in Fig. 1.1 show a monotonic decrease [Sor03; Zhu06; Gad10].

The main motivation of the present work is to investigate the evolution of quadrupole collectivity toward  $N = 40$  in more detail. For this purpose, lifetimes of excited states in  $^{58,60,62}\text{Cr}$  were measured with the recoil distance Doppler-shift (RDDS) technique, which allows a model-independent determination of reduced transition strengths. The present experiment was performed at the National Superconducting Cyclotron Laboratory (NSCL) at the Michigan State University (MSU).

Prior to the experiment, only the  $B(E2; 2_1^+ \rightarrow 0_{\text{gs}}^+)$  value in  $^{58}\text{Cr}$  was known from a Coulomb-excitation experiment performed at intermediate energies [Bür05]. In addition, a complimentary Coulomb-excitation experiment on  $^{58,60,62}\text{Cr}$  was performed in 2010. The results were published in 2012 [Bau12] and support the predicted increase of collectivity. Still, information on transition strengths for higher-lying transitions are mandatory to describe the structure of these nuclei in more detail, e.g. in terms of the nuclear shape.

This part of the thesis reports on the results of this experiment for  $^{58,60,62}\text{Cr}$  as well as for neighbouring nuclei, in particular  $^{59,61,63}\text{Mn}$ .

## 1.1. The Recoil Distance Doppler-Shift Technique and its Application at NSCL

Lifetimes of excited states in neutron-rich chromium isotopes were measured with the established RDDS technique (see Ref. [Dew12] for an extended review), which can be applied to investigate level lifetimes in the ps range. Following the systematics in neighbouring iron and chromium isotopes as well as theoretical predictions, level lifetimes for low-lying yrast states in  $^{58,60,62}\text{Cr}$  within the range of 1 ps to 200 ps were expected, which made the RDDS technique applicable. Using the present experiment as a guideline, its application at NSCL is briefly outlined in the following.

A radioactive cocktail beam is produced by fragmentation of a  $^{82}\text{Se}$  ( $E = 140 \text{ MeV}/u$ ) beam on a  $^9\text{Be}$  production target. The cocktail beam is then filtered for the desired isotope (here:  $^{59,61,63}\text{Mn}$ ) via the in-flight separation technique using the fragment separator A1900 [Mor03] (see Sec. 2.1).

The purified cocktail beam is guided to the experimental place located right in front of the S800 spectrograph [Baz03], where it impinges on a secondary target foil located in the plunger device. Here, (excited) states in the nucleus of interest are populated by means of a suiting reaction mechanism (e.g. knockout, Coulomb excitation or multi-nucleon removal reactions). In the experiment at hand, a light and highly absorptive Be target<sup>1</sup> is placed at the secondary target position, which is well-suited for the required one-proton

---

<sup>1</sup>The isotope  $^9\text{Be}$  has no bound state. In the optical model it can be considered as a highly absorptive disk to incident particles.

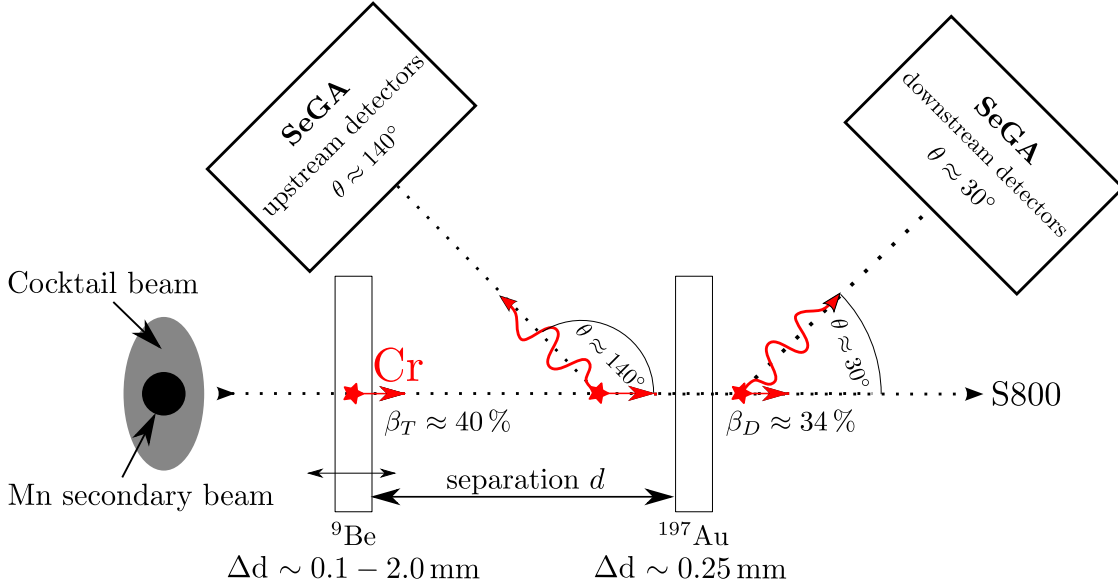


Figure 1.2.: Schematic sketch of the recoil distance Doppler-shift technique applied at the NSCL using the plunger device TRIPLEX (two-foil configuration), the Segmented Germanium Array and the magnetic spectrograph S800 in combination with fast radioactive beams. Foil thicknesses  $\Delta d$  refer to the present experiment.

knockout reaction mechanism.

Recoils leaving the experimental target have typically an energy of  $90 \text{ MeV}/u$ , corresponding to recoil velocities with respect to the speed-of-light (from now on called  $\beta$  velocity,  $\beta = v/c$ ) of  $\beta_T \approx 0.4$ . A degrader made of gold is placed in a well-defined but adjustable separation with respect to the target and allows to slow down the recoils to  $\beta_D \approx 0.34$ .

The decay of an excited state follows the nuclear decay law and, thus, has a characteristic time behaviour. A detector placed at a polar angle  $\theta$  with respect to the recoil trajectory will observe a Doppler-shifted energy  $E_{ds}$  compared to the intrinsic  $\gamma$ -ray energy  $E_0$  which depends on the  $\beta$  velocity as well as the polar angle  $\theta$  according to:

$$E_{ds}(\beta, \theta) = E_0 \frac{\sqrt{1 - \beta^2}}{1 - \beta \cos \theta} \quad (1.1)$$

Simplified speaking and neglecting decays within a foil, the de-excitations can take place either between the foils (characterized by the  $\beta$  velocity  $\beta_T$ ) or behind the degrader (characterized by the  $\beta$  velocity  $\beta_D$ ). The energy deposition of the experimentally detected  $\gamma$  ray will therefore depend on the recoil position at the time of the emission. As a result, for each transition two peaks (labelled fast or target component ( $\beta_T$ ) and slow or degrader component ( $\beta_D$ )) will occur in the  $\gamma$ -ray spectrum (at Doppler-shifted energies). The intensity ratio between the two peaks depends on the foil separation, the time behaviour of the feeding pattern as well as the level lifetime  $\tau$ .

If the flight time through a foil is of the order of the lifetime, slowing-down processes will have a significant impact on the line shape and, hence, need to be taken into account

in the analysis. The Segmented Germanium Array (SeGA) was used in the present experiment for the detection of  $\gamma$  rays, with detectors placed in two rings at  $\theta \approx 30^\circ$  and  $\theta \approx 140^\circ$  with respect to the beam axis.

Recoils leaving the plunger device enter the magnetic spectrograph S800 and are identified by means of time-of-flight and energy-loss measurements. In addition, the recoil trajectory is reconstructed and the  $\gamma$ -ray energies are Doppler-reconstructed event by event, for which the recoil velocity vector behind the plunger foils as measured with S800 is taken into account.

A schematic sketch depicting the application of the RDDS technique at NSCL is shown in Fig. 1.2.

### Major Differences Compared to Standard Plunger Experiments

Compared to standard plunger experiments as performed, e.g., at the Cologne FN tandem facility, the discussed experiment differs in various aspects, of which the most important ones shall be outlined.

First, the required recoil identification demands the use of a degrader instead of a stopper. Due to the large recoil velocities, a separation of fast and slow component is feasible for  $\Delta\beta = \beta_T - \beta_D \gtrsim 6\%$ , with the precise value depending on the energy of the  $\gamma$ -ray transition and the detector angle.

Second, the beam energies are significantly higher. They are of the order of a few MeV/ $u$  in standard experiments, while at NSCL they are around 100 MeV/ $u$  for (filtered) radioactive beams produced by in-flight separation. It is therefore mandatory to take into account relativistic effects, such as Doppler broadening, the Lorentz boost and relativistic aberration effects.

Third, typical beam intensities at NSCL with the present setup are around  $10^3$  to  $10^5$  pps and, hence, much lower compared to stable beam intensities of  $\sim 1 - 2$  pA ( $\sim 10^{12}$  pps). For compensation, the relativistic beam energies allow to use significantly thicker foils with thicknesses between few hundred micrometers and few millimetres. Still, experiments at the NSCL are low statistics experiments. Therefore only few foil separations are measured and the analysis is limited to particle- $\gamma$  (instead of particle- $\gamma\gamma$ ) coincidences.

Fourth, lifetime experiments at the NSCL using fast beams are typically performed with direct reactions, which – compared to fusion evaporation – are characterized by low  $\gamma$ -ray multiplicities.

Fifth and as a consequence of the large recoil velocities of  $\sim 100$   $\mu\text{m}/\text{ps}$  in combination with thick targets, the line shape of the observed  $\gamma$ -ray transition is often influenced by slowing-down and solid-angle effects.

---

## 2. Experimental Setup

The present experiment was performed at the National Superconducting Cyclotron Laboratory at Michigan State University, USA. The NSCL facility plays a pivotal role in experimental nuclear structure as well as nuclear reaction physics and is one of the leading facilities<sup>1</sup> for experiments using the in-flight separation technique<sup>2</sup> [Mor04], which is employed to produce radioactive beams at intermediate energies ( $E \sim 100$  MeV/ $u$ ) with high purities.

Main purpose of the experiment was a measurement of low-lying level lifetimes in  $^{58,60,62}\text{Cr}$ , which were populated by one-proton knockout from radioactive secondary beams  $^{59,61,63}\text{Mn}$ . For collective nuclei, the cross section of electromagnetic Coulomb interactions (at intermediate energies) exceeds the one-nucleon knockout reaction cross section usually by one order of magnitude. Still, the knockout reaction is a powerful tool since it benefits from the dominating nuclear interaction, thereby enabling – in the case of even-even nuclei – a population of states beyond the first  $2^+$  state.

For the present experiment, the settings of the fragments separator were optimized for each secondary beam to ensure high absolute secondary beam intensities while maintaining high beam purities. In addition, the plunger foil configurations were adjusted to the expected secondary beam intensities and level lifetimes. As a consequence, the experiment was divided into three parts characterized by three different experimental settings: The first setting was optimized for the secondary beam  $^{59}\text{Mn}$ , while the second and third settings were optimized for the secondary beams  $^{61}\text{Mn}$  and  $^{63}\text{Mn}$ , respectively.

This chapter is structured as follows: In Sec. 2.1 the development of primary and secondary radioactive beams is described. Here, the focus is on the filtering of the cocktail beam using the A1900 fragment separator. In Sec. 2.2 the S800 spectrograph, its focal-plane detector system and its use for the particle identification is discussed. In Sec. 2.3 the plunger device TRIPLEX and the chosen foil configurations are explained. In the final Sec. 2.4 of this chapter, the Segmented Germanium Array (SeGA) for the detection of  $\gamma$  rays is described.

### 2.1. Development and Purification of the Cocktail Beam

The Coupled Cyclotron Facility (CCF) [Mil01] provided a primary beam of  $^{82}\text{Se}$ , which was accelerated in the cyclotrons K500 and K1200 to an energy of 140 MeV/ $u$ .

---

<sup>1</sup>The leading role will be further cemented by the upcoming Facility for Rare Isotope Beams (FRIB) located at MSU, which will allow quantitative measurements in very exotic nuclei using fast, stopped and re-accelerated rare isotope beams.

<sup>2</sup>The GSI facility in Germany and the RIKEN facility in Japan follow a similar approach at higher beam energies.

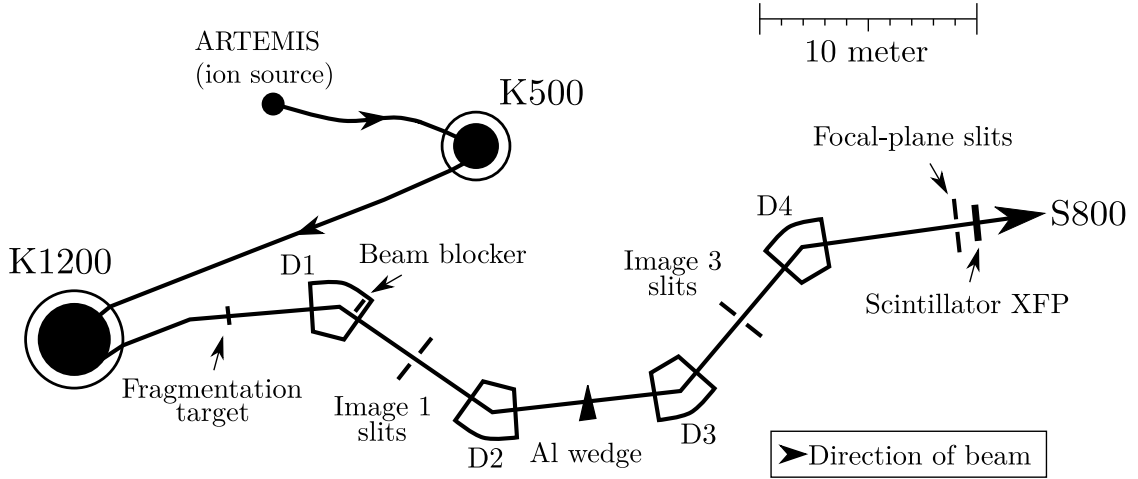


Figure 2.1.: Schematic sketch depicting the primary beam development (CCF) and the filtering of the secondary cocktail beam (A1900). The direction of the beam is indicated by arrows. Scintillators, fragmentation target, wedge and relevant slit systems are shown. See text for details.

The development of the primary beam<sup>3</sup> began with the extraction of  $^{82}\text{Se}$  out of the electron cyclotron resonance (ECR) ion source ARTEMIS [Koi00]. Following a pre-acceleration,  $^{82}\text{Se}$  particles were axially injected into the K500 cyclotron, in which they were accelerated up to an energy of  $12.24\text{ MeV}/u$ . The K1200 cyclotron was then used to accelerate the particles to their final energy of  $140\text{ MeV}/u$ . The cyclotron was operated at a radio frequency set to  $23.1392\text{ MHz}$ .

The primary beam of  $^{82}\text{Se}$  was then guided to the (primary)  $^9\text{Be}$  fragmentation target (FT) placed at the object point of the fragment separator A1900 [Mor03]. The induced fragmentation reactions produced a radioactive cocktail beam that consisted of a vast variety of isotopes south-west of  $^{82}_{34}\text{Se}$  ( $1 \leq Z \leq 34, 1 \leq N \leq 48$ ). The A1900 separated the constituents of the cocktail beam according to their magnetic rigidities,  $B\rho$ . The main components of the A1900 are two pairs of magnetic dipoles (D1/D2 and D3/D4), a wedge-formed aluminium degrader placed in-between these pairs, various slit systems as well as retractable detectors for particle-identification purposes (see Fig. 2.1 for a schematic sketch).

The wedge-formed aluminium degrader fulfils two purposes: First, its shape leads to an energy loss  $\Delta E$  that depends on the recoil position along the dispersive axis. Fast recoils are thereby stronger decelerated compared to slow recoils. This has a focusing effect with respect to the energy. Second, the  $Z^2$  dependence of the stopping power reduces the contribution of undesired isotopes with different atomic number but comparable rigidities. To limit the amount of (unreacted) primary beam particles, a beam stopper is placed at

<sup>3</sup>The experiment was proposed with a primary beam of  $^{76}\text{Ge}$ , but it was performed with a then available beam of  $^{82}\text{Se}$ . The fragmentation cross sections for the relevant Mn isotopes remain almost unchanged (see Refs. [Tar09; Tar13]), but still, there were two advantages: First,  $^{82}\text{Se}$  was available with a higher beam intensity ( $35\text{ pA}$  vs  $25\text{ pA}$ ). Second,  $^{82}\text{Se}$  was provided with a higher beam energy ( $140\text{ MeV}/u$  vs.  $130\text{ MeV}/u$ ), which is beneficial for the filtering of the secondary beams.

	Setting 1	Setting 2	Setting 3
Primary Beam	$^{82}\text{Se}$ with $E = 140$ MeV/ $u$		
FT $^9\text{Be}$ – thickness [ $\frac{\text{mg}}{\text{cm}^2}$ ]	352	540	517
$B\rho$ of D1/D2 [Tm]	3.76189	3.73340	3.89370
Image 1 slits [mm]	[-16:16]	[-22.5:22.5]	[-29.25:29.25]
Momentum acceptance $\pm\Delta p$ [%]	1.09	1.53	1.98
Wedge – $0^\circ$ thickness [ $\frac{\text{mg}}{\text{cm}^2}$ ]	390	240	180
$B\rho$ of D3/D4 [Tm]	3.36680	3.48130	3.70659
Focal-plane slits [mm]	[-5:5]	[-5:5]	[-5:5]
Secondary beams	$^{59}\text{Mn}$ , $^{60}\text{Fe}$	$^{61}\text{Mn}$ , $^{62}\text{Fe}$ , $^{63}\text{Fe}$ , $^{60}\text{Cr}$	$^{63}\text{Mn}$ , $^{64}\text{Fe}$ , $^{65}\text{Fe}$ , $^{61}\text{Cr}$
Intensity $^x\text{Mn}$ [pps]	$2.55 \cdot 10^5$	$1.82 \cdot 10^4$	$1.37 \cdot 10^3$
Energy before XFP $^x\text{Mn}$ [MeV/ $u$ ]	93.7	91.6	97.4
Purity at A1900 FP $^x\text{Mn}$ [%]	53	40	16

Table 2.1.: Information on the A1900 settings and key properties of the secondary cocktail beams. The quoted secondary beam intensities and energies were provided by the A1900 group. See text for details.

the exit of the first dipole magnet D1. The image 1 slits between D1 and D2 define in first order the momentum acceptance of A1900, while the image 3 slits between D3 and D4 in combination with the focal-plane slits improve the beam purity.

A 109- $\mu\text{m}$ -thick plastic (BC404) scintillator (XFP) placed at the focal plane of A1900 is used for timing purposes, which during the experiment allows to identify the constituents of the cocktail beam by a time-of-flight measurement. Relevant quantities describing the experimental settings of A1900 and basic secondary beam properties are listed in Table 2.1. In Ref. [Mor03], the resolving power  $R$  of A1900 is quantified by  $R = 2915$ .

Downstream of the A1900 focal plane the particles follow a transfer line ( $\sim 25$  m in length) toward the S800 spectrograph, which is explained in the following section.

## 2.2. The Spectrograph S800

After passing the transfer line, the secondary beam particles enter the S800 spectrograph [Baz03], which is shown schematically in Fig. 2.2. The S800 consists of two parts:

- **The analysis line**

This part fulfills beam-tuning purposes. It begins at the object point of S800 and ends at the experimental position where in the present experiment the plunger apparatus is placed. This position can be regarded as the pivot point of S800.

- **The spectrograph**

The main components of the spectrograph are two  $75^\circ$  dipoles and the focal-plane detector system [Yur99].

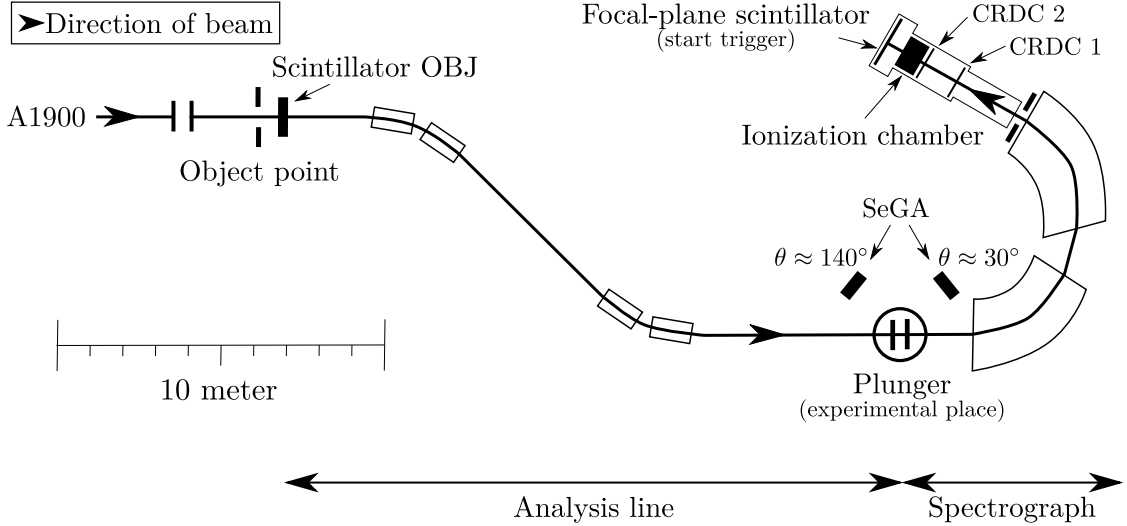


Figure 2.2.: Schematic sketch of the S800 spectrograph, that consists of analysis line and spectrograph. See text for details.

The S800 was used in *focused mode*, which enables the maximum momentum acceptance and in which the coordinates of fragments/recoils at the S800 focal plane are sensitive to the incoming beam/recoil momenta.

The object point holds a 130- $\mu\text{m}$ -thick plastic (BC404) scintillator (OBJ) for timing purposes which can be used for rates up to 1 MHz. The beam is guided from the object point toward the pivot point, where the plunger device is placed. Reacted and unreacted particles enter the spectrograph which separates them according to their rigidities. A slit system is placed right in front of the focal-plane detector system to prevent unreacted secondary beam particles from entering the focal-plane detector system.

### Cathode Readout Drift Chambers

The first component of the S800 focal-plane detector system is a pair of two Cathode Readout Drift Chambers (CRDC) [Fuc92] which are divided by a separation of 1 m. A CRDC is essentially a gas-filled detector with a sub-mm position resolution, nominatively given by 0.5 mm [Yur99]. The active area is  $\pm 28$  cm (dispersive direction) times  $\pm 13$  cm (non-dispersive direction), while the active depth is 1.5 cm.

Information on the dispersive coordinate ( $x$ ) is obtained by a multi-cathode method (pad width 2.54 mm), while information on the non-dispersive coordinate is obtained by measuring the electron drift time following recoil-induced ionizations. The CRDCs are filled with 80 %  $\text{CF}_4$  and 20 % isobutane at a gas pressure of 140 Torr [Yur99]. Due to the comparably slow electron drift velocities  $v_e \sim 50 \mu\text{m}/\text{ns}$ , the safe operation of the CRDC detectors is limited to rates of few kHz.

Since both CRDCs measure ( $x, y$ ) coordinates, the trajectory vector of particles entering the focal plane can be determined.

### Path Reconstruction

Knowing the properties of the magnetic field in the S800 spectrograph, the trajectory at the focal plane, the recoil mass  $m$  as well as its charge state  $Q$ , the ion optics code COSY INFINITY [Mak06] is used to calculate the transfer matrix  $\mathbf{S}$  to describe the particle transfer from the S800 pivot position (T) to its focal plane (FP).

This allows to reconstruct the recoil velocity vector at the pivot point, i.e. the position of the plunger degrader. Practically, the following relation is valid<sup>4</sup>:

$$\begin{pmatrix} -\alpha_{\text{T}} \\ y_{\text{T}} \\ \beta_{\text{T}} \\ \Delta E_{\text{T}}/E_{\text{kin}}^{\text{ref}} \end{pmatrix} = \mathbf{S}^{-1} \begin{pmatrix} -x_{\text{FP}} \\ -\alpha_{\text{FP}} \\ y_{\text{FP}} \\ \beta_{\text{FP}} \end{pmatrix} \quad (2.1)$$

In this formula,  $\alpha(\beta)$  is the angle between reference path and (non-)dispersive axis given in radian. Similarly,  $x(y)$  are coordinates along the dispersive (non-dispersive) axis given in meters.  $\Delta E_{\text{T}}/E_{\text{kin}}^{\text{ref}}$  is the ratio of the kinetic energy difference between experimental and reference energy  $\Delta E_{\text{T}} = E_{\text{kin}}^{\text{exp}} - E_{\text{kin}}^{\text{ref}}$  to the kinetic energy of a reference particle which moves along the reference trajectory.

For such a reference particle, the product  $(\beta\gamma)^{\text{ref}}$  of  $\beta$  velocity and Lorentz factor  $\gamma$  is given according to:

$$(\beta\gamma)^{\text{ref}} = \frac{B\rho [\text{Tm}]}{3.107} \cdot \frac{Q}{m [\text{amu}]} \quad (2.2)$$

Here,  $B\rho$  is the rigidity of the S800 dipoles,  $Q$  is the charge state of the reference particle and  $m$  is its mass given in atomic mass units (amu) [Wan12]. From this relationship, the kinetic energy of the reference particle is given according to

$$E_{\text{kin}}^{\text{ref}} [\text{MeV}] = m [\text{MeV}/c^2] \cdot c^2 \cdot (\gamma^{\text{ref}} - 1) \quad (2.3)$$

### Segmented Ionization Chamber

Downstream of the CRDC detectors, a 16-fold segmented ionization chamber is placed to measure the energy loss of traversing particles. The ion chamber is filled with P10 (90 % Ar, 10 % CH<sub>4</sub>) at a typical pressure of 300 Torr [Yur99].

### Focal-plane Scintillator

In the experiment at hand, the last relevant component of the focal-plane detector system is a 1-mm-thick plastic scintillator, which provides the time reference relevant for the CRDCs as well as auxiliary detector components, such as SeGA. In the experiment, this scintillator triggers the event recording.

## 2.3. The Plunger Device TRIPLEX

The experiment was performed with the three-foil plunger device TRIPle PLunger for EXotic beams (TRIPLEX) [Iwa16], which was designed and manufactured at the Institut für Kernphysik (IKP) in Cologne. A picture of the device is shown in Fig. 2.3. The

<sup>4</sup>The signs are a result of differences between the experimental and the COSY coordinate systems.

## 2. Experimental Setup

discussed experiment was part of a short campaign in which TRIPLEX was used for the first time (see Refs. [Nic14; Nic15] for results of the accompanying experiment).

Compared to the already existing NSCL/Köln plunger device [Dew06], TRIPLEX can be used with three foils. This enables refined experimental applications of the RDDS technique, e.g. covering two distinct lifetime ranges within one foil setting (see Ref. [Iwa16] for details). In TRIPLEX, the position of the second foil holder is mechanically fixed. Hence, this foil defines the reference point, e.g. with respect to the surrounding  $\gamma$ -ray detector array.

The first and third foil holder can be moved along the beam axis with respect to the second foil holder. From a technical point of view this is achieved by a mechanical construction using three tubes of different diameters. Bearings with high precision and low tolerances allow a sliding movement of the outer and inner tube with respect to the central tube, where the latter is coupled to the second foil holder. Displacements up to 30 mm (corresponding to a flight time (particle frame) of roughly 230 ps for  $\beta = 0.4$ ) are feasible and limited by the maximum stroke of the built-in linear actuators (Nexact<sup>®</sup> N-381 manufactured by Physik Instrumente (PI) GmbH & Co. KG) which contain optical encoders to measure displacements with a resolution of 10 nm.

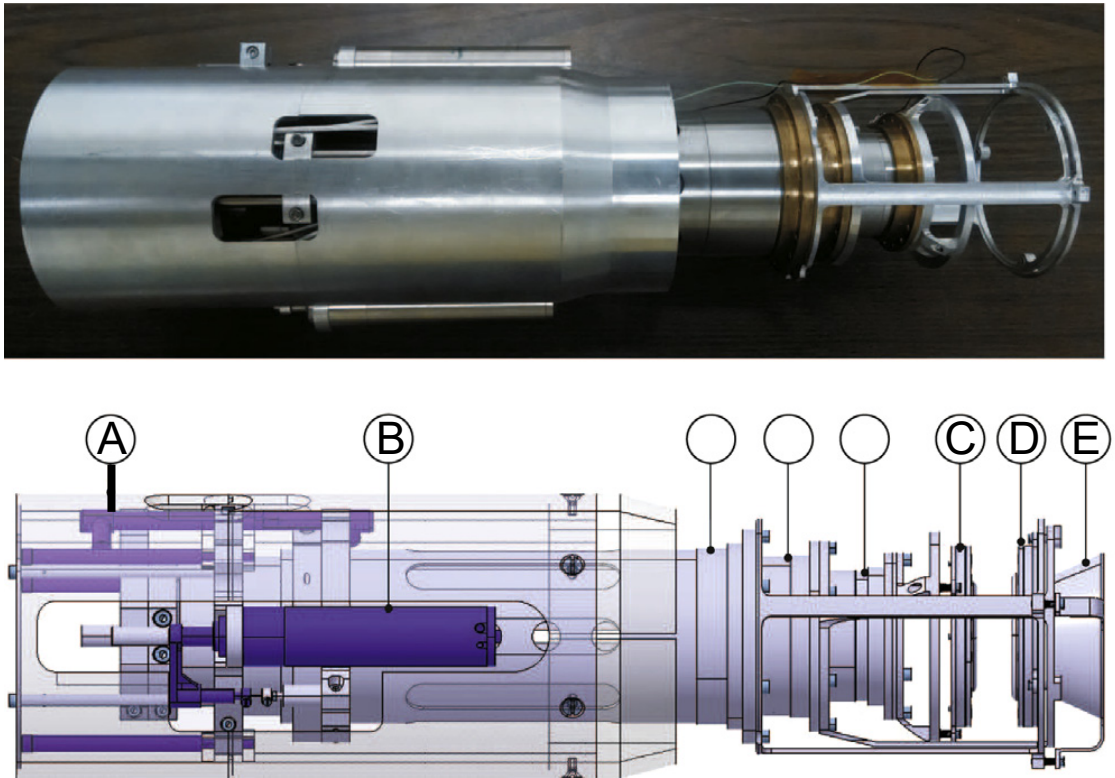


Figure 2.3.: (*Top*) Photograph of the TRIPLEX device without foil holders. (*Bottom*) Schematic sketch of TRIPLEX. A micrometer probe (A), a linear actuator (B) and foil holders (C,D,E) are identified [Iwa16]. Reprinted with permission from Elsevier.

	Setting 1	Setting 2	Setting 3
Plunger Target ( $^9\text{Be}$ )	287	520	1289
Plunger Degradar ( $^{197}\text{Au}$ )	252	252	252
Polyester Film (Mylar <sup>®</sup> )	50	50	50

Table 2.2.: Information on the plunger foil thicknesses (in  $\mu\text{m}$ ) for each experimental setting. See Sec. 3.2.3 for details.

The linear actuators are coupled mechanically to the first and third foil holder, respectively. The coupling is to some extent flexible and, hence, a motor movement may not induce a real displacement of the corresponding foil, e.g. in case of high friction<sup>5</sup>. For this purpose two axial micrometer probes (GTL 21/22 manufactured by TESA Technology) with an active range of 5 mm are coupled to the first and third foil holder.

A beryllium foil was used in the present experiment as a secondary target material and, hence, it was mounted onto the first foil holder. Beryllium was chosen because of its low mass and its absorptive character [Tos01]. The first is favourable for the kinematics, while the latter improves the cross section of knockout reactions. A gold foil was mounted onto the second foil holder and was used as a degrader. A thin polyester film was placed onto the third holder, which significantly reduced the contribution of incompletely ionized particles. In particular, the influence of the  $24^+$  charge state of Mn was drastically reduced, which lowered the number of secondary beam particles in the S800 focal plane significantly.

Due to the almost linear relationship between production yield and target thickness, it is in principal desired to use thick targets. This, however, is limited by two constraints: First, the recoil energy (downstream of the plunger device) has to be sufficiently large ( $E \geq 40 \text{ MeV}/u$ ) to allow an unambiguous event correlation. Second, it is desired to minimize the contribution of de-excitations taking place within a foil, because such decays affect the line shape.

A reduction of the recoil  $\beta$  velocity by  $\sim 6\%$  is sufficient to separate fast and slow components in the Doppler-reconstructed  $\gamma$ -ray spectrum. The thickness of the gold degrader was therefore chosen to be close 250  $\mu\text{m}$ .

The thicknesses of all utilized foils are listed in Table 2.2.

## 2.4. The Segmented Germanium Array

The Segmented Germanium Array (SeGA) in plunger configuration consists of 15 SeGA detectors [Mue01] and was used to detect prompt  $\gamma$  rays. Each SeGA detector houses a cylindrical HPGe crystal which has a length of 8 cm and a diameter of 7 cm. The outer contacts of the crystals are electrically segmented (see Fig. 2.4). The crystal is divided into eight disks (labelled from A to H) with thicknesses of 10 mm. Each disk is divided

<sup>5</sup>Due to the high precision of the bearing unit, a significant contribution from friction is in principal not expected. However, the device showed temperature-dependent friction effects which was traced back to different elongation coefficients of the used materials. This problem was solved in 2016.

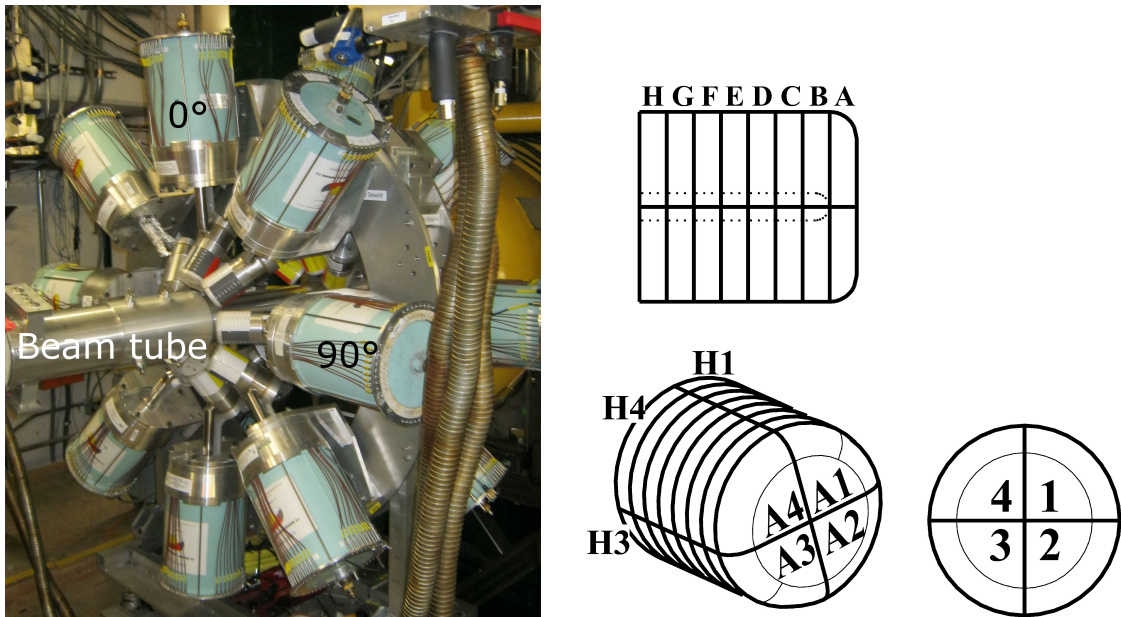


Figure 2.4.: *Left*: Photograph of SeGA in plunger configuration focused on the upstream detectors at  $\theta \approx 140^\circ$  surrounding the beam pipe. The azimuthal angles are printed into the picture for  $\varphi = 0^\circ$  and  $90^\circ$ . *Right*: Segmentation of the SeGA crystals as taken from Ref. [Mue01]. Reprinted with permission from Elsevier.

into four equally sized quarters (labelled from 1 to 4). To maximize the benefits from the segmentation, the crystal axis is placed perpendicular to the connection line between reference point (plunger degrader) and detector centre position, see Fig. 2.4.

In total, energy and time information are collected from each of the 32 segments as well as from the core. In the analysis, the Doppler reconstruction is applied to the full energy collected in the core using the angle of the segment with the largest energy deposition. Information on the intrinsic and expected total detector resolution can be found in Sec. 3.1.2.3.

The detectors were placed in two rings around the beam axis. The downstream (upstream) detector ring is placed at an angle of  $\theta \approx 30^\circ$  ( $\theta \approx 140^\circ$ ) with respect to the beam axis. In total seven and eight detectors were placed in the detector ring at  $\theta \approx 30^\circ$  and  $\theta \approx 140^\circ$ , respectively. The azimuthal angles  $\varphi$  of the detectors were given by  $0^\circ$ ,  $45^\circ$ ,  $90^\circ$ ,  $135^\circ$ ,  $180^\circ$ <sup>6</sup>,  $225^\circ$ ,  $270^\circ$  and  $315^\circ$ . Precise information on the determination of the SeGA geometry can be found in Sec. 3.1.1. A photograph of SeGA as it was used in the experiment is depicted in Fig. 2.4.

<sup>6</sup>This detector is missing in the downstream ring due to the limited space at the entrance of the S800 spectrograph.

---

## 3. Data Preparation

It was mandatory to apply various calibrations and corrections to the raw experimental data before solid information could be extracted. These calibrations and corrections will be discussed in this chapter.

In Sec. 3.1 the various steps needed for the SeGA detectors are described. The following sections clarify the preparation of plunger (Sec. 3.2) and S800 data (Sec. 3.3).

### 3.1. The SeGA in Plunger Configuration

As can be readily seen from Eq. 1.1, a reasonable Doppler reconstruction requires to know the (effective) polar angle  $\theta$ , i.e. the angle between the velocity vector of the particle when the  $\gamma$ -ray is emitted and the detection position of the  $\gamma$ -ray, with high precision. In addition, the geometry of the germanium array has to be mapped accurately into the (GEANT4) simulation to enable a precise description of subtleties, such as full photo-peak efficiencies and solid-angle effects. The determination of the SeGA geometry is explained in Sec. 3.1.1.

For each of the three plunger-foil configurations, measurements with a standard  $^{152}\text{Eu}$  source (see Sec. 3.1.2) placed at various positions within the plunger housing were performed and fulfilled several purposes:

1. Matching the response signals of cores as well as segments to real energy values, see Sec. 3.1.2.1.
2. Evaluation of the full photo-peak efficiency, depending on the source position and foil configuration, see Sec. 3.1.2.2.
3. Determination of the intrinsic detector resolutions, see Sec. 3.1.2.3.
4. Matching the  $\gamma$ -time signals of the SeGA detectors, see Sec. 3.1.2.4.

#### 3.1.1. Geometry of the SeGA Detectors

To motivate the necessity of a precise knowledge on the array geometry, it is instructive to see the effect of a slightly misaligned detector array on the Doppler-reconstructed  $\gamma$ -ray spectrum. This can be visualized by simulation tool-kits, e.g. based on GEANT4.

For this purpose, consider hypothetical prompt  $\gamma$ -rays with an energy of 1 MeV which are emitted from recoils moving along the beam axis with  $\beta = 0.4$ . Geometric mismatches are forced into the Doppler-reconstruction which lead to systematic shifts in the Doppler-reconstructed  $\gamma$ -ray spectrum. Here, the assumed detector geometry is realistic and mimics the experimental one. Results are shown for the downstream detector ring in Fig. 3.2.

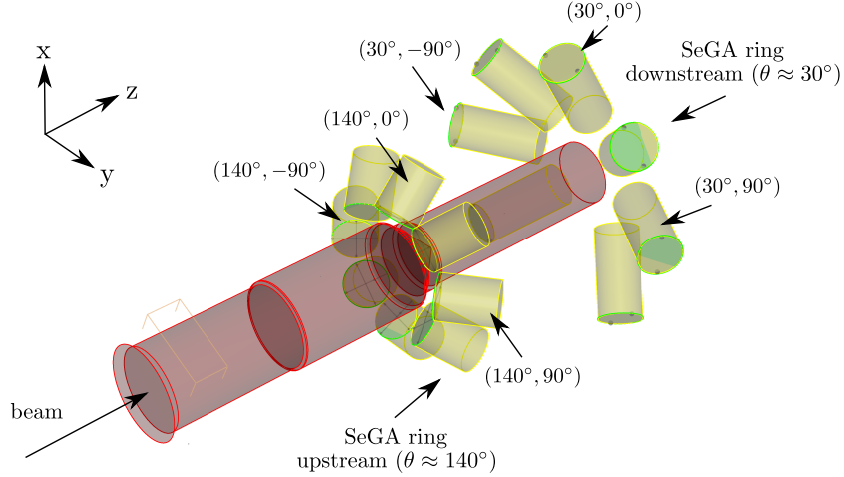


Figure 3.1.: Schematic drawing of components scanned in the laser measurement, showing the beam tube (red) and SeGA detectors (green). The dots in the downstream detector ring ( $\theta \approx 30^\circ$ ) correspond to the position of screws placed on the backside of the crystal housing from which the axial segmentation can be referred. For the upstream detectors ( $\theta \approx 140^\circ$ ) a grid on the front caps can be seen, which coincides with the quarterly segmentation. The orientation of the associated coordinate system is illustrated in the upper left corner.

First, a forced mismatch of  $\Delta r(x, y) = 10$  mm in the area perpendicular to the beam axis is introduced. As can be seen in Fig. 3.2, this increases the peak width (in terms of FWHM) in the Doppler-reconstructed  $\gamma$ -ray spectrum by almost 4 keV, which corresponds to a relative increase of the resolution by 60 %. The peak centroid, however, appears at the expected energy.

Second, a forced mismatch of  $\Delta z = 10$  mm (along the beam axis) is introduced. This affects the polar angles systematically and shifts the centroids of the Doppler-reconstructed peaks in both rings by  $\sim 6$  keV toward higher energies, while the energy resolutions remain essentially unchanged.

To minimize systematic uncertainties in the analysis, characteristic positions and orientations of the SeGA detectors as well as the beam pipe housing the TRIPLEX device were measured with a laser scan using a commercial system manufactured by FARO Technologies Inc.. The result is illustrated in Fig. 3.1.

The corresponding orthogonal coordinate system in which the positions are given is chosen as follows: The origin coincides with the pivot point of the S800 spectrograph. The  $z$  axis coincides with the beam axis, the  $x$  axis shows vertically upward and the  $y$  axis is chosen such that the coordinate system follows a right-handed orientation, e.g. it points to the right with respect to the beam direction. With respect to the magnetic rigidities of S800, the  $x$  axis is then the dispersive axis, while the  $y$  axis is the non-dispersive axis of the spectrograph.

In this reference frame the mean focus position of the SeGA detectors was found to be at  $(x, y, z) = (0, 0, -54$  mm), with variations smaller than 2 mm. With respect to this

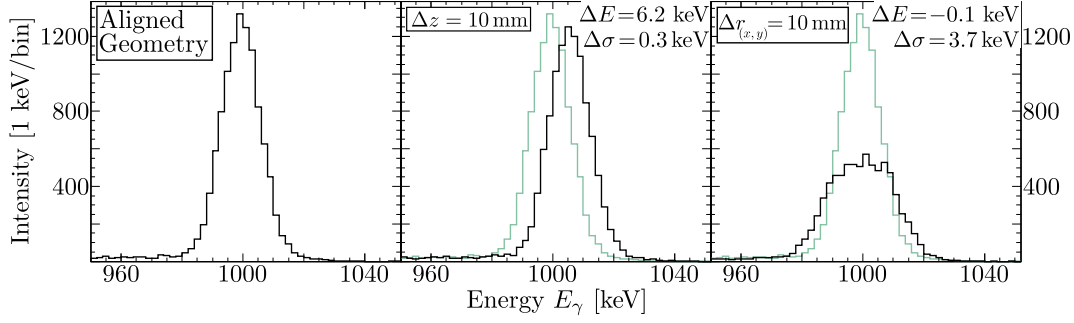


Figure 3.2.: Influence of systematic errors in the detector geometries on the Doppler-reconstructed  $\gamma$ -ray spectrum in the downstream detector ring as investigated with a GEANT4 simulation. *Left*: Doppler-reconstructed  $\gamma$ -ray spectrum for a perfectly aligned Detector geometry. *Centre*: Doppler-reconstructed  $\gamma$ -ray spectrum assuming a systematic upstream shift of 10 mm. *Right*: Doppler-reconstructed  $\gamma$ -ray spectrum assuming a systematic shift of 10 mm in the area perpendicular to the beam axis. Changes in the centroid energy ( $\Delta E$ ) and the peak resolution ( $\Delta\sigma$ ) are written into the spectra.

focus point, the mean radial distance to the detectors were given by 29.9 and 23.7 cm for the downstream and upstream detector ring, respectively. The mean polar angles were quantified to  $30.6^\circ$  and  $140.6^\circ$ .

It was intended to align the plunger degrader at  $(x, y, z) = (0, 0, -52 \text{ mm})$ <sup>1</sup>. Regarding the analysis, the precise  $z$  coordinate of the plunger degrader was determined by an iterative process until self-consistency was achieved between experimental and simulated Doppler-reconstructed  $\gamma$ -ray spectrum with respect to the  $2_1^+ \rightarrow 0_{\text{gs}}^+$   $\gamma$ -ray transition energy of the corresponding chromium isotope. For the latter, the transition energy was taken from literature. Best results were achieved for  $z$  coordinates of -44 mm (first and second setup) and -48 mm (third setup). The displacement within the  $(x, y)$  area was determined by minimizing the peak width of the same transition in the Doppler-reconstructed  $\gamma$ -ray spectrum.

### 3.1.2. Data Taken with a Standard $^{152}\text{Eu}$ Source

Several data runs with a standard  $^{152}\text{Eu}$  source (activity  $A_0 = 26.0 \text{ kBq}$ ) were recorded before and after the experiment while the plunger device was located at its nominative experimental position. For each of the three plunger foil configurations (characterized by varying Be target thicknesses) three  $\gamma$ -ray spectra with distinct source positions and foil separations were recorded (see Fig. 3.3). Each of these runs was recorded for around 30 minutes.

These data sets allow a.) to match the response signals to real energies, b.) to investigate position-dependent effects (e.g. due to changing solid angles), c.) to investigate gain stabilities and d.) to determine absolute full photo-peak efficiencies as well as detector resolutions.

<sup>1</sup>For this purpose a mechanical stick with a well-defined length was used to push the plunger device into position.

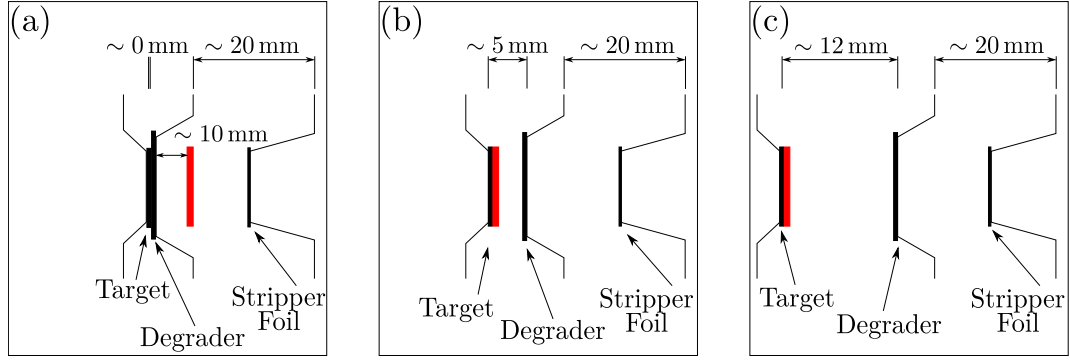


Figure 3.3.: Positions of the  $^{152}\text{Eu}$  source for which SeGA data was recorded. *Left:* Source (depicted in red) placed downstream of the degrader while target and degrader are in contact. *Middle:* Source placed on the target surface with a foil separation of  $\sim 5$  mm. *Right:* Source placed on the target surface with a foil separation of  $\sim 12$  mm. The separation between second and third foil was around 20 mm in all cases.

### 3.1.2.1. Energy-Channel-Matching of Core and Segmental Signals

Information on  $\gamma$ -ray energies for transitions following the decay of  $^{152}\text{Eu}$  were taken from Ref. [NDS152]. For the matching of the core signals, only transitions in the energy range 121 to 1528 keV characterized by sufficiently strong intensities (usually larger than 1%) and non-overlapping transitions of comparable intensities were taken into account. A list of the considered transitions can be found in Appendix A. To extend the energy-matched region toward higher energies<sup>2</sup>, additional background transitions (see Sec. 3.1.3) at 1460.8 ( $^{40}\text{K}$ ), 1764.5 ( $^{214}\text{Bi}$ ) and 2614.5 keV ( $^{208}\text{Tl}$ ) were also taken into account.

The corresponding core response was fitted for each SeGA detector to the  $\gamma$ -ray energy using linear, quadratic and cubic functions. Non-linearities in the SeGA response in the low and high ( $>1.5$  MeV) energy range were reported prior to this work (see, e.g. [Cra10b]), where the latter were traced back to non-linearities in the response of the Ortec AD413 ADCs [Lid04].

In the present experiment, non-linearities were observed for all detectors. While for some detectors these could be corrected by assuming a quadratic dependence, for others a cubic term was mandatory. Only the detector placed at  $(\theta, \phi) \approx (30^\circ, 90^\circ)$  was prone to severe non-linearities. Typical reduced  $\chi^2$  values for the linear, quadratic and cubic fits were around 200, 60 and 10, respectively.

As a consequence, a cubic polynomial expression was used for the energy-channel matching. As examples of the quality, the residuals of the gain matching are shown in Fig. 3.4 for a typical as well as for the most problematic detector placed at  $(\theta, \phi) \approx (30^\circ, 90^\circ)$ . Using the cubic fit, deviations between fitted and literature values for  $\gamma$ -ray energies below 2 MeV were in general smaller than 0.2 keV, with two exceptions:

<sup>2</sup>This is in particular important for the downstream detector ring as a consequence of the Doppler-shift toward higher energies.

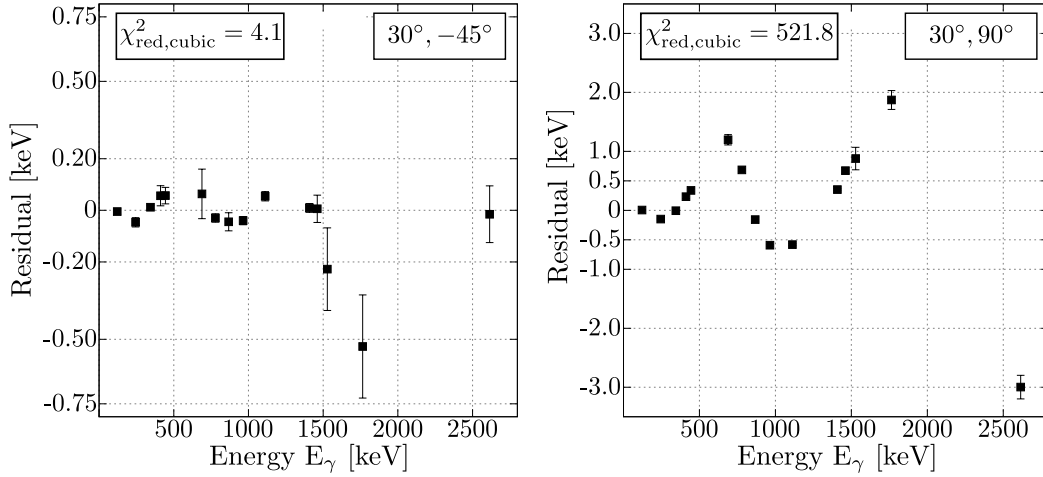


Figure 3.4.: Quality of the energy-channel matching using a cubic function. *Left*: Representative residuals of the detector placed at  $(\theta, \phi) \approx (30^\circ, -45^\circ)$ . *Right*: Residuals of the problematic detector placed at  $(\theta, \phi) \approx (30^\circ, 90^\circ)$  which shows severe non-linearities.

- The detector at  $(\theta, \phi) \approx (30^\circ, 90^\circ)$  suffered from severe non-linearities which could be observed in all  $^{152}\text{Eu}$  runs and affected the full energy range.
- The detector at  $(\theta, \phi) \approx (140^\circ, 135^\circ)$  suffered from gain instabilities, leading to a double-peak structure at low energies and a severe low-energy tail at higher energies.

Possible gain shifts were investigated by comparing energy matching parameters corresponding to  $^{152}\text{Eu}$  data recorded before and after the experiment. The systematic uncertainty is estimated to be 1 keV for Doppler-reconstructed energies below 1500 keV and 2 keV for higher energies, which is reasonable to account also for gain shifts, which in most cases were well below 0.5 keV.

In a following step, the segment responses were gain-matched using the calibrated core energies. For this purpose, the data was restricted to  $\gamma$ -ray events with multiplicity  $M = 1$ . The correlation of segment response versus calibrated core energy is fitted with a quadratic function in the energy range 50 to 1500 keV, see Fig. 3.5.

### 3.1.2.2. Full Photo-Peak Efficiencies

The full photo-peak efficiencies  $\epsilon_P(E_{\gamma,i})$  at specific  $\gamma$ -ray energies  $E_{\gamma,i}$  were determined for each of the  $^{152}\text{Eu}$  runs according to

$$\epsilon_P(E_{\gamma,i}) = \frac{I_{\gamma,i}^{\text{exp}}}{\Delta t \cdot p_{\gamma,i}^{\text{abs}} \cdot A \cdot LT} \quad (3.1)$$

with the experimental intensity  $I_{\gamma,i}^{\text{exp}}$ , the measuring time  $\Delta t$ , the probability to observe the transition per decay  $p_{\gamma,i}^{\text{abs}}$  taken from [IAEA07; NDS152] (see Appendix A), the activity  $A$  of the  $^{152}\text{Eu}$  source and the lifetime  $LT$  as evaluated from DAQ scalers. Various

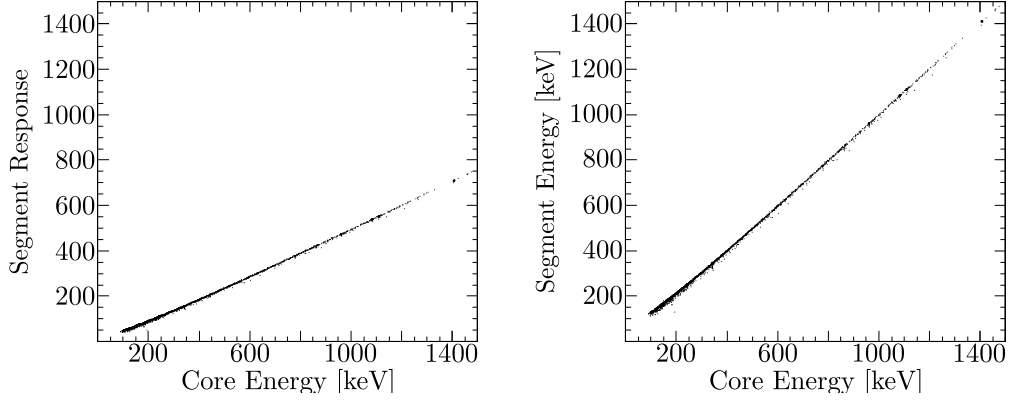


Figure 3.5.: Matching of the segment response to the core signal for events with multiplicity  $M = 1$ . The left figure shows the unmatched case while the right figure shows the matched response following the procedure described in the text.

analytical functions, e.g. the expression introduced by Gray [Gra85], were tested for their abilities to describe the experimental data points. The smallest  $\chi^2$  was achieved using the formula introduced in Ref. [Deb84], which describes the efficiency according to:

$$\epsilon(E_\gamma) = a \log E_\gamma + b \frac{\log E_\gamma}{E_\gamma} + c \frac{\log^2 E_\gamma}{E_\gamma} + d \frac{\log^4 E_\gamma}{E_\gamma} + e \frac{\log^5 E_\gamma}{E_\gamma} \quad (3.2)$$

Whenever it is referred to quantitative experimental full photo-peak efficiencies in the following, this function is used.

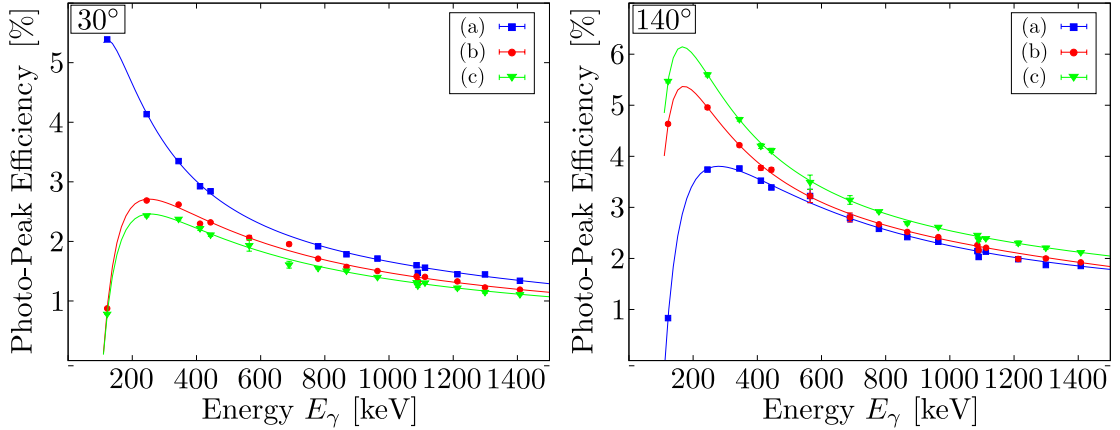


Figure 3.6.: Comparison of full-photo peak efficiencies  $\epsilon_P$  for three different source positions – labelled (a), (b) and (c) (see Fig. 3.3 for clarification) – as determined for the foil configuration of the first experimental setup. For each data set the best fit using Eq. 3.2 is shown.

As an example, the results of the foil configuration of the first experimental setup are shown for both detector rings in Fig. 3.6. The qualitative behaviour of the shown data can

Detector	a	b	FWHM	Detector	a	b	FWHM
(30°, 0°)	5.79	4.59	3.57	(140°, 0°)	5.20	3.17	3.14
(30°, 45°)	7.29	4.13	3.68	(140°, 45°)	6.49	3.41	3.39
(30°, 90°)	4.79	3.15	3.09	(140°, 90°)	4.88	3.95	3.28
(30°, 135°)	4.16	3.98	3.19	(140°, 135°)	5.82	3.36	3.28
(30°, 180°)	-	-	-	(140°, 180°)	4.24	5.32	3.56
(30°, -135°)	5.08	4.09	3.37	(140°, -135°)	5.28	3.96	3.35
(30°, -90°)	4.79	5.23	3.42	(140°, -90°)	5.94	4.03	3.45
(30°, -45°)	9.79	3.18	4.29	(140°, -45°)	5.95	3.10	3.24
Ring	5.79	4.41	3.50	Ring	5.57	3.59	3.13

Table 3.1.: Resolution parameters (see Eq. 3.3) of single SeGA detectors in the downstream (*left*) and upstream (*right*) detector ring as deduced from summed data of all  $^{152}\text{Eu}$  runs recorded prior to the experiment and the FWHM (in keV) at 1408 keV as a signature for the detector resolution. The bottom line lists the same result for the full detector ring using the integrated statistics.

be understood due to the influence of solid-angle as well as shadowing effects. In addition, the plots highlight that the efficiency at low energies is strongly position dependent. The efficiency curve of the downstream detectors shows a distinct knee around 220 keV when the source is placed between target and degrader, which vanishes if the source is placed downstream of the degrader.

In the upstream detector ring this knee can be seen for all source positions, but its energy is correlated to the source position. The efficiency of the upstream detector ring reduces, as expected, if the source is placed downstream of the degrader.

### 3.1.2.3. Intrinsic Detector Resolutions and Doppler Broadening

After the gain matching, the statistics of all  $^{152}\text{Eu}$  runs recorded prior to the experiment were added to quantify the intrinsic resolution of each of the 15 SeGA detectors. The FWHM were determined by fitting Gaussian functions to transitions in the energy range 121 keV to 1550 keV using the function

$$\text{FWHM}(E_\gamma) [\text{keV}] = \sqrt{a + b \cdot E_\gamma [\text{keV}]} \quad (3.3)$$

This procedure was repeated for the summed spectrum for both detector rings. The results are listed in Table 3.1. Depending on the detector, the FWHM (at 1408 keV) varied between 3.1 keV and 3.9 keV in the present experiment.

As a result of the relativistic recoil velocities, the observed  $\gamma$ -ray resolution in the laboratory frame are also affected by a significant Doppler broadening (DB), which is a direct consequence of the aperture of the SeGA segments. This is an intrinsic effect and, hence, was not correctable with the present setup.

The relative contribution of Doppler broadening to the energy resolution ( $\Delta E^{\text{DB}}$ ) ob-

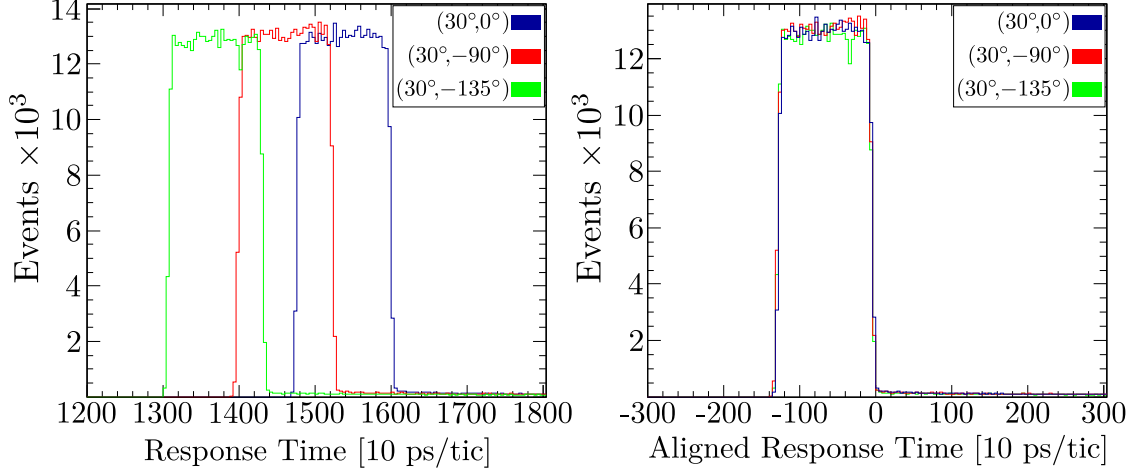


Figure 3.7.: Matching of the  $\gamma$ -time information, illustrated for three detectors. *Left*: Raw  $\gamma$ -time information. *Right*: Corrected  $\gamma$ -time information.

served in a Doppler-reconstructed  $\gamma$ -ray spectra can be quantified via:

$$\frac{\Delta E^{\text{DB}}}{E_{\gamma}^0} = \frac{\beta \sin \theta}{1 - \beta \cos \theta} \Delta \theta_s \quad (3.4)$$

Here,  $\Delta \theta_s$  is the opening angle of the detector segment. In the discussed experiment, the mean full opening angles of segments were  $\sim 1.8^\circ$  (downstream ring) and  $\sim 2.5^\circ$  (upstream ring), respectively. Consider, for instance, the de-excitation of the  $2_1^+$  state in  $^{58}\text{Cr}$  ( $E_{\gamma} = 881$  keV) while moving with a  $\beta$  velocity of  $\beta = 0.4$ . The Doppler broadening increases the total resolution (FWHM) by 8.6 keV in the downstream ring and 5.9 keV in the upstream ring.

#### 3.1.2.4. SeGA Response Timing

Using  $^{152}\text{Eu}$  data, the time information from the core signals of the SeGA detectors were matched to each other. For this purpose, the right shoulder of the  $\gamma$ -time response is shifted to zero using a constant term (see Fig. 3.7 for illustration).

#### 3.1.3. Background Measurement

The natural background radiation was measured before ( $\approx 2.75$  hours) and shortly after ( $\approx 0.2$  hours) the experiment. The resulting total  $\gamma$ -ray spectra are shown in Fig. 3.8. A comparison of both background spectra reveal that no severe activation took place. The 1460-keV line of  $^{40}\text{K}$  is the strongest contribution to the background spectrum. During the analysis special care was given to avoid random coincidences correlated to background and non Doppler-shifted  $\gamma$  rays in general from contaminating relevant peaks.

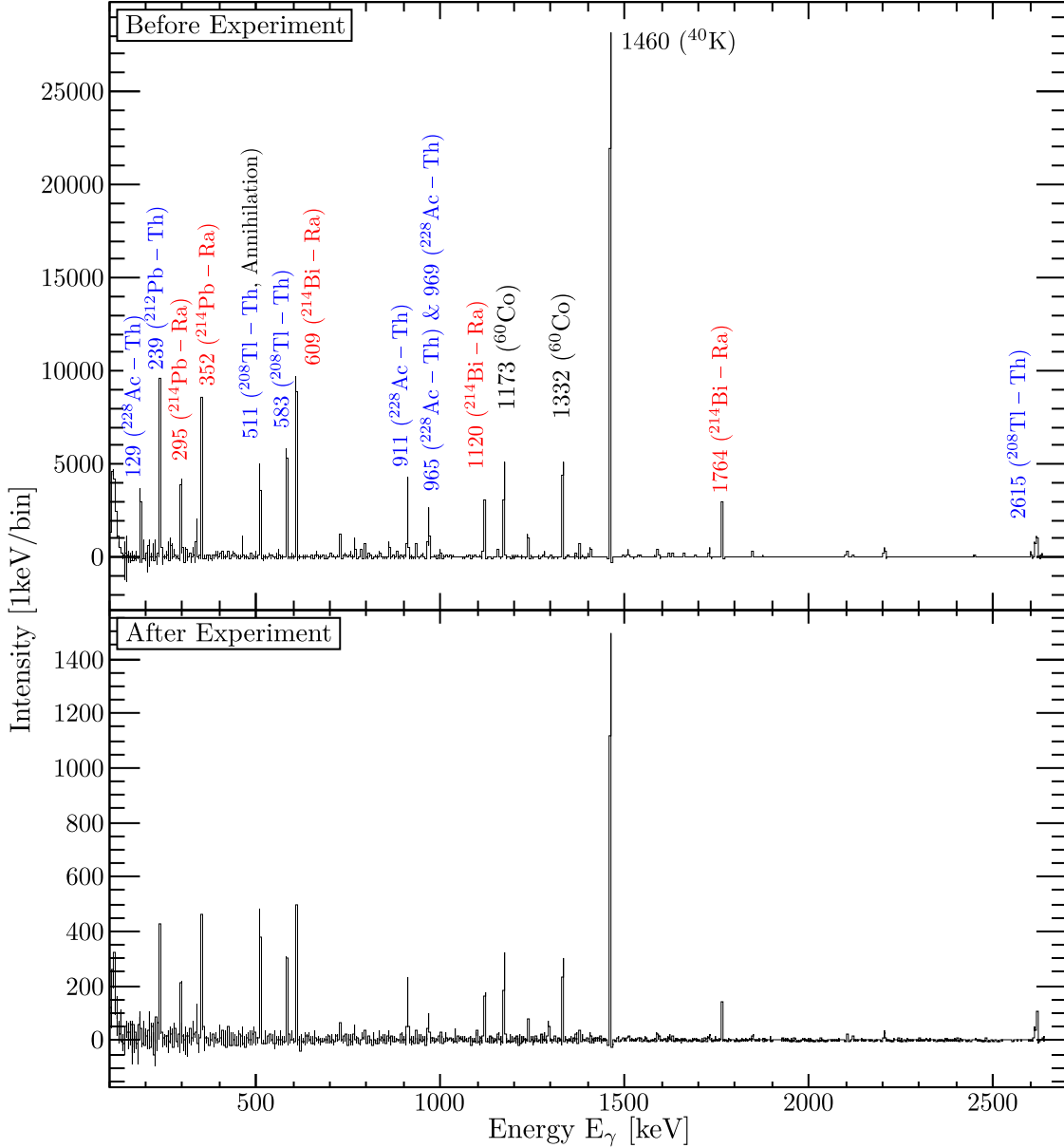


Figure 3.8.: The spectra show the (natural) background radiation as recorded with SeGA before (*top*) and after (*bottom*) the experiment. Each transition is identified and labelled with the corresponding transition energy  $E_\gamma$ , the mother nucleus and – if applicable – the corresponding decay chain.

### 3.1.4. Doppler Reconstruction

The separability of the plunger peaks - labelled fast (slow) component for decays upstream (downstream) the degrader - depends crucially on the Doppler reconstruction, for which both angle and recoil velocity information are taken into account. This is illustrated in Fig. 3.9, which shows Doppler-shifted and Doppler-reconstructed  $\gamma$ -ray spectra correlated

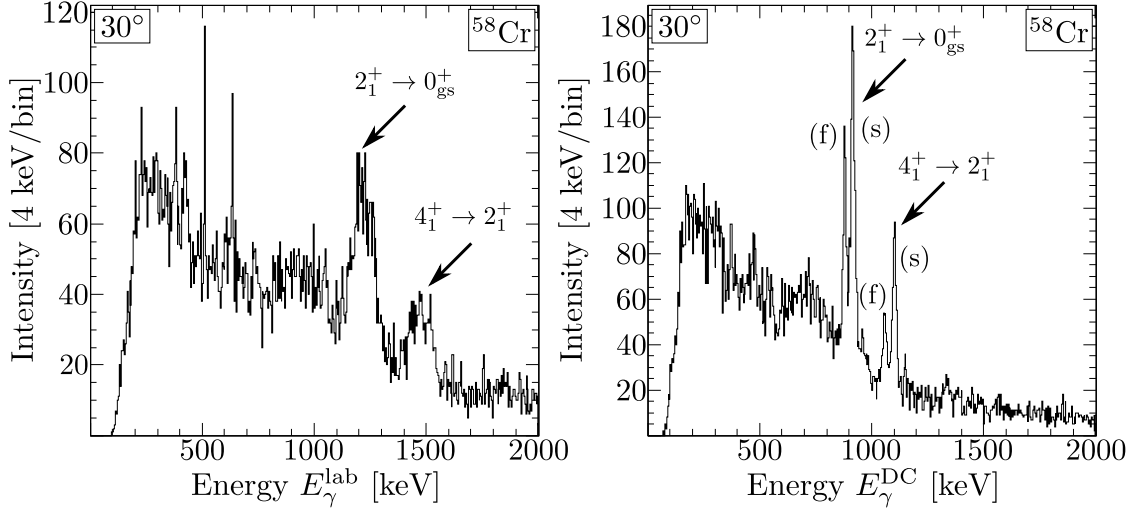


Figure 3.9.: Effect of the Doppler reconstruction on the peak separability. Shown are Doppler-shifted (*left*) and Doppler-reconstructed (*right*)  $\gamma$ -ray spectra of the downstream detector ring correlated to  $^{58}\text{Cr}$  for a 4-mm foil separation. In the latter, fast (f) and slow (s) components are identified.

to  $^{58}\text{Cr}$  recorded for the foil distance of 4 mm. The Doppler reconstruction is performed event-by-event using the  $\beta$  velocity determined with S800 and a trajectory-corrected detector<sup>3</sup> angle  $\theta$ . The energy of the slow component in the Doppler-reconstructed  $\gamma$ -ray spectrum is essentially given by the literature value of the corresponding transition.

<sup>3</sup>The mean scattering angle in the analysis of  $^{58,60,62}\text{Cr}$  were measured with S800 to  $1.6(10)^\circ$ ,  $1.3(10)^\circ$  and  $1.2(14)^\circ$ . The values in brackets refer to the corresponding root mean square error. In general, the scattering angles were distributed between 0 and  $5^\circ$ .

## 3.2. Plunger Device

Typical foil thicknesses used in RDDS experiments at NSCL are of the order of a few hundred micrometers. Due to the comparably large thicknesses, they are glued directly onto the corresponding cones. As a consequence and in contrast to common plunger experiments, the surface cannot be smoothed and, depending on the material, inherent surface structures are practically unavoidable.

As a consequence, the *zero offset*  $\Delta x_0$  describing the gap between electrical  $x_e$  and absolute contact position  $x_0$ , is often larger than in typical plunger experiments. For the latter, zero offsets of 5 to 10  $\mu\text{m}$  are achievable.

### 3.2.1. Calculation of Zero Offsets

The plunger foils were aligned optically prior to the experiment. The electrical contact point  $x_e$  is taken as a reference point, which is defined as the outermost point for which the foils are just in electrical contact. Distance calibrations using the capacitance method [Ale70] were performed before and after the experiments. For this purpose, a well-defined voltage pulse is applied to the first degrader foil. This induces a voltage signal in the target foil whose amplitude is inversely proportional to the foil separation  $x_i$ . The smallest separation in such a *distance calibration*<sup>4</sup> corresponds to the electrical contact point  $x_e$  and the largest separation is usually around 1 mm.

In first order approximation, the amplitude of the induced voltage  $U(x)$  shows the distance dependent behaviour known from a plate capacitor, i.e.  $U \propto 1/x$ . The (mean) zero offset<sup>5</sup> is then given as the cutting point of the linearly extrapolated  $1/U(x)$  signal with the position axis,  $U^{-1}(x) \stackrel{!}{=} 0$ . Higher order effects due to stray capacitances, e.g. induced by the plunger housing as well as cones, distort this relationship and decrease the slope of  $1/U(x)$ .

To take this into account the standard approach is to assume a constant capacitance that is placed in parallel to the plunger foils mimicked by  $U_0$ , which leads to a corrected signal according to:

$$\frac{1}{U_{\text{corr}}}(x) = \frac{1}{U(x) + U_0} \quad (3.5)$$

Here, the constant  $U_0 = -1.3\text{ V}$  was chosen for all distance calibrations and all three setups. The result is illustrated for a distance calibration used in the first setup in Fig. 3.10. With a standard plunger device this approach works rather well and usually leads to a

<sup>4</sup>In standard plunger experiments, distance calibrations are needed to perform automatic distance corrections to compensate changing foil separations which, in particular, are induced by thermal expansions as a consequence of energy losses in the foils. Although the energy losses at NSCL are significantly larger (factor of  $\sim 10^2$ ), the lower beam intensities (factor of  $\sim 10^{-5}$ ) dominate. Hence, thermal effects are less critical and the feedback mode was switched off while the logging of separations based on the distance calibrations was still activated.

<sup>5</sup>An alternative approach to calculate the zero offset is based on the analysis of already known lifetimes. The zero offset is then determined by minimizing the discrepancy between analysed and known lifetime. This method works well if the lifetime is known with very good precision and if the statistics of the experiment allows a precise lifetime determination. In the present experiment this was not the case and, hence, this approach is no option.

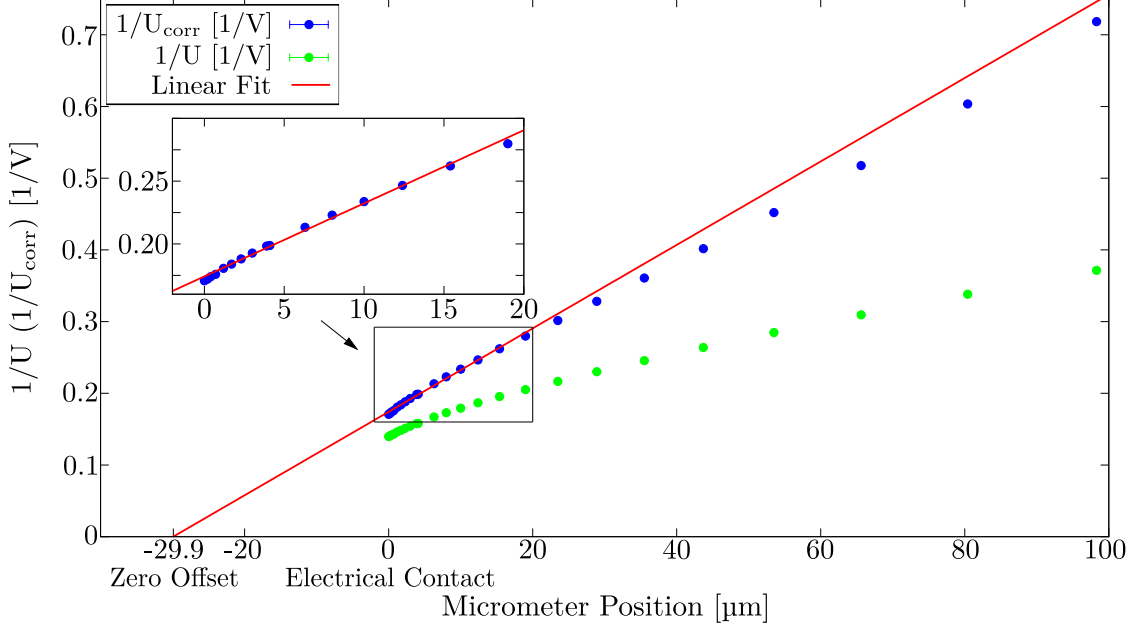


Figure 3.10.: Determination of the zero offset in the first experimental setup using the *corrected* distance-calibration data (blue points). In addition, the *raw* distance-calibration points are shown in green. The zero offset was determined by a linear extrapolation (red) to  $-29.9 \mu\text{m}$ .

linear relationship for foil separations up to  $\sim 100 \mu\text{m}$ . In the present experiment, deviations from the linear trend occur already for separations (with respect to the electrical contact  $x_e$ ) larger than  $\sim 15 \mu\text{m}$ , although an improvement of the linearity is obvious. Hence, only a small fitting range with a width of around  $20 \mu\text{m}$  was taken into account to evaluate the zero offset.

A reason for this behaviour may be given in terms of a stronger distant-dependent effect of stray capacitances. Compared to the usual foil configuration with approximately cylindrical symmetry, quadratic foils with a diameter of  $5 \text{ cm}$  are commonly used in plunger experiments at NSCL. These foils are most often mounted in a sheared orientation with

Setup	Before Experiment		After Experiment		$\Delta x_0^{\text{ana}} [\mu\text{m}]$
	$\Delta x_0 [\mu\text{m}]$	$\Delta x_0^{\text{micro}} [\mu\text{m}]$	$\Delta x_0 [\mu\text{m}]$	$\Delta x_0^{\text{micro}} [\mu\text{m}]$	
1	-29.9	-263.9	-29.0	-273.5	$-29.5 \pm 10.0_{\text{sys}}$
2	-25.8	-65.4	-23.0	-75.7	$-24.4 \pm 10.0_{\text{sys}}$
3	-24.4	-18.0	-27.6	-19.7	$-26.0 \pm 10.0_{\text{sys}}$

Table 3.2.: Determination of zero offsets  $\Delta x_0$  by extrapolation of the capacitance signal for distance calibrations performed before and after the experiment. In addition, corresponding (relative) micrometer values  $\Delta x_0^{\text{micro}}$  are listed which show a shift of  $\sim 10 \mu\text{m}$ . The last column lists the adopted zero offsets.

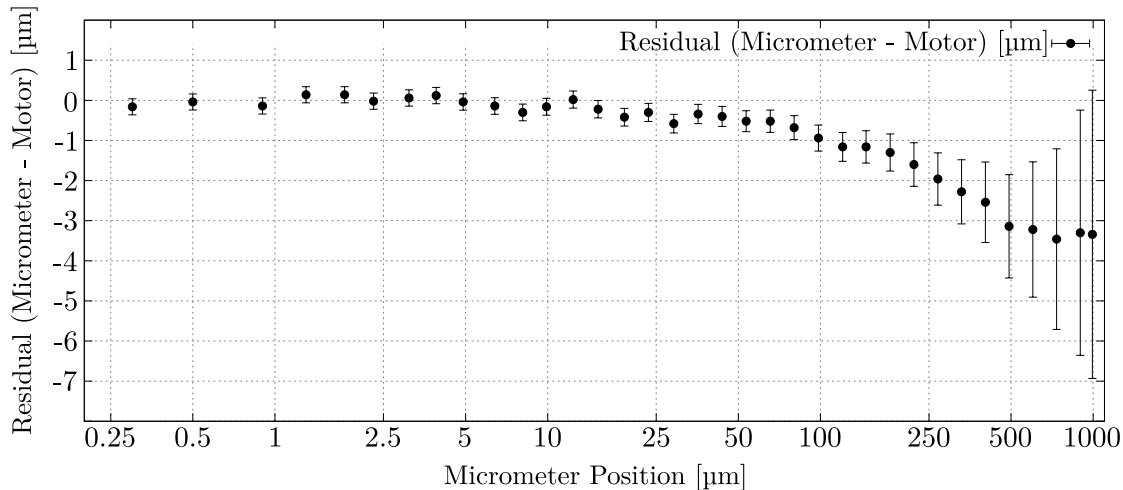


Figure 3.11.: Investigation of differences between micrometer and motor encoder position. The plot shows the difference between these two values versus the micrometer position based on the distance calibration recorded in the third setup. The data is normalized to zero at electrical contact.

respect to each other which distorts the  $1/x$  relationship of  $U(x)$ .

The zero offsets  $\Delta x_0$  were determined for each setup from distance calibrations performed before and after the experiment. The resulting zero offsets  $\Delta x_0$  and corresponding micrometer positions are listed in Table 3.2.

The zero offsets behave rather constant within each setup but the position of the extrapolated zero position on the micrometer scale appears to shift. This is consistent with an observation made during the experiment.

Setup	Foil Separations [ $\mu\text{m}$ ]
1	$25.2(\pm 0.4_{\text{stat}} \pm 10_{\text{sys}})$
	$53.1(\pm 0.6_{\text{stat}} \pm 10_{\text{sys}})$
	$83.0(\pm 0.5_{\text{stat}} \pm 10_{\text{sys}})$
	$521.5(\pm 2.0_{\text{stat}} \pm 10_{\text{sys}})$
	$4039(\pm 30_{\text{sys}})$
2	$170.8(\pm 0.6_{\text{stat}} \pm 10_{\text{sys}})$
	$325.0(\pm 2.0_{\text{stat}} \pm 10_{\text{sys}})$
	$480.0(\pm 5.0_{\text{stat}} \pm 10_{\text{sys}})$
	$4024(\pm 30_{\text{sys}})$
3	$25.9(\pm 3.0_{\text{stat}} \pm 10_{\text{sys}})$
	$7026(\pm 45_{\text{sys}})$

Table 3.3.: Adopted absolute plunger foil separations used in the experiments. See text for details.

Within the first hours after mounting the plunger device into the beam tube, the

Foil	Setup	Material	$T_{\text{nom}}$ [ $\mu\text{m}$ ]	$T_{\text{mass}}$ [ $\mu\text{m}$ ]	$T_{\Delta E}$ [ $\mu\text{m}$ ]
Target	1	$^9\text{Be}$	300	286.8(58)	287.4(18)
Target	2	$^9\text{Be}$	500	518.6(104)	519.5(54)
Target	3	$^9\text{Be}$	1300		1288.6(94)
Degrader	1,2,3	$^{197}\text{Au}$	250	253.0(51)	251.5(30)
Stripper foil	1,2,3	$\text{C}_{10}\text{H}_8\text{O}_4$	50.1		

Table 3.4.: Foil thicknesses as quoted by the manufacturer ( $T_{\text{nom}}$ ), as deduced from a mass measurement ( $T_{\text{mass}}$ ) and as determined from energy measurements using S800 ( $T_{\Delta E}$ ). See text for details.

induced voltage signal had decreased without any external changes. Comparing the two distance calibrations with each other, one can see that this drift is consistent with an overall displacement of up to 10  $\mu\text{m}$ . No significant change of the slope of the distance-calibration curve could be observed, so that the relationship between induced voltage and (absolute) foil separation remained unaffected. In conclusion, the systematic error in the zero offset is estimated to be 10  $\mu\text{m}$ .

### 3.2.2. Calculation of Absolute Foil Separations

To quantify the experimental plunger foil separations, the induced voltage signals are used to calculate the (mean) separation with respect to the micrometer scale and the zero offset is added. Separations larger than 2 mm are out of the micrometer range and, hence, one has to rely on the distance information from the motor encoder. Although the position resolution of the latter is well below 1  $\mu\text{m}$  (relative non-linearities smaller than 0.1%), experimental deviations may occur due to the fact that the mechanical coupling of the motor axis to the foil holders shows minimal flexibility.

To see if this was the case, the linearity between the motor encoder signal and the position given by the micrometer was investigated using distance calibration data. In Fig. 3.11 the difference between motor and micrometer positions (normalized to zero at the electrical contact position) is shown as a function of the micrometer value. The drawn errors reflect a reliable estimate of non-linearities in the motor and micrometer position<sup>6</sup>. One can observe relative deviations of less than 1.0% up to 300  $\mu\text{m}$  and less than 0.5% for larger separations. This is a general observation made for all recorded distance calibration. The systematic uncertainties of the largest separations (i.e. the ones for which only the motor offered distance information) was estimated to be 0.5%. The measured foil separations are listed in Table 3.3.

### 3.2.3. Plunger Foil Thicknesses

The beryllium target foils and the gold degrader were manufactured by the Goodfellow Group. Compared to the nominative foil thickness ( $T_{\text{nom}}$ ), the manufacturer quotes tol-

<sup>6</sup>The uncertainty of the micrometer position depends on its position and is given according to  $\Delta L$  [ $\mu\text{m}$ ]= $0.2 + 2.4 \cdot (L[\text{mm}])^2$ . For the motor position a relative uncertainty of 0.1% is assumed, which is supported by calibrations performed by the manufacturer.

erances up to  $\pm 10\%$ , which was insufficient for the desired precision. To improve this situation, foil thicknesses were determined in two ways.

First, a *mean* thickness ( $T_{\text{mass}}$ ) was deduced from a mass measurement with a high-precision scale. The thickness of the target foil used in the third setup could not be determined in this way since it was already glued onto a target holder. In addition, the quoted thickness of the stripper foil was determined by a micrometer. Corresponding mean thicknesses labelled  $T_{\text{mass}}$  were calculated using tabulated densities and assuming a foil surface of  $2500(50)\text{ mm}^2$ .

Second, the *local* foil thicknesses  $T_{\Delta E}$  were experimentally deduced from energy measurements with S800 and assuming calculated energy losses provided by the tool ATIMA [Ati]. The thicknesses are corrected for the mean scattering angle as measured with S800. The systematic error of this method due to the modelled stopping powers is assumed to be 1%. The results are summarized in Table 3.4.

### 3.3. S800 Calibration

In the present experiment the S800 spectrograph fulfilled two main purposes:

- An improvement of the Doppler-reconstructed  $\gamma$ -ray spectrum by taking into account the reconstructed recoil-velocity vector behind the plunger foils. For this task it is crucial that the CRDC detectors provide precise position information (see Sec. 3.3.1).
- An identification of recoils by means of a (path-corrected) time-of-flight ( $TOF$ ) and an energy-loss ( $\Delta E$ ) measurements. For this task the ionisation chamber (see Sec. 3.3.2) and the time-of-flight signals (see Sec. 3.3.3) need to be (empirically) calibrated.

#### 3.3.1. Calibration of the CRDC Detectors

This section outlines the calibration of the CRDC detectors.

##### 3.3.1.1. CRDC – Signal Matching in the Dispersive Direction

An incident particle induces a signal in several adjacent pads. Assuming an optimal configuration, the given distribution follows a Gaussian curve, whose centroid may then be used to determine the position along the dispersive axis.

In the experiment all pads are read out separately. As a consequence, the distribution of the raw response signals differs from the expected Gaussian shape, thus the concluded position is erroneous. Therefore, individual pads are gain matched to a reference pad via a linear function using several secondary beam species (up to five in most cases). The reference pad is typically close to the centre of the CRDC detector. As a representative example, the result of this calibration procedure is illustrated in Fig. 3.12.

The dispersion of individual secondary beams was insufficient to illuminate the complete focal plane. The gain matching was therefore not universal and, hence, this procedure had

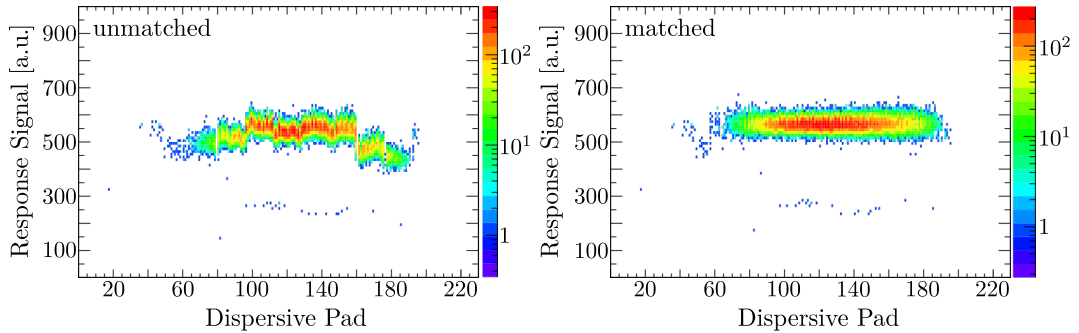


Figure 3.12.: Signal matching of a CRDC detector along the dispersive direction. Shown are the raw (*left*) and gain-matched (*right*) results of the second CRDC detector in the first setup with data correlated to  $^{58}\text{Cr}$  taken from the target-only run. One can see a slightly off-centred distribution with only marginal noise contributions.

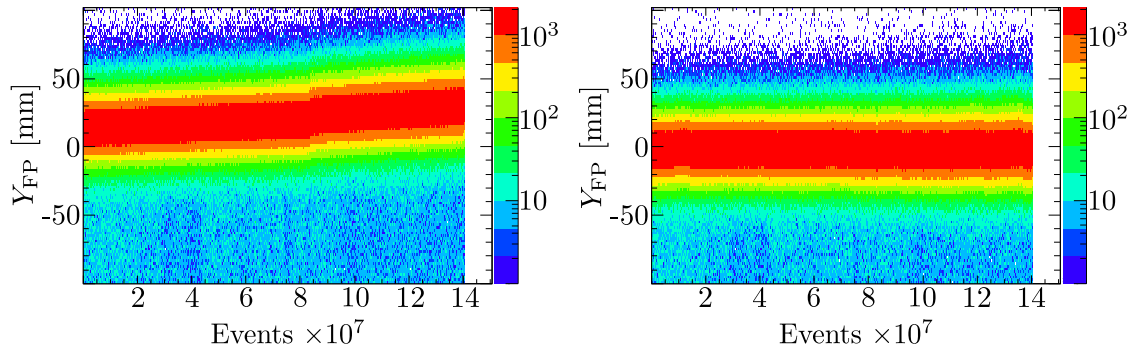


Figure 3.13.: Influence of pressure changes on the deduced non-dispersive position  $y_{\text{FP}}$  as measured with a CRDC detector. Shown are raw (*left*) and corrected (*right*) distributions that were recorded with the second CRDC detector during the second part of the experiment.

to be repeated for some of the investigated side products, whose  $B\rho$  deviated significantly from the experimental magnetic rigidity which therefore led to off-centred distributions in the CRDCs.

### 3.3.1.2. CRDC – Drift-Time Corrections Along the Non-Dispersive Axis

Position information along the non-dispersive axis is deduced from the electron drift time, which is correlated to the given gas pressure in the detector. Gradual pressure changes affect the drift time and, hence, the deduced position.

The mean drift times are matched run-by-run to a reference run. The latter preceded or followed a mask calibration (see Sec. 3.3.1.3). The result is illustrated in Fig. 3.13.

### 3.3.1.3. CRDC – Matching to Absolute Positions

So called *mask runs* were performed at several points during the experiment. These runs allow to map the measured coordinates to absolute positions. The masks have a characteristic and well-known slit/dot pattern (see Fig. 3.14 for a technical drawing). During a mask run, these masks are placed in front of each of the CRDC detectors, while the dipole rigidities are varied in such a way that the full focal plane is illuminated along the dispersive axis. The raw signals (see top figure in Fig. 3.15) are then linearly fitted to absolute positions given by the technical drawing. The slope along the dispersive axis is fixed to 2.54 mm, which equals the width of each pad.

While this approach reproduced the  $x$  position quite nicely (see middle figure in Fig. 3.15), the  $y$  positions were prone to correlations with the  $x$  position. The former is therefore corrected using an  $x$  dependent offset which was estimated from the dots with a nominative  $y = 0$  mm position. The fully calibrated result is shown at the bottom of Fig. 3.15.

## 3.3.2. Calibration of the Ionisation Chamber

The response signals of the sixteen segments of the ionisation chamber were matched to the response signal of the first segment. The signal matching was performed with

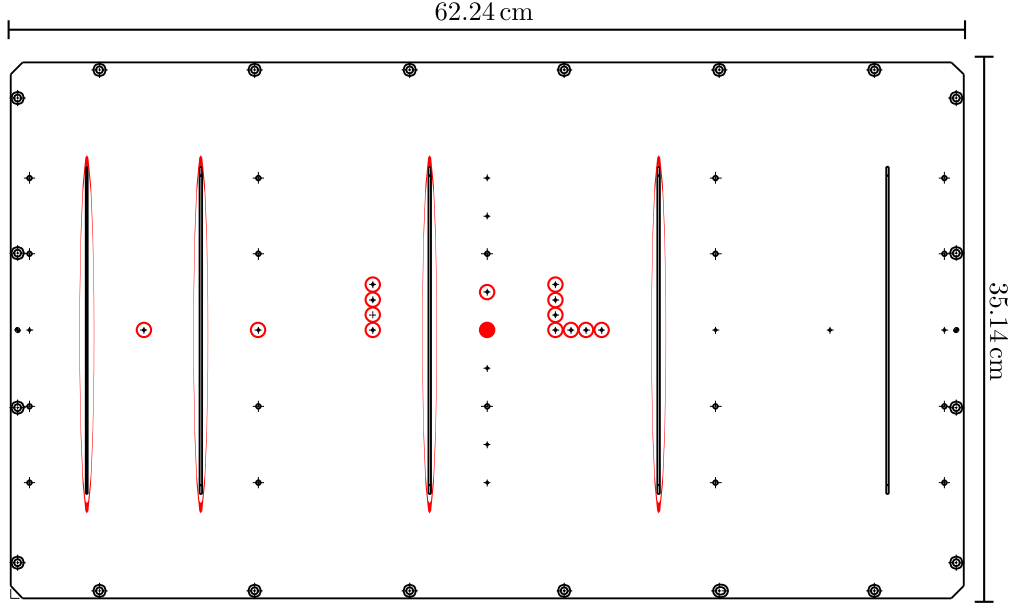


Figure 3.14.: Technical drawing of a CRDC mask. Positions circled with red rings are considered in the matching process. The full red circle corresponds to the centre position in the  $(x, y)$  plane,  $(x, y) = (0, 0)$ .

beam-only data, using between three and eight different secondary beams. In the final event building the signals of all (firing) segments were added and the mean energy loss (in arbitrary units) was calculated for particle-identification purposes.

The response signals were weakly correlated to the recoil trajectory (see Fig. 3.16), which is a manifestation of the kinetic energy dependence of the stopping power and elementary geometry. An empirical correction is applied according to

$$\Delta E_{\text{corr}} = \Delta E_{\text{raw}} + c_x \cdot x_{\text{FP}} + c_y \cdot y_{\text{FP}} \quad (3.6)$$

The parameters  $c_x, c_y$  are determined by minimizing the correlation between  $\Delta E_{\text{corr}}$  and  $x_{\text{FP}}, y_{\text{FP}}$ . The effect of this correction is also shown in Fig. 3.16.

### 3.3.3. Correction of Time-of-Flight Signals

The weak run shifts in the time-of-flight signals provided by the scintillators were corrected run-by-run. The time-of-flight signal between the S800 object point and the S800 focal plane is mandatory for a reasonable recoil identification since it is effectively used to resolve different masses (see, e.g., Fig. C.1 in the Appendix). However, the raw time-of-flight signals are too broad and therefore insufficient to resolve different isotopes. An empirical correction is applied to remove the correlations between time-of-flight signals and recoil trajectories at the focal plane.

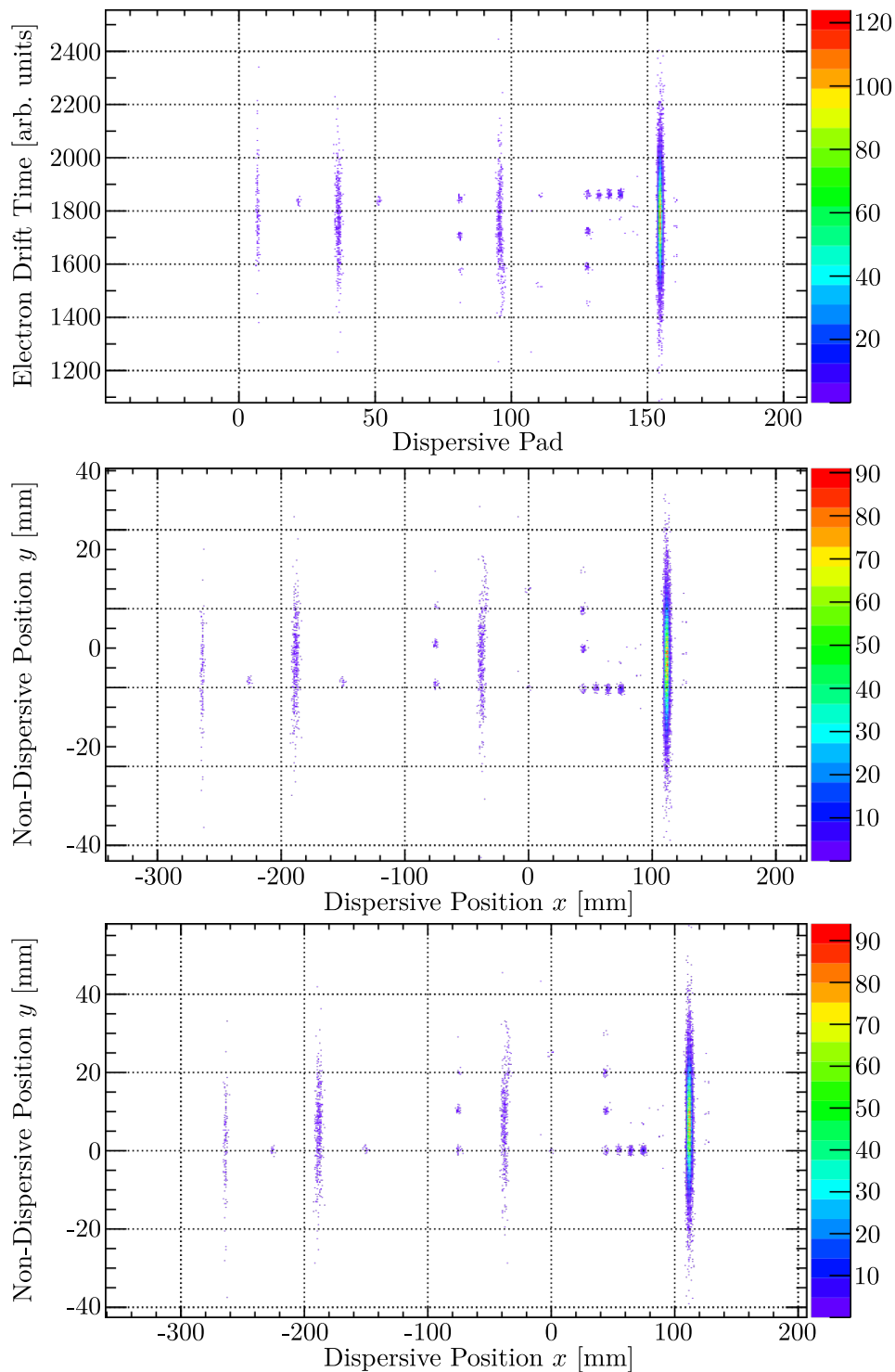


Figure 3.15.: Illustration of the CRDC matching procedure in  $x$  and  $y$  directions. *Top*: Raw coordinates. *Centre*: Matched positions without  $y(x)$  correction. *Bottom*: Matched positions with additional  $y(x)$  correction. Shown are results taken from the first CRDC during the third setup.

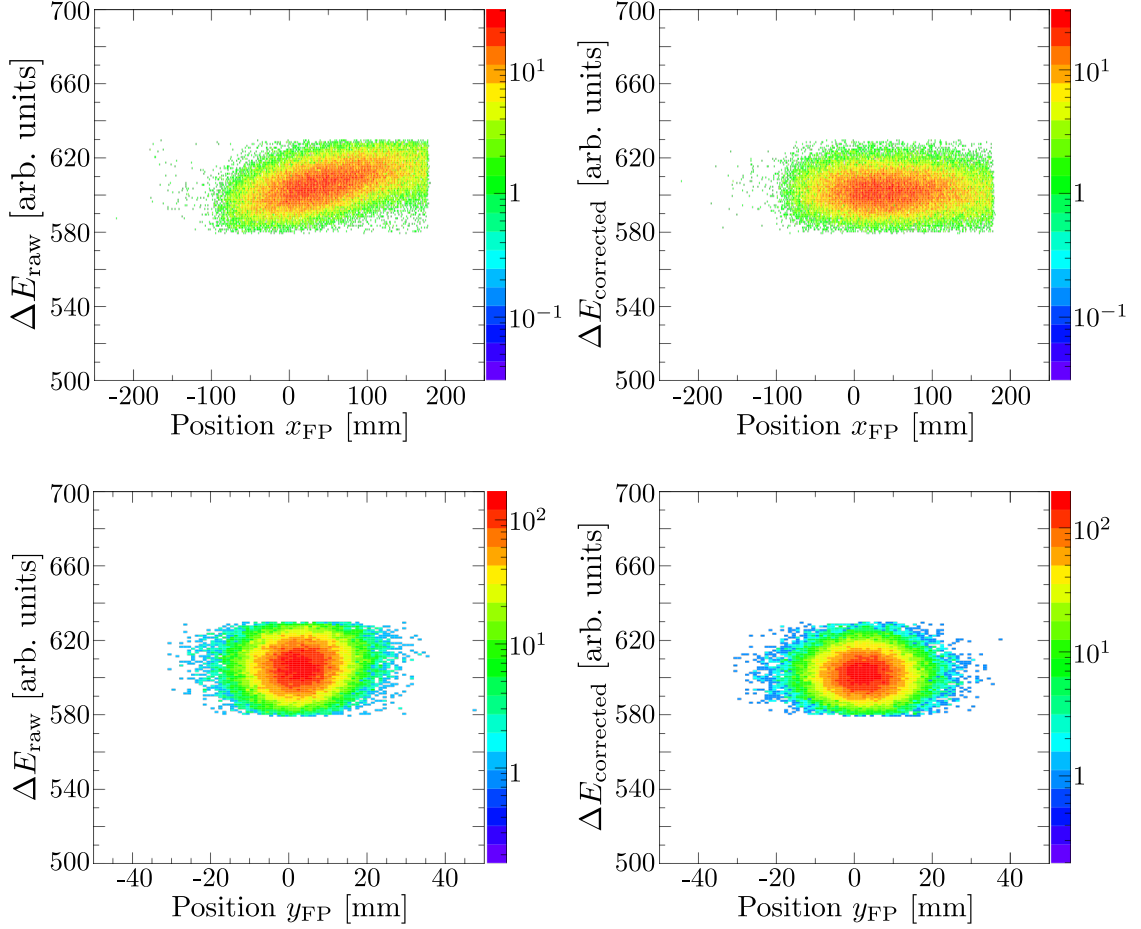


Figure 3.16.: Empirical correction of the energy-loss signals. The *left (right)* figures show the correlations between uncorrected (corrected) energy losses and focal plane  $x, y$  positions  $x_{\text{FP}}, y_{\text{FP}}$ , respectively (*top row, bottom row*). The histograms show data recorded during the target-only run in the first setup correlated to  $^{58}\text{Cr}$ .

The following correlations are considered for this purpose:

- Correlation between the dispersive position at the focal plane ( $x_{\text{FP}}$ ) and the time of flight
- Correlation between the angle along the dispersive axis at the focal plane ( $\alpha_{\text{FP}}$ ) and the time of flight

The aim is to remove these correlations by means of an empirical correction according to:

$$TOF_{\text{OBJc}} = TOF_{\text{OBJ,raw}} + c_{\alpha} \cdot \alpha_{\text{FP}} + c_x \cdot x_{\text{FP}} \quad (3.7)$$

The parameters  $c_{\alpha}$  and  $c_x$  are determined by minimizing the peak width in the projection  $TOF_{\text{OBJc}}$ .

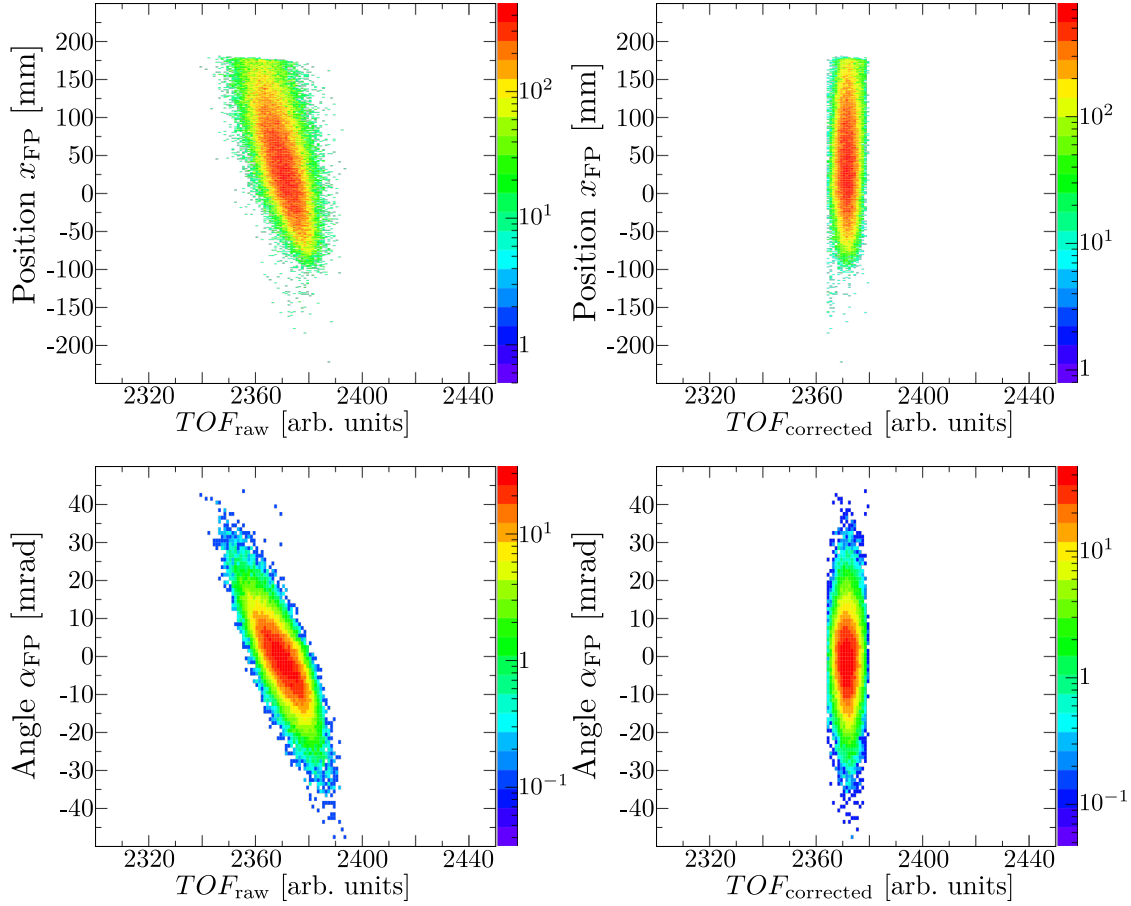


Figure 3.17.: Empirical correction of the time-of-flight signal between S800 object-point and S800 focal-plane scintillators. Shown are correlations between  $x_{\text{FP}}$  and time of flight (*top row*) as well as between  $\alpha_{\text{FP}}$  and time of flight (*bottom row*) before (*left*) and after (*right*) applying the correction. The histograms show data taken during the target-only run in the first setup correlated to  $^{58}\text{Cr}$ .

### Resolving power

The effective mass resolving power<sup>7</sup> for reaction products was on average close to 100 in the first experimental setup and close to 80 in the third experimental setup due to the larger momentum acceptance.

With respect to the  $Z$  separation, the effective resolving power was close to 45 in all three setups. The effective resolving powers are qualitatively illustrated in Appendix C in which the particle-identification correlations are shown for selected cases.

<sup>7</sup>The mass resolving power is defined as  $m/\Delta m$ . Here,  $m$  is the mass number of the isotope and  $\Delta m$  is the peak width in terms of the FWHM.

### 3.4. Particle Identification and Gate Conditions

Various gate conditions need to be applied to improve the peak-to-background ratio in Doppler-reconstructed  $\gamma$ -ray spectra. The most relevant correlations for this purpose shall be briefly discussed in this section. A schematic overview of the experimental setup is shown in Fig. 3.18, in which key signals allowing an improvement of the peak-to-background ratio are pointed out.

#### Selection of a Secondary Beam (Incoming Gate)

The secondary beams are identified by the time-of-flight difference  $TOF_{XFP} - TOF_{OBJ}$ , which corresponds to the time of flight between the A1900 focal plane and the S800 object-point scintillator (labelled  $TOF_{in}$ ). As a consequence of the momentum spread, an unambiguous selection of specific secondary beams was in many cases practically impossible (see Fig. 5.1 for illustration). Still, this gate is mandatory, because even if this gate is ambiguous, the population of a specific isotope is typically induced by one dominating reaction channel.

#### Particle Identification of Reacted Particles

Recoils are predominantly identified by employing the  $\Delta E - TOF$  method. Here, information on the (corrected) energy loss  $\Delta E_{corr}$  is deduced from the ionisation chamber at the S800 focal plane while the relevant  $TOF$  signal is given by the empirically corrected signal  $TOF_{OBJ}$ . Such correlation plots are shown in Appendix C for all setups and for various incoming gates. These plots also illustrate the achieved PID resolution.

For the first experimental setup, this approach was sufficient to achieve a clean recoil-gated  $\gamma$ -ray spectrum. In the second and third experimental setup, however, this general statement cannot be made for all of the investigated isotopes. Here, it was sometimes necessary to cut on specific recoil trajectories as enabled by the CRDC detectors, which essentially is a  $B\rho$  cut. Fig. 3.19 illustrates the improving peak-to-background ratios by successive application of gate conditions.

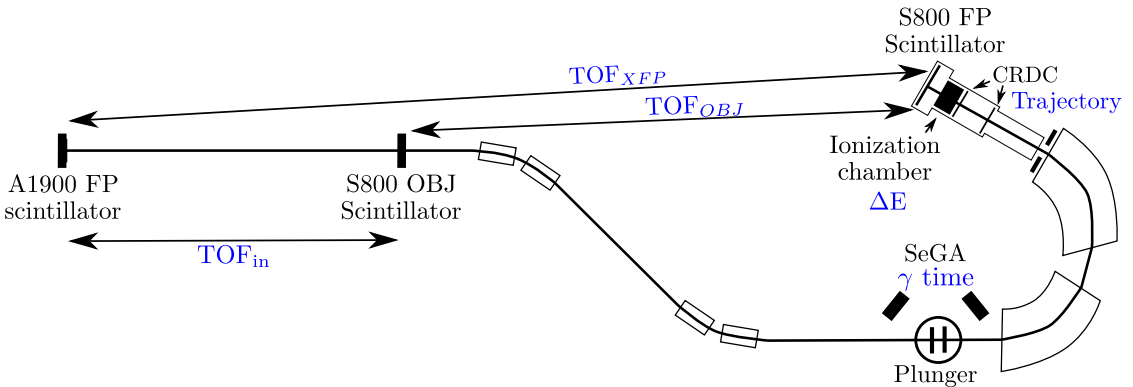


Figure 3.18.: Schematic sketch of the experimental setup in which the most helpful signals to improve the peak-to-background ratio are identified in blue.

## SeGA Timing Information

Depending on the  $\gamma$ -ray energy, an additional cut condition on the prompt  $\gamma$ -time response may improve the peak-to-background ratio. However, one must be aware that low-energy  $\gamma$  rays are influenced by a time walk introduced by the Constant Fraction Discriminator (CFD) during the signal processing.

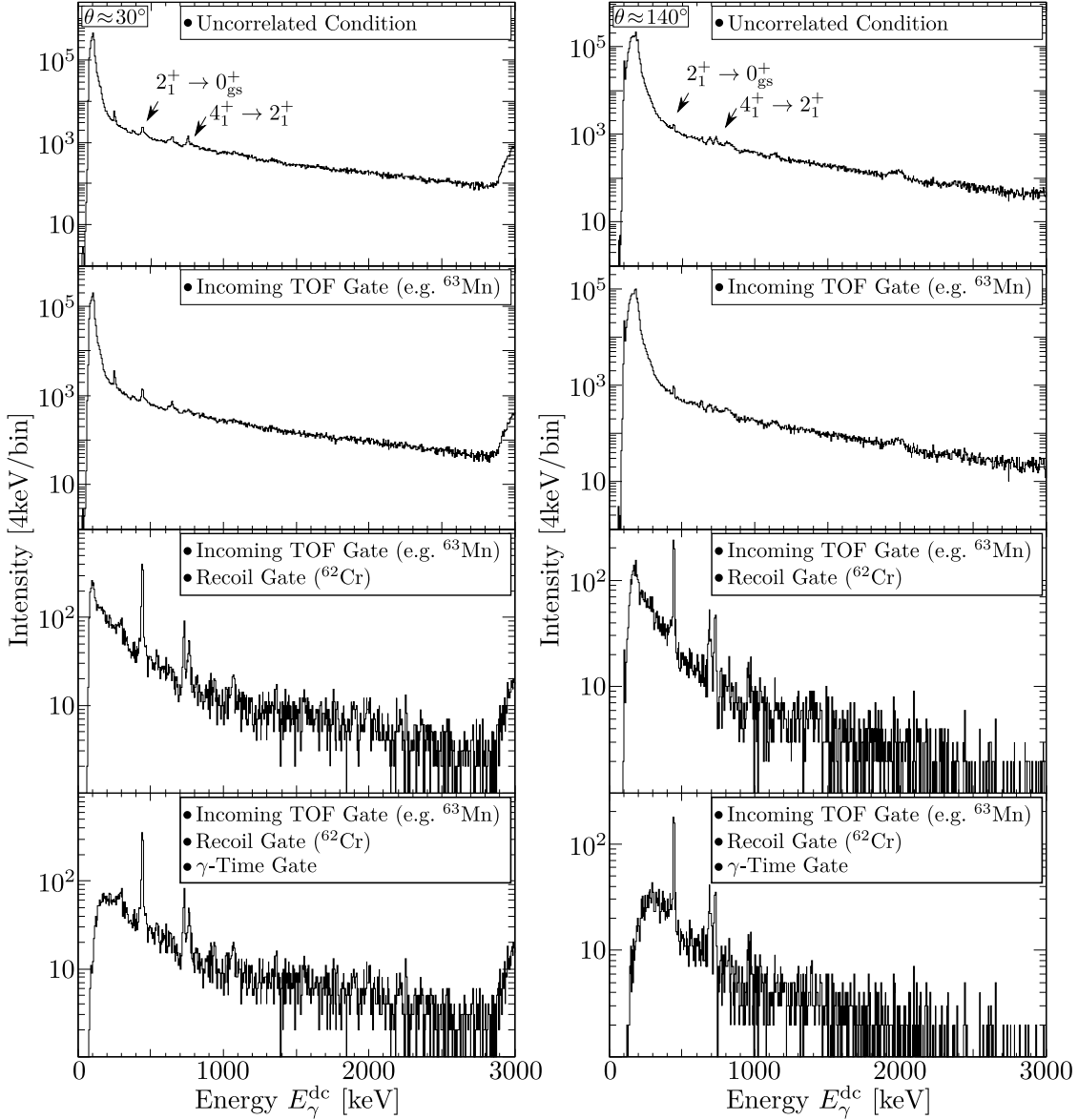


Figure 3.19.: Application of various gate conditions (listed in the inserts) and their impacts on the peak-to-background ratio in the Doppler-reconstructed  $\gamma$ -ray spectrum of the downstream (*left*) and upstream (*right*) detector ring. The shown statistics was recorded with the third experimental setup.

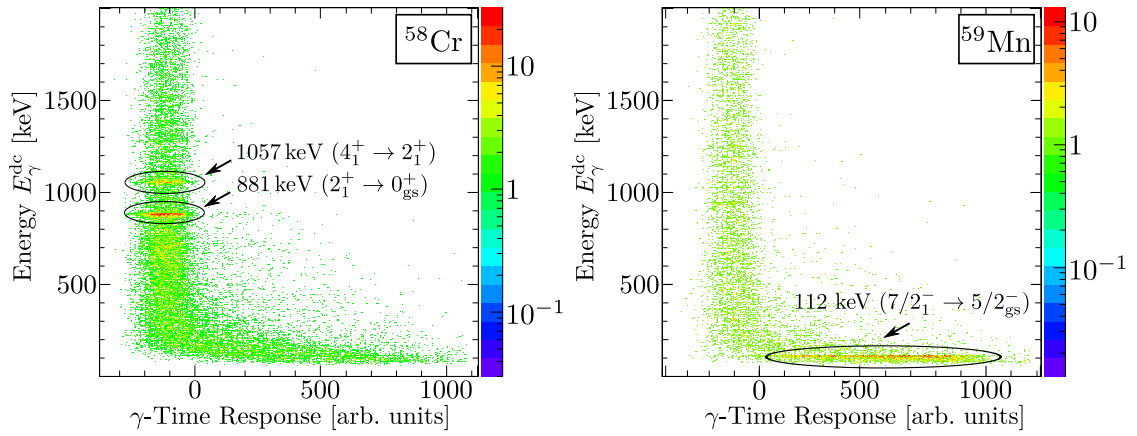


Figure 3.20.: Correlation plots showing the Doppler-reconstructed  $\gamma$ -ray energy versus the SeGA  $\gamma$ -time response for  $^{58}\text{Cr}$  (*left*) and  $^{59}\text{Mn}$  (*right*), respectively. Note the distinctively different time behaviour as a result of the CFD time walk. Both data sets are taken from the target-only run of the first experimental setup.

This is illustrated in Fig. 3.20, which shows an unproblematic ( $^{58}\text{Cr}$ ) and a problematic case ( $^{59}\text{Mn}$ ).

---

## 4. Analysis

The focus of the experiment was set on the determination of level lifetimes in  $^{58,60,62}\text{Cr}$ . However, the large variety of the secondary beams in combination with various open reaction channels (apart from the one-proton knockout) excited states in neighbouring nuclei with sufficient statistics which allowed a quantitative analysis. As a consequence, it was also possible to investigate level lifetimes and to identify  $\gamma$ -ray transitions in such neighbouring nuclei in the vicinity of  $N = 40$ .

### 4.1. Determination of Transition Energies

Within the present work,  $\gamma$ -ray transitions with sufficient yield for a clear assignment were investigated. The SeGA geometry was fixed as described in Sec. 3.1.1. The quoted errors with respect to the  $\gamma$ -ray energies include the following effects:

- A statistical uncertainty given by the fitting procedure.
- If the lifetime of the corresponding state is known and small,  $\tau \leq 100$  ps, the systematic error is estimated at 1 keV ( $E_{\gamma}^{\text{ds}} \leq 1500$  keV) or 2 keV ( $E_{\gamma}^{\text{ds}} > 1500$  keV). Here,  $E^{\text{ds}}$  denotes the Doppler-shifted  $\gamma$ -ray energies in the downstream detector ring.
- If the level lifetime was unknown and could not be determined, a systematic relative error of 0.5 % is assumed, which is supposed to safely cover lifetime effects, see Fig. 4.3 for illustration.

### 4.2. Lifetime Estimates from Decay Curves

For cross checking purposes, lifetimes of the  $2_1^+$ ,  $4_1^+$  states in  $^{58,60,62}\text{Cr}$  were estimated by analysing their decay curves. This can be considered as a reasonable starting point of any further and more detailed discussion. This was performed as follows:

First, the experimental decay scheme was fixed. Regarding  $^{58,60}\text{Cr}$ , target-only data was used for this purpose. This was impossible for  $^{62}\text{Cr}$  due to the lack of target-only data for this nucleus. In this case, the added statistics of both investigated foil separations was used.

The fast (f) and slow (s) components in the Doppler-reconstructed  $\gamma$ -ray spectra are fitted with Gaussian functions, leading to intensities  $I_f$  and  $I_s$ . Both are corrected for the following effects:

- Assuming mean recoil  $\beta$  velocities  $\beta_f$  (behind target) and  $\beta_s$  (behind degrader) as well as mean detector polar angles  $\bar{\theta}^{\text{lab}}$ , mean Doppler-shifted energies  $E_{\gamma(f,s)}^{\text{lab}}$  in the

laboratory frame were evaluated and cross-checked with the experimental raw  $\gamma$ -ray spectrum. For these energies  $E_{\gamma(f,s)}^{\text{lab}}$ , the intensities were corrected for the efficiency using an empirical description (see Sec. 3.1.2.2).

- The intensities were corrected for the Lorentz boost (see Eq. 4.2), which describes the velocity dependent radial  $\gamma$ -ray emission probability.
- The intensities were normalized to a given total intensity, leading to intensities  $\tilde{I}_f$  and  $\tilde{I}_s$ , respectively.

The largest plunger foil separation was used to quantify the contribution of degrader excitations to the total intensity  $\tilde{I}_{\text{tot}}$ . This contribution was then subtracted from  $\tilde{I}_s$  for all separations.

The foil separations  $d_i$  were translated into effective distances  $d_{i,\text{eff}}$ , which took into account the absolute foil separation  $d_i$  (see Sec. 3.2.2) and for both target and degrader half the foil thicknesses  $T_T$  and  $T_D$  (see Sec. 3.2.3):

$$d_{i,\text{eff}} = d_i + \frac{1}{2}(T_T + T_D) \quad (4.1)$$

The effective separations were then path-corrected assuming a mean scattering angle  $\theta_s$  as measured with S800. In a last step, these distances were translated into the time frame using the mean recoil  $\beta$  velocity behind the target,  $\beta_f$ , for which the effect of time dilation was incorporated.

The Bateman equations [Bat10] allow to formulate for the given decay scheme an analytical expression of  $N_J(t) := \tilde{I}_s / (\tilde{I}_s + \tilde{I}_f)$  for each state  $J$ . Level lifetimes are then determined by fitting  $N_J$  to the given data points, beginning with the state with the highest excitation energy. The only free parameter in this fit is the level lifetime of interest. All other parameters are fixed.

For completeness, it has to be stressed that this procedure lacks precision in several ways, of which only one shall be mentioned: The assumption of Gaussian functions to describe the peaks neglects all effects influencing the line shape, e.g. slowing-down effects and changes with respect to the effective detection angle. The former is relevant for very short lifetimes<sup>1</sup> and the latter is crucial for long lifetimes,  $\tau \geq 100$  ps.

### 4.3. Determination of Level Lifetimes Using a Realistic Monte Carlo Simulation

Lifetimes were determined using the dedicated Monte Carlo simulation G4LIFETIMEG. This tool was developed at the NSCL and has been continuously improved over the last decade (see Refs. [Adr09; Lem12]). The tool is written in C++ and utilizes the GEANT4 Toolkit [Ago03], e.g. to describe the interaction of radiation and matter. The generated events are then written into ROOT [Bru97] compatible files.

The ingredients of the simulations are fed in by an input file that describes relevant experimental conditions (e.g. incoming beam properties, detector geometry, foil configuration, reaction parameters and experimental decay schemes). The simulation tool

<sup>1</sup>Short lifetime in this context refers to the flight time of recoils through the foils.

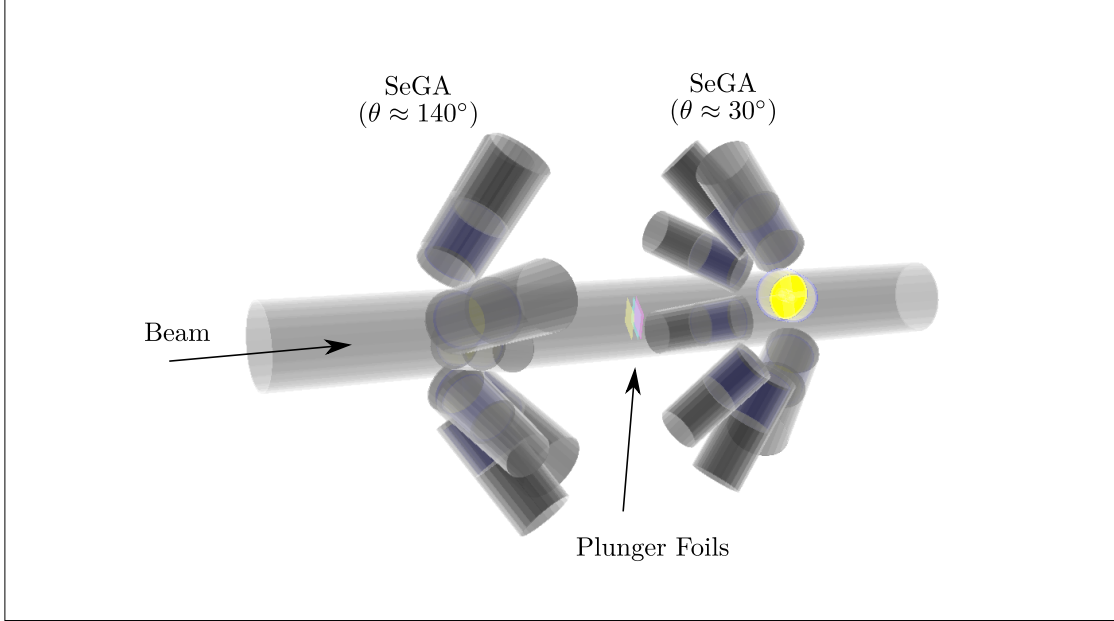


Figure 4.1.: Replication of the experimental geometry as provided by G4LIFETIMEG. Shown are the plunger foils, the upstream and downstream (left and right) detector crystals and their housings as well as the beam pipe.

provides an accurate description of the geometry with respect to foils, beam pipe and SeGA detectors. The geometry is illustrated in Fig. 4.1. Within this work, few modifications to this toolkit (see Sec. 4.3.3) were applied to suit the experimental needs of the present experiment.

#### 4.3.1. Relativistic effects

The description of relativistic effects relevant to RDDS experiments at intermediate energies (such as time dilation/Lorentz contraction, Doppler-broadening and aberration effects/Lorentz boost) is incorporated in the simulation.

The Lorentz boost for a particle moving along the beam axis affects the  $\gamma$ -ray intensity distribution in the laboratory frame according to

$$\frac{d\Omega_{\text{lab}}}{d\Omega_{\text{par}}} = \frac{1 - \beta^2}{(1 + \beta \cos \theta_{\text{par}})^2} = \frac{(1 - \beta \cos \theta_{\text{lab}})^2}{1 - \beta^2} \quad (4.2)$$

The index lab(par) denotes values given in the laboratory(particle) frame. In addition, the aberration effect,  $\cos \theta_{\text{lab}} = (\cos \theta_{\text{par}} + \beta)/(1 + \beta \cos \theta_{\text{par}})$ , describes the change of the emission angle in the laboratory frame compared to the particle frame due to the non-vanishing recoil velocity.

The impact of the Lorentz boost on the present experiment is sketched in Fig. 4.2 for the given recoil velocities. The effect leads essentially to an increase of  $\gamma$ -ray intensity observed in the downstream detector ring by a factor of  $\sim 2$  and, hence, to a decrease of  $\gamma$ -ray intensities observed in the upstream detector ring. This explains why – in case of sparse  $\gamma$ -ray yields – the analysis focuses on data from the downstream detector ring.

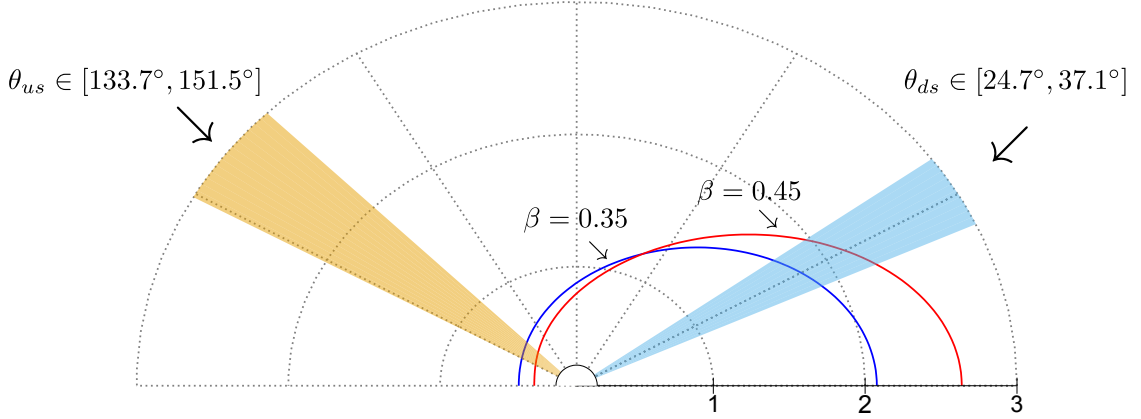


Figure 4.2.: Effect of the Lorentz boost on the  $\gamma$ -ray distribution observed in the laboratory frame for  $\beta$ -velocities of  $\beta = 0.35, 0.45$  (blue and red curve). The solid angles covered by the SeGA detectors are depicted for the downstream (blue) and upstream (orange) detector rings.

#### 4.3.2. Effect of the Level Lifetime on the Line Shape

Due to its realistic physical and geometrical description, the toolkit can be applied to estimate the influence of the level lifetime on the line shape in the Doppler-reconstructed spectrum. The effect is illustrated in Fig. 4.3 for both detector rings. This leads to the following conclusions:

- The effect of the level lifetime on the line shape is more pronounced in the downstream detector ring. This can be explained by the relationship between the experimental  $\gamma$ -ray emission angle and the emission coordinates, which changes more rapidly for the downstream detector ring.
- In both detector rings, the low-energy shoulder of the peak is distinctively more distorted compared to the high-energy shoulder.
- The energy of the peak maximum in the Doppler-reconstructed  $\gamma$ -ray spectrum is correlated to the level lifetime  $\tau$ . The peak maximum shifts toward lower energies for increasing level lifetimes. This effect is slightly more pronounced in the downstream detector ring compared to the upstream detector ring.
- With the present geometry, the effect becomes measurable for  $\tau \sim 100$  ps assuming recoil velocities of  $\beta \approx 0.4$ .

#### 4.3.3. Changes to the Code G4LifeTimeG

The already existing code was modified in some respects within the present work. Two major changes are briefly outlined in this section.

- While G4LIFETIMEG is able to reproduce the full-energy peak efficiencies quite accurately for  $\gamma$ -ray energies larger than 200 keV, deviations occur in particular at

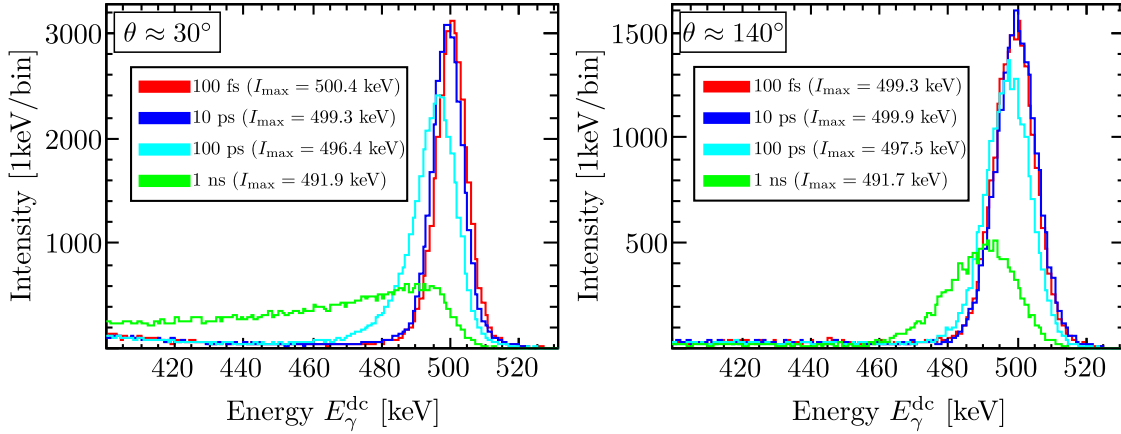


Figure 4.3.: Effect of the level lifetime on the line shape in the Doppler-reconstructed  $\gamma$ -ray spectra of the downstream (*left*) and upstream (*right*) detector ring for  $\tau = 100$  fs, 10 ps, 100 ps and 1 ns. The values in brackets quote the energy of the largest peak amplitudes. The generated  $\gamma$ -ray spectra are the result of a 100 MeV/ $u$  beam impinging on a 100  $\mu\text{m}$  Be foil, which excites a state at 500 keV.

smaller energies. For illustration, see Fig. 4.4 (top and middle), which shows an experimental spectrum taken with a  $^{152}\text{Eu}$  source and its simulated counterpart. One can readily identify deviations, in particular at low  $\gamma$ -ray energies. The dominating reason for this behaviour is the inability of the simulation to describe effects related to electronic components, e.g. by gain settings. To mimic such effects, the simulated efficiencies are empirically corrected using two piecewise linear functions. This improves the agreement significantly, as can be seen at the bottom of Fig. 4.4. The analysis of the different data sets showed that the chosen parameters were quite universal and, hence, they were held constant for all experimental parts.

- For simplification, the G4LIFETIMEG tool-kit uses fixed probability distributions (often Gaussian distributions) to simulate input parameters such as the energy distribution of the incoming beam. Experimental cases exist for which such simple distributions are unsuited, see Fig. 5.1 for illustration. The S800 spectrograph measures the kinematic properties with high precision. Hence, a routine was implemented that allows to perform Monte Carlo simulations with user-defined probability densities to describe the kinematics in more detail.

## 4.4. Error Estimates

After fixing the detector geometry, the beam and recoil kinematics as well as the feeding scheme, level lifetimes can be analysed. For this purpose, lifetime assumptions are fed into the simulation tool-kit and their values are varied in discrete steps. For each lifetime assumption a  $\chi^2$  was calculated following a modified version of the Least-squares method

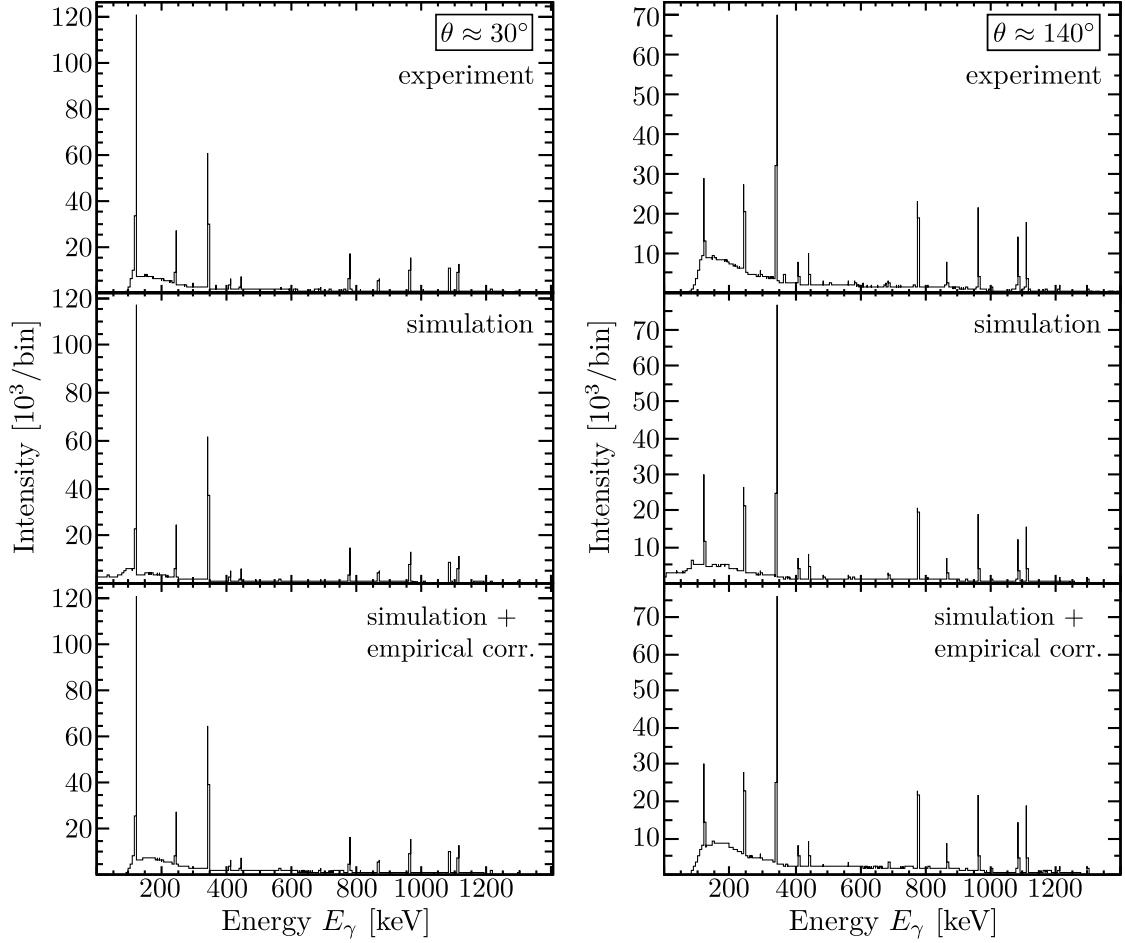


Figure 4.4.: Comparison of experimental (*top*) and simulated (*middle*)  $\gamma$ -ray spectra related to  $^{152}\text{Eu}$  standard source measurements for the downstream (*left*) and upstream (*right*) detector ring. The bottom figure shows simulated spectra after applying an empirical correction, which in particular affects efficiencies at low  $\gamma$ -ray energies.

using:

$$\chi^2 = \sum_{d_j} \sum_{\text{ds,us}} \sum_i \left( \frac{I_{\text{exp}}(i) - I_{\text{sim}}(i)}{\Delta I_{\text{exp}}(i)} \right)^2 \quad (4.3)$$

where  $I_{\text{exp}}(i)$  ( $I_{\text{sim}}(i)$ ) is the intensity of the experimental (simulated) spectrum in bin  $i$ . In order to increase the sensitivity for lifetime effects, only bins  $i$  covering the relevant transition were taken into account.

The binning was chosen such that (a) the amplitudes of fast and slow components in the Doppler-reconstructed  $\gamma$ -ray spectrum were clearly identifiable and (b) the influences of statistical artefacts in the experimental data were minimized. Under these conditions the extracted  $\chi^2$  was essentially insensitive to further increases in the binning. A binning of 4 keV/bin was usually the reasonable choice although in some cases the binning had to be increased to 8 keV/bin, especially in cases of low statistics.

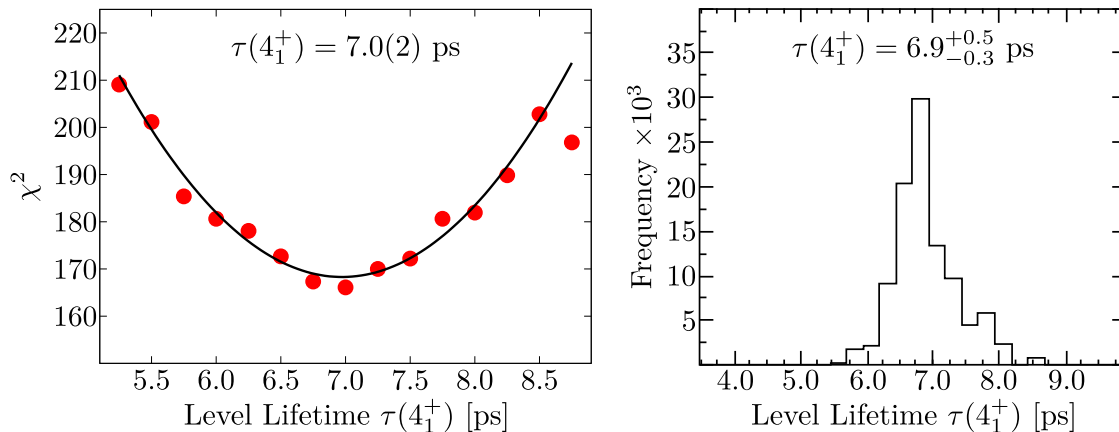


Figure 4.5.: Determination of the mean lifetime and the statistical error of the  $4_1^+$  state in  $^{62}\text{Cr}$  using the standard  $\chi^2$  method (*left*) and the present approach (*right*). The errors of the  $\chi^2$  method are deduced from lifetimes with  $\chi^2 + 1$ .

The sum is taken over both detector rings (ds and us) and all foil separations  $d_j$ . The detailed procedure is described in the following.

### Determination of Mean Lifetimes and Statistical Errors

A transition is distributed within an experimental spectrum over several bins  $i$  and each bin  $i$  contains  $N_i$  events. Hence, from a statistical point of view and according to the maximum likelihood method, the experimental spectrum is in agreement with a modified version, for which the number of events in each bin  $i$  is randomly varied following the Poisson distribution. Within this modified  $\gamma$ -ray spectrum the total peak intensity of a  $\gamma$ -ray transition is expected to deviate from the total peak intensity as seen in the original experimental spectrum. With respect to RDDS measurements, both peaks are affected and the influence of these variations on the deduced lifetime  $\tau$  reflect the experimental uncertainty due to the underlying Poisson statistics.

For the determination of mean level lifetimes and statistical errors in  $^{58,60,62}\text{Cr}$ ,  $n = 10^4$  modified spectra were generated in which variations affected only the transition of interest. Each modified spectrum was then compared to sets of simulated spectra for which different lifetimes were assumed. For each comparison the  $\chi^2$  was calculated according to Eq. 4.3 and scanned for the best-fitting lifetime assumption. A histogram showing the frequency of the best-fitting lifetime was then filled. This histogram resembled then the probability density for the lifetime based on the available data and the mean value of this probability density was taken as the quoted value, while the 16 % and 84 % quantiles were references for the quoted statistical error. A comparison of this approach with the standard  $\chi^2$  method is depicted in Fig. 4.5, which shows results for the  $4_1^+$  state in  $^{62}\text{Cr}$ . As expected, both approaches are in agreement but in this particular case the present approach leads to slightly larger and asymmetric errors.

### Determination of Additional Errors

The input parameters  $p_i$  used in G4LIFETIMEG were derived from experimental observables and, hence, were prone to uncertainties. The following error sources were considered:

- Uncertainties related to the contribution of degrader excitations
- Uncertainties related to the observed feeding structures (intensities as well as lifetimes)
- Zero offsets with respect to the foil separations
- Recoil velocity distributions behind the target

In the present work, the effects of uncertainties related to these parameters were disentangled from the pure statistical error. The errors originating from uncertain zero offsets as well as recoil energies were considered as systematic, those related to degrader excitations and feeding uncertainties as statistical.

The parameters  $p_i$  within the simulation were varied in discrete steps around  $\langle p_i \rangle$ . For each varied parameter  $p_i$ , the above mentioned method was repeated to obtain the mean lifetime as a function of  $p_i$ . In first order a linear relationship is expected, giving access to the partial derivative  $\frac{\partial \tau}{\partial p_i}$ . The uncertainty  $\Delta p_i$  for parameter  $p_i$  was either given directly by experimental uncertainties or had to be estimated. The individual statistical errors were added in quadrature. The given total error is calculated as the sum of statistical and systematic error.

## 4.5. Calculation of Transition Strengths and Related Signatures

The *transition probability*  $T$  for a  $\gamma$ -ray emission characterized<sup>2</sup> by multipolarity  $\sigma\lambda, \mu$  can be expressed as follows (see Refs. [Bla79; Mor76] and references therein):

$$T(\sigma\lambda, \mu) = \frac{8\pi(\lambda + 1)}{\lambda [(2\lambda + 1)!!]^2} \cdot \frac{1}{\hbar} \cdot \left( \frac{E_\gamma}{\hbar c} \right)^{2\lambda+1} \cdot |\langle f | \hat{\mathcal{M}}(\sigma\lambda, \mu) | i \rangle|^2 \quad (4.4)$$

Here,  $\hat{\mathcal{M}}(\sigma\lambda, \mu)$  denotes the associated multipole transition operator. Summing over all sub-processes  $\mu$  allows to formulate the *total transition probability* with respect to the transition  $I_i \rightarrow I_f$  (with initial and final nuclear spins  $I_{i,f}$ ) according to:

$$\begin{aligned} T(\sigma\lambda) &= \sum_{\mu, m_f} T(\sigma\lambda, \mu | I_i m_i \rightarrow I_f m_f) \\ &= \frac{8\pi(\lambda + 1)}{\lambda [(2\lambda + 1)!!]^2} \cdot \frac{1}{\hbar} \cdot \left( \frac{E_\gamma}{\hbar c} \right)^{2\lambda+1} \cdot B(\sigma\lambda; I_i \rightarrow I_f) \end{aligned}$$

The quantity  $B(\sigma\lambda; I_i \rightarrow I_f)$  is called *reduced transition probability* or *reduced transition strength* and is related to the matrix elements describing the electromagnetic transition as follows:

$$B(\sigma\lambda; I_i \rightarrow I_f) = \sum_{\mu, m_f} |\langle I_f m_f | \hat{\mathcal{M}}(\sigma\lambda, \mu) | I_i m_i \rangle|^2$$

With respect to electric and magnetic transitions they are related to the reduced matrix elements:

$$\begin{aligned} B(E\lambda; I_i \rightarrow I_f) &= \frac{1}{2I_i + 1} |\langle I_f | \hat{Q}_\lambda | I_i \rangle|^2 \\ B(M\lambda; I_i \rightarrow I_f) &= \frac{1}{2I_i + 1} |\langle I_f | \hat{M}_\lambda | I_i \rangle|^2 \end{aligned}$$

### $B(E2)$ values for pure E2 transitions

Taking into account branching ratios  $BR$  and de-excitations by inner conversion<sup>3</sup> quantified by the coefficient  $\alpha_{IC}(E_\gamma)$ , the  $B(E2)$  value can be written explicitly:

$$B(E2; I_i \rightarrow I_f) = \frac{2(5!!)^2}{24\pi} \cdot \frac{BR}{1 + \alpha_{IC}} \cdot \left( \frac{\hbar c}{E_\gamma} \right)^5 \cdot \frac{\hbar}{\tau} \quad (4.5)$$

Including numerical values<sup>4</sup> and neglecting the influence of branching ratios as well as of inner conversions, Eq. 4.5 reduces to:

$$B(E2; I_i \rightarrow I_f) [e^2 \text{fm}^4] = 816 \cdot \frac{1}{(E_\gamma [\text{MeV}])^5} \cdot \frac{1}{\tau [\text{ps}]}$$

<sup>2</sup>Here,  $\sigma$  denotes the character of the radiation (electric or magnetic),  $\lambda$  is the carried angular momentum and  $\mu = m_i - m_f$  is the difference between initial and final magnetic sub state.

<sup>3</sup>With respect to the present experimental data, inner conversion is irrelevant since the recoils are completely ionized.

<sup>4</sup>The following values are assumed:  $e^2 = 1.44 \text{ MeV fm}$ ,  $\hbar c = 197.33 \text{ MeV fm}$  and  $\hbar = 6.582 \cdot 10^{-22} \text{ MeV s}$ .

### Mixed E2/M1 transitions

In some cases a transition can be realized by more than one electromagnetic mode. With respect to the present work, most important are  $\Delta I = 1$  transitions, which – if allowed by the selection rules – can be realized by competing E2 and M1 transitions. The square of the *multipole mixing ratio*  $\delta_{\text{E2/M1}}$  is defined as the ratio of the corresponding total transition probabilities:

$$\delta_{\text{E2/M1}}^2 = \frac{T(\text{E2}; I_i \rightarrow I_i - 1)}{T(\text{M1}; I_i \rightarrow I_i - 1)} = \frac{3}{100} \cdot \frac{B(\text{E2})}{B(\text{M1})} \cdot \left( \frac{E_\gamma}{\hbar c} \right)^2 \quad (4.6)$$

$$= 6.97 \cdot 10^{-5} \cdot (E_\gamma [\text{MeV}])^2 \cdot \frac{B(\text{E2}) [e^2 \text{fm}^4]}{B(\text{M1}) [\mu_N^2]} \frac{\mu_N^2}{e^2 \text{fm}^4 \text{MeV}^2} \quad (4.7)$$

The identity  $\hbar c = 6.582 \cdot 10^{14} \text{ e T fm}^2$  and the nuclear magneton  $\mu_N = 3.152 \cdot 10^{-14} \text{ MeV/T}$  were used in the second step. For such a mixed E2/M1 transition, the level lifetime  $\tau$  (in ps) is given in terms of:

$$\tau [\text{ps}] = \frac{BR}{1 + \alpha_{\text{IC}}} \cdot \frac{\delta^2}{1 + \delta^2} \cdot \frac{1}{(E_\gamma [\text{MeV}])^5} \cdot \frac{816}{B(\text{E2}; I_i \rightarrow I_i - 1) [e^2 \text{fm}^4]} \quad (4.8)$$

### Intrinsic quadrupole moments in the rotational model

In the rotational model, the (absolute) intrinsic quadrupole moments  $|Q_0(I_i)|$  for  $K = 0$  bands can be derived from stretched  $B(\text{E2}; I_i \rightarrow I_i - 2)$  values using the following formula [Mor76]:

$$B(\text{E2}; I_i \rightarrow I_i - 2) = Q_0^2 \cdot \frac{5}{16\pi} \cdot \frac{3}{2} \cdot \frac{I(I-1)}{(2I+1)(2I+3)} \quad (4.9)$$

With respect to the ground-state band the connection between intrinsic quadrupole moment  $|Q_0|$  and quadrupole deformation parameter  $\beta$  is made as follows:

$$|Q_0| = \frac{3}{\sqrt{5\pi}} Z e R_0^2 \beta_2, \quad R_0 = 1.2 A^{1/3} \text{fm} \quad (4.10)$$

Within this work, the  $B(\text{E2})$  values and derived properties are calculated by a Monte Carlo simulation, for which the lifetime and the associated uncertainty is taken as an input parameter. The median of the hereby generated distribution corresponds to the adopted  $B(\text{E2})$  value, while the associated errors are deduced from the quantiles q(16 %) and q(84 %), respectively.

## 5. Results

The experimental results of the discussed experiment are presented in this chapter. An overview of all nuclei for which experimental signatures, i.e.  $\gamma$ -ray transitions and level lifetimes, were determined can be found in Table 5.1.

In Sec. 5.1 the (strongest) constituents of the cocktail beams are discussed with respect to their intensities and (mean) energies. Furthermore, it is illustrated that the unambiguous identification for some of the secondary beams purely by means of the time-of-flight signal  $TOF_{in}$  was not possible.

Since the focus of the present experiment was set on the determination of level lifetimes in  $^{58,60,62}\text{Cr}$ , the experimental results for these nuclei are discussed in detail in Sec. 5.2 ( $^{58}\text{Cr}$ ), Sec. 5.3 ( $^{60}\text{Cr}$ ) and Sec. 5.4 ( $^{62}\text{Cr}$ ), respectively. All other nuclei are discussed in briefer terms. Two dimensional correlation plots illustrating the particle identification of (reacted) recoils are shown in Appendix C.

Isotope	Setup	Section	$\gamma$ -Ray Transitions	Level Lifetimes
$^{64}\text{Fe}_{38}$	3	5.8	✓	✓
$^{63}\text{Mn}_{38}$	3	5.7.3	✓	✓
$^{61}\text{Mn}_{36}$	2,3	5.7.2	✓	✓
$^{59}\text{Mn}_{34}$	1	5.7.1	✓	✓✓
$^{62}\text{Cr}_{38}$	1	5.4	✓/ (✓✓)	✓✓
$^{60}\text{Cr}_{36}$	1	5.3	✓/ (✓✓)	✓✓
$^{58}\text{Cr}_{34}$	1	5.2	✓/ (✓✓)	✓✓
$^{57}\text{Cr}_{33}$	1	5.6.1	✓	✓✓
$^{56}\text{V}_{33}$	1	5.5.1	✓✓	-
$^{55}\text{V}_{32}$	1	5.5.2	✓	✓✓

Table 5.1.: List of nuclei for which either  $\gamma$ -ray transitions or level lifetimes were determined within this work. Entries marked with ✓ have been observed prior to this work, while entries marked with ✓✓ indicate new results.

### 5.1. Composition of the Cocktail Beams

For all three experimental setups, data without any material at the target position (*beam-only data*) was recorded which offers the cleanest fingerprints of secondary beams in the radioactive cocktail beam reaching the S800 focal plane. Beam-only data is advantageous since the S800 focal-plane detector system can be used to unambiguously identify the secondary beams.

The cocktail beams will be briefly discussed for each experimental setup. The time-of-

Setup	Particle	Energy $\bar{E}_{S800}$ (A MeV)	Total Rate $R_{tot}$ (pps)	$I_{rel}$ (%)
1	$^{59}\text{Mn}$	92.25(3)	$1.80(2) \cdot 10^5$	64.6(8)
	$^{60}\text{Fe}$	96.17(4)	$8.80(12) \cdot 10^4$	31.5(4)
	$^{58}\text{Cr}$	88.09(3)	$3.15(9) \cdot 10^3$	1.14(3)
	$^{56}\text{V}$	87.00(4)	$1.11(5) \cdot 10^3$	0.40(2)
2	$^{61}\text{Mn}$	92.18(3)	$1.99(3) \cdot 10^4$	58.1(9)
	$^{62}\text{Fe}$	96.25(3)	$9.26(17) \cdot 10^3$	27.0(5)
	$^{64}\text{Co}$	96.74(4)	$1.77(5) \cdot 10^3$	5.2(2)
	$^{60}\text{Cr}$	87.90(5)	$9.15(33) \cdot 10^2$	2.7(1)
	$^{59}\text{Cr}$	91.30(5)	$6.86(27) \cdot 10^2$	2.0(1)
	$^{58}\text{V}$	86.81(5)	$4.48(21) \cdot 10^2$	1.3(1)
	$^{63}\text{Fe}$	93.00(6)	$4.30(20) \cdot 10^2$	1.3(1)
3	$^{64}\text{Fe}$	102.37(4)	$3.99(5) \cdot 10^3$	29.5(4)
	$^{66}\text{Co}$	102.93(4)	$3.32(5) \cdot 10^3$	24.5(3)
	$^{63}\text{Mn}$	98.00(3)	$3.29(5) \cdot 10^3$	24.3(3)
	$^{65}\text{Fe}$	98.84(3)	$1.64(3) \cdot 10^3$	12.1(2)
	$^{61}\text{Cr}$	96.88(4)	$2.33(6) \cdot 10^2$	1.7(1)
	$^{62}\text{Mn}$	101.55(4)	$2.13(5) \cdot 10^2$	1.6(1)
	$^{62}\text{Cr}$	96.33(5)	$1.15(3) \cdot 10^2$	0.9(1)
	$^{60}\text{V}$	92.06(6)	$3.08(15) \cdot 10^1$	0.2(1)

Table 5.2.: Identification of secondary beams and their properties. Experimental mean energies  $\bar{E}_{S800}$  were measured with S800. The calculated total rates  $R_{tot}$  assume a primary beam intensity of 35 pA. The table lists results as deduced from beam-only data. See text for details.

flight spectra  $TOF_{in}$  based on beam-only data are shown for all setups in Fig. 5.1, which also include a precise identification of the components enabled by the S800 focal-plane detector system.

Table 5.2 lists all individual secondary beams for each of the three experimental setups, complemented by corresponding mean energies  $\bar{E}_{S800}$  as measured with the S800 spectrograph, total rates  $R_{tot}$  as well as relative intensities  $I_{rel}$  (with respect to the total particle yield). The quoted errors of the mean energies  $\bar{E}_{S800}$  incorporate statistical and systematic uncertainties, the latter originating from an estimated uncertainty of 5 mT for the  $B\rho$  setting and an estimated uncertainty of 5 mm for the dispersive position as measured at the focal plane of S800. The total rate  $R_{tot}$  is calculated according to:

$$R_{tot} [1/s] = N \cdot \frac{1}{\Delta t [s]} \cdot \frac{35 [\text{pA}]}{I_{beam}^{run} [\text{pA}]} \cdot \frac{1}{LT} \quad (5.1)$$

Here,  $N$  is the (gated) number of events assigned to a specific isotope,  $\Delta t$  is the duration of the beam-only run,  $I_{beam}^{run}$  is the primary beam intensity used in the beam-only run, 35 pA is the nominative primary beam intensity and  $LT$  is the lifetime of the data acquisition (DAQ) system. The latter was deduced from scaler information. The quoted

errors incorporate statistical and systematic effects, the latter being estimated to 2 %.

In the first experimental setup,  $^{59}\text{Mn}$  ( $I_{\text{rel}} = 65\%$ ) and  $^{60}\text{Fe}$  (32 %) were the strongest components of the cocktail beam. A separation of the incoming beams using time-of-flight signals  $TOF_{\text{in}}$  was feasible in most cases. Only the secondary beams  $^{58}\text{Cr}$  and  $^{56}\text{V}$  overlap, which, however, was irrelevant to the present work due to their low intensities.

In the second experimental setup,  $^{61}\text{Mn}$  (58 %) and  $^{62}\text{Fe}$  (27 %) were the strongest secondary beams. A minimal overlap in the  $TOF_{\text{in}}$  spectrum could not be avoided. In addition, the number of secondary beams with comparable yields was significantly larger compared to the first experimental setup, making contaminations practically unavoidable. However, the relative contribution of these contaminants was rather small and affected the analysis only marginally.

In the third and last experimental setup, four secondary beams with comparable relative intensities appeared in the cocktail beam:  $^{63}\text{Mn}$  (24 %),  $^{64}\text{Fe}$  (29 %),  $^{66}\text{Co}$  (25 %) and  $^{65}\text{Fe}$  (12 %). Here, none of the secondary beams could be fully selected without contaminations by means of the incoming time-of-flight signal  $TOF_{\text{in}}$ .

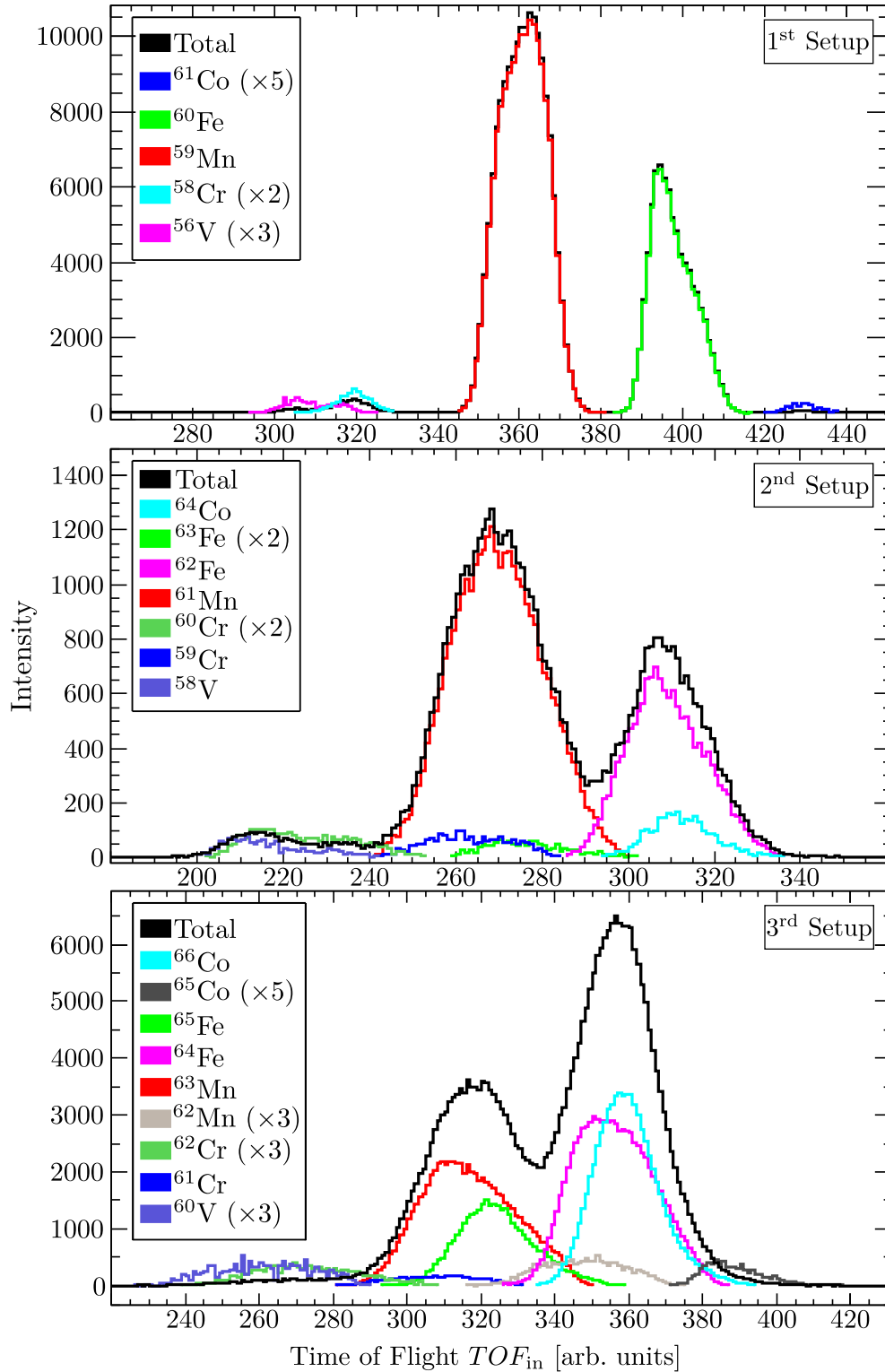


Figure 5.1.: Time-of-flight spectra ( $TOF_{in}$ ) correlated to beam-only data. An unambiguous identification of individual secondary beams (see inserts) was performed by applying additional gate conditions on signatures measured with S800. See text for details.

## 5.2. $^{58}\text{Cr}_{34}$ - Measurement of $\gamma$ -Ray Transition Energies and Level Lifetimes

Most precise information on the level scheme in  $^{58}\text{Cr}$  is available from  $\beta$  decay studies of  $^{58}\text{V}$  [Pri01; Man03] as well as from  $\gamma$ -ray spectroscopy following deep-inelastic reactions [Mar06; Zhu06].

Prior to this experiment, knowledge on transition strengths was only available for the  $2_1^+ \rightarrow 0_{\text{gs}}^+$  transition from Coulomb-excitation experiments performed at intermediate energies, quantified by  $B(\text{E}2; 2_1^+ \rightarrow 0_{\text{gs}}^+) = 197(56) e^2\text{fm}^4$  [Bür05]<sup>1</sup> and  $172(25) e^2\text{fm}^4$  [Bau12], respectively.

In the present experiment, the production yield of  $^{58}\text{Cr}$  was largest in the first experimental setup following one-proton knockout from  $^{59}\text{Mn}$ .

### Observation of $\gamma$ -Ray Transitions in Target-Only Data

Doppler-reconstructed  $\gamma$ -ray spectra of  $^{58}\text{Cr}$  taken with only the plunger target at the experimental position (*target-only data*) are shown in Fig. 5.2. These spectra were recorded for 5.5 hours. In total,  $6.9 \cdot 10^4$  events were assigned to  $^{58}\text{Cr}$ .

$\mathbf{J_i \rightarrow J_f}$	$\mathbf{E_\gamma^{\text{lit}}}$ (keV)	$\mathbf{E_\gamma^{\text{exp}}}$ (keV)	$\mathbf{I_\gamma}$ (%)
$2_1^+ \rightarrow 0_{\text{gs}}^+$	880.5(2)	880.3(12)	100.0(15)
$4_1^+ \rightarrow 2_1^+$	1057.4(2)	1057.0(12)	60.5(31)
$6_1^+ \rightarrow 4_1^+$	1280.4(3)	1283(3)	11.0(7)
$5^{(-)} \rightarrow 4_1^+$	1372.5(3)	1373(9)	6.9(6)
No assignment	–	1108(8)	5.7(5)
No assignment	–	1767(14)	4.7(4)
No assignment	–	2154(16)	4.6(4)
No assignment	–	1687(11)	3.0(3)
No assignment	–	1495(10)	2.6(3)
No assignment	–	1520(11)	1.0(2)

Table 5.3.: (First setup –  $^{58}\text{Cr}$  – target-only data) Observed transitions in descending order by relative intensities. The quoted errors include statistical and systematic uncertainties. Quoted intensities are relative to the  $2_1^+ \rightarrow 0_{\text{gs}}^+$  transition. See text for more details.

<sup>1</sup>Bürger *et al.* deduced this value in a set of experiments on  $^{54,56,58}\text{Cr}$  performed with the RISING setup at GSI, in which the  $B(\text{E}2; 0_{\text{gs}}^+ \rightarrow 2_1^+)$  values were determined by normalizing on the literature  $B(\text{E}2)$  value in  $^{54}\text{Cr}$ . This literature value is a result of various Coulomb-excitation experiments performed in the 1960's and 70's. More precise measurements in  $^{54}\text{Cr}$  may be feasible with modern techniques and instruments, which would allow to re-evaluate the  $B(\text{E}2)$  values published in Ref. [Bür05].

This corresponds to a production cross section of 7(2) mb, if assuming a primary beam intensity of 35(7) p nA, a transmission of 90(10) % as well as a lifetime of the DAQ of 88 % as deduced from scaler information. The strongest peaks at 880 and 1057 keV are assigned to the yrast transitions  $2_1^+ \rightarrow 0_{gs}^+$  and  $4_1^+ \rightarrow 2_1^+$ , the latter with an intensity of 60.5 % relative to the former. The  $6_1^+ \rightarrow 4_1^+$  transition at 1283 keV (11.0 %) can also be identified. Zhu *et al.* [Zhu06] observed a transition with 1460 keV which they tentatively assigned to the  $(8^+) \rightarrow 6_1^+$  transition. However, the present spectra indicate no evidence for a peak at this specific energy. The peak at 1373 keV (6.9 %) is assigned to the  $5^{(-)} \rightarrow 4_1^+$  transition ( $E_{\gamma, \text{lit}} = 1372.5$  keV).

Additional peaks appear at 1108 (5.7 %), 1495 (2.6 %), 1520 (1.0 %), 1687 (3.0 %), 1767 (4.7 %) and 2154 keV (4.6 %) which were not reported prior to this work.

Unfortunately, due to the sparse statistics and missing information on angular correlations and  $\gamma$ -ray coincidences, their origins are unclear and, hence, they remain unassigned and were not placed in the decay scheme. Furthermore, a careful glance at the 1373-keV peak shows a shoulder on the low-energy flank for the downstream detector ring. This cannot be seen in the upstream ring, although here an additional peak with low intensity appears right between the 1282 and 1373-keV transitions.

Information on the observed transitions are summarized in Table 5.3.

### Determination of Level Lifetimes

In total data for five different foil separations – 25, 53, 83, 521 and 4039  $\mu\text{m}$  – were recorded within eight hours. The first four separations were chosen to deduce the lifetime of the  $4_1^+$  state, the largest separation was selected to quantify the contribution of degrader excitations. A decay scheme as depicted in Fig. 5.2 was assumed for the investigation of lifetimes. The contribution of excitations in the degrader (and long-living feeders) was evaluated to 34(2) %.

Due to the sparse statistics of the  $6_1^+ \rightarrow 4_1^+$  and  $5^{(-)} \rightarrow 4_1^+$  transitions, the statistics of the foil separations 25, 53 and 83  $\mu\text{m}$  were added<sup>2</sup> – labelled *short separations* – to investigate the lifetimes of the associated mother states. Data from the foil separation of 4039  $\mu\text{m}$  was used for cross-checking purposes. Lifetimes were analysed using G4LIFETIMEG and the best result (with respect to the downstream detector ring) is shown in Fig. 5.3.

The observed peak-to-background ratios with respect to these transitions are small for both detector rings. It can be seen that the fast component of the  $6_1^+ \rightarrow 4_1^+$  transition dominates already in the spectra showing the statistics of the short separations. The best agreement was found for  $\tau_{\text{sim}}(6_1^+) = 1.0(5)$  ps. With respect to the decay of the  $5^{(-)}$  state, no clear sign of a fast component can be seen in the downstream detector ring for the short separations. This is in agreement with a lower lifetime limit of 5 ps. However, in the upstream detector ring a peak occurs at the energy expected for the fast component. For the 4-mm foil distance, the data of the downstream detector ring is consistent with a level lifetime of 40 ps. The statistical significance is rather low and, as a consequence, only a lower lifetime limit is adopted,  $\tau_{\text{sim}}(5^{(-)}) > 5$  ps.

The lifetimes of the  $4_1^+$  and  $2_1^+$  states were first evaluated by analysing the decay curves (see Appendix B), assuming a decay scheme as depicted in Fig. 5.2. The anal-

<sup>2</sup>With respect to simulated spectra, the weights of different contributions to the total statistics were deduced from the number of events in the experimental outgoing particle gate.

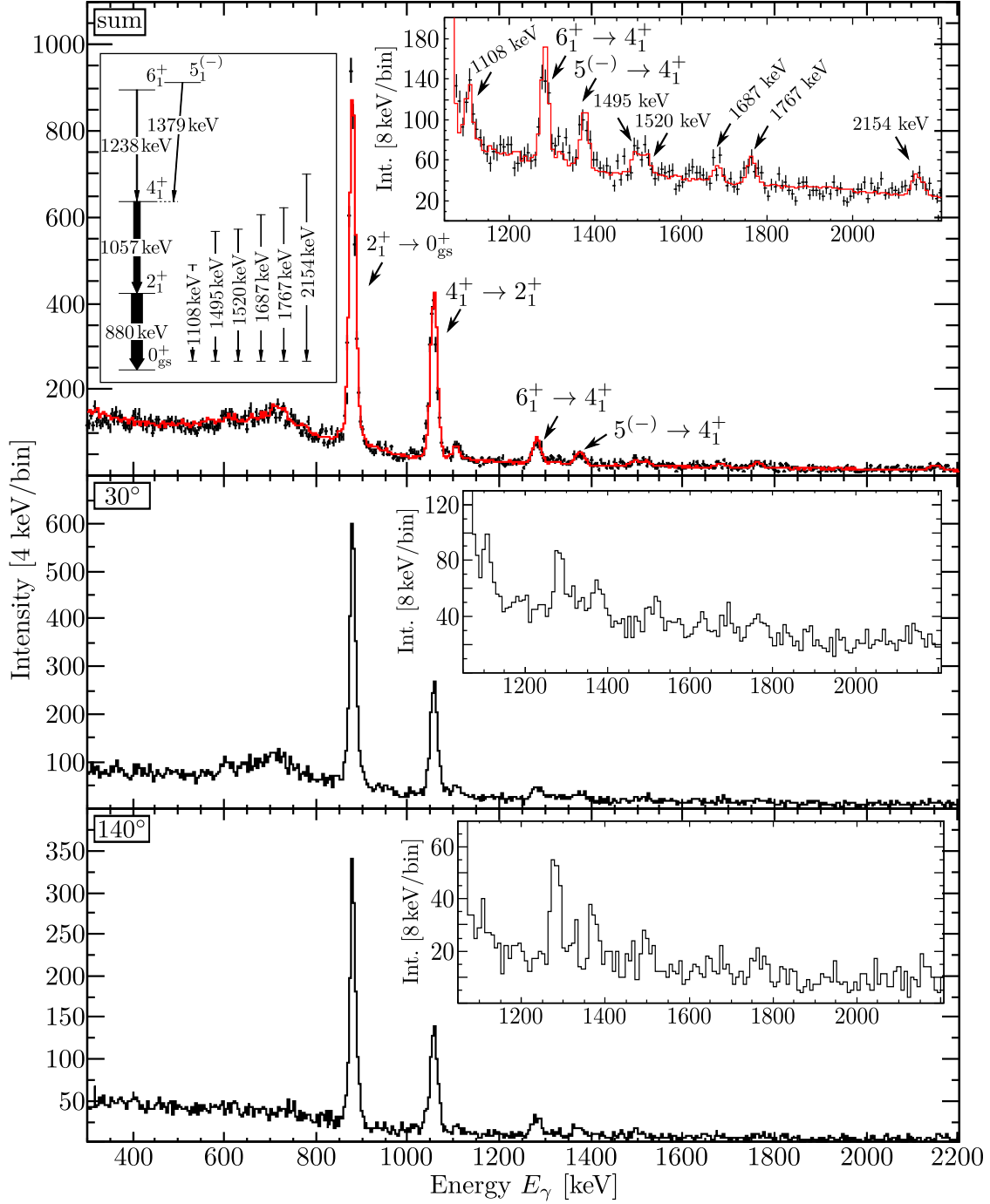


Figure 5.2.: (First setup –  $^{58}\text{Cr}$  – target-only data) Doppler-reconstructed  $\gamma$ -ray spectra after population by one-proton knockout from  $^{59}\text{Mn}$ . The responses of all SeGA detectors (*top*), downstream SeGA detectors (*middle*) and upstream SeGA detectors (*bottom*) are shown. The total experimental spectrum is overlaid by the best-fitting simulation (red) for which the depicted decay scheme was taken into account. Here, the widths of the arrows reflect the relative intensities.

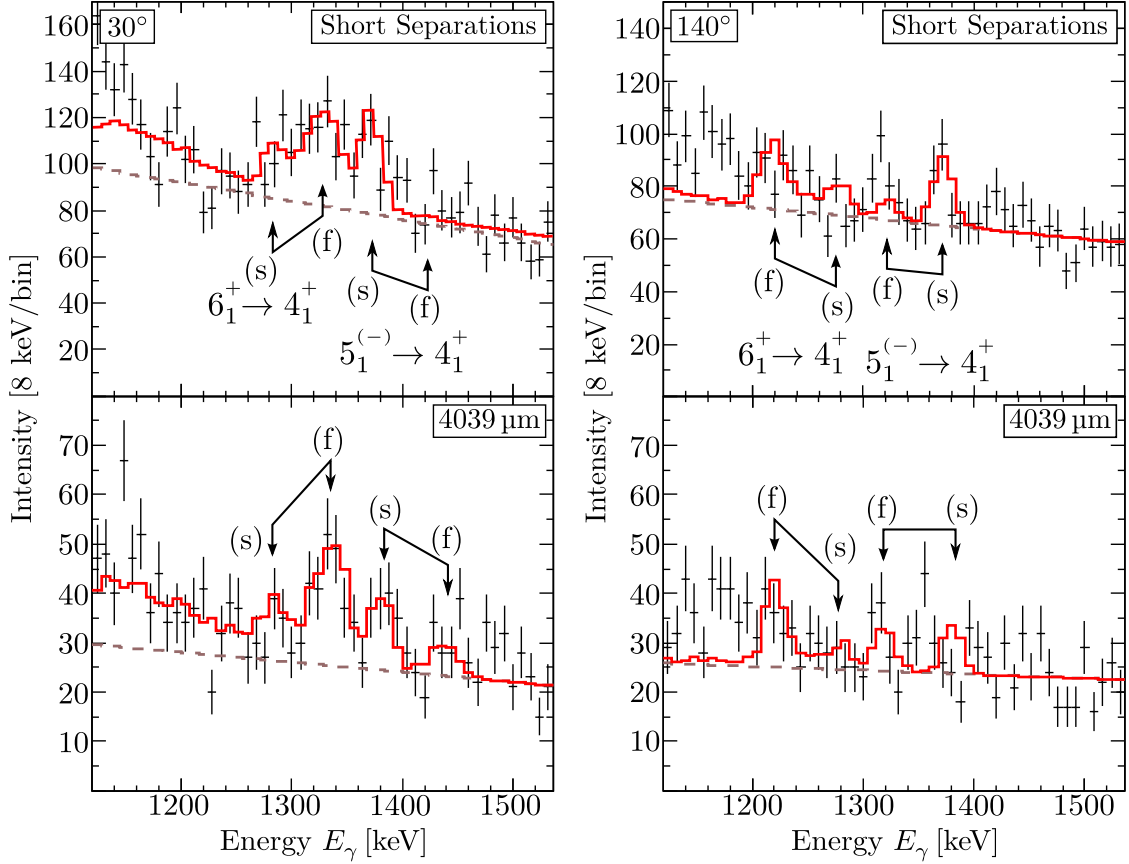


Figure 5.3.: (First setup –  $^{58}\text{Cr}$  – plunger data) Investigation of the lifetimes for the  $6_1^+$  and  $5_1^{(-)}$  states. Shown are experimental (black) and simulated (red) Doppler-reconstructed  $\gamma$ -ray spectra using G4LIFETIMEG, for which lifetimes of  $\tau(6_1^+) = 1.0$  ps and  $\tau(5_1^{(-)}) = 40$  ps were assumed. Fast (f) and slow (s) components are identified. See text for details.

ysis of the decay curves reveal a weighted mean lifetime of  $\tau_{\text{DC}}(4_1^+) = 2.5(3)$  ps and  $\tau_{\text{DC}}(2_1^+) = 6.3(16)$  ps.

Using the Monte Carlo approach, best results were found for  $\tau_{\text{sim}}(4_1^+) = 2.8(5)$  ps and  $\tau_{\text{sim}}(2_1^+) = 6.8(8)$  ps, respectively. Experimental and best-fitting simulated  $\gamma$ -ray spectra are shown in Fig. 5.4.

The quoted errors include pure statistical effects directly related to the transition-of-interest as well as additional uncertainties. The latter of which were investigated following the method described in Sec. 4.4. Both states of interest were prone to uncertainties with respect to the zero offset, the recoil velocities, degrader excitations as well as feeding uncertainties. Their effects on the lifetimes of the  $4_1^+$  and  $2_1^+$  states are listed in Table 5.4. With respect to the lifetime of the  $4_1^+$  state, the possibility of feeding by the experimentally observed yet unassigned  $\gamma$  rays is considered assuming an associated level lifetime of 1.0 ps.

Uncertainties with respect to imprecisely known feeding structures and degrader excita-

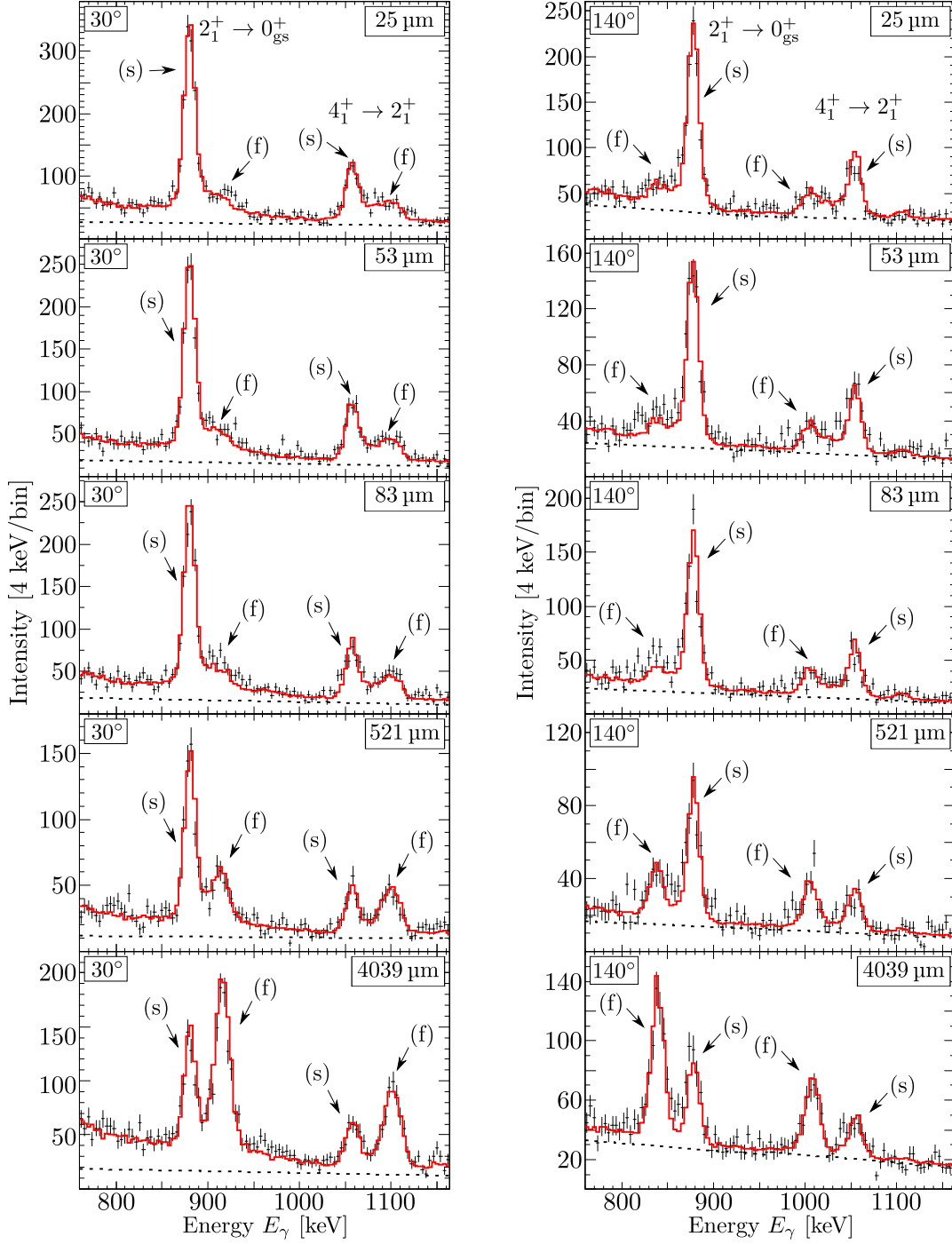


Figure 5.4.: (First setup –  $^{58}\text{Cr}$  – plunger data) Comparison of experimental (black) and best-fitting simulated Doppler-reconstructed  $\gamma$ -ray spectra (red) generated with G4LIFETIMEG. Lifetimes of  $\tau(4_1^+) = 2.8\ \text{ps}$  and  $\tau(2_1^+) = 6.8\ \text{ps}$  were assumed for the latter. Feeding from the  $6_1^+ \rightarrow 4_1^+$  and  $5_1^{(-)} \rightarrow 4_1^+$  transitions was incorporated with relative intensities according to the feeding scheme depicted in Fig. 5.2. Spectra for foil separations  $25\ \mu\text{m}$  (top),  $53$ ,  $83$ ,  $521$  and  $4039\ \mu\text{m}$  (bottom) are shown for downstream (left) and upstream (right) detector rings.

$J_i^\pi$	Parameter $p_i$	$\langle p_i \rangle$	$\frac{\partial \tau \text{ (ps)}}{\partial p_i}$	$\Delta p_i$	$\frac{\partial \tau}{\partial p_i} \Delta p_i \text{ (ps)}$
$2_1^+$	Zero offset $\Delta x_0$ [ $\mu\text{m}$ ]	30	0.01	10	0.10
	Recoil velocity $\beta_T$	40.75	-0.28	0.1	0.03
	Degrader excitation [%]	34.0	-0.13	2.0	0.26
	Lifetime $\tau_{\text{sim}}(4_1^+)$ [ps]	2.8	-0.76	0.5	0.37
	Feeding from $4_1^+$ state [%]	60.5	-0.07	3.1	0.22
$4_1^+$	Zero offset $\Delta x_0$ [ $\mu\text{m}$ ]	30	0.01	10	0.10
	Recoil velocity $\beta_T$	40.75	-0.09	0.1	0.01
	Degrader excitation [%]	34.0	-0.08	2.0	0.16
	Lifetime $\tau_{\text{sim}}(6_1^+)$ [ps]	1.0	-0.13	0.5	0.07
	Feeding from $6_1^+$ state [%]	11.0	-0.01	0.7	0.01
	Lifetime $\tau_{\text{sim}}(5_1^{(-)})$ [ps]	5	-0.001	$^{+200}_{-0}$	$^{+0.0}_{-0.2}$
	Feeding from $5_1^{(-)}$ state [%]	6.9	-0.05	0.6	0.03
	Feeding with $\tau = 1$ ps	0	-0.01	$^{+17}_{-0}$	$^{+0.0}_{-0.17}$

Table 5.4.: Investigation of the influence of specific uncertainties on the level lifetimes of the  $2^+$  and  $4^+$  states in  $^{58}\text{Cr}$ . The bottom line corresponds to the possibility of feeding by the unassigned transitions assuming a total given initial population between  $N_0 = 0$  and  $N_0 = 17\%$ .

tions have the largest influence on the lifetime error. The uncertainty of the zero offset leads to an additional error with non-vanishing weight but which is almost independent of the lifetime. It is interesting to note that the error related to the recoil velocity has only marginal effects.

The final results, including corresponding  $B(E2)$  values, are summarized and compared to previous measurements in Table 5.5. The present  $B(E2; 2_1^+ \rightarrow 0_{\text{gs}}^+)$  barely agrees with the weighted-mean of previous results [Bür05; Bau16].

$J_i \rightarrow J_f$	$E_\gamma^{\text{lit}}$ (keV)	$\tau_{\text{sim}}(J_i)$ (ps)	$\tau_{\text{DC}}(J_i)$ (ps)	$B(E2; \downarrow)_{\text{sim}}$ ( $e^2\text{fm}^4$ )	$B(E2; \downarrow)_{\text{lit}}$ ( $e^2\text{fm}^4$ )
$2_1^+ \rightarrow 0_{\text{gs}}^+$	880.5(2)	6.8(8)	6.3(16)	$226^{+30}_{-26}$	180(20)
$4_1^+ \rightarrow 2_1^+$	1057.4(3)	2.8(5)	2.5(3)	$221^{+48}_{-33}$	-
$6_1^+ \rightarrow 4_1^+$	1280.4(3)	1.0(5)	-	$228^{+186}_{-76}$	-
$5_1^{(-)} \rightarrow 4_1^+$	1372.5(3)	$>5$	-	-	-

Table 5.5.: Results of the lifetime analysis in  $^{58}\text{Cr}$ . The quoted literature  $B(E2)$  value is the weighted mean of  $172(25) e^2\text{fm}^4$  [Bau12] and  $197(56) e^2\text{fm}^4$  [Bür05]. See text for details.

### 5.3. $^{60}\text{Cr}_{36}$ - Measurement of $\gamma$ -Ray Transition Energies and Level Lifetimes

Sorlin *et al.* [Sor03] were first to identify a candidate for the  $2_1^+ \rightarrow 0_{\text{gs}}^+$  transition in  $^{60}\text{Cr}$  with 646(1) keV by investigating prompt  $\gamma$  rays following the  $\beta$  decay of  $^{60}\text{V}$ . Further studies of  $^{60}\text{Cr}$  using a  $^{64}\text{Ni}$  induced multi-nucleon transfer reaction on a  $^{238}\text{U}$  target [Mar06] and a fusion evaporation study [Zhu06] revealed further excited levels at low energies.

A proton inelastic scattering experiment [Aoi09] concluded a deformation length of  $\delta = 1.12(16)$  fm for  $^{60}\text{Cr}$ , while a Coulomb-excitation experiment at intermediate energies measured a  $B(\text{E}2)$  value of  $B(\text{E}2; 2_1^+ \rightarrow 0_{\text{gs}}^+) = 221(29) e^2\text{fm}^4$  [Bau12]. Both results indicate an increase in quadrupole deformation compared to neighbouring  $^{58}\text{Cr}$ .

Within the present work, the prime investigation of  $^{60}\text{Cr}$  was performed in the second experimental setup, in which  $^{60}\text{Cr}$  was predominately populated by one-proton knockout from the secondary beam  $^{61}\text{Mn}$ .

#### Observation of $\gamma$ -Ray Transition in Target-Only Data

Doppler-reconstructed  $\gamma$ -ray spectra of  $^{60}\text{Cr}$  recorded with only the plunger target at the experimental position are depicted in Fig. 5.5, which show the statistics of 2.5 hours. Since  $^{61}\text{Mn}$  overlaps in the incoming time-of-flight gate with other secondary beams (e.g.  $^{63}\text{Fe}$ ), contributions of other reactions to the population of  $^{60}\text{Cr}$  cannot be rigorously excluded. However, this hypothesis is not supported by an analysis of the recoil kinematics, in particular with respect to the velocity distribution as measured with S800.

The strongest peaks at 644 and 818 keV are associated with the two lowest yrast transitions  $2_1^+ \rightarrow 0_{\text{gs}}^+$  and  $4_1^+ \rightarrow 2_1^+$ . The latter of which has a relative intensity of 58 % with respect to the former.

$\mathbf{J_i \rightarrow J_f}$	$\mathbf{E_\gamma^{\text{lit}}}$ (keV)	$\mathbf{E_\gamma^{\text{exp}}}$ (keV)	$\mathbf{I_\gamma}$ (%)
$2_1^+ \rightarrow 0_{\text{gs}}^+$	643.9(2)	644.0(14)	100(5)
$4_1^+ \rightarrow 2_1^+$	816.8(4)	818.0(17)	57.6(72)
$6_1^+ \rightarrow 4_1^+$	985.3(2)	984(4)	14.7(27)
No assignment	-	1138(8)	4.1(9)
No assignment	-	1338(9)	10.8(21)
No assignment	-	1598(8)	6.0(14)

Table 5.6.: (Second setup –  $^{60}\text{Cr}$  – target-only data) The table lists all observed  $\gamma$ -ray transitions related to  $^{60}\text{Cr}$ . The quoted errors include statistical and systematic effects. Quoted intensities are relative to the  $2_1^+ \rightarrow 0_{\text{gs}}^+$  transition. See text for details.

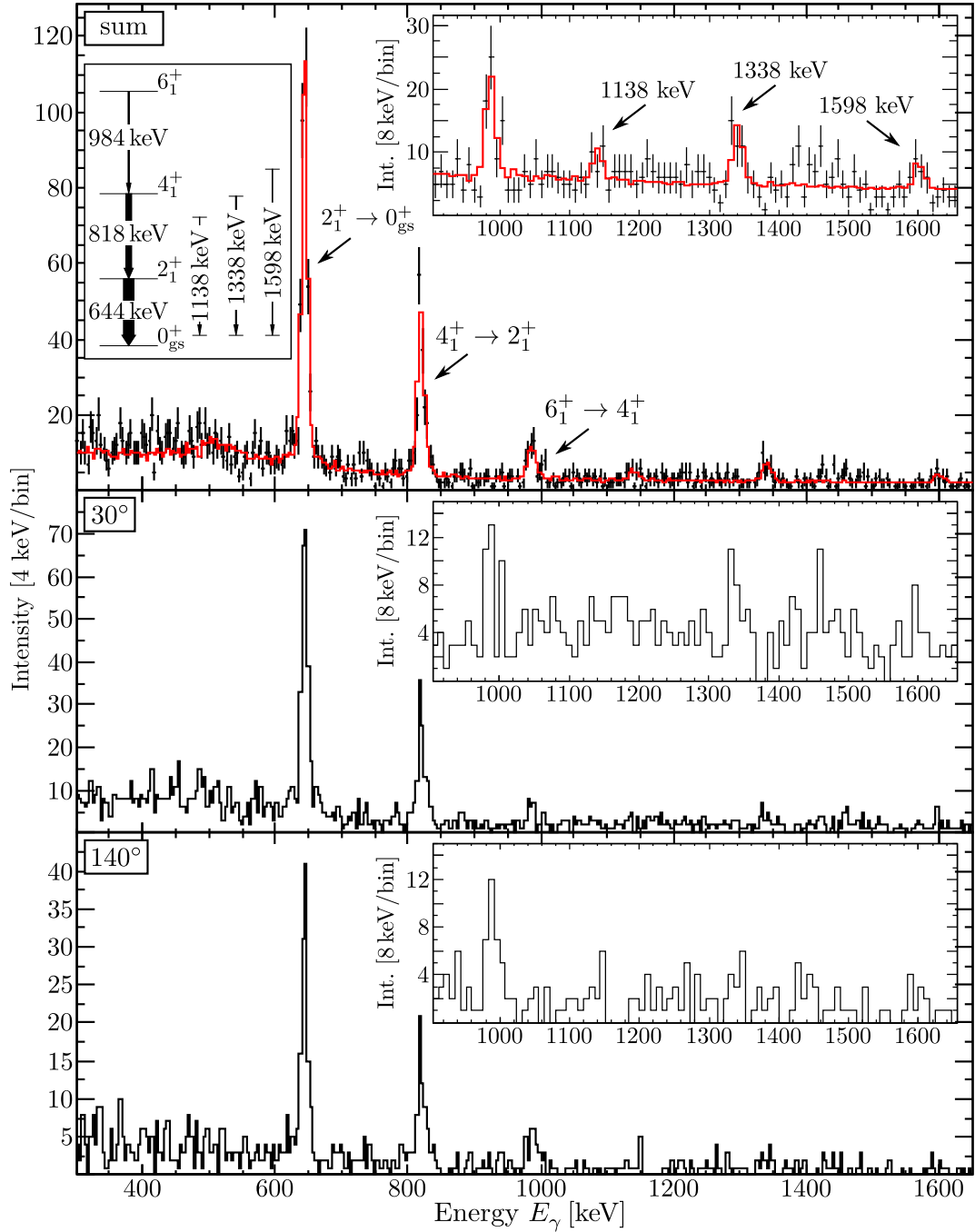


Figure 5.5.: (Second setup –  $^{60}\text{Cr}$  – target-only data) Experimental Doppler-reconstructed  $\gamma$ -ray spectra (black) of  $^{60}\text{Cr}$  populated by one-proton knockout from  $^{61}\text{Mn}$ . The responses of all SeGA detectors (*top*), downstream SeGA detectors (*centre*) and upstream SeGA detectors (*bottom*) are shown. The total experimental spectrum is overlaid with the best-fitting simulation (red) assuming the depicted decay scheme.

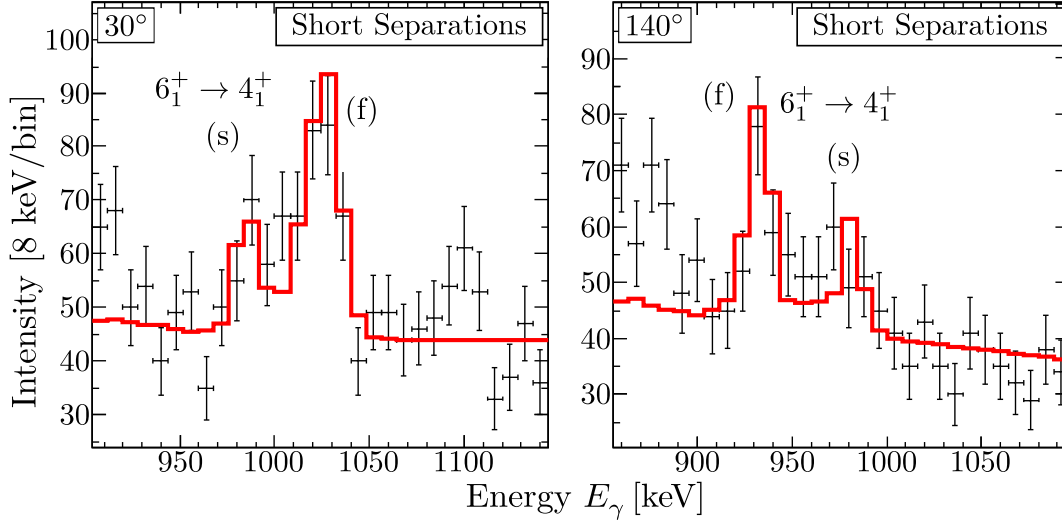


Figure 5.6.: (Second setup –  $^{60}\text{Cr}$  – plunger data) Investigation of the lifetime of the  $6_1^+$  state. Shown are experimental (black) and best-fitting simulated (red) Doppler-reconstructed  $\gamma$ -ray spectra. The latter were generated assuming a prompt lifetime of  $\tau(6_1^+) = 2.2$  ps. See text for details.

The  $6_1^+ \rightarrow 4_1^+$  transition at 984 keV can be seen with an intensity of 15 %. Within the spectrum there is no significant indication of a peak at 1031 keV, which Zhu *et al.* [Zhu06] tentatively assigned to the  $(8_1^+) \rightarrow 6_1^+$  transition.

Still, the spectrum exhibits signatures of further transitions. In particular, a peak occurs at 1338 keV (11 %) in both detector rings. Additional peaks appear with less significance at 1138 (4 %) and 1598 keV (6 %). Similar to the case of  $^{58}\text{Cr}$ , also their origin is unclear and, hence, they are incorporated into the feeding scheme. Information on the observed transitions are summarized in Table 5.6.

## Determination of Level Lifetimes

In total data for four different foil separations – 171, 325, 480 and 4024  $\mu\text{m}$  – were recorded within a total of 32 hours. A decay scheme as depicted in Fig. 5.5 was assumed for the investigation of level lifetimes.

Based on the largest foil separation, the degrader excitation was determined to  $19(2)\%<sup>3</sup>$ , which – accounting for the increased target thicknesses – is in agreement with the one observed in the analysis of  $^{58}\text{Cr}$ .

Due to the sparse  $\gamma$ -ray yield of the  $6_1^+ \rightarrow 4_1^+$  transition, the Doppler-reconstructed  $\gamma$ -ray spectra corresponding to the separations 171, 325 and 480  $\mu\text{m}$  were added to investigate the lifetime of  $6_1^+$  state. The different statistical contributions of the individual separations to the total statistics were taken into account by normalizing on the number of events in the particle gate. The lifetime was analysed using G4LIFETIMEG and the best

<sup>3</sup>For the decay of the  $2_1^+$  state the drift time between the foils with respect to the 4-mm foil separation was of the order of the lifetime and, hence, only the  $4_1^+ \rightarrow 2_1^+$  transition was used to estimate the contribution of degrader excitations.

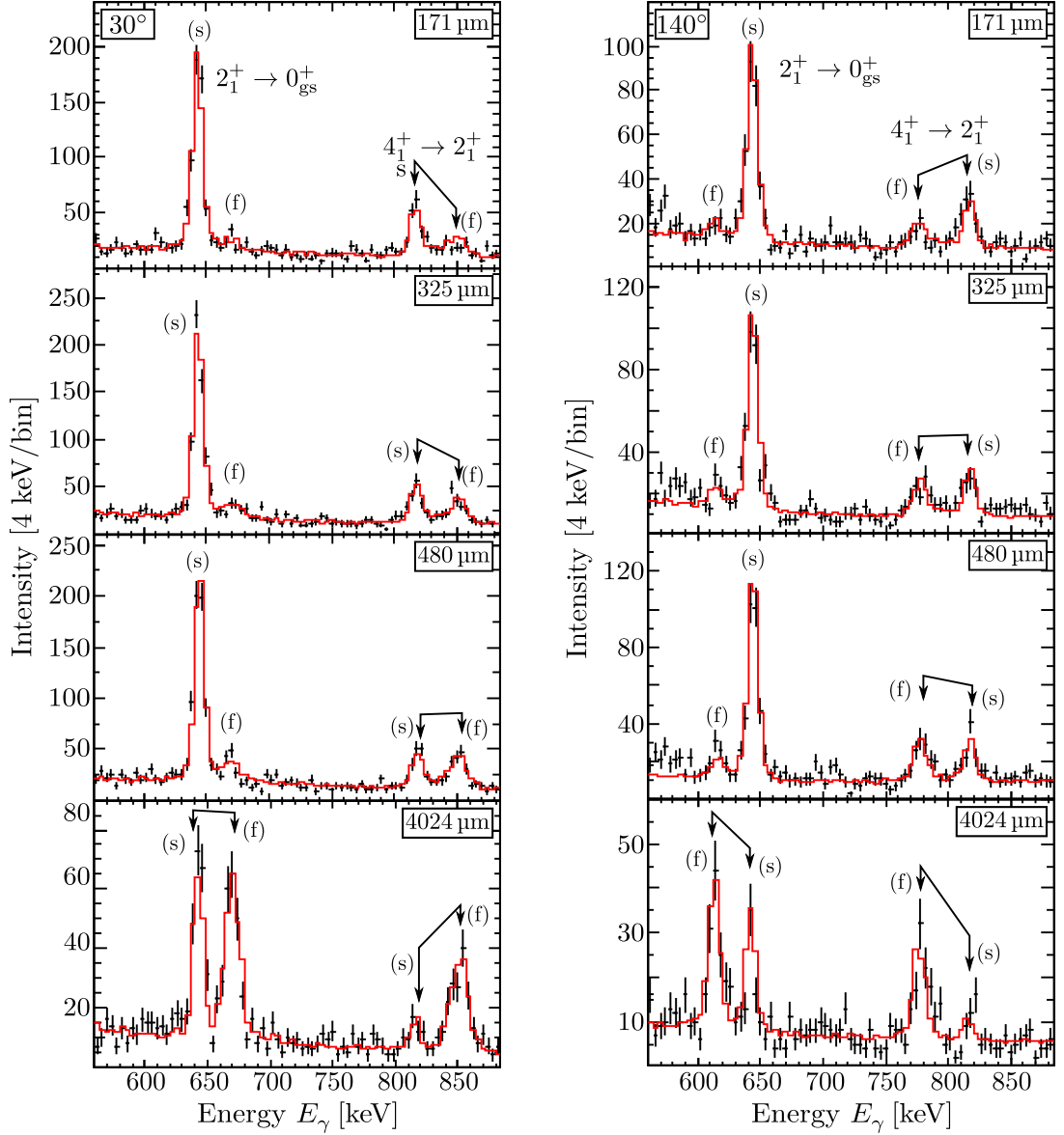


Figure 5.7.: (Second setup –  $^{60}\text{Cr}$  – plunger data) Comparison of experimental (black) and best-fitting simulated (red) Doppler-reconstructed  $\gamma$ -ray spectra. For the latter, level lifetimes of  $\tau(4_1^+) = 5.4$  ps and  $\tau(2_1^+) = 27$  ps were assumed. Feeding from the  $6_1^+ \rightarrow 4_1^+$  is incorporated according to the feeding scheme depicted in Fig. 5.5. Spectra for plunger separations 171  $\mu\text{m}$  (*top*) 325, 480 and 4024  $\mu\text{m}$  (*bottom*) are shown for both downstream (*left column*) and upstream (*right column*) detector ring.

result is depicted in Fig. 5.6. The best agreement was found for  $\tau_{\text{sim}}(6_1^+) = 2.2(8)$  ps. Lifetimes of the  $4_1^+$  and  $2_1^+$  states were evaluated by analysing their decay curves (see Appendix B). The analysis reveals a weighted mean lifetime of  $\tau_{\text{DC}}(2_1^+) = 27.3(37)$  ps and  $\tau_{\text{DC}}(4_1^+) = 5.6(10)$  ps, respectively.

$J_i^\pi$	Parameter $p_i$	$\langle p_i \rangle$	$\frac{\partial \tau \text{ (ps)}}{\partial p_i}$	$\Delta p_i$	$\frac{\partial \tau}{\partial p_i} \Delta p_i \text{ (ps)}$
$2_1^+$	Relevant foil separation [ $\mu\text{m}$ ]	4024	0.01	30	0.3
	Recoil velocity $\beta_T$	40.18	-0.86	0.1	0.09
	Degrader excitation [%]	19.0	-0.60	2.0	1.20
	Lifetime $\tau_{\text{sim}}(4_1^+)$ [ps]	5.4	-0.68	$^{+0.7}_{-0.9}$	$^{+0.61}_{-0.48}$
	Feeding from $4_1^+$ state [%]	57.6	-0.07	7.2	0.50
$4_1^+$	Zero offset $\Delta x_0$ [ $\mu\text{m}$ ]	24	0.01	10	0.10
	Recoil velocity $\beta_T$	40.18	-0.17	0.1	0.02
	Degrader excitation [%]	19.0	-0.12	2.0	0.24
	Lifetime $\tau_{\text{sim}}(6_1^+)$ [ps]	2.2	-0.42	0.8	0.34
	Feeding from $6_1^+$ state [%]	14.7	-0.03	2.7	0.08
	Feeding with $\tau = 2.2$ ps	0	-0.03	$^{+20.9}_{-0}$	$^{+0.0}_{-0.63}$

Table 5.7.: Investigation of the influence of specific uncertainties on the  $2_1^+$  and  $4_1^+$  level lifetimes in  $^{60}\text{Cr}$ . The bottom line corresponds to the possibility of feeding with  $\tau = 2.2$  ps by observed, yet unassigned transitions assuming a total given initial population between  $N_0 = 0$  and  $N_0 = 20.9\%$ .

Using the Monte Carlo simulation, best results were found for  $\tau_{\text{sim}}(4_1^+) = 5.4^{+0.7}_{-0.9}$  ps and  $\tau_{\text{sim}}(2_1^+) = 27.0(26)$  ps. Experimental and best-fitting simulated Doppler-reconstructed  $\gamma$ -ray spectra are shown in Fig. 5.7.

The quoted errors cover statistical and additional effects. With respect to the latter, individual contributions are listed in Table 5.7. With respect to the lifetime of the  $4_1^+$  state, the possibility of feeding by experimentally observed, yet unassigned,  $\gamma$ -rays is considered, for which a lifetime of 2.2 ps of the associated mother states was assumed. Similar to  $^{58}\text{Cr}$ , uncertainties related to feeding and degrader excitations contribute strongest to the lifetime error. Due to the larger level lifetimes compared to  $^{58}\text{Cr}$ , the relative error introduced by the uncertainty with respect to the zero position is smaller.

The final results for  $^{60}\text{Cr}$ , including corresponding transition strengths, are summarized and compared to previous measurements in Table 5.8. Comparable to  $^{58}\text{Cr}$ , the present  $B(\text{E}2; 2_1^+ \rightarrow 0_{\text{gs}}^+)$  agrees barely with the previous result [Bau12].

$J_i \rightarrow J_f$	$E_\gamma^{\text{lit}}$ (keV)	$\tau_{\text{sim}}(J_i)$ (ps)	$\tau_{\text{DC}}(J_i)$ (ps)	$B(\text{E}2; \downarrow)_{\text{sim}}$ ( $e^2\text{fm}^4$ )	$B(\text{E}2; \downarrow)_{\text{lit}}$ ( $e^2\text{fm}^4$ )
$2_1^+ \rightarrow 0_{\text{gs}}^+$	643.9(2)	27.0(26)	27.3(37)	$274^{+29}_{-24}$	221(29) [Bau12]
$4_1^+ \rightarrow 2_1^+$	816.8(4)	$5.4^{+0.7}_{-0.9}$	5.6(10)	$417^{+62}_{-59}$	-
$6_1^+ \rightarrow 4_1^+$	985.3(2)	2.2(8)	-	$397^{+313}_{-105}$	-

Table 5.8.: Results of the lifetime analysis in  $^{60}\text{Cr}$ . See text for details.

## 5.4. $^{62}\text{Cr}_{38}$ - Measurement of $\gamma$ -Ray Transition Energies and Level Lifetimes

Sorlin *et al.* [Sor03] were first to observe a candidate for the  $2_1^+ \rightarrow 0_{\text{gs}}^+$  transition with  $E_\gamma = 446(1)$  keV. Candidates for the  $4_1^+ \rightarrow 2_1^+$  transition were identified both in a proton inelastic scattering experiment performed at RIKEN ( $E_\gamma = 734(10)$  keV) [Aoi09] and in an inelastic scattering experiment performed at the NSCL ( $E_\gamma = 725(9)$  keV) [Gad10]. Both measurements confirmed the  $2_1^+ \rightarrow 0_{\text{gs}}^+$  transition energy as proposed in Ref. [Sor03]. From the proton inelastic scattering experiment [Aoi09] the deformation length  $\delta$  is known to be  $\delta = 1.36(14)$  for  $^{62}\text{Cr}$ .

The  $B(\text{E}2; 2_1^+ \rightarrow 0_{\text{gs}}^+)$  is known from a Coulomb-excitation experiment performed at intermediate energies [Bau12]. The authors published  $B(\text{E}2)$  values of  $325(44) e^2\text{fm}^4$  (Coulomb-excitation cross section) and  $321_{-49}^{+60} e^2\text{fm}^4$  (lifetime estimate by a line-shape analysis), which exceeds the value in neighbouring  $^{60}\text{Cr}$  by over 40 %.

In the present experiment, the investigation of  $^{62}\text{Cr}$  was solely possible in the third experimental setup, in which  $^{62}\text{Cr}$  was predominately populated by one-proton knockout of the secondary beam  $^{63}\text{Mn}$  on the  $^9\text{Be}$  target.

### Observation of $\gamma$ -Ray Transitions in Summed Plunger Data

Due to the limited measuring time, no target-only data was recorded in the third experimental setup. To deduce information on the experimental excitation scheme, plunger data for both measured foil separations – 26 and 7026  $\mu\text{m}$  – were added to increase the  $\gamma$ -ray yield.

It is worth to mention that it was practically impossible to apply an unambiguous gate condition on reactions solely induced by the secondary beam  $^{63}\text{Mn}$ . While it may theoretically be possible that  $^{62}\text{Cr}$  was also produced by reactions with the second strongest beam in the incoming gate ( $^{64}\text{Fe}$ ), the two-proton knockout is expected to have a significantly smaller cross section.

The resulting Doppler-reconstructed  $\gamma$ -ray spectra are depicted in Fig. 5.8 and reflect the total statistics of 96 hours.

$\mathbf{J_i \rightarrow J_f}$	$\mathbf{E_\gamma^{\text{lit}}}$ (keV)	$\mathbf{E_\gamma^{\text{exp}}}$ (keV)	$\mathbf{I_\gamma}$ (%)
$2_1^+ \rightarrow 0_1^+$	446.1(9)	446.0(12)	100(2)
$4_1^+ \rightarrow 2_1^+$	729.0(67)	729.5(15)	55.7(44)
No assignment	-	1019(3)	16.9(8)

Table 5.9.: (Third setup –  $^{62}\text{Cr}$  – summed plunger data) The table lists all  $\gamma$ -rays transitions correlated to  $^{62}\text{Cr}$ . The quoted errors include statistical and systematic uncertainties. Quoted intensities are relative to the  $2_1^+ \rightarrow 0_{\text{gs}}^+$ . See text for details.

The strongest peaks at 446 and 729 keV are assigned to the  $2_1^+ \rightarrow 0_{\text{gs}}^+$  and  $4_1^+ \rightarrow 2_1^+$  transitions. The latter has a relative intensity of 56% compared to the former. It is noteworthy that no third peak occurs simultaneously in the Doppler-reconstructed  $\gamma$ -ray spectra of both detector rings at the same energy.

However, compared to  $E = 1019$  keV a peak is visible at a larger (downstream ring) and a lower (upstream ring) energy. The energy gap between these two peaks coincides with the one related to the  $4_1^+ \rightarrow 2_1^+$  transition after scaling for the increase in energies. Hence, it is possible that these peaks are manifestation of the fast component of a short-

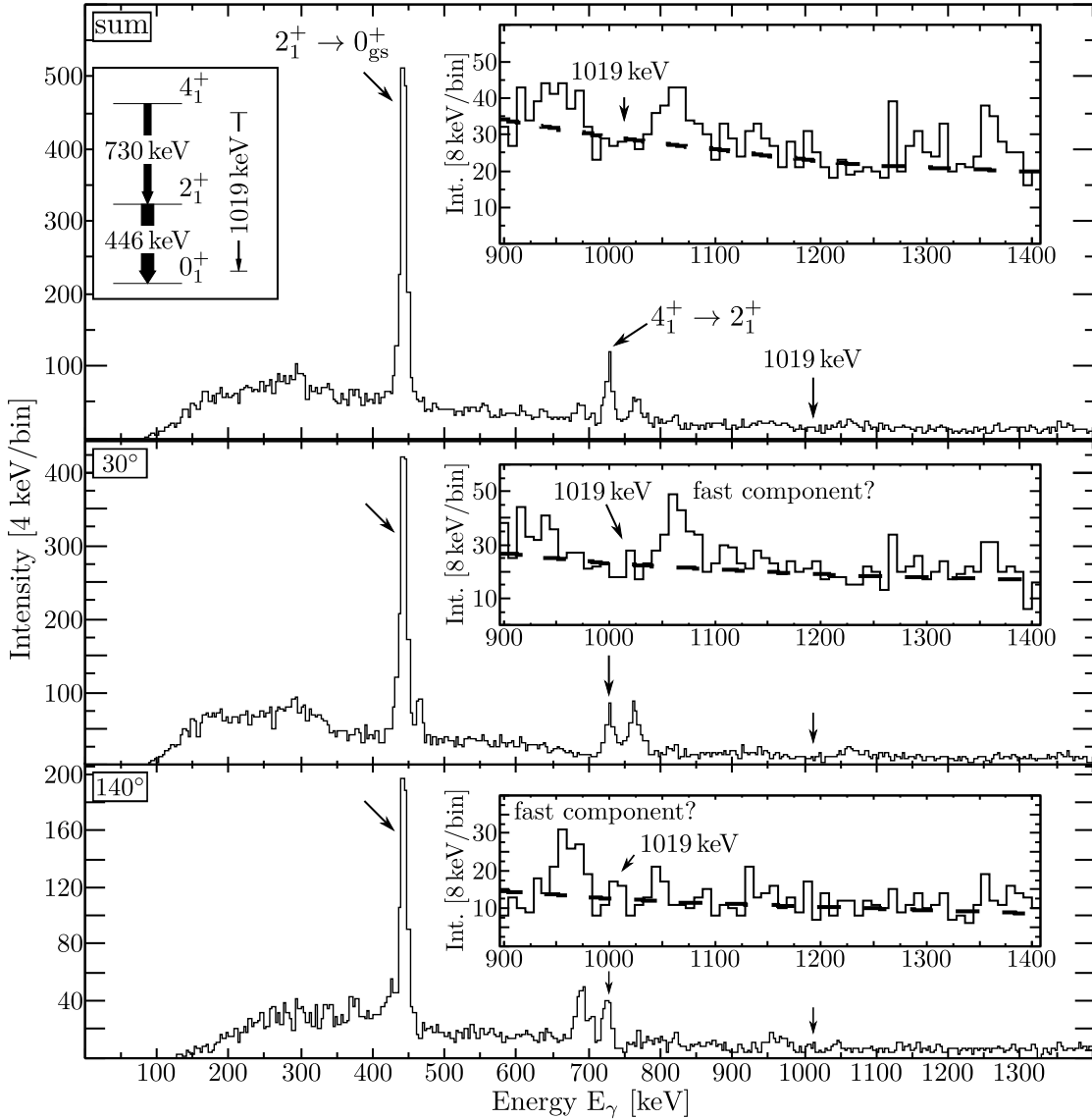


Figure 5.8.: (Third setup -  $^{62}\text{Cr}$  - summed plunger data) Doppler-reconstructed  $\gamma$ -ray spectra of  $^{62}\text{Cr}$  populated by one-proton knockout from  $^{63}\text{Mn}$ . The statistics of all SeGA detectors (*top*), the downstream SeGA detectors (*middle*) and the upstream SeGA detectors (*bottom*) are shown. See text for details.

living state. If this is the case, its intensity is given by 17%. Following the systematics with respect to the initial populations, it appears possible that this peak corresponds to the  $6_1^+ \rightarrow 4_1^+$  transition which was not reported prior to this work. Information on the observed transitions are summarized in Table 5.9.

### Determination of Level Lifetimes

Data for two different foils separations – 26 and 7026  $\mu\text{m}$  – were recorded in the third setup. The small separation was chosen to deduce the lifetime of the  $4_1^+$  state, the large separation was useful to quantify the contribution of degrader excitation (based on the decay of the  $4_1^+$  state) and to determine the lifetime of the  $2_1^+$  state.

Data related to the  $4_1^+ \rightarrow 2_1^+$  transition in the upstream detector ring is contaminated by the 511-keV line, which is incorporated into the simulated spectra as generated by G4LIFETIMEG. For the lifetime analysis a decay scheme as depicted in Fig. 5.8 was assumed.

Although the origin of the peaks close to 1019 keV could not be resolved within the present work, a lifetime analysis was performed assuming that the observed peaks are associated to fast components related to a transition with  $E_\gamma = 1019$  keV. The corresponding experimental and simulated spectra are shown in Fig. 5.9. The data is in agreement with an upper lifetime limit of 3.0 ps.

The lifetimes of the  $4_1^+$  and  $2_1^+$  states were determined by analysing their decay curves (see Appendix B). Best results were found for lifetimes  $\tau_{\text{DC}}(2_1^+) = 116(17)$  ps and  $\tau_{\text{DC}}(4_1^+) = 6.9(8)$  ps, which include an assumed systematic error of 10%.

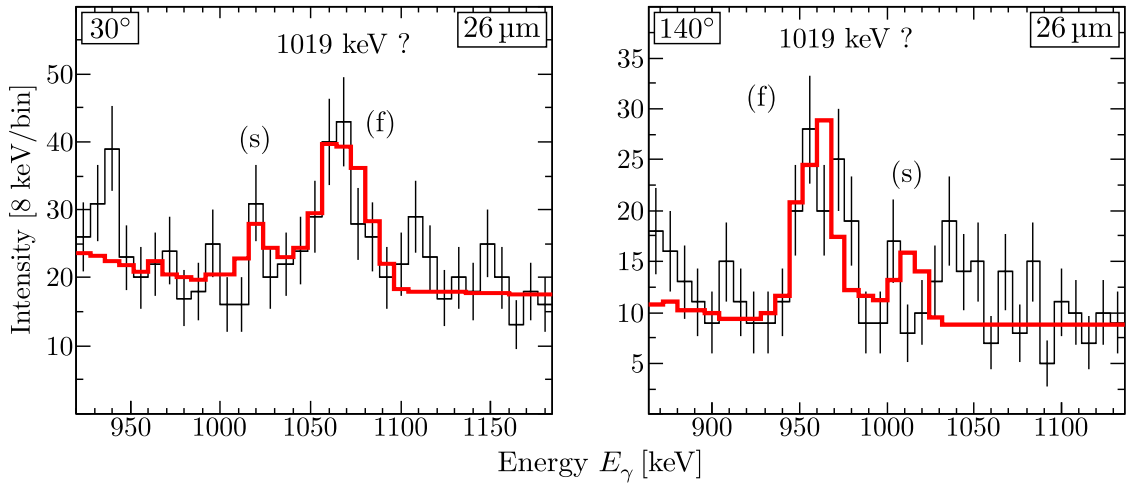


Figure 5.9.: (Third setup –  $^{62}\text{Cr}$  – plunger data) Investigation of the lifetime of a hypothetical state whose decay is realized by a transition with  $E_\gamma = 1019$  keV. The experimental data is shown in black, while the simulated spectra are shown in red. For the latter a lifetime of  $\tau = 2.0$  ps is assumed. The spectra show the statistics related to the separation of 26  $\mu\text{m}$  for the downstream (*left*) and upstream (*right*) detector ring. See text for details.

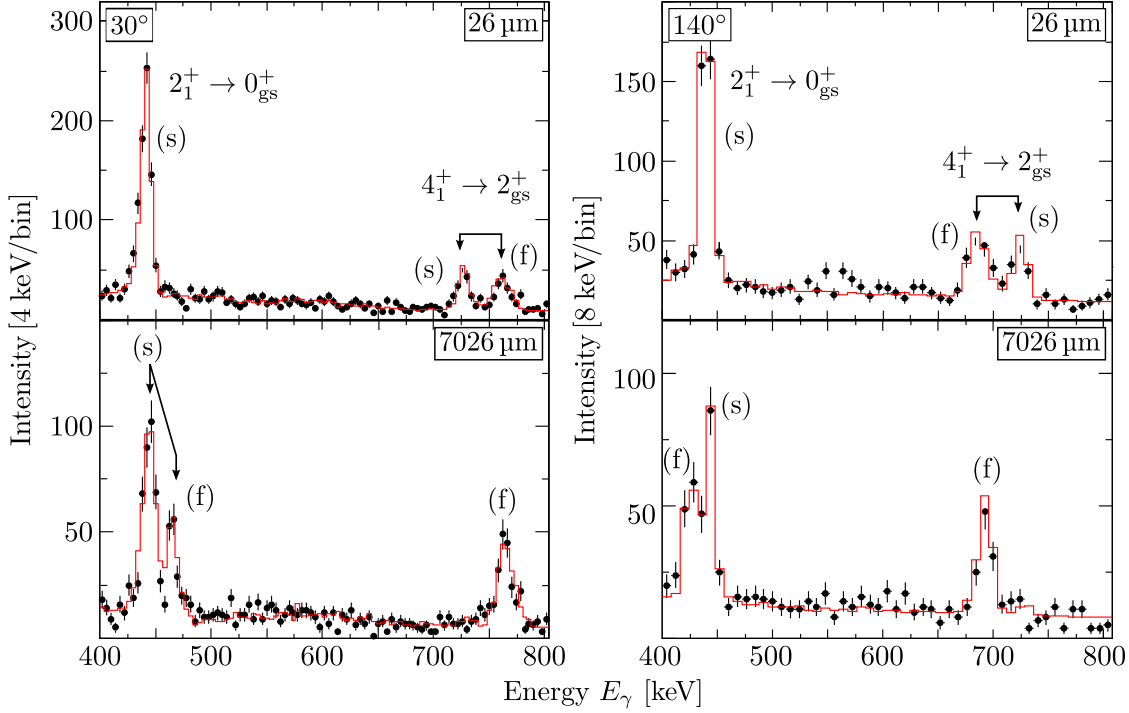


Figure 5.10.: (Third setup –  $^{62}\text{Cr}$  – plunger data) Comparison of experimental (black) and best-fitting simulated (red) Doppler-reconstructed  $\gamma$ -ray spectra. For the latter, level lifetimes of  $\tau(4_1^+) = 6.9$  ps and  $\tau(2_1^+) = 125$  ps were assumed. Shown are the statistics of the downstream (*left*) and upstream detector ring (*right*) corresponding to foil separations  $26\ \mu\text{m}$  (*top*) and  $7026\ \mu\text{m}$  (*bottom*).

$J_i^\pi$	Parameter $p_i$	$\langle p_i \rangle$	$\frac{\partial \tau \text{ (ps)}}{\partial p_i}$	$\Delta p_i$	$\frac{\partial \tau}{\partial p_i} \Delta p_i$ (ps)
$2_1^+$	Sensitive foil separation [ $\mu\text{m}$ ]	7026	0.01	45	0.45
	Recoil velocity $\beta_T$	39.45	-3.91	0.1	0.39
	Degrader excitation [%]	8	-1.77	2.0	3.5
	Lifetime $\tau_{4_1^+}$ [ps]	6.9	-1.66	$^{+0.7}_{-0.8}$	$^{+1.2}_{-1.3}$
	Feeding from $4_1^+$ state [%]	55.7	-0.16	4.4	0.7
$4_1^+$	Zero offset $\Delta x_0$ [ $\mu\text{m}$ ]	26	0.01	10	0.10
	Recoil velocity $\beta_T$	39.45	-0.20	0.1	0.02
	Degrader excitation [%]	8	-0.13	2.0	0.26
	Feeding with $\tau = 2.5$ ps	0	-0.02	$^{+20}_{-0}$	$^{+0.0}_{-0.4}$

Table 5.10.: Influence of specific uncertainties on the level lifetimes with respect to the  $2_1^+$  and  $4_1^+$  states in  $^{62}\text{Cr}$ . With respect to the  $4_1^+$  state, the feeding possibility by a  $6_1^+$  state with  $\tau = 2.5$  ps is considered (bottom line).

$\mathbf{J}_i \rightarrow \mathbf{J}_f$	$E_\gamma^{\text{lit}}$ (keV)	$\tau_{\text{sim}}(\mathbf{J}_i)$ (ps)	$\tau_{\text{DC}}(\mathbf{J}_i)$ (ps)	$B(\text{E}2;\downarrow)_{\text{sim}}$ ( $e^2\text{fm}^4$ )	$B(\text{E}2;\downarrow)_{\text{lit}}$ ( $e^2\text{fm}^4$ )
$2_1^+ \rightarrow 0_{\text{gs}}^+$	446.1(9)	$125_{-10}^{+11}$	116(17)	$371_{-30}^{+32}$	$321_{-49}^{+60}$ [Bau12] 325(44) [Bau12]
$4_1^+ \rightarrow 2_1^+$	728(3)	$6.9_{-0.8}^{+0.7}$	6.9(8)	$582_{-46}^{+76}$	-

Table 5.11.: Results of the lifetime analysis in  $^{62}\text{Cr}$ . See text for details.

Using the Monte Carlo simulation, best results were achieved for  $\tau_{\text{sim}}(4_1^+) = 6.9_{-0.8}^{+0.7}$  ps and  $\tau_{\text{sim}}(2_1^+) = 125_{-10}^{+11}$  ps. Experimental and best-fitting simulated  $\gamma$ -ray spectra are shown in Fig. 5.10.

In addition to the statistical error, the effect of specific uncertainties on the deduced lifetimes of the  $2_1^+$  and  $4_1^+$  states were investigated and the results are listed in Table 5.10. Motivated by the population schemes in neighbouring  $^{58,60}\text{Cr}$ , the effect of feeding from a  $6_1^+$  state with  $\tau = 2.5$  ps and relative intensities between 0 and 20 % on the level lifetime of the  $4_1^+$  state was investigated. Such a feeding and the contribution of degrader excitations have the strongest effect on the error of  $\tau(4_1^+)$ . Also for the  $2_1^+$  state, feeding and degrader excitation uncertainties increase the error of the lifetime significantly.

The results are summarized and compared to previous measurements in Table 5.11. The present  $B(\text{E}2; 2_1^+ \rightarrow 0_{\text{gs}}^+)$  is in fair agreement with the previous result [Bau16].

## 5.5. Vanadium Isotopes

### 5.5.1. $^{56}\text{V}_{33}$ - Measurement of $\gamma$ -Ray Transition Energies

Very little is known about excited levels and  $\gamma$ -ray transitions in  $^{56}\text{V}$ . Mantica *et al.* [Man03b] investigated the  $\beta$  decay of  $^{56}_{22}\text{Ti}$  and observed  $\gamma$  rays with energies of 668 and 1006 keV. These transitions were confirmed later on by Liddick *et al.* [Lid04] using a comparable approach on the  $\beta$  decay of  $^{56}_{21}\text{Sc}$ . No further  $\gamma$  rays related to decays in  $^{56}\text{V}$  were reported prior to this work.

Unfortunately, a similar picture can be drawn for the directly neighbouring odd-odd isotopes  $^{54}\text{V}$  and  $^{58}\text{V}$ . In  $^{54}\text{V}$ , few  $\gamma$  rays were observed but the assignment to specific levels is tentative for most of the cases [NDS54]. Still, it is interesting to note that in  $^{54}\text{V}$  a low-lying  $\mu\text{s}$  isomer at 108 keV was observed [Grz98]. In  $^{58}\text{V}$ , only a transition with 114 keV [Gau05] was observed, but no corresponding lifetime was reported.

#### Observation of $\gamma$ -Ray Transitions in Target-Only Data

The best  $\gamma$ -ray yield of  $^{56}\text{V}$  was found in the first experimental setup following the multi-nucleon removal reaction from the secondary beam  $^{59}\text{Mn}$  on the  $^9\text{Be}$  target. The corresponding Doppler-reconstructed  $\gamma$ -ray spectrum is depicted in Fig. 5.11.

The peak with the largest  $\gamma$ -ray yield appears at 151 keV. On its high-energy shoulder another structure can be seen at 160 keV which may either indicate an independent transition or reflect a statistical artefact

Ordered with decreasing intensities, further peaks can be identified at 220, 304, 446, 530 and 1140 keV, respectively. Furthermore, two peaks occur close to 210 keV and 312 keV. Due to their immediate proximity to more intense peaks at 220 and 304 keV it is possible that they are no individual peaks but rather correspond to these transitions.

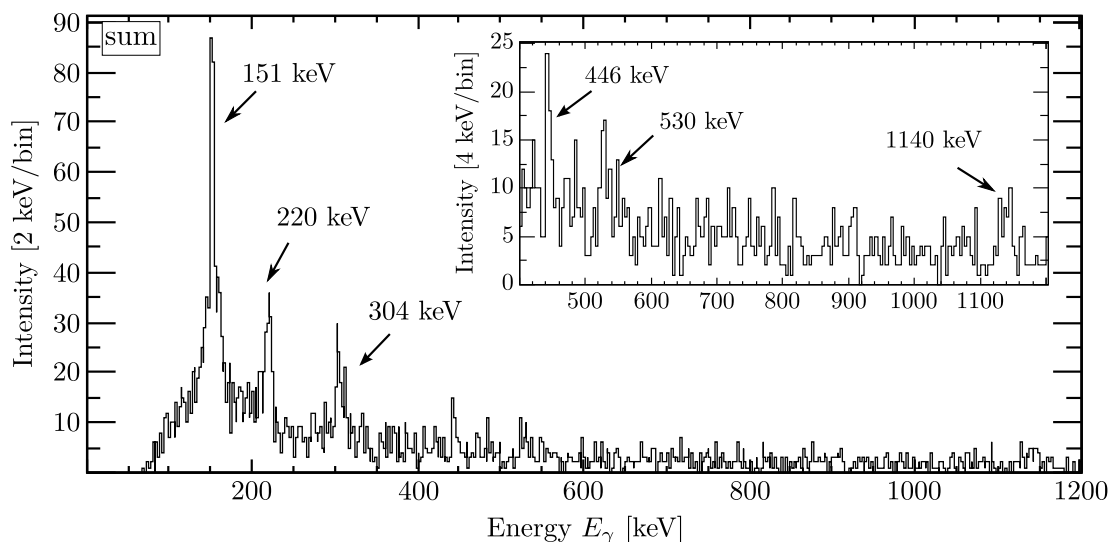


Figure 5.11.: (First setup –  $^{56}\text{V}$  – target-only data) Doppler-reconstructed  $\gamma$ -ray spectrum, showing the added statistics of all SeGA detectors.

$\mathbf{J_i \rightarrow J_f}$	$\mathbf{E_\gamma^{exp}}$ (keV)
No assignment	151.2(11)
No assignment	219.8(20)
No assignment	304.4(28)
No assignment	446.1(32)
No assignment	529.8(31)
No assignment	1140(5)

Table 5.12.: (First setup –  $^{56}\text{V}$  – target-only data) The table lists the identified  $\gamma$ -ray transitions as observed in the total Doppler-reconstructed  $\gamma$ -ray spectrum. See text for details.

### 5.5.2. $^{55}\text{V}_{32}$ - Measurement of $\gamma$ -Ray Transition Energies and Level Lifetimes

Mantica *et al.* identified excited structures in  $^{55}\text{V}$  by investigating promptly-emitted  $\gamma$  rays following the  $\beta$  decay of  $^{55}\text{Ti}$  [Man03b]. The knowledge was extended by studies performed at the ANL [Zhu07; Dea11], for which  $^{48}\text{Ca}$  induced fusion-evaporation reactions on a  $^9\text{Be}$  target were used. No level lifetimes in  $^{55}\text{V}$  were reported prior to this work.

#### Observation of $\gamma$ -ray Transitions in Target-Only Data

The  $\gamma$ -ray yield of  $^{55}\text{V}$  was largest in data from the first experimental setup following multi-nucleon removal reactions from  $^{59}\text{Mn}$ . A Doppler-reconstructed  $\gamma$ -ray spectrum of the target-only run is depicted in Fig. 5.12, which shows the full  $\gamma$ -ray yield correlated to  $^{55}\text{V}$ .

The dominant peak at 322 keV ( $I_{\text{rel}} = 100\%$ ) corresponds to the  $5/2_1^- \rightarrow 7/2_{\text{gs}}^-$  transition. The  $5/2_1^-$  state is known to be fed by transitions with 1247 keV ( $(3/2_2^-) \rightarrow 5/2_1^-$ ) as well as with 348 keV ( $3/2_1^- \rightarrow 5/2_1^-$ ). Indeed, in Fig. 5.12 a peak close to 348 keV can be identified, but its assignment to the  $3/2_1^- \rightarrow 5/2_1^-$  is misleading because it is the 511-keV line shifted to such energies by the Doppler-reconstruction. The 1247-keV transition was not observed.

The  $3/2_1^- \rightarrow 7/2_{\text{gs}}^-$  transition at  $E_\gamma = 668$  keV is visible with a relative intensity of 43% compared to the 322-keV transition. Furthermore, a third peak occurs at 1439 keV which is assigned to the known  $11/2_1^- \rightarrow 7/2_{\text{gs}}^-$  transition. It cannot be excluded that the  $11/2_1^-$  state is fed by a known feeder with  $E_\gamma = 1075$  keV. If so, its contribution is small.

#### Determination of Level Lifetimes

The level lifetimes of the  $11/2_1^-$  and  $5/2_1^-$  states were investigated using data from  $^{59}\text{Mn}$  induced reactions within the first experimental setup. The statistics of the  $3/2_1^- \rightarrow 7/2_{\text{gs}}^-$  transition with  $E_\gamma = 672$  keV was too sparse and, hence, a reliable analysis of the  $3/2_1^-$ -

$\mathbf{J_i \rightarrow J_f}$	$\mathbf{E_\gamma^{lit}}$ (keV)	$\mathbf{E_\gamma^{exp}}$ (keV)	$\mathbf{I_\gamma}$ (%)
$11/2_1^- \rightarrow 7/2_{gs}^-$	1433.1(10)	1439(11)	164(37)
$5/2_1^- \rightarrow 7/2_{gs}^-$	323.1(5)	322.4(21)	100(13)
$3/2_1^- \rightarrow 7/2_{gs}^-$	672.0(2)	668.0(54)	43(17)

Table 5.13.: (First setup –  $^{55}\text{V}$  – target-only data) The table lists all observed  $\gamma$ -ray transitions. The quoted  $\gamma$ -ray energies include statistical and systematic uncertainties. See text for details.

state lifetime was not possible. Due to the insufficient  $\gamma$ -ray yield in the upstream detector ring, only data from the downstream detectors was considered. In addition, data from short separations of 25, 53 and 83  $\mu\text{m}$  were summed for experimental and simulated data, where for the latter relative weights were deduced from the separation-dependent particle yields.

Experimental and best-fitting simulated  $\gamma$ -ray spectra are shown in Fig. 5.13. For the transition  $5/2_1^- \rightarrow 7/2_{gs}^-$  with  $E_\gamma = 323$  keV a fast component can only be seen for the 4039- $\mu\text{m}$  foil separation. A lifetime assumption of  $\tau(5/2_1^-) = 60(12)$  ps offers best results. The statistical error is 10 % and the systematic error is estimated to be of the same order.

Considering the  $11/2_1^- \rightarrow 7/2_{gs}^-$  transition with  $E_\gamma = 1433$  keV, a shifted component can already be seen in the summed spectrum of the short separations. This can be reproduced by assuming an (effective) lifetime of 5 ps. For larger separations the statistical significance is rather low, but the agreement is still reasonable for this lifetime assumption. The results are summarized in Table 5.14.

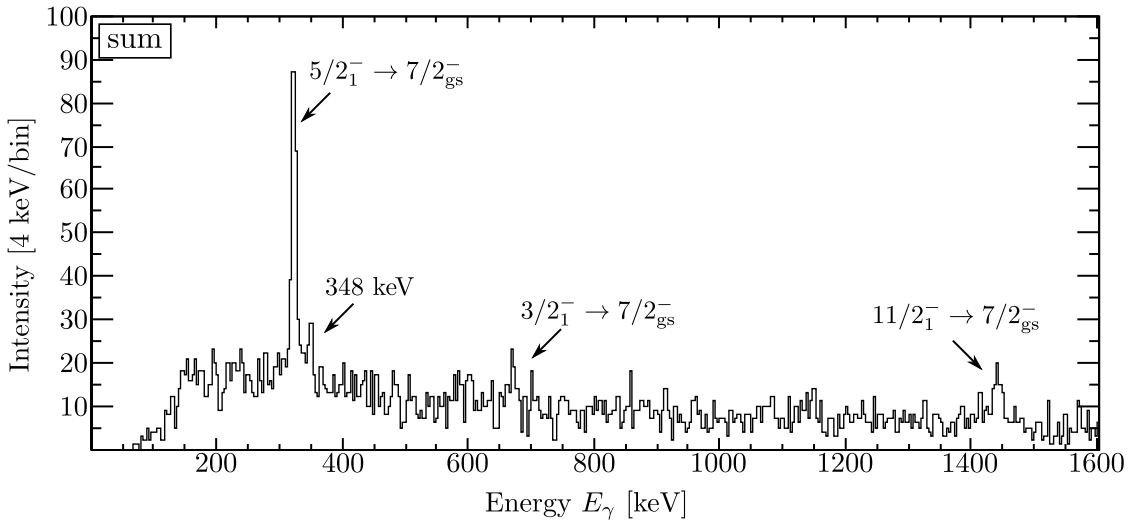


Figure 5.12.: (First setup –  $^{55}\text{V}$  – target-only data) Doppler-reconstructed  $\gamma$ -ray spectrum correlated to  $^{55}\text{V}$  after multi-nucleon removal reactions from  $^{59}\text{Mn}$  on the  $^9\text{Be}$  plunger target. The spectrum shows the statistics of all detectors.

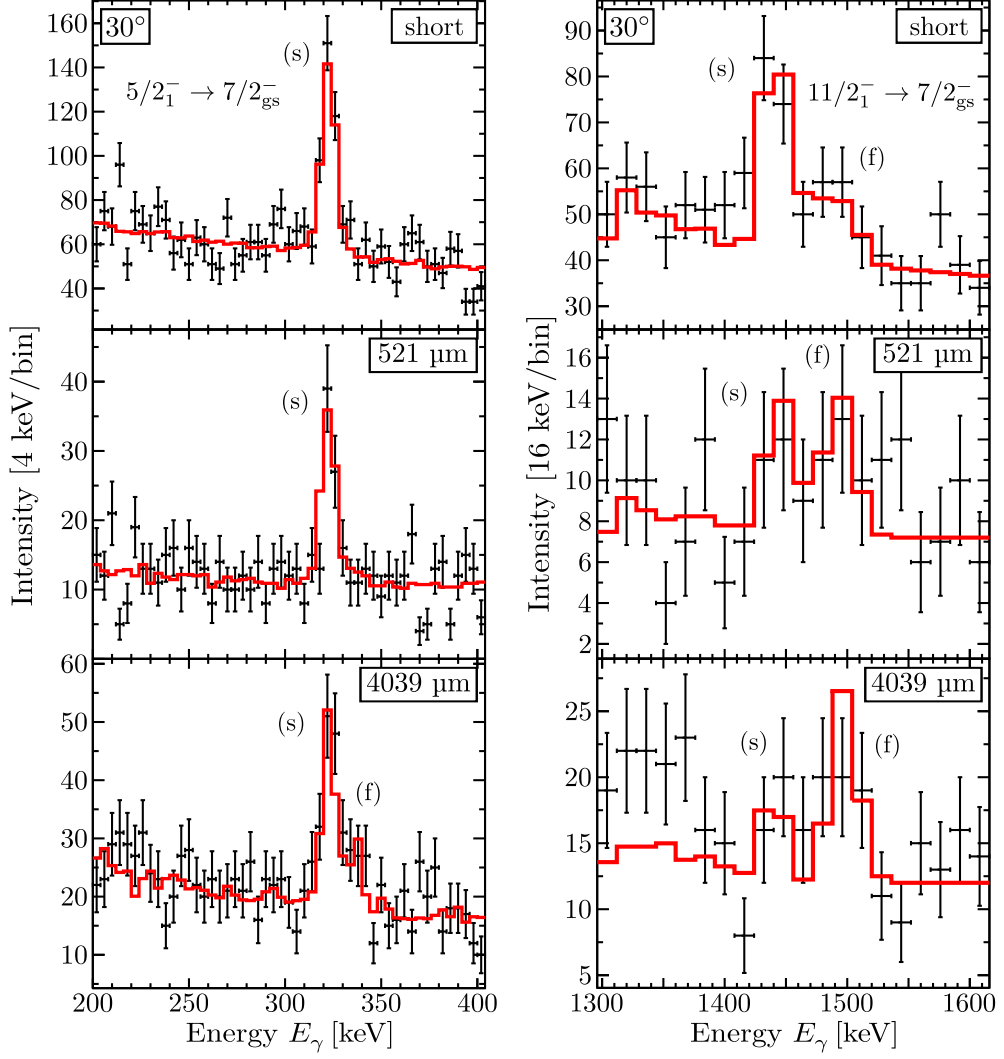


Figure 5.13.: (First setup –  $^{55}\text{V}$  – plunger data) Comparison of experimental (black) and best-fitting simulated (red)  $\gamma$ -ray spectra focusing on the transitions  $5/2_1^- \rightarrow 7/2_{\text{gs}}^-$  (left) and  $11/2_1^- \rightarrow 7/2_{\text{gs}}^-$  (right). The simulated spectra were generated assuming  $\tau(5/2_1^-) = 60$  ps and  $\tau(11/2_1^-) = 5$  ps, respectively. The top spectra show the summed statistics of foil separations 25, 53 and 83  $\mu\text{m}$ , while the middle (bottom) spectra show the statistics for 521  $\mu\text{m}$  (4039  $\mu\text{m}$ ).

$\mathbf{J_i \rightarrow J_f}$	$\mathbf{E_\gamma^{\text{lit}}}$ (keV)	$\mathbf{\tau_{\text{sim}}(\mathbf{J_i})}$ (ps)
$5/2_1^- \rightarrow 7/2_{\text{gs}}^-$	323.1(5)	60(12)
$11/2_1^- \rightarrow 7/2_{\text{gs}}^-$	1433.1(10)	5(2)

Table 5.14.: Results of the lifetime analysis in  $^{55}\text{V}$ . See text for details.

## 5.6. Other Chromium Isotopes

### 5.6.1. $^{57}\text{Cr}_{33}$ - Measurement of Level Lifetimes

First information on excited states were reported by prompt  $\gamma$ -ray spectroscopy following the  $\beta$  decay of  $^{57}\text{V}$  [Man03]. Deacon *et al.* [Dea05] performed the first in-beam study of excited states and extended the level scheme to higher spins. No information on level lifetimes in  $^{57}\text{Cr}$  were known prior to this work.

#### Observation of $\gamma$ -Ray Transitions in Target-Only Data

Excited states in  $^{57}\text{Cr}$  were predominantly populated in the first experimental setup by multi-nucleon removal reactions from  $^{59}\text{Mn}$ . Experimental and best-fitting simulated Doppler-reconstructed  $\gamma$ -ray spectra corresponding to target-only data are shown in Fig. 5.14. All identifiable peaks could be assigned to transitions published in Ref. [Dea05].

The peak close to 515 keV may either represent the  $11/2_1^{(-)} \rightarrow 9/2_1^{(-)}$  transition at 516.9 keV or the  $(13/2_1^-) \rightarrow 11/2_1^{(-)}$  transition at 513.4 keV. The  $(13/2_1^-)$  state decays by a competing branch with  $E_\gamma = 1031$  keV whose relative intensity slightly exceeds the one of the 513-keV branch. However, this transition was not observed and it is therefore reasonable to assume that the intensity of this peak is at least dominated by the  $11/2_1^{(-)} \rightarrow 9/2_1^{(-)}$  transition.

Based on published branching ratios [Dea05], the simulated spectra were generated using the following initial populations:  $N_0(5/2_1^-) = 43(2)\%$ ,  $N_0(5/2_2^-) = 21(3)\%$ ,  $N_0(7/2_1^-) = 15(3)\%$ ,  $N_0(9/2_1^{(+)}) = 8(5)\%$ ,  $N_0(13/2_1^{(+)}) = 6(2)\%$ ,  $N_0(9/2_1^{(-)}) = 4(4)\%$  and  $N_0(11/2_1^{(-)}) = 20(4)\%$ . The quoted errors are purely statistical and do not include systematic effects, e.g. due to error propagations induced by the feeding uncertainties.

#### Lifetime Estimates for $^{57}\text{Cr}$

The observed level scheme in  $^{57}\text{Cr}$  is quite rich and, as a consequence, a certain amount of statistics is mandatory to control the various parameters, e.g. initial populations and level lifetimes. Practically, the  $\gamma$ -ray yield related to  $^{57}\text{Cr}$  was sparse and, hence, a rigorous analysis was not feasible. Still, it was tried to evaluate at least estimates for level lifetimes based on data from the downstream detector ring. For this purpose, data taken for the short separations of 25, 53 and 83  $\mu\text{m}$  were added, which was sufficient to differentiate between short ( $\sim 2$  ps) and longer (effective) lifetimes.

A feeding scheme as depicted in Fig. 5.14 was assumed. Level lifetimes were fixed from top to bottom with respect to the excitation energies. The large errors, foremost due to

State	$13/2_1^{(+)}$	$9/2_1^{(+)}$	$11/2_1^{(-)}$	$9/2_1^{(-)}$	$7/2_1^-$	$5/2_2^-$	$5/2_1^-$
Lifetime (ps)	5	10	3.5	1	8	1	30

Table 5.15.: Lifetime estimates in  $^{57}\text{Cr}$ . See text for details.

uncertainties in the initial populations, make a thorough treatment of errors questionable. As a consequence, the determined lifetimes should be treated as an educated guess, although it is evident that they lead to an acceptable agreement between experimental and simulated spectra, which is illustrated in Fig. 5.15. The best-fitting lifetime estimates are summarized in Table 5.15.

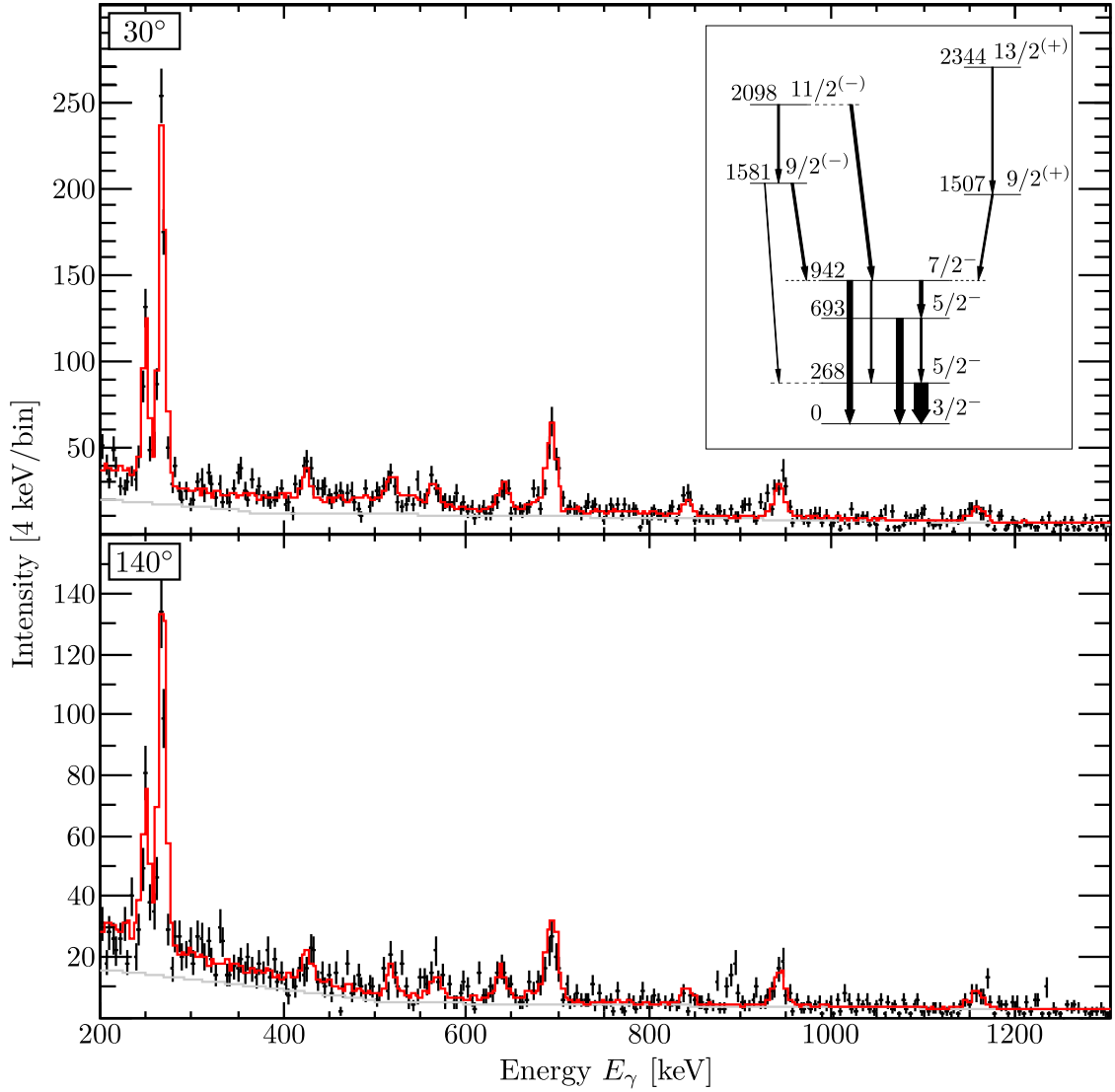


Figure 5.14.: (First setup –  $^{57}\text{Cr}$  – target-only data) Experimental Doppler-reconstructed  $\gamma$ -ray spectra (black) are shown for the response signals of the downstream (*top*) and the upstream (*bottom*) SeGA detector ring in target-only data. The best-fitting simulated spectra are shown for both detector rings in red and were generated assuming the depicted decay scheme. The widths of the arrows mimic the relative intensities. See text for details.

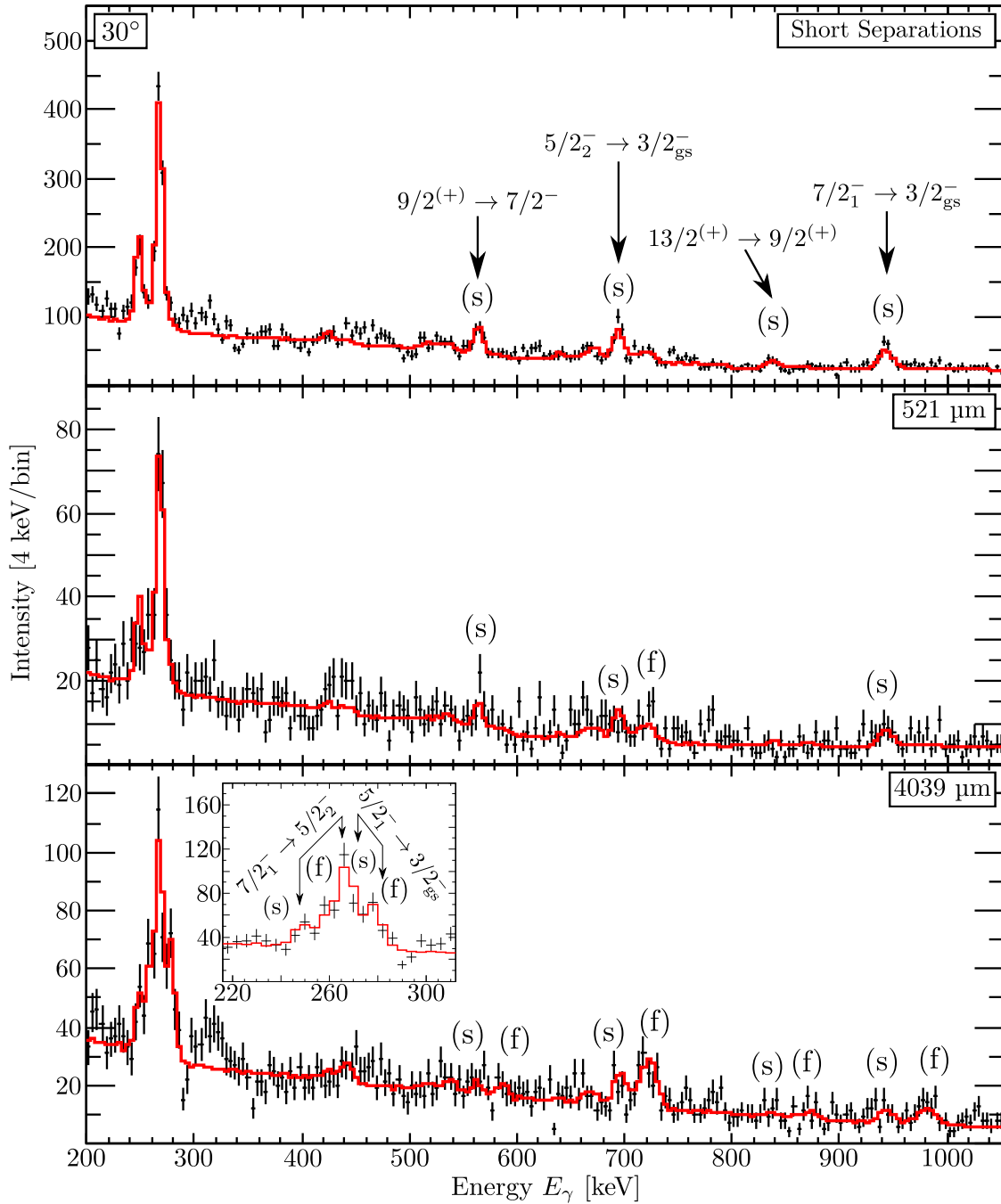


Figure 5.15.: (First setup –  $^{57}\text{Cr}$  – plunger data) Comparison of experimental (black) and simulated (red) Doppler-reconstructed  $\gamma$ -ray spectra. The simulated spectra were generated assuming a decay scheme as depicted in Fig. 5.14. The following level lifetimes were assumed:  $\tau(13/2_1^{(+)}) = 5$  ps,  $\tau(9/2_1^{(+)}) = 10$  ps,  $\tau(11/2_1^{(-)}) = 3.5$  ps,  $\tau(9/2_1^{(-)}) = 1$  ps,  $\tau(7/2_1^-) = 8$  ps,  $\tau(5/2_2^-) = 1$  ps and  $\tau(5/2_1^-) = 30$  ps.

## 5.7. Manganese Isotopes

### 5.7.1. $^{59}\text{Mn}_{34}$ - Measurement of Level Lifetimes

First information on excited states in  $^{59}\text{Mn}$  were reported by Liddick *et al.* [Lid05] using prompt  $\gamma$ -ray spectroscopy following the  $\beta$  decay of  $^{59}\text{Cr}$ . Multi-nucleon transfer reactions enabled a slight extension of the known level scheme [Val08]. So far, the most precise information on  $\gamma$ -ray transitions and branching ratios stem from a  $\gamma$ -ray spectroscopy experiment [Ste10] which was performed at the ANL with the detector array GAMMA-SPHERE. No information on mixing ratios are available for  $^{59}\text{Mn}$ .

Only the the lifetime of the  $11/2_1^-$  state is known so far ( $\tau(11/2_1^-) = 2.63(40)$  ps), from which the  $B(E2; 11/2_1^- \rightarrow 7/2_1^-)$  value was deduced to  $111_{-15}^{+21} e^2\text{fm}^4$  [Kli17].

#### Observation of $\gamma$ -ray Transitions in Target-Only Data

The best  $\gamma$ -ray yield correlated to  $^{59}\text{Mn}$  was found in the first experimental setup, where excited states in  $^{59}\text{Mn}$  were populated by one-proton knockout from  $^{60}\text{Fe}$ . Spectra showing the  $\gamma$ -ray yield of the target-only run are depicted in Fig. 5.16. The most prominent peak at  $E_\gamma \sim 110$  keV ( $7/2_1^- \rightarrow 5/2_{\text{gs}}^-$ ) can only be seen in the downstream detector ring<sup>4</sup>.

$\mathbf{J_i \rightarrow J_f}$	$\mathbf{E_\gamma^{\text{lit}}}$ (keV)	$\mathbf{E_\gamma^{\text{exp}}}$ (keV)	$\mathbf{I_\gamma}$ (%)
$7/2_1^- \rightarrow 5/2_{\text{gs}}^-$	112.1(1)	110.5(20)	100(2)
No assignment	1237.8(4)	1237.4(31)	20(2)
$9/2_1^- \rightarrow 7/2_1^-$	936.6(1)	936.1(15)	18.0(20)
$11/2_1^- \rightarrow 7/2_1^-$	1188.7(1)	1190.0(22)	10.7(18)
$11/2_1^- \rightarrow 9/2_1^-$	252.5(1)	249.3(36)	1.6(5)

Table 5.16.: (First setup –  $^{59}\text{Mn}$  – target-only data) The table lists all observed  $\gamma$ -ray transitions in target-only data. The quoted errors include statistical and systematic uncertainties. See text for details.

The target-only data reveal reasonable arguments to assume a comparably long lifetime ( $\tau > 300$  ps) for this state:

- The line shape has a pronounced low-energy tail in the Doppler-reconstructed  $\gamma$ -ray spectrum. In fact, this flank would most likely be even more pronounced if the Doppler-shifted energies were higher and, hence, further away from the energy threshold.
- Compared to the given literature value (112.1(1) keV [Ste10]), the peak maximum (108.1(10) keV) is shifted toward lower energies.

<sup>4</sup>This transition was not observed in the upstream detector ring because the corresponding Doppler-shifted energies were below the threshold.

Further peaks appear at 936 keV ( $9/2_1^- \rightarrow 7/2_1^-$ ), 1190 keV ( $11/2_1^- \rightarrow 7/2_1^-$ ) and 1237 keV<sup>5</sup>. The transition  $11/2_1^- \rightarrow 9/2_1^-$  at  $\sim 250$  keV can only be seen with very sparse statistics. Based on known branching ratios [Ste10], the transition  $9/2_1^- \rightarrow 5/2_{gs}^-$  is expected at  $E_\gamma = 1049$  keV, although with very small intensity. Such a peak could not be identified unambiguously in the experimental spectra.

No further peaks were observed, in particular not close to energies at which feeding transitions of the  $9/2_1^-$  and  $11/2_1^-$  are expected. The observed  $\gamma$ -ray transitions are listed in Table 5.16.

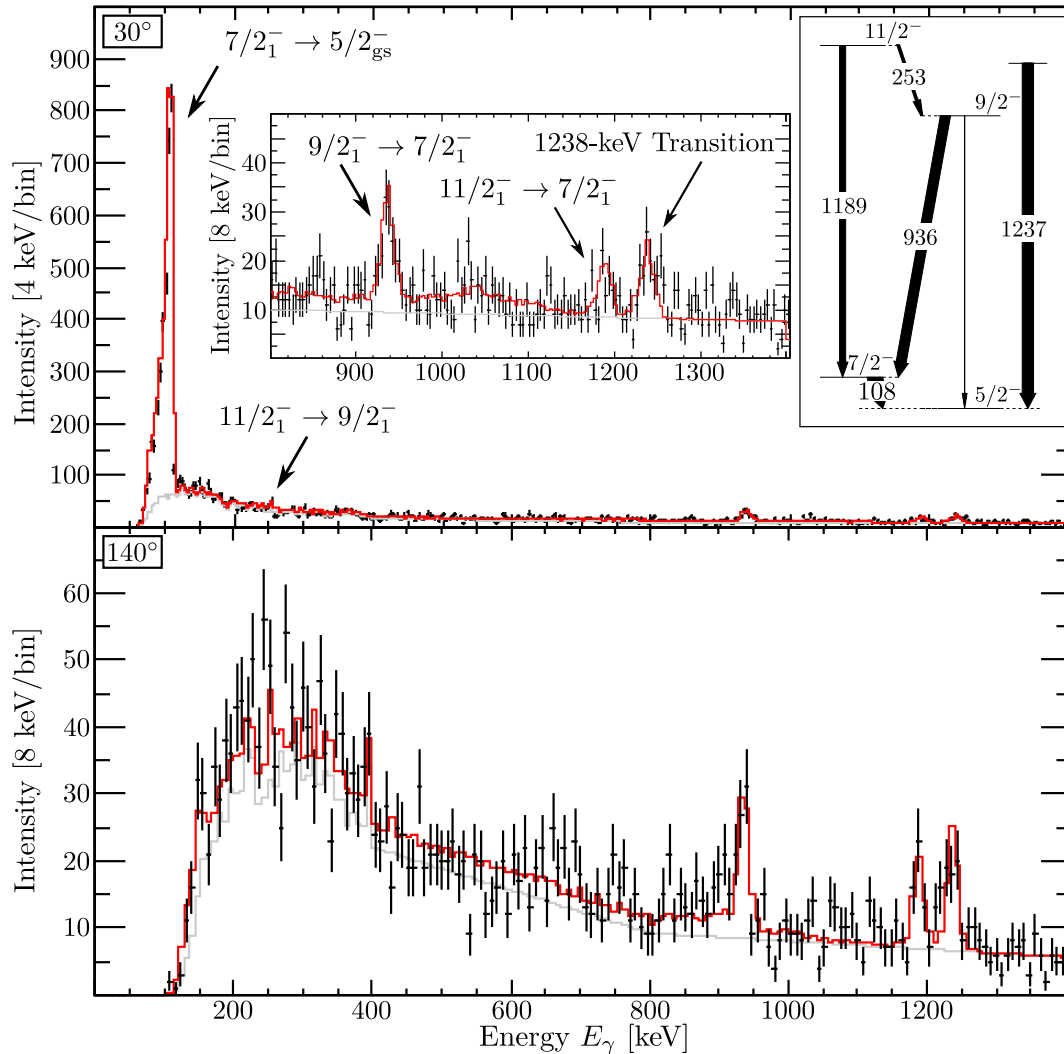


Figure 5.16.: (First setup –  $^{59}\text{Mn}$  – target-only data) Doppler-reconstructed experimental (black) and best-fitting simulated (red)  $\gamma$ -ray spectra. Shown are the statistics of the downstream (*top*) and upstream detector ring (*bottom*). See text for details.

<sup>5</sup>A transition with this specific energy was observed in Ref. [Lid05], but has not been assigned to a transition yet.

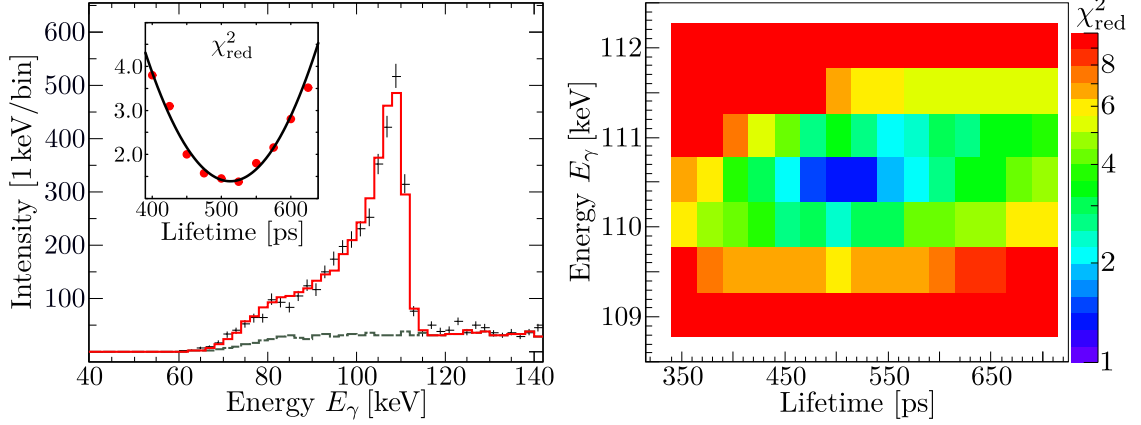


Figure 5.17.: (First setup –  $^{59}\text{Mn}$  – target-only data) *Left*: Line-shape analysis of the  $7/2_1^- \rightarrow 5/2_{\text{gs}}^-$  transition using target-only data. The experimental Doppler-reconstructed  $\gamma$ -ray spectrum of the downstream detector ring is shown in black while the best-fitting simulated  $\gamma$ -ray spectrum is shown in red. Best agreement is found for  $E_\gamma = 110.5$  keV and  $\tau(7/2_1^-) = 525$  ps. The inset shows the reduced  $\chi^2$  values for different lifetime assumptions with a fixed energy  $E_\gamma = 110.5$  keV. *Right*: Reduced  $\chi^2$  distribution for  $\tau(7/2^-)$  as a function of  $\gamma$ -ray energy and lifetime.

### Determination of Level Lifetimes

The chosen foil separations of the first experimental setup were insensitive to the long lifetime of the  $7/2_1^-$  state. However, an investigation of the lifetime was possible by analysing the line shape of the  $7/2_1^- \rightarrow 5/2_{\text{gs}}^-$  transition. Unfortunately, in this particular case such an analysis is aggravated due to the low  $\gamma$ -ray energies close to the threshold and the sophisticated description of the  $\gamma$ -ray background at such low energies.

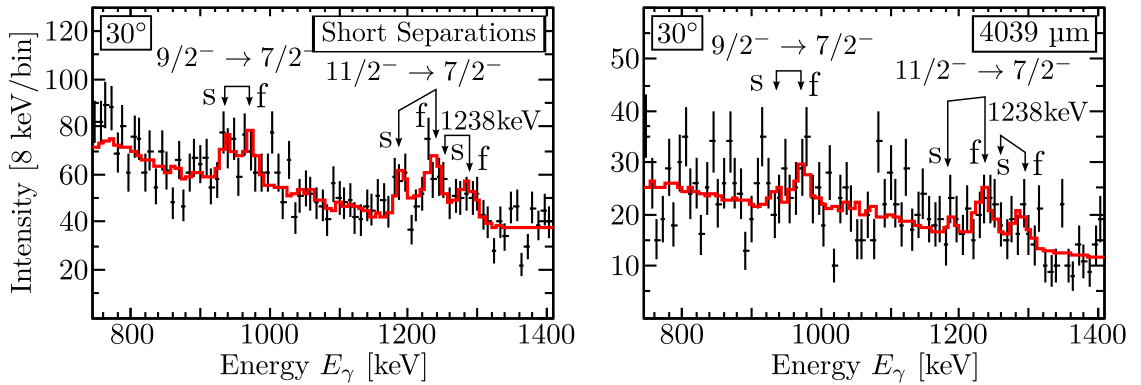


Figure 5.18.: (First setup –  $^{59}\text{Mn}$  – plunger data) Comparison of experimental (black) and simulated (red) Doppler-reconstructed  $\gamma$ -ray spectra. For the best simulation level lifetimes of  $\tau(9/2^-) = 1.5$  ps,  $\tau(11/2^-) = 2.0$  ps and  $\tau(E_\gamma = 1238 \text{ keV}) = 1.8$  ps were assumed. See text for details.

$\mathbf{J}_i \rightarrow \mathbf{J}_f$	$E_\gamma^{\text{lit}}$ (keV)	$\tau_{\text{sim}}(\mathbf{J}_i)$ (ps)	$B(\mathbf{E}2; \downarrow)_{\text{sim}}$ ( $e^2\text{fm}^4$ )	$B(\mathbf{E}2; \downarrow)_{\text{lit}}$ ( $e^2\text{fm}^4$ )
$7/2_1^- \rightarrow 5/2_{\text{gs}}^-$	112.1(1)	$525_{-50}^{+125}$	-	-
$9/2_1^- \rightarrow 7/2_1^-$	936.6(1)	1.5(7)	-	-
$9/2_1^- \rightarrow 5/2_1^-$	936.6(1)	1.5(7)	$10_{-10}^{+16}$	-
$11/2_1^- \rightarrow 7/2_1^-$	1188.7(1)	2.0(8)	$145_{-50}^{+99}$	$111_{-15}^{+21}$ [Kli17]
No assignment	1237.8(4)	1.8(7)	-	-

Table 5.17.: Results of the lifetime analysis in  $^{59}\text{Mn}$ . Information on  $\gamma$ -ray energies are taken from Refs. [Ste10; Lid05].

These difficulties lead to comparably large errors, in particular toward longer lifetimes. A comparison of best-fitting simulated and experimental spectra is shown in Fig. 5.17. The  $\gamma$ -ray background was modelled using  $\gamma$ -ray data correlated to  $^{58}\text{Cr}$  which show no sign of low-energy transitions. The lifetime was determined by a  $\chi^2$  analysis in two dimensions ( $\gamma$ -ray energy and level lifetime as free parameters), see Fig. 5.17. Best agreement ( $\chi_{\text{red, min}}^2 = 1.38$ ) was found for  $E_\gamma = 110.5\text{ keV}$  and  $\tau(7/2^-) = 525(25)\text{ ps}$ . It must be stressed that a satisfactory description of the line shape was practically impossible when assuming the published  $\gamma$ -ray transition energy of  $112.1(1)\text{ keV}$  [Ste10]. To take into account the uncertainties related to the detector response at such low energies, the systematic error was estimated to  $\Delta_{\text{sys}} = {}_{-25}^{+100}$ .

Due to the small  $\gamma$ -ray yields related to decays of higher-lying states, only the response of the downstream detector ring was used to determine their lifetimes. In addition, the statistics of the foil separations 25, 53 and 83  $\mu\text{m}$  were added (*short separations*). The experimental and best-fitting simulated  $\gamma$ -ray spectra are shown in Fig. 5.18. Best agreement was found for  $\tau_{\text{sim}}(11/2_1^-) = 2.0(8)\text{ ps}$  and  $\tau_{\text{sim}}(9/2_1^-) = 1.5(7)\text{ ps}$ . With respect to the mother state of the 1238-keV transition, best results are given for  $\tau_{\text{sim}} = 1.8(7)\text{ ps}$ . The  $B(\mathbf{E}2; 11/2_1^- \rightarrow 7/2_1^-)$  value was determined<sup>6</sup> to  $145_{-50}^{+99}\text{ e}^2\text{fm}^4$ , which is in agreement with a previous result published in Ref. [Kli17].

Similarly, the  $B(\mathbf{E}2; 9/2_1^- \rightarrow 5/2_{\text{gs}}^-)$  was determined from  $\tau(9/2^-)$  to  $10_{-10}^{+16}\text{ e}^2\text{fm}^4$ , assuming a branching ratio of 2.2% for the  $9/2^- \rightarrow 5/2^-$  transition [Ste10]. Reduced transition probabilities related to the  $7/2_1^- \rightarrow 5/2_{\text{gs}}^-$  and  $9/2_1^- \rightarrow 7/2_1^-$  transitions could not be determined due to unknown mixing ratios. The results are summarized in Table 5.17.

<sup>6</sup> Assuming a branching ratio of 84.8(44)% for the  $11/2_1^- \rightarrow 7/2_1^-$  transition, taken from Ref. [Ste10].

### 5.7.2. $^{61}\text{Mn}_{36}$ - Measurement of Level Lifetimes

Excited structures in  $^{61}\text{Mn}$  were observed in multi-nucleon transfer reaction studies [Val08; Chi10], prompt  $\gamma$ -ray spectroscopy following  $\beta$  decay [Cra09] as well as in an Coulomb-excitation experiment [VdW09]. So far, the assignment to specific  $J^\pi$  is only tentative for all excited states.

From the Coulomb-excitation experiment, the  $B(E2; (7/2_1^-) \rightarrow 5/2_{\text{gs}}^-)$  value was evaluated to  $428(57) e^2\text{fm}^4$ . Neither level lifetimes nor mixing ratios in  $^{61}\text{Mn}$  were known prior to this work.

#### Identification of $\gamma$ -ray Transitions

$^{61}\text{Mn}$  was populated in the second setup by one-proton knockout from  $^{62}\text{Fe}$  and in the third setup by various multi-nucleon removal reaction channels. The former data set offers slightly more statistics while the third setup benefits from a larger foil separation (7 mm compared to 4 mm in the second setup), which is essential to determine  $\tau(7/2_1^-)$  by means of the RDDS technique.

Although target-only data was recorded in the second setup, the statistics was insufficient to enable clear and unambiguous assignments apart from the dominating  $7/2_1^- \rightarrow 5/2_{\text{gs}}^-$  transition.

$\mathbf{J_i \rightarrow J_f}$	$\mathbf{E_\gamma^{\text{lit}}}$ (keV)	$\mathbf{E_\gamma^{\text{exp}}}$ (keV)	$\mathbf{I_\gamma}$ (%)
$(7/2_1^-) \rightarrow 5/2_{\text{gs}}^-$	156.7(1)	155.6(15)	100(5)
$(9/2_1^-) \rightarrow (7/2_1^-)$	878.3(5)	880(5)	11(4)
$(11/2_1^-) \rightarrow (7/2_1^-)$	1124.6(5)	1127(5)	29(5)
$(11/2_1^-) \rightarrow (9/2_1^-)$	247.5(4)	-	< 5

Table 5.18.: (Second setup –  $^{61}\text{Mn}$  – plunger data) The table lists all  $\gamma$ -ray transitions observed in summed data taken with short foil separations (171, 325 and 480  $\mu\text{m}$ ). The corresponding spectrum of the downstream detector ring is shown in Fig. 5.19. The quoted energies include statistical and systematic uncertainties. Relative intensities are normalized to the  $7/2_1^- \rightarrow 5/2_{\text{gs}}^-$  transition. See text for details.

A Doppler-reconstructed  $\gamma$ -ray spectrum correlated to  $^{61}\text{Mn}$  showing the summed statistics of the downstream detector ring for short foil separations (171, 325 and 480  $\mu\text{m}$ ) is depicted in Fig. 5.19. As already indicated, the  $\gamma$ -ray spectrum is dominated by the peak at 157 keV which corresponds to the  $(7/2_1^-) \rightarrow 5/2_{\text{gs}}^-$  transition. Further peaks occur at 880 keV ( $(9/2_1^-) \rightarrow (7/2_1^-)$ ) and 1127 keV ( $(11/2_1^-) \rightarrow (9/2_1^-)$ ).

In addition, a weak structure with less statistics appears close to 250 keV which may represent<sup>7</sup> the transition  $(11/2_1^-) \rightarrow (9/2_1^-)$ .

<sup>7</sup>It is worth to mention that the experimental  $\gamma$ -ray yields of the  $(11/2_1^-) \rightarrow (7/2_1^-)$  and  $(11/2_1^-) \rightarrow (9/2_1^-)$  transitions are reproduced simultaneously if branching ratios of  $> 85\%$  and  $< 15\%$  are

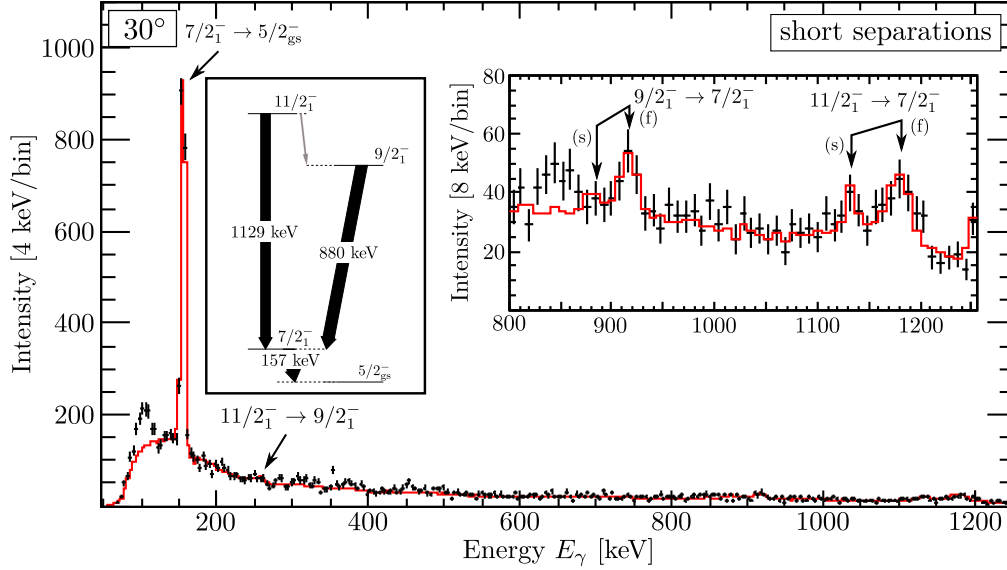


Figure 5.19.: (Second setup –  $^{61}\text{Mn}$  – plunger data) Experimental (black) and best-fitting simulated (red) Doppler-reconstructed  $\gamma$ -ray spectrum are shown for the added statistics of data taken at 171, 325 and 480  $\mu\text{m}$  as detected in the downstream detector ring. Peaks are identified and the experimentally observed decay scheme is shown. Lifetimes of  $\tau(7/2_1^-) = 140$  ps,  $\tau(9/2_1^-) = 1.5$  ps and  $\tau(11/2_1^-) = 3.2$  ps were assumed to generate the simulated spectrum. See text for details.

It cannot be excluded that the  $(11/2_1^-) \rightarrow (7/2_1^-)$  is contaminated by a transition with  $E_\gamma = 1142(21)$  keV which was observed in the  $\beta$ -decay study [Cra09], although with very sparse statistics. Apart from that, no further peaks were identified, in particular none of the transitions known to feed the  $(11/2_1^-)$  and  $(9/2_1^-)$  states. The experimentally observed transitions, their energies as well as their relative intensities as observed in the present experiment are listed in Table 5.18.

### Determination of Level Lifetimes

Lifetimes of the  $(9/2_1^-)$  and  $(11/2_1^-)$  states were analysed in the second experimental using the added statistics of the foil separations 171, 325 and 480  $\mu\text{m}$ . A comparison of experimental and best-fitting simulated Doppler-reconstructed  $\gamma$ -ray spectra is depicted in Fig. 5.19.

Best results are achieved for  $\tau_{\text{sim}}((11/2_1^-)) = 3.2(10)$  ps and  $\tau_{\text{sim}}((9/2_1^-)) = 1.5_{-1.5}^{+0.8}$  ps. A  $B(\text{E}2; (11/2_1^-) \rightarrow (7/2_1^-))$  value equal to  $121_{-50}^{+76} e^2\text{fm}^4$  is deduced from the level lifetime of the  $(11/2_1^-)$  state as well as a branching ratio of 85(15) %. This is comparable to the case of  $^{59}\text{Mn}$ .

With respect to the  $(7/2_1^-) \rightarrow 5/2_{\text{gs}}^-$  transition, none of the  $\gamma$ -ray spectra recorded in the second part of the experiment show any indication of a fast component. An estimate of the level lifetime was achieved by means of a line-shape analysis using the summed

assumed, which is in agreement with the quoted value in ENSDF [ENSDF].

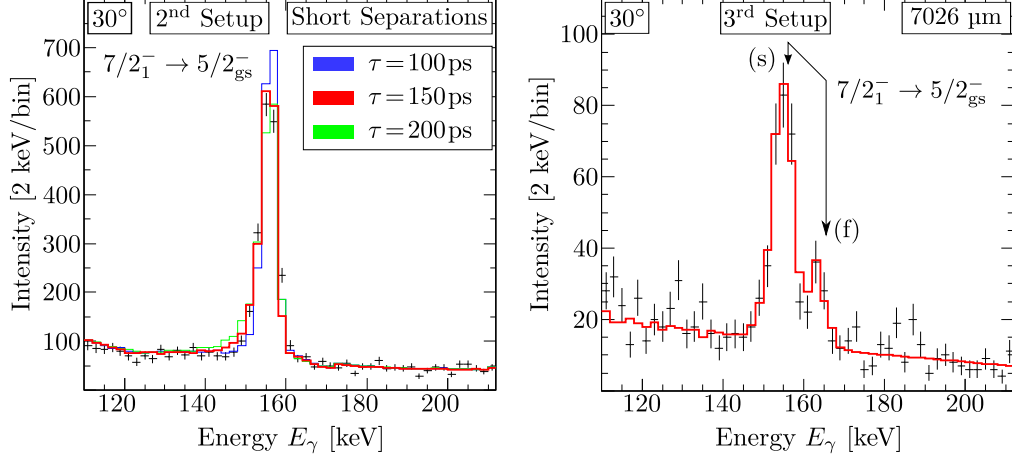


Figure 5.20.: (Second and third setup –  $^{61}\text{Mn}$  – plunger data) Lifetime analysis of the  $(7/2_1^-)$  state in  $^{61}\text{Mn}$ . *Left*: Line-shape analysis of the  $(7/2_1^-) \rightarrow 5/2_{gs}^-$  transition for different lifetime assumptions (blue, red and green). Best agreement is found for  $\tau((11/2_1^-)) = 150$  ps. *Right*: Comparison of experimental (black) and best-fitting simulated spectrum (red) for the foil separation of 7026  $\mu\text{m}$  recorded in the third setup. Best agreement is found for  $\tau((7/2_1^-)) = 140$  ps. See text for details.

statistics of the short separations 171, 325 and 480  $\mu\text{m}$ . The best agreement was found for  $\tau((7/2_1^-)) = 150(30)$  ps (see Fig. 5.20).

As mentioned before, excited states in  $^{61}\text{Mn}$  were also populated in the third setup. Here, the foil separation of 7026  $\mu\text{m}$  was sufficient to reveal a fast component of the  $(7/2_1^-) \rightarrow 5/2_{gs}^-$  transition, which enables a proper RDDS analysis. Best results are found for  $\tau_{\text{sim}}((7/2_1^-)) = 140(15)$  ps.

A comparison of experimental and best-fitting simulated spectra is depicted in Fig. 5.20. Combining this level lifetime with the published  $B(E2)$  value, the (absolute) E2-M1 mixing ratio  $|\delta|$  is evaluated to  $|\delta| = 0.084(7)$  and the  $B(M1; (7/2_1^-) \rightarrow 5/2_{gs}^-)$  is determined to  $0.104(23) \mu_N^2$ .

Adopted results are summarized in Table 5.19.

$\mathbf{J_i} \rightarrow \mathbf{J_f}$	$E_\gamma^{\text{lit}}$ (keV)	$\tau_{\text{sim}}(\mathbf{J_i})$ (ps)	$B(E2; \downarrow)_{\text{sim}}$ ( $e^2\text{fm}^4$ )	$B(E2; \downarrow)_{\text{lit}}$ ( $e^2\text{fm}^4$ )	$B(M1; \downarrow)$ ( $\mu_N^2$ )
$(7/2_1^-) \rightarrow 5/2_{gs}^-$	156.7(1)	140(15)	-	428(57)[VdW09]	0.104(23)
$(9/2_1^-) \rightarrow (7/2_1^-)$	878.3(5)	$1.5^{+0.8}_{-1.5}$	-	-	-
$(11/2_1^-) \rightarrow (7/2_1^-)$	1124.6(5)	3.2(10)	$121^{+76}_{-50}$	-	-

Table 5.19.: Results of the lifetime analysis in  $^{61}\text{Mn}$ . Energies of the  $\gamma$ -ray transition are taken from Ref. [Val08]. See text for details.

### 5.7.3. $^{63}\text{Mn}_{38}$ - Measurement of Level Lifetimes

Only three  $\gamma$ -ray transitions were assigned to  $^{63}\text{Mn}$  based on experiments using prompt  $\gamma$ -ray spectroscopy following multi-nucleon transfer reactions [Val08] and inelastic scattering [Bau16]. So far, their assignment to specific transitions is only tentative.

The  $\gamma$ -ray of 248.4(5) keV was proposed to feed the ground state [Val08]. Following the systematics along the odd- $A$  Mn isotopes, the authors proposed it as a candidate for the  $(7/2_1^-) \rightarrow 5/2_{\text{gs}}^-$  transition.

In Ref. [Bau16],  $\gamma$ -rays at 375(5) keV and 637(5) keV were tentatively assigned to the transitions  $(11/2_1^-) \rightarrow (9/2_1^-)$  and  $(9/2_1^-) \rightarrow (7/2_1^-)$ . The authors motivated their assignments by  $\gamma\gamma$ -correlations (although with very sparse statistics), by systematics as well as by comparison to state-of-the-art shell-model calculations using the LNPS interactions.

In Ref. [Bau16] level lifetimes were determined for the states with  $J_i^\pi = (7/2_1^-)$ ,  $(9/2_1^-)$  and  $(11/2_1^-)$  by means of a line-shape analysis.

#### Identification of Observable Transitions

Excited states in  $^{63}\text{Mn}$  were populated with sufficient statistics in the third experimental setup by means of one-proton knockout from  $^{64}\text{Fe}$ .

Doppler-reconstructed  $\gamma$ -ray spectra related to the foil separation 26  $\mu\text{m}$  are shown in Fig. 5.22. The most prominent peak in this spectrum corresponds to the  $(7/2_1^-) \rightarrow 5/2_{\text{gs}}^-$  transition. For both rings, the second strongest peak – significantly weaker but still identifiable – appears close to 635 keV although at different energies: In the downstream and upstream detector ring its energy is close to 670 keV and 600 keV, respectively.

These peaks can be explained consistently as fast components of a 637-keV transition

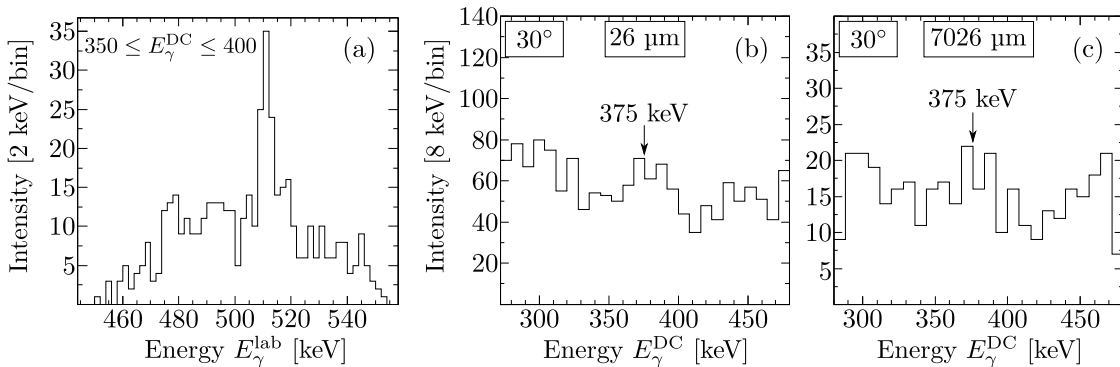


Figure 5.21.: (Third setup –  $^{63}\text{Mn}$  – Discussion of the problematic 375 keV transition)  
 (a) Doppler-*shifted*  $\gamma$ -ray spectrum (downstream detector ring) correlated to Doppler-*reconstructed* energies between 350 and 400 keV. Here, the 511-keV line can be identified without any effort. (b,c) Doppler-reconstructed  $\gamma$ -ray spectrum for foil separations 26  $\mu\text{m}$  (b) and 7026  $\mu\text{m}$  (c), respectively. These spectra indicate no significant peak evolution assuming a transition with  $E_\gamma \approx 375$  keV. Hence, there is no experimental evidence of such a transition in the present experimental data.

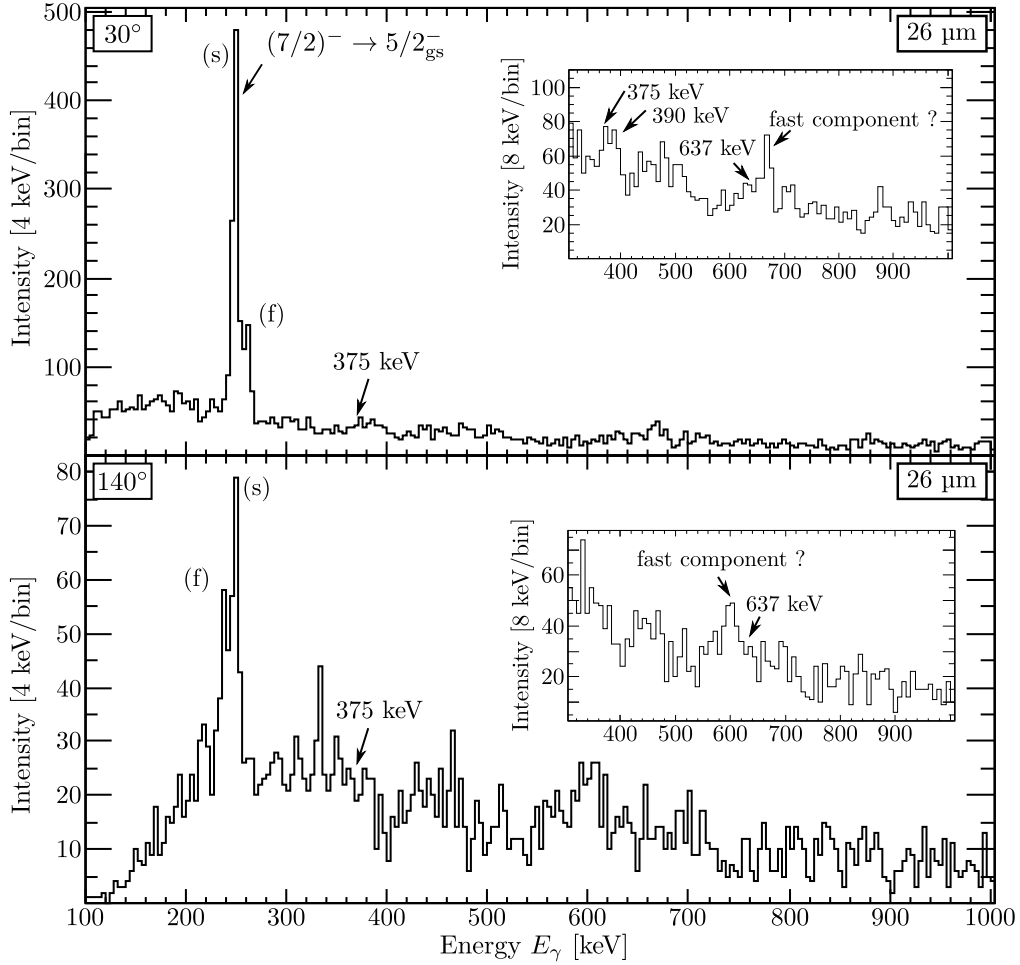


Figure 5.22.: (Third setup –  $^{63}\text{Mn}$  – plunger data) Experimental Doppler-reconstructed  $\gamma$ -ray spectra corresponding to a foil separation of  $26\ \mu\text{m}$  and showing the statistics of the downstream (*top*) and upstream (*bottom*) detector ring. See text for details.

which has been observed already prior to the present work [Bau16].

Only the  $\gamma$ -ray spectrum of the downstream detector ring reveals an additional peak at  $E_\gamma = 370\ \text{keV}$ . On first sight, one is tempted to identify this peak with the transition at  $375(5)\ \text{keV}$  proposed in Ref. [Bau16]. However, careful analysis questions such an assignment:

- The peak can only be observed in the downstream detector (see Fig. 5.21). There is no clear evidence of a peak at such an energy in the upstream detector ring. Moreover, it is - at least - contaminated by the  $511\text{-keV}$  transition and appears only close to  $375\ \text{keV}$  as a consequence of the applied Doppler correction<sup>8</sup>.

<sup>8</sup>In Ref. [Bau16], the  $375\text{-keV}$  peak was observed using similar recoil energies but with SeGA and GRETINA detectors placed at different polar angles, e.g.  $\theta = 37^\circ$  and  $90^\circ$  for the SeGA detectors. In their data this peak was observed simultaneously in all detector rings.

- In the downstream detector ring, another peak for the fast component (assuming, of course, that  $E_\gamma = 375$  keV belongs to a real transition). However, the intensity ratio of these peaks shows no evolution when increasing the separation to  $7026 \mu\text{m}$  (see Fig. 5.21).

Hence, it is therefore reasonable to assume that this peak is at least contaminated by the 511-keV line. As a consequence, a lifetime analysis is impossible based on the present data. Apart from these, the spectra offer no evidence for additional observable transitions.

### Investigation of Level Lifetimes

Lifetimes were investigated assuming a very simple decay scheme which consisted of the 637-keV transition feeding the  $(7/2_1^-)$  state. A comparison of experimental and best-fitting simulated spectra focusing on the 637-keV transition is depicted in Fig. 5.23. Assuming that this is a real transition, it must correspond to a short-living state since already for the close separation of  $26 \mu\text{m}$  most of the intensity is found within the fast components. From  $26 \mu\text{m}$  to  $7026 \mu\text{m}$  there is no significant evidence of an evolving peak ratio with respect to this transition. The spectra are compatible with an upper lifetime

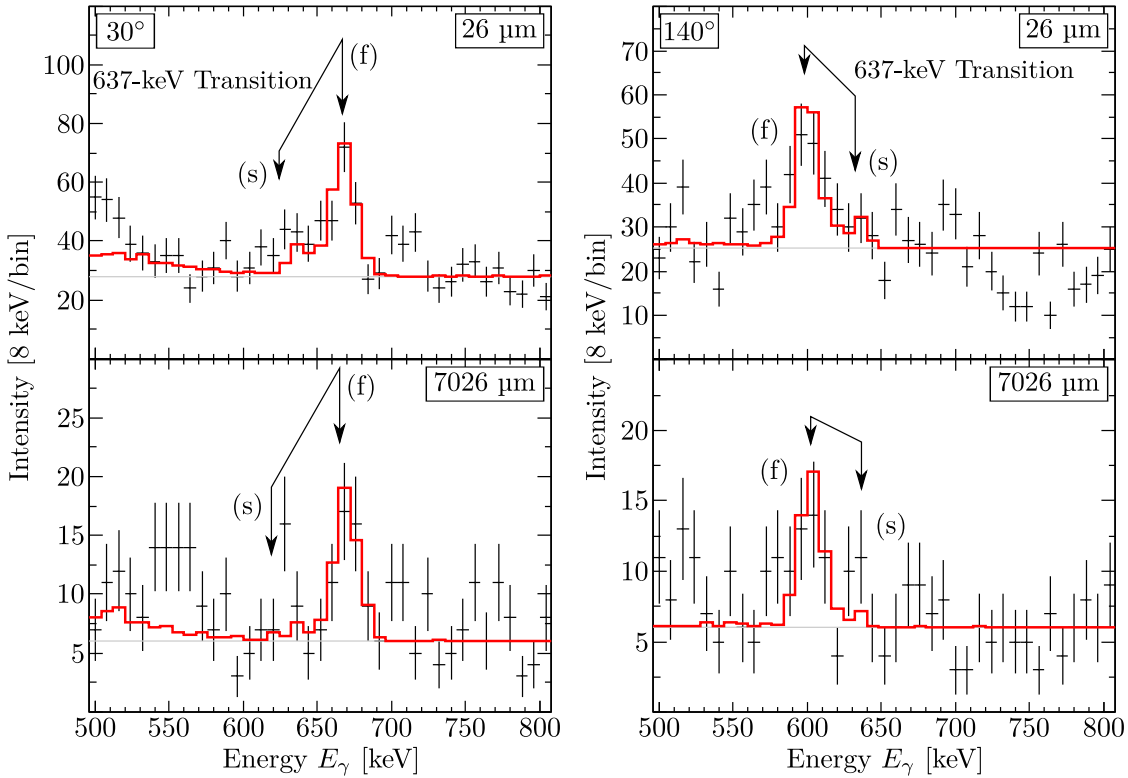


Figure 5.23.: (Third setup –  $^{61}\text{Mn}$  – plunger data) Comparison of experimental (black) and best-fitting simulated (red) Doppler-reconstructed  $\gamma$ -ray spectra for foil separations of  $26 \mu\text{m}$  (*top*) and  $7026 \mu\text{m}$  (*bottom*) to investigate the lifetime of the state associated with the 637 keV transition. The simulated spectra were generated assuming an effective level lifetime of 2 ps.

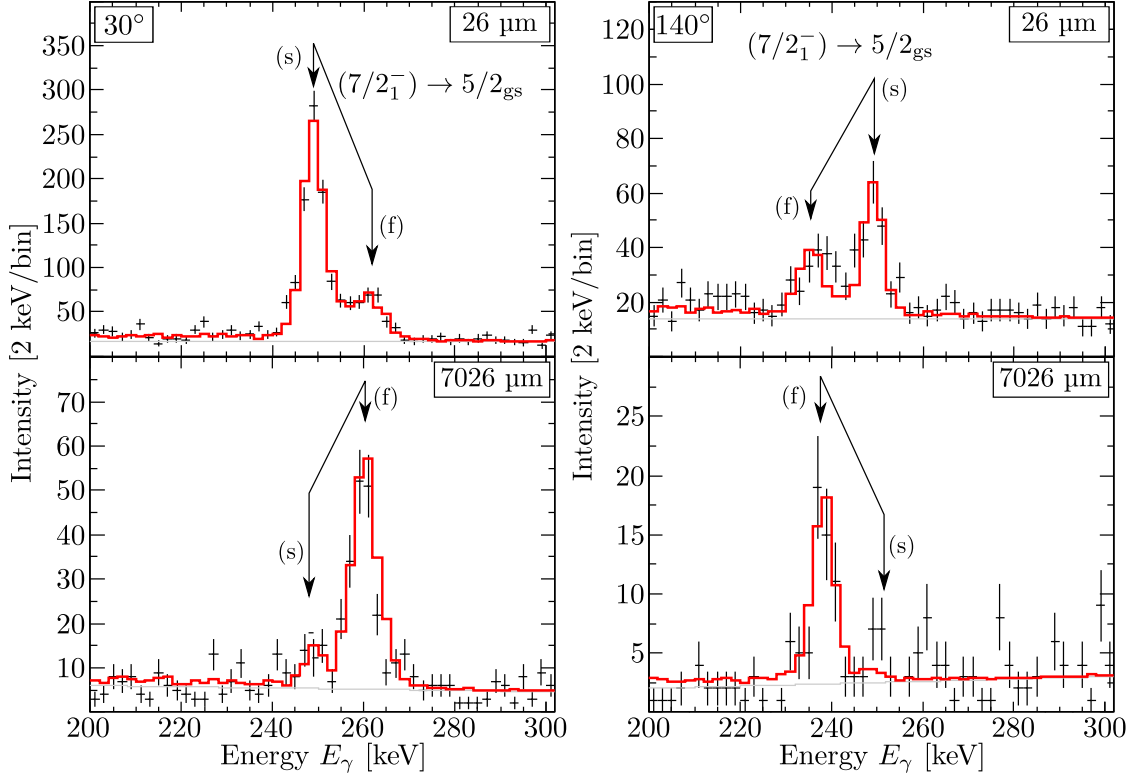


Figure 5.24.: (Third setup –  $^{63}\text{Mn}$  – plunger data) Comparison of experimental (black) and best-fitting simulated (red) Doppler-reconstructed  $\gamma$ -ray spectra for foil separations of  $26\ \mu\text{m}$  (*top*) and  $7026\ \mu\text{m}$  (*bottom*) to investigate the lifetime of the  $(7/2_1^-)$  state. The simulated spectra were generated assuming a level lifetime of 17 ps.

limit of 3 ps, which is in agreement with the previous result published in Ref. [Bau16].

Fig. 5.24 illustrates the comparison of experimental and best-fitting simulated spectra with respect to the  $(7/2_1^-) \rightarrow 5/2_{\text{gs}}^-$  transition. Here, best agreement is found for  $\tau((7/2_1^-)) = 17(3)$  ps, which exceeds the previous value reported from a line-shape analysis in Ref. [Bau16] by a factor of two. Results are summarized in Table 5.20.

$\mathbf{J_i \rightarrow J_f}$	$\mathbf{E_\gamma^{\text{lit}}}$ (keV)	$\mathbf{\tau_{\text{sim}}(\mathbf{J_i})}$ (ps)	$\mathbf{\tau_{\text{lit}}(\mathbf{J_i})}$ (ps)
$(7/2_1^-) \rightarrow 5/2_{\text{gs}}^-$	248.4(5) [Val08]	17(3)	8.5(5) [Bau12]
$(9/2_1^-) \rightarrow (7/2_1^-)$	637(5) [Bau16]	<3	0.9(6) [Bau12]

Table 5.20.: Results of the lifetime analysis in  $^{63}\text{Mn}$ . See text for details.

## 5.8. $^{64}\text{Fe}_{38}$ - Measurement of Level Lifetimes

Most precise information on the level scheme in  $^{64}\text{Fe}$  stems from a multi-nucleon transfer experiment [Hot06]. The yrast structures are known up to the the  $6^+$  state while levels in sidebands have been assigned only tentatively.

Reduced transition strengths for the  $2_1^+ \rightarrow 0_{\text{gs}}^+$  transition were determined in two RDDS measurements. The first experiment was performed at GANIL ( $B(E2) = 470_{-110}^{+210} e^2\text{fm}^4$  [Lju10]). The second one was performed at NSCL and determined the  $B(E2)$  with higher precision ( $B(E2) = 344(33) e^2\text{fm}^4$  [Rot11]).

A recent plunger experiment also performed at GANIL [Kli17] concluded an upper limit for the  $4_1^+$  state lifetime according to  $\tau(4_1^+) < 1.8 \text{ ps}$ , which corresponds to a lower limit for the  $B(E2)$  value of  $420 e^2\text{fm}^4$ . This is in agreement with the value in the neighbouring even-even isotone  $^{62}\text{Cr}$ .

### Determination of Level Lifetimes

Excited states in  $^{64}\text{Fe}$  were populated with the third experimental setup by various reaction channels, which could not be disentangled completely. The strongest reaction channels are Coulomb excitation and multi-nucleon removal reactions induced by  $^{66}\text{Co}$ . Due to the substantial contribution of Coulomb excitation the treatment of degrader ex-

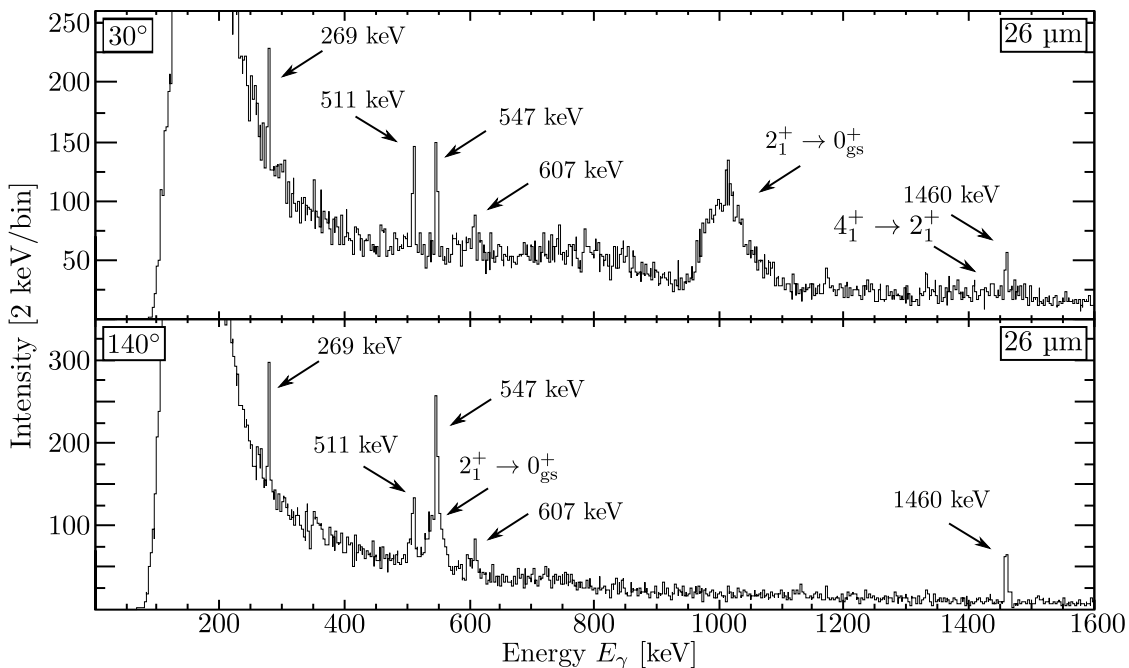


Figure 5.25.: (Third setup –  $^{64}\text{Fe}$  – plunger data) Raw  $\gamma$ -ray spectrum correlated to  $^{64}\text{Fe}$  showing data of the 26- $\mu\text{m}$  foil separation. Several non-broadened transitions can be readily identified. In particular, the Doppler-broadened part of the  $2_1^+ \rightarrow 0_{\text{gs}}^+$  in the upstream detector ring is contaminated by the 547-keV transition in gold (Coulomb excitation in the degrader). See text for details.

citations is more complicated compared to the other presented cases. In addition, the Doppler-shifted  $\gamma$ -ray spectrum (see Fig. 5.25) clearly shows several non-broadened transitions associated to Coulomb excitation, background transitions (see Sec. 3.1.3) and the 511-keV line. Particularly noteworthy is the 547-keV transition (Coulomb excitation in gold) that contaminates the  $2_1^+ \rightarrow 0_{\text{gs}}^+$  transition in the upstream detector ring. A similar problem appears in the spectrum of the downstream detector ring which is caused by the Doppler-reconstruction applied to the 1460-keV transition which contaminates the components of the  $4_1^+ \rightarrow 2_1^+$  transition.

Doppler-reconstructed experimental and best-fitting simulated  $\gamma$ -ray spectra are depicted in Fig. 5.26. The  $2_1^+ \rightarrow 0_{\text{gs}}^+$  transition dominates. Both fast and slow component of the  $4_1^+ \rightarrow 2_1^+$  transition can be identified clearly at 26  $\mu\text{m}$ . The observation of a slow component can be explained by two circumstances:

- The (effective) lifetime of the  $4_1^+$  state is around 4 ps. Such a lifetime would be in significant disagreement with the upper value of 1.8 ps reported in Ref. [Kli17]. A weak peak close to 1370 keV appears in the data of the upstream detector ring which is supposed to represent the doublet consisting of the  $(5_1^-) \rightarrow 4_1^+$  (1078 keV)

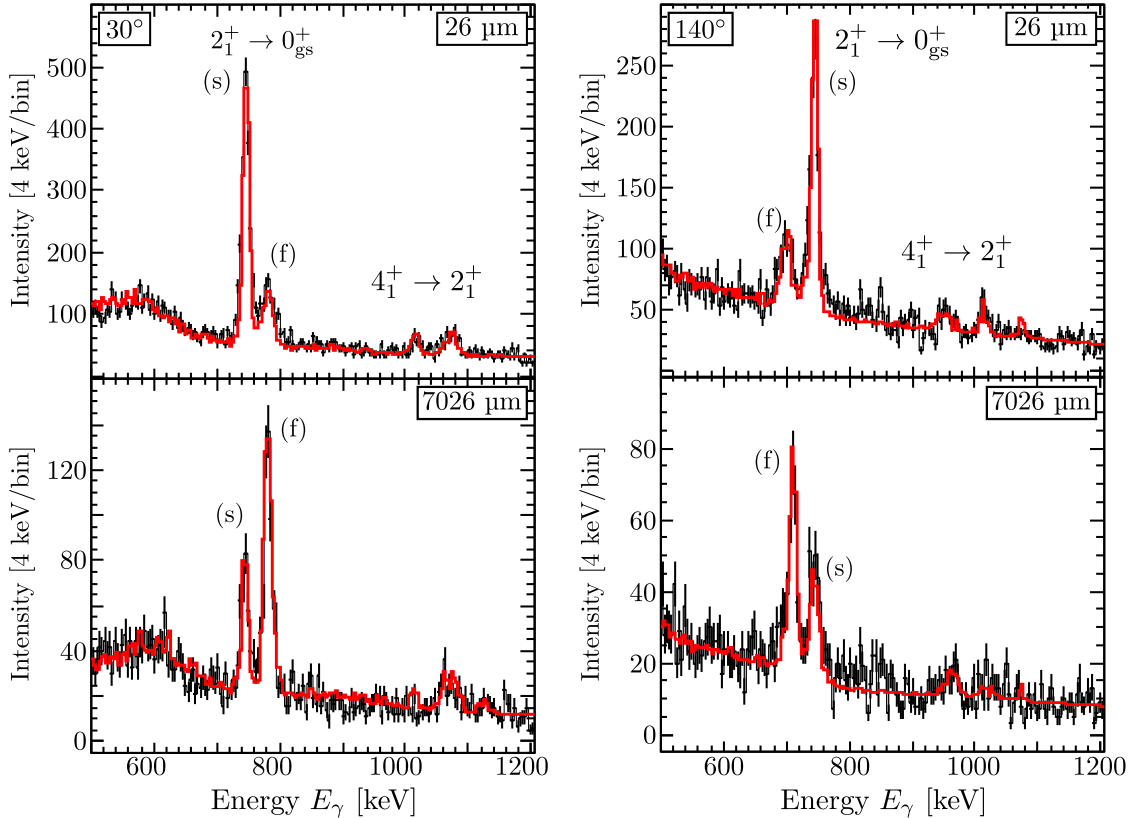


Figure 5.26.: (Third setup –  $^{64}\text{Fe}$  – plunger data) Investigation of level lifetimes. Compared are experimental (black) and best-fitting simulated (red) Doppler-reconstructed  $\gamma$ -ray spectra for the downstream (*left*) and upstream (*right*) detector ring. See text for details.

and  $6_1^+ \rightarrow 4_1^+$  (1079 keV) transitions. While the lifetime of the  $6_1^+$  state is expected to be rather short ( $\sim 1$  ps), the lifetime of the  $5_1^-$  state is expected to be significantly larger (see discussion of  $^{58}\text{Cr}$  in Sec. 5.2).

- The contribution of degrader excitations is significantly larger compared to the case of  $^{62}\text{Cr}$  (see Sec. 5.4).

The Doppler-reconstructed  $\gamma$ -ray spectra correlated to 7026  $\mu\text{m}$  indicate a severe contribution to the degrader component of the  $2_1^+ \rightarrow 0_{\text{gs}}^+$  transition. The observed evolution of the intensity ratios cannot be explained consistently by a long (effective) lifetime. Hence, at least for the  $2_1^+$  state the degrader excitation is larger compared to the analysis of, e.g.,  $^{62}\text{Cr}$ . This can be understood in terms of Coulomb excitation/inelastic scattering of the secondary beam  $^{64}\text{Fe}$  in the plunger degrader.

Such inelastic scattering may also increase the degrader excitation relevant for the analysis of the  $4_1^+$  state lifetime. However, the spectra related to 7026  $\mu\text{m}$  do not reveal a pronounced slow component which makes the first assumption more likely.

A reasonable description of the line shapes were achieved by assuming two decay branches:

- **Target-dominated reactions**

- Initial populations  $N_0(2_1^+) = 72\%$ ,  $N_0(4_1^+) = 18\%$ ,  $N_0(6^+/5^-) = 10\%$
- Level lifetimes  $\tau(2_1^+) = 9.0$  ps,  $\tau(4_1^+) = 2.0$  ps,  $\tau(6_1^+/5_1^-)_{\text{eff}} = 70$  ps
- Relative strength of this reaction: 100 %

- **Degrader-dominated reaction (Coulomb excitation)**

- $N_0(2_1^+) = 100\%$
- $\tau(2_1^+) = 9.0$  ps
- Relative strengths of this reaction: 60 %

For the  $2_1^+$  state a lifetime of 9(3) ps was determined. The quoted error includes uncertainties with respect to the initial populations. This corresponds to a  $B(\text{E}2)$  value of  $391_{-99}^{+187} e^2\text{fm}^4$ , which agrees with previous results of  $B(\text{E}2) = 470_{-110}^{+210} e^2\text{fm}^4$  [Lju10] and  $B(\text{E}2) = 344(33) e^2\text{fm}^4$  [Rot11].

## 5.9. Summary

This section summarizes the experimental results of the present work with respect to new candidates for  $\gamma$ -ray transitions, level lifetimes, transition strengths and mixing ratios.

Isotope	$\gamma$ -Ray Energies (keV)
$^{58}\text{Cr}$	1108(8), 1764(14), 2154(16), 1687(11), 1495(10), 1520(11)
$^{60}\text{Cr}$	1138(8), 1338(9), 1598(8)
$^{62}\text{Cr}$	1019(3)
$^{56}\text{V}$	151.2(11), 219.8(20), 304.4(28), 446.1(32), 529.8(31), 1140(5)

Table 5.21.: Candidates for  $\gamma$ -ray transitions

Isotope	Lifetime $\tau$ (ps)			$B(\text{E}2)$ ( $\text{e}^2\text{fm}^4$ )		
	$2_1^+$	$4_1^+$	$6_1^+$	$2_1^+ \rightarrow 0_{\text{gs}}^+$	$4_1^+ \rightarrow 2_1^+$	$6_1^+ \rightarrow 4_1^+$
$^{58}\text{Cr}$	6.8(8)	2.8(5)	1.0(5)	$226_{-26}^{+30}$	$221_{-33}^{+48}$	$228_{-76}^{+186}$
$^{60}\text{Cr}$	27.0(26)	$5.4_{-0.9}^{+0.7}$	2.2(8)	$274_{-24}^{+29}$	$417_{-59}^{+62}$	$397_{-105}^{+313}$
$^{62}\text{Cr}$	$125_{-10}^{+11}$	$6.9_{-0.8}^{+0.7}$	-	$371_{-30}^{+32}$	$582_{-45}^{+76}$	-

Table 5.22.: Results for chromium isotopes.

Isotope	$\tau(7/2_1^-)$ (ps)	$\tau(9/2_1^-)$ (ps)	$\tau(11/2_1^-)$ (ps)	$B(\text{E}2; 11/2_1^- \rightarrow 7/2_1^-)$ ( $\text{e}^2\text{fm}^4$ )	$ \delta _{\text{E}2/\text{M}1}$
$^{59}\text{Mn}$	$525_{-50}^{+125}$	1.5(7)	2.0(8)	$145_{-50}^{+99}$	-
$^{61}\text{Mn}$	140(15) <sup>†</sup>	$1.5_{-1.5}^{+0.8\dagger}$	3.2(10) <sup>†</sup>	$121_{-50}^{+76}$	0.084(7)
$^{63}\text{Mn}$	17(3) <sup>†</sup>	< 3 <sup>†</sup>	-	-	-

Table 5.23.: Results for manganese isotopes. The associated state has been assigned only tentatively if the corresponding lifetime is marked with <sup>†</sup>.

Isotope	$\tau(2_1^+)$ (ps)	$B(\text{E}2; 2_1^+ \rightarrow 0_{\text{gs}}^+)$ ( $\text{e}^2\text{fm}^4$ )
$^{64}\text{Fe}$	9(3)	$391_{-99}^{+187}$

Table 5.24.: Results for  $^{64}\text{Fe}$ .

Isotope	$\tau(5/2_1^-)$ (ps)	$\tau(11/2_1^-)$ (ps)
$^{55}\text{V}$	60(12)	5(2)

Table 5.25.: Results for  $^{55}\text{V}$ .

---

## 6. Discussion

### 6.1. Qualitative Discussion for Even-Even Nuclei

#### Evolution of Collectivity in Terms of $E(2_1^+)$ and $B(E2; 2_1^+ \rightarrow 0_{gs}^+)$

The evolutions of  $2_1^+$ -state energies as well as of  $B(E2; 2_1^+ \rightarrow 0_{gs}^+)$  values are illustrated in Fig. 6.1 for even-even nuclei with  $20 \leq Z \leq 28$  and  $20 \leq N \leq 46$ , which in particular include the results for  $^{58,60,62}\text{Cr}$  of the present work.

At the neutron shell closure  $N = 28$ , all depicted isotopes are characterized locally by high  $E(2_1^+)$  and corresponding small  $B(E2; 2_1^+ \rightarrow 0_{gs}^+)$  values. At  $N = 32$ , a strikingly different behaviour is observed for the even-even isotones:  $^{52}\text{Ca}$ ,  $^{54}\text{Ti}$  and  $^{56}\text{Cr}$  ( $Z \leq 24$ ) exhibit a local rise in the  $2_1^+$  state energy and small  $B(E2; 2_1^+ \rightarrow 0_{gs}^+)$  values ( $^{54}\text{Ti}$  and  $^{56}\text{Cr}$ ). These signatures suggest a weak and very localized (sub-)shell closure at  $N = 32$  (see, e.g., Ref. [Ste13]) which collapses toward Fe and Ni. From  $^{56}\text{Cr}$  ( $^{58}\text{Fe}$ ) to  $^{58}\text{Cr}$  ( $^{60}\text{Fe}$ ), the  $E(2_1^+)$  values decrease (increase) and the transition probabilities increase (decrease). Of particular interest at this point is the trend toward  $N = 40$ . At  $N = 40$ , only  $^{68}\text{Ni}$  exhibits a local rise in the  $2_1^+$  state energy and a drop in the  $B(E2; 2_1^+ \rightarrow 0_{gs}^+)$  value.

Reducing the number of protons by two and four, the iron and chromium isotopes show signatures of rapidly evolving quadrupole collectivity toward  $N = 40$ , which establishes at  $N = 34$  (Cr) and  $N = 36$  (Fe), respectively. Compared to iron, chromium isotopes exhibit lower  $2_1^+$ -state energies and slightly larger  $B(E2)$  values which indicate a more pronounced onset of collectivity in chromium isotopes. A saturation of collectivity is observed for both iron and chromium around  $N = 38, 40$ . The present experimental data on  $2_1^+$ -state energies does not indicate a continuation of the substantial increase in collectivity beyond  $N = 40$ .

Works of T. Otsuka [Ots01; Ots05; Ots10] propose the monopole component of the proton-neutron tensor force as one of the driving forces behind shell evolution, i.e. the evolution of single particle energies (SPE) as a function of valence particles. This contributes to the nuclear force as a result of the interaction between shells with the same angular momentum  $l$  but different nuclear spin  $j$  due to anti-aligned spins. Its influence on the SPE in the even-even  $N = 40$  isotones (Ni, Cr and Fe) is sketched qualitatively in Fig. 6.2.

At  $N = 40$ , the attraction between the proton  $f_{7/2}$  and the neutron  $f_{5/2}$  orbitals is strongest in  $^{68}\text{Ni}$  compared to  $^{66}\text{Fe}$  and  $^{64}\text{Cr}$  since for  $^{68}\text{Ni}$  the  $\pi f_{7/2}$  orbital is fully occupied. By decreasing the number of protons in the  $\pi f_{7/2}$  orbital by two (iron) and four (chromium), the SPE of the  $\nu f_{5/2}$  orbital is shifted toward higher energies. As a consequence, the  $N = 40$  gap<sup>1</sup> is reduced when protons are removed from  $f_{7/2}$ .

One side effect is a changing order of the  $\nu f_{5/2}$  and  $\nu p_{1/2}$  orbitals. This contributes to

---

<sup>1</sup>Such a shell evolution is explicitly obtained, for instance, with the effective LNPS interaction [Len10].

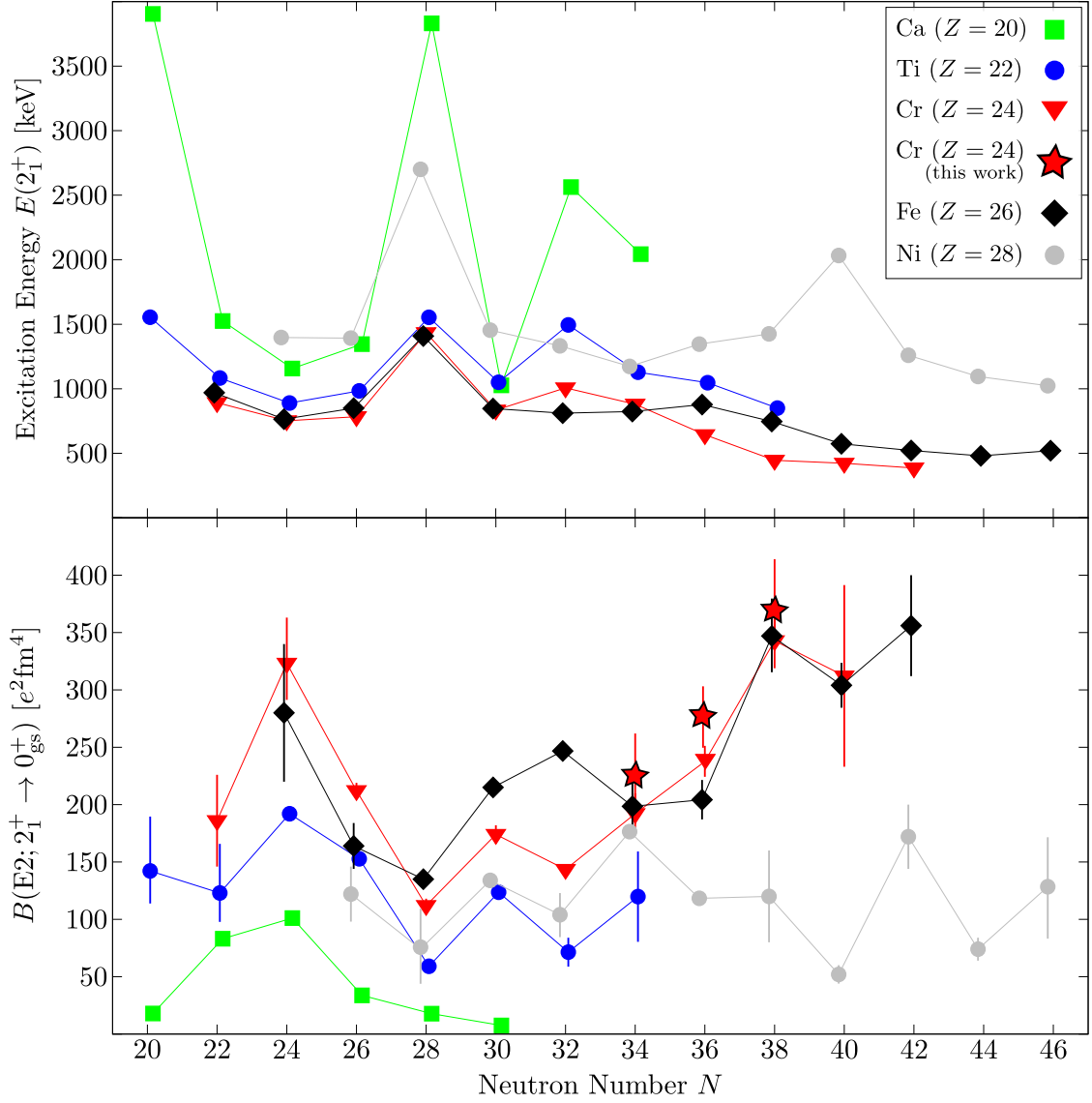


Figure 6.1.: Evolution of  $E(2_1^+)$  and  $B(E2; 2_1^+ \rightarrow 0_{gs}^+)$  values in even-even nuclei with  $20 \leq Z \leq 28$  and  $20 \leq N \leq 46$ . The precise results are tabulated in Appendix D.

the shallow shell gap at  $N = 32$  for which experimental evidence was already found, e.g. in  $^{52}\text{Ca}$  [Ste13].

### Qualitative Discussion of the Nuclear Shape

While  $E(2_1^+)$  values and  $B(E2; 2_1^+ \rightarrow 0_{gs}^+)$  are useful signatures to follow the evolution of quadrupole collectivity, e.g. along an isotopic chain, they do not carry (model-independent) information on the nuclear shape.

The energy ratio  $R_{42} = E(4_1^+)/E(2_1^+)$  as well as the similarly defined transition-strength

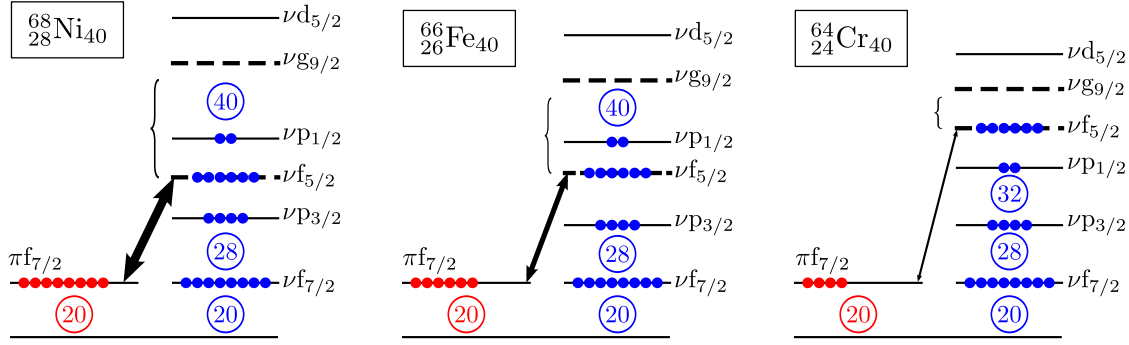


Figure 6.2.: Qualitative influence of the monopole interaction produced by the tensor force on the single-particle energy of the neutron  $f_{5/2}$  orbital in  $N = 40$  isotones  $^{68}\text{Ni}$ ,  $^{66}\text{Fe}$  and  $^{64}\text{Cr}$ .

ratio  $B_{42} = B(E2; 4_1^+ \rightarrow 2_1^+)/B(E2; 2_1^+ \rightarrow 0_{\text{gs}}^+)$  are convenient signatures to classify the nuclear shape related to the collective structures.

A first helpful indication is given by geometric models ( $N \rightarrow \infty$ ), e.g. in terms of the harmonic vibrator ( $R_{42} = B_{42} = 2$ ) and the rigid rotor model [Dav58] ( $R_{42} = 3.33$ ,  $B_{42} = 1.42$ ). An  $R_{42}$  value smaller than two is expected for excited states dominated by single-particle excitation.  $R_{4/2}$  values around 2.5 are typically observed in transitional nuclei. A  $B_{42}$  value greater than one is a general feature shared by all collective models, whereas values close to one are usually observed in nuclei near shell closures in which the seniority is a good quantum number [Res04].

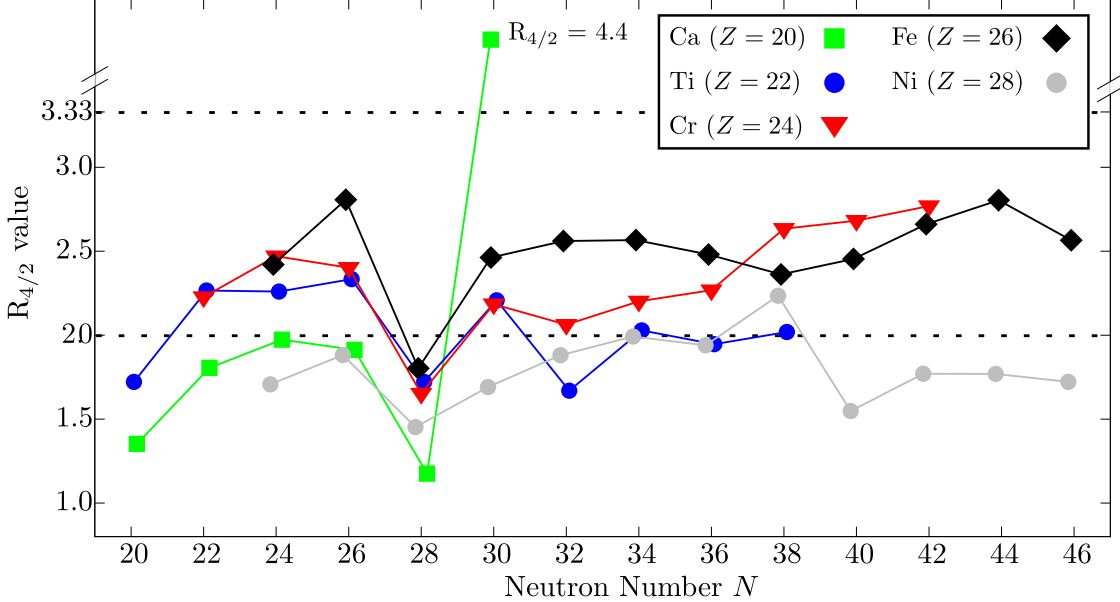


Figure 6.3.: Evolution of  $R_{42}$  ratios in even-even nuclei characterized by  $20 \leq Z \leq 28$  and  $20 \leq N \leq 46$ . The precise values are derived from the tabulated values in Appendix D.

$A\text{Cr}$	$J_1^+$	$ Q_0 (\text{efm}^2)$	$ \beta_2 $
$^{58}\text{Cr}$	$2_1^+$	$106_{-6}^{+9}$	$0.27_{-0.01}^{+0.02}$
	$4_1^+$	$88_{-7}^{+11}$	$0.22_{-0.01}^{+0.03}$
	$6_1^+$	$86_{-15}^{+31}$	$0.22_{-0.04}^{+0.08}$
$^{60}\text{Cr}$	$2_1^+$	$117_{-6}^{+7}$	$0.29_{-0.01}^{+0.02}$
	$4_1^+$	$121_{-8}^{+13}$	$0.30_{-0.02}^{+0.03}$
	$6_1^+$	$112_{-16}^{+28}$	$0.28_{-0.04}^{+0.07}$
$^{62}\text{Cr}$	$2_1^+$	$136_{-7}^{+8}$	$0.33_{-0.01}^{+0.02}$
	$4_1^+$	$143_{-8}^{+12}$	$0.35_{-0.02}^{+0.03}$

Table 6.1.: Absolute intrinsic quadrupole moments  $|Q_0|$  and quadrupole deformation parameters  $\beta_2$  for low-lying yrast states in  $^{58,60,62}\text{Cr}$ .

Fig. 6.3 illustrates the evolution of  $R_{42}$  values. Beginning at  $N = 32$ , the  $R_{42}$  values along the chromium isotopes increase gradually and monotonously toward  $N = 42$ . This indicates a trend from a vibrational ( $R_{42} = 2.18$  in  $^{54}\text{Cr}$ ) to a transitional behaviour in  $^{66}\text{Cr}$  ( $R_{42} = 2.77$ ). In comparison, the  $R_{42}$  values in iron isotopes behave surprisingly stable from  $N = 30$  to  $N = 40$  and propose transitional behaviour. Toward  $N = 44$ , the  $R_{42}$  values increase up to 2.8.

Limited to the present data, the  $B_{42}$  value in  $^{58}\text{Cr}$  is close to 1,  $B_{42} = 0.99_{-0.18}^{+0.24}$ . From  $^{58}\text{Cr}$  to  $^{60}\text{Cr}$ , the  $B_{42}$  value increases to  $B_{42} = 1.52_{-0.25}^{+0.28}$  and remains close to this value for  $^{62}\text{Cr}$  ( $B_{42} = 1.58_{-0.20}^{+0.25}$ ). This proposes rotor-like behaviour of  $^{60,62}\text{Cr}$  which, however, is not reflected within the corresponding transitional-like  $R_{42}$  values.

In the rotational limit, absolute intrinsic quadrupole moments  $|Q_0|$  (Eq. 4.9) and quadrupole deformation parameters  $\beta_2$  (Eq. 4.10) can be deduced from the  $B(\text{E}2)$  values. Although this limit is a crude simplification it offers a rough idea on such qualitative properties. Quantitative results for  $|Q_0|$  and  $\beta_2$  are listed in Table 6.1.

As expected, the calculated  $|Q_0|$  values in  $^{58}\text{Cr}$  indicate that the rigid rotor model is unsuited to describe this nucleus properly. The agreement improves for  $^{60,62}\text{Cr}$ , for which the  $|Q_0|$  values behave rather constant along the yrast line. In addition, the  $\beta_2$  parameters indicate an increasing quadrupole deformation from  $^{58}\text{Cr}$  to  $^{62}\text{Cr}$ . For the latter, a large deformation of  $\beta_2 \sim 0.33$  is suggested.

A proton inelastic scattering experiment was performed by Aoi and colleagues [Aoi09] to determine the deformation lengths  $\delta$  in  $^{60,62}\text{Cr}$ . The deformation length  $\delta$  can be translated into the quadrupole deformation parameter  $\beta_2$  with the following equation:

$$\beta_2 = \delta/R, \quad R = r_0 A^{1/3} \quad (6.1)$$

Assuming  $r_0 = 1.2\text{fm}$ , the deformation lengths measured by Aoi lead to  $\beta_2 = 0.24(3)$  fm ( $^{60}\text{Cr}$ ) and  $\beta_2 = 0.29(3)$  ( $^{62}\text{Cr}$ ). It is worth to mention that both values agree with the present estimates.

## 6.2. The Interacting Boson Approximation

The Interacting Boson Model (IBM) [Iac87] follows an algebraic approach to describe collective properties of atomic nuclei, in particular in the medium and heavy mass region. From a physical point of view, its basic idea is the assumption that valence fermions couple to pairs with  $l = 0$  and  $l = 2$ . The original version (IBM-1) does not distinguish between protons and neutrons, so that excited structures and collective properties are described by the pairwise coupling of  $s$  ( $l = 0$ ) and  $d$  ( $l = 2$ ) bosons.

The IBM has undergone substantial modifications - e.g., proton and neutron fluids are distinguished in the IBM-2, while the IBM-3 allows to describe odd- $A$  nuclei. While these descriptions may be closer to reality, they are accompanied by an increasing degree of freedom. Due to the relatively scarce number of experimental observables in neutron-rich chromium isotopes, the following discussion is therefore restricted<sup>2</sup> to the IBM-1.

### Generators and Dynamical Symmetries

Using  $s$  and  $d$  bosons, the elementary creation and annihilation operators are given by  $d_m^\dagger$ ,  $s^\dagger$ ,  $\tilde{d}_m$  and  $\tilde{s}$  with  $m$  being the magnetic quantum number. The coupling of any of these operators can be expressed by the following operators  $G_{J,M}^{i,j}$ :

$$\begin{aligned} G_{0,0}^{s,s} &= \left[ s^\dagger \times \tilde{s} \right]_0^{(0)} \\ G_{2,M}^{s,d} &= \left[ s^\dagger \times \tilde{d} \right]_M^{(2)} \quad -2 \leq M \leq 2, \Delta M = 1 \\ G_{2,M}^{d,s} &= \left[ d^\dagger \times \tilde{s} \right]_M^{(2)} \quad -2 \leq M \leq 2, \Delta M = 1 \\ G_{J,M}^{d,d} &= \left[ d^\dagger \times \tilde{d} \right]_M^{(J)} \quad J = 0, 1, 2, 3, 4 \text{ and } -J \leq M \leq J, \Delta M = 1 \end{aligned}$$

From a group theoretical point of view it can be shown that these 36 operators are the generators of the unitary algebra  $U(6)$  in Racah's form. Starting from  $U(6)$  one can obtain three sub-algebras whose operators close under the algebras  $O(6)$ ,  $U(5)$  and  $SU(3)$ . These algebras, called *dynamical symmetries*, are associated with the three paradigms of the geometric model, e.g. the harmonic vibrator ( $U(5)$ ), the symmetric rotor ( $SU(3)$ ) and the  $\gamma$ -soft rotor ( $O(6)$ ). Realistic nuclei can be depicted in the so called *Casten symmetry triangle* whose vertices are the dynamical symmetries, see Fig. 6.4.

#### 6.2.1. Choice of the IBM-1 Hamiltonian

With respect to the neutron-rich chromium isotopes one is confronted with nuclei for which experimental information is quite sparse. Here, the focus is set on a qualitative description within the IBM framework. As a consequence of the sparse experimental data, a limitation of the degrees of freedom is necessary. However, it must be ensured that this truncation does not lead to a substantial simplification of the solution space.

<sup>2</sup>In Ref. [Kot14], the authors performed systematic IBM-2 calculations for neutron-rich even-even chromium and iron isotopes ( $30 \leq N \leq 40$ ) using the Talmi Hamiltonian.

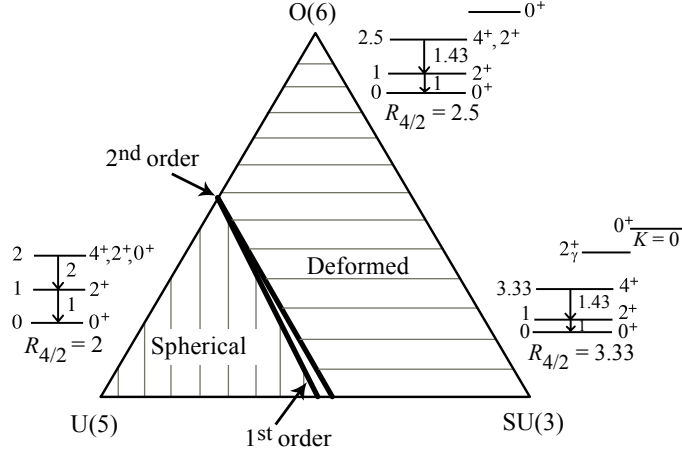


Figure 6.4.: Casten triangle, taken with permission from Ref. [Cas07].

According to [Iac87], any nuclei on the transition line from U(5) to SU(3) can be expressed as a multipole expansion by the following Hamiltonian:

$$H_{U(5) \leftrightarrow SU(3)} = \alpha_0 \hat{n}_d + \alpha_1 \hat{L} \cdot \hat{L} + \alpha_2 \hat{Q} \cdot \hat{Q}$$

Similarly, transitional nuclei along the U(5) to O(6) and SU(3) to O(6) line can be described using the Hamiltonians:

$$\begin{aligned} H_{U(5) \leftrightarrow O(6)} &= \beta_0 \hat{n}_d + \hat{P}^\dagger \cdot \hat{P} + \beta_1 \hat{L} \cdot \hat{L} + \beta_2 \hat{U} \cdot \hat{U} \\ H_{SU(3) \leftrightarrow O(6)} &= \gamma_0 \hat{P}^\dagger \cdot \hat{P} + \gamma_1 \hat{L} \cdot \hat{L} + \gamma_2 \hat{U} \cdot \hat{U} + \gamma_3 \hat{V} \cdot \hat{V} \end{aligned}$$

In detail, the appearing multipole operators are given in terms of the  $s, d$  boson operators as follows [Iac87]:

$$\begin{aligned} \hat{n}_d &= (d^\dagger \cdot \tilde{d}) \\ \hat{P} &= \frac{1}{2}(\tilde{d} \cdot \tilde{d}) - \frac{1}{2}(\tilde{s} \cdot \tilde{s}) \\ \hat{L}_{(m)} &= \sqrt{10} \left[ d^\dagger \times \tilde{d} \right]_{(m)}^{(1)} \\ \hat{Q}_{(m)} &= \left[ d^\dagger \times \tilde{s} + s^\dagger \times \tilde{d} \right]_{(m)}^{(2)} - \frac{1}{2} \sqrt{7} \left[ d^\dagger \times \tilde{d} \right]_{(m)}^{(2)} \\ \hat{U}_{(m)} &= \left[ d^\dagger \times \tilde{d} \right]_{(m)}^{(3)} \\ \hat{V}_{(m)} &= \left[ d^\dagger \times \tilde{d} \right]_{(m)}^{(4)} \end{aligned}$$

To cover the complete configuration space all contributions, including hexadecapole term, have to be taken into account, leading to the following Hamiltonian:

$$H = c_1 \hat{n}_d + c_2 \hat{P}^\dagger \cdot \hat{P} + c_3 \hat{L} \cdot \hat{L} + c_4 \hat{Q} \cdot \hat{Q} + c_5 \hat{U} \cdot \hat{U} + c_6 \hat{V} \cdot \hat{V} \quad (6.2)$$

In the consistent  $Q$ -formalism [War82], a modified version of the quadrupole operator,

$$\hat{Q}^x = \left[ d^\dagger \times \tilde{s} + s^\dagger \times \tilde{d} \right]^{(2)} + \chi \left[ d^\dagger \times \tilde{d} \right]^{(2)} \quad (6.3)$$

is used in the Hamiltonian as well as in the quadrupole transition operator,  $\hat{T}(E2) = e_b \hat{Q}^x$ . As a consequence, the monopole term can be expressed by one of the other multipole operators. The parameters  $c_5, c_6$  for the octupole and hexadecapole term are usually quite small and hence, affect the result only marginally. Therefore the Hamiltonian (Eq. 6.2) reduces to:

$$\hat{H} = \epsilon \hat{n}_d + \lambda \hat{L} \cdot \hat{L} + \kappa \hat{Q}^x \cdot \hat{Q}^x \quad (6.4)$$

To visualize the geometric shape, the potential energy surface (PES) is plotted in the  $(\beta, \gamma)$  plane. The potential  $V(\beta, \gamma)$  is deduced by calculating the expectation value of the Hamiltonian in the coherent state [Die80; Gin80]. It is given quantitatively by the following expression:

$$V(\beta, \gamma) = \frac{1}{1 + \beta^2} (\epsilon N \beta^2 + 6N \lambda \beta^2 + \kappa N (5 + (1 + \chi^2) \beta^2)) + \frac{\kappa N}{(1 + \beta^2)^2} \left( \frac{(N - 1) \left( \frac{2\chi^2 \beta^4}{7} - 4\sqrt{\frac{2}{7}} \beta^3 \cos(3\gamma) + 4\beta^2 \right)}{(1 + \beta^2)^2} \right) \quad (6.5)$$

### 6.2.2. IBM-1 Calculations for Neutron-Rich Cr Isotopes

IBM-1 calculations for  $^{56,58,60,62}\text{Cr}$  were performed with the code ARBMODEL [Hei08].  $^{48}\text{Ca}$  was used as a boson vacuum in all cases. A fixed boson charge of 0.058 eb was used to calculate  $B(E2)$  values.

Parameters  $\epsilon, \lambda, \kappa$  and  $\chi$  were determined for each isotope by means of a  $\chi^2$  minimization between available experimental data (shown in Fig. 6.5) and calculated IBM-1 signatures. Here, in addition to the experimental errors, also uncertainties due to the simplified model are taken into account. The latter are quantified by  $\Delta E/E = 0.5, 1.0\%$  for level energies (yrast, non-yrast) and  $\Delta B(E2) = 20 e^2 \text{fm}^4$  for reduced transition strengths.

The parameters leading to the best fits are listed in Table 6.2, the resulting level schemes are compared to the available experimental data in Fig. 6.5.

The large  $\chi^2$  for  $^{56}\text{Cr}$  can be traced back to the reproduction of the level energies. Still,

Nucleus	$N_b$	$\epsilon$	$\lambda$	$\kappa$	$\chi$	$e_b$	$\chi^2$
$^{56}\text{Cr}$	4	0.805	0.022	0.022	-1.05	0.058	63
$^{58}\text{Cr}$	5	0.900	0.013	-0.023	-0.71	0.058	5.2
$^{60}\text{Cr}$	6	0.670	0.012	-0.014	-0.68	0.058	18.2
$^{62}\text{Cr}$	7	0.520	0.021	-0.024	-0.69	0.058	1.3

Table 6.2.: List of boson numbers  $N_b$ , best-fitting IBM-1 parameters  $\epsilon, \lambda, \kappa, \chi$  (in MeV), the boson charge (in eb) and the corresponding reduced  $\chi^2$  values.

the overall agreement for  $^{56}\text{Cr}$  is rather good.

For  $^{58}\text{Cr}$ , the level energies are reproduced with very good accuracy. Discrepancies occur with respect to the  $B(E2)$  values, in particular with respect to the  $B_{42}$  ratio. This discrepancy is not surprising: The experimental  $B_{42}$  value indicates non-collective behaviour, which is not reflected in the level scheme. However, due to their large experimental errors, their effects on the  $\chi^2$  value are rather small.

In  $^{60}\text{Cr}$ , a very good agreement between experimental and calculated level energies as

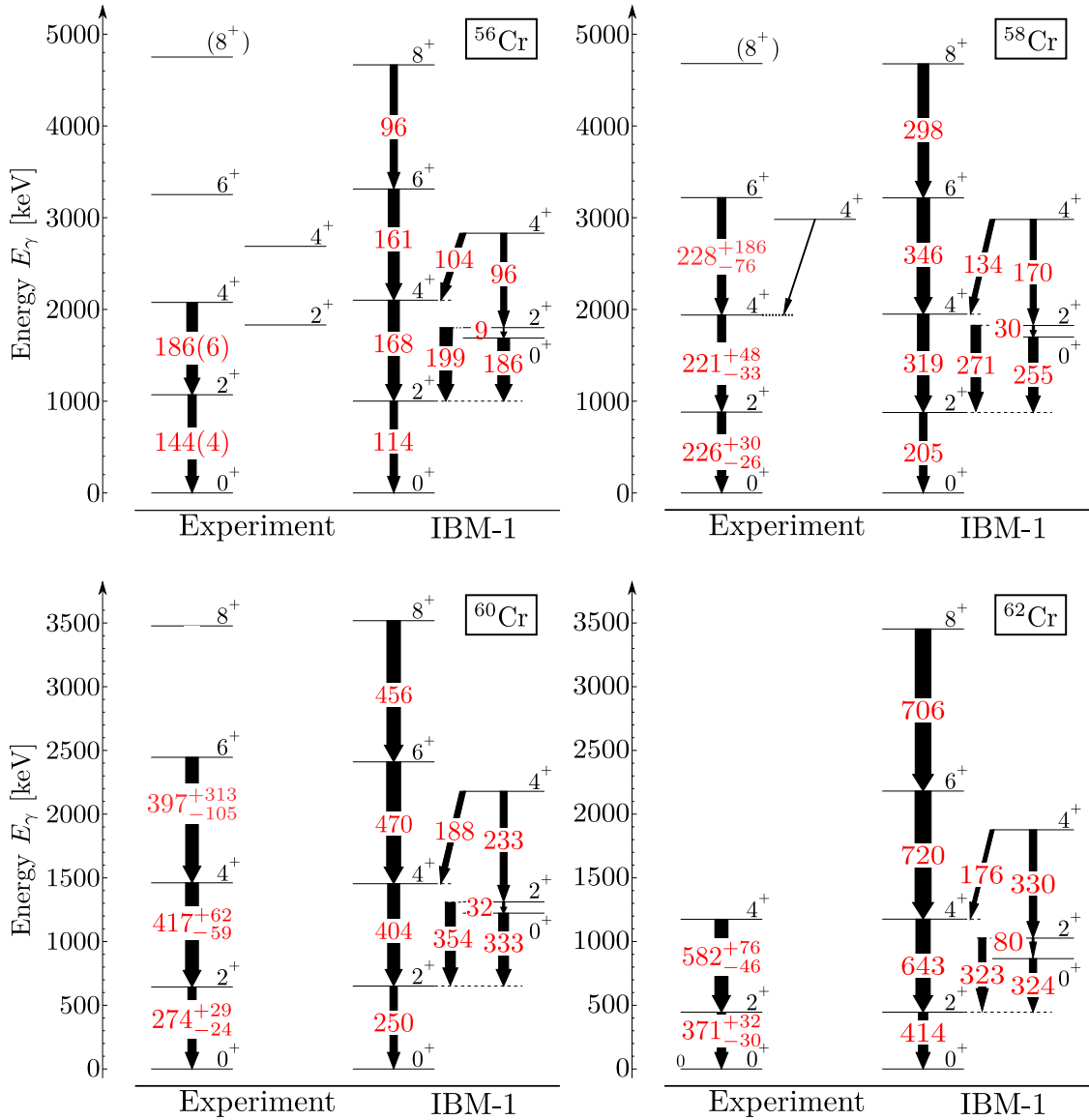


Figure 6.5.: Comparison of experimental level scheme and best-fitting IBM-1 calculations for  $^{56,58,60,62}\text{Cr}$ .  $B(E2)$  values (in  $e^2\text{fm}^4$ ) are written in red. See text for details.

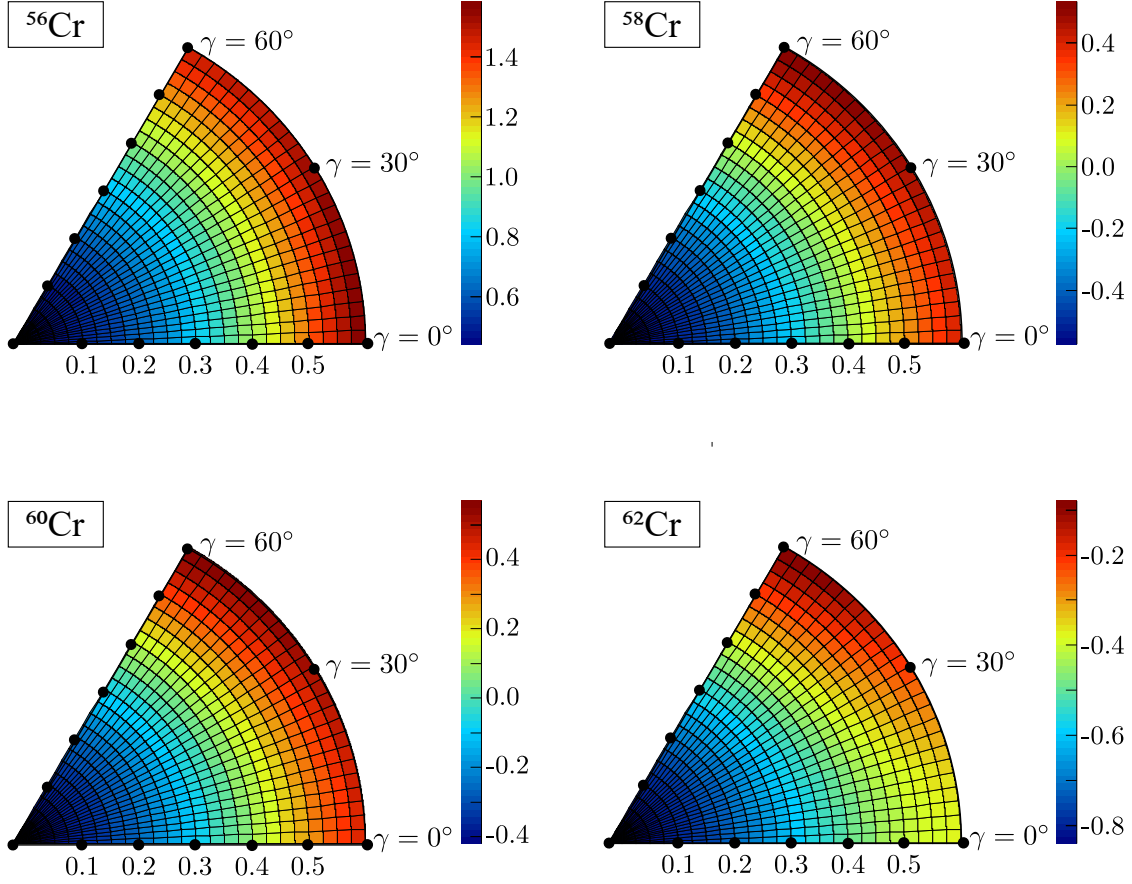


Figure 6.6.: Potential energy surfaces for even  $^{56-62}\text{Cr}$  isotopes according to Eq. 6.5 using parameters listed in Table 6.2.

well as  $B(E2)$  values is achieved. All available experimental values are reproduced by the IBM-1 calculations.

In  $^{62}\text{Cr}$ , only few experimental observables are known which are comparably easy to fit. It is interesting to note that calculations predict for the  $6^+ \rightarrow 4^+$  transition an energy of 1005 keV which is close to the candidate observed in the lifetime analysis (1019 keV, see Sec. 5.4). The increase in collectivity observed in  $B(E2)$  values is overestimated by the IBM-1 fit. In this case, the agreement can be improved by using a smaller boson charge.

The corresponding potential energy surfaces of  $^{56,58,60,62}\text{Cr}$  are depicted in Fig. 6.6. The enhanced quadrupole deformation toward  $^{62}\text{Cr}$  ( $\beta \approx 0.3$ ) is not reflected in the IBM-1 calculations. The minimum of the potential energy surface of  $^{56,58,60}\text{Cr}$  is spherical, evolving towards some deformation in  $\beta$  for  $^{62}\text{Cr}$ . For the latter, the minimum is still spherical but it is quite shallow. With respect to the evaluated parameters, the missing deformation can be readily explained by the large  $\epsilon$  parameter which is associated with spherical structures.

### 6.2.3. Comparison of $^{58,60,62}\text{Cr}$ with the Critical Point Symmetry E(5)

F. Iachello introduced the analytical E(5) limit [Iac00] by solving the Bohr Hamiltonian [Boh52] for a flat potential that depends only on  $\beta$ . Purpose of this limit is to describe nuclei at the critical point of a (second order) phase transition from U(5) (harmonic vibrator) to O(6) ( $\gamma$ -soft rotor).

The corresponding Hamiltonian is analytically solvable and it was shown [Iac00] that excited levels within this limit can be described in terms of quantum numbers  $\xi$  and  $\tau$ . Here,  $\xi$  labels major families while  $\tau$  denotes phonon-like structures within one family. A schematic spectrum for this limit is illustrated in Fig. 6.7.

Characteristic signatures of the E(5) limit are given in terms of energy ratios (e.g.  $R_{42} = E(4^+)/E(2^+) = 2.20$  and  $R_{62} = E(6^+)/E(2^+) = 3.59$ ), transition-rate ratios (e.g.  $B_{42} = \frac{B(E2; 4_1^+ \rightarrow 2_1^+)}{B(E2; 2_1^+ \rightarrow 0_{gs}^+)} = 1.68$  and  $B_{62} = \frac{B(E2; 6_1^+ \rightarrow 4_1^+)}{B(E2; 2_1^+ \rightarrow 0_{gs}^+)} = 2.21$ ), branching ratios and statements on forbidden transitions.

Casten and Zamfir proposed  $^{134}\text{Ba}$  as a candidate for the E(5) limit [Cas00], with strongest evidence coming from energy ratios as well as characteristic  $B(E2)$  ratios from excited  $0^+$  states. Only recently, new experimental signatures in  $^{140}\text{Sm}$  were determined (e.g. the  $B_{42}$  ratio) and a reasonable agreement with E(5) was found [Kli16].

In 2006, Märginean and colleagues observed that the low-lying level energies are in reasonable agreement with the E(5) limit. It has to be stressed, that only few light-mass E(5) candidates were identified so far.

The E(5) limit corresponds to the infinite boson limit. In addition to the fact that E(5) is an extreme simplification, in a finite system, such as the atomic nucleus, structural

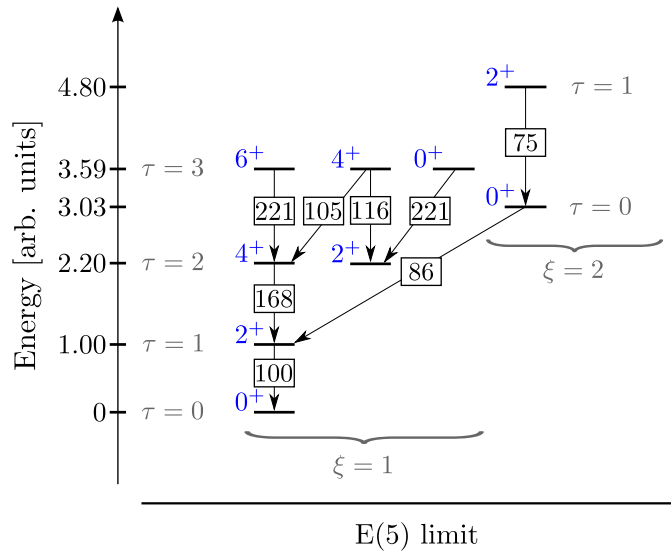


Figure 6.7.: Schematic representation of the low-lying level scheme of the E(5) spectrum showing only states with even nuclear spin. The level energies are normalized to  $E(2_1^+) = 1$ , while reduced transition strengths are normalized to  $B(E2; 2_1^+ \rightarrow 0_{gs}^+) = 100$ . This figure is reproduced from Ref. [Iac00].

Sig.	E(5)	<sup>58</sup> Cr		<sup>60</sup> Cr		<sup>62</sup> Cr	
		Exp	E(5) <sup>IBM</sup>	Exp	E(5) <sup>IBM</sup>	Exp	E(5) <sup>IBM</sup>
$R_{42}$	2.20	2.20	2.20	2.27	2.19	2.64	2.18
$R_{62}$	3.59	3.66	3.55	3.89	3.53	-	3.50
$B_{42}$	1.68	$0.98^{+0.24}_{-0.18}$	1.38	$1.52^{+0.28}_{-0.25}$	1.44	$1.58^{+0.25}_{-0.20}$	1.48
$B_{62}$	2.21	$1.0^{+0.76}_{-0.34}$	1.40	$1.45^{+0.76}_{-0.40}$	1.56	-	1.68

Table 6.3.: Comparison of experimental signatures with the E(5) limit and an IBM-1 representation of the E(5) limit, labelled E(5)<sup>IBM</sup>. See text for details.

changes can only occur in discrete steps. As a consequence, it has to be expected that the transitional character in real nuclei is muted and that the finite nucleon number affects the expected E(5) signatures. Within the IBM-1 framework, the Hamiltonian  $H = \epsilon n_d + AP^\dagger \cdot P$  can be applied to study the shape-phase transition from U(5) to O(6) [Cas00]. Here the critical point corresponds to a specific ratio of the coefficients given by

$$\epsilon/A = 2(N_B - 1)$$

This choice can be considered as the IBM-1 representation of E(5) (labelled E(5)<sup>IBM</sup>) which incorporates finite boson-number effects.

The experimental signatures in <sup>56,58,60</sup>Cr are now compared to the E(5) and E(5)<sup>IBM</sup> predictions in Table 6.3. It is worth to note that the signatures of E(5)<sup>IBM</sup> and E(5) are quite similar with respect to the energy ratios. However, the finite boson number affects the  $B_{42}$  and  $B_{62}$  considerably and leads to smaller of  $B_{42}$  and  $B_{62}$  values in E(5)<sup>IBM</sup> compared to E(5).

For <sup>58</sup>Cr, the experimental  $B_{42}$  ratio disagrees with the E(5) limit as well as with the E(5)<sup>IBM</sup> representation. The experimental  $B_{62}$  ratio agrees only with E(5)<sup>IBM</sup>. For both representations the energy ratios are in good agreement with the experimental values in <sup>58</sup>Cr.

For <sup>60</sup>Cr, experimental  $B_{42}$  and  $B_{62}$  ratios agree with the E(5) limit as well as the IBM-1 representation of E(5). With respect to the energy ratios, the agreement is still reasonable, although slightly worse compared to <sup>58</sup>Cr.

For <sup>62</sup>Cr, the experimental  $B_{42}$  value is in good agreement with E(5) and E(5)<sup>IBM</sup>. However, the experimental  $R_{42}$  value exceeds the predicted value of E(5) considerably.

In summary, the best overall agreement is found for <sup>60</sup>Cr. For <sup>58</sup>Cr, the energy ratios are in very good agreement but its interpretation as an E(5) candidate is not supported by the experimental  $B_{42}$  and  $B_{62}$  ratios of the present work.

It must be stressed that the experimental data is too sparse for a solid assignment. To shed a better light on the proposed E(5) nature of <sup>58,60</sup>Cr, information on excited structures in side bands (in particular with respect to excited 0<sup>+</sup> states) as well as intra-band transition strengths are strongly needed to achieve a better understanding of the transitional nature of neutron-rich rich chromium isotopes.

### 6.3. Shell Model Framework

The neutron-rich  $N = 40$  region is known for rapid shell evolution which challenges consistent theoretical descriptions. Hence, it offers benchmark tests for modern and established interactions.

Beyond  $N \approx 36$ , well-established interactions of the  $fp$  space, such as KB3G [Pov01] and GXFP1a [Hon02; Hon05], are incapable to reproduce the experimentally observed rapid increase in quadrupole collectivity along the iron and chromium isotopes as referred from  $E(2_1^+)$  and  $B(E2)$  values, see e.g. Refs. [Aoi09; Lju10].

The lacking compatibility of these interactions to describe the neutron-rich Cr and Fe isotopes proposes that the enhancement of collectivity is triggered rather by neutron than by proton excitations. Indeed, studies in the neutron-rich even-even Fe [Lun07; Rot11] and Cr isotopes [Bau12] showed that the inclusion of the neutron  $0g_{9/2}$ ,  $1d_{5/2}$  orbitals to the valence space is crucial to reproduce the enhanced collectivity. The role of the neutron  $1d_{5/2}$  orbital in this development was discussed in Ref. [Cau02] and has been understood in terms of the quasi-SU(3) space [Zuk94] spanned by the quadrupole partners  $g_{9/2}$  and  $d_{5/2}$ .

In 2010, Lenzi and colleagues introduced the semi-empirical interaction LNPS [Len10]. Its capability to reproduce experimental observables in the vicinity of  $N = 40$  has been shown in various works, see Refs. [Cra13; Gad14; Lou13; Rec12; Rec13]. Its predictive power will be tested in this chapter with respect to the neutron-rich chromium isotopes. Only recently, modifications were applied to the LNPS interaction [San15], which affected the monopole as well as pairing parts of the effective Hamiltonian and which led to a slightly enhanced  $gd-gd$  monopole strength. The modified interaction, called LNPS- $m$ , improves the agreement with experimental data, in particular for neutron-rich isotopes [San15]. The results for  $^{59,61,63}\text{Mn}$  will be compared in Sec. 6.3.2 to shell-model calculations using the established  $fp$  interaction KB3G as well as the modified LNPS- $m$  interaction.

Calculations with the KB3G interaction were performed by the author of the present thesis at the University of Cologne using the shell-model code NUSHELLX@MSU [Bro14]. Large-scale shell-model results using the LNPS interaction were provided by S.M. Lenzi [Len15; Len17] and were executed using the code ANTOINE [Cau99].

#### 6.3.1. Comparison of $^{58,60,62}\text{Cr}$ with the LNPS Interaction

LNPS calculations were performed in an extended valence space, which covers the full  $pf$  shell (protons) as well as the  $f_{5/2}pg_{9/2}d_{5/2}$  orbitals (neutrons). Modified effective charges ( $e_\pi = 1.31 e$ ,  $e_\nu = 0.46 e$ ) as derived in Ref. [Duf96] were used to calculate  $B(E2)$  values. Fig. 6.8 illustrates a comparison between LNPS calculations and experimental results for the lowest yrast structures. Precise results of the shell-model calculations can be found in Appendix E.1.

In  $^{58}\text{Cr}$ , the LNPS interaction reproduces the energy of the first  $2_1^+$  state almost perfectly. Compared to the experimental value, the LNPS interaction predicts the  $4_1^+$  and  $6_1^+$  states to be  $\sim 200$  keV lower in energy. Hence, the shell-model  $R_{42}$  value is close to the vibrational limit. LNPS underestimates the present  $B(E2; 2_1^+ \rightarrow 0_{gs}^+)$  value in  $^{58}\text{Cr}$  by almost 20 %. The experimental  $B(E2; 4_1^+ \rightarrow 2_1^+)$  value as well as the  $B(E2; 6_1^+ \rightarrow 4_1^+)$

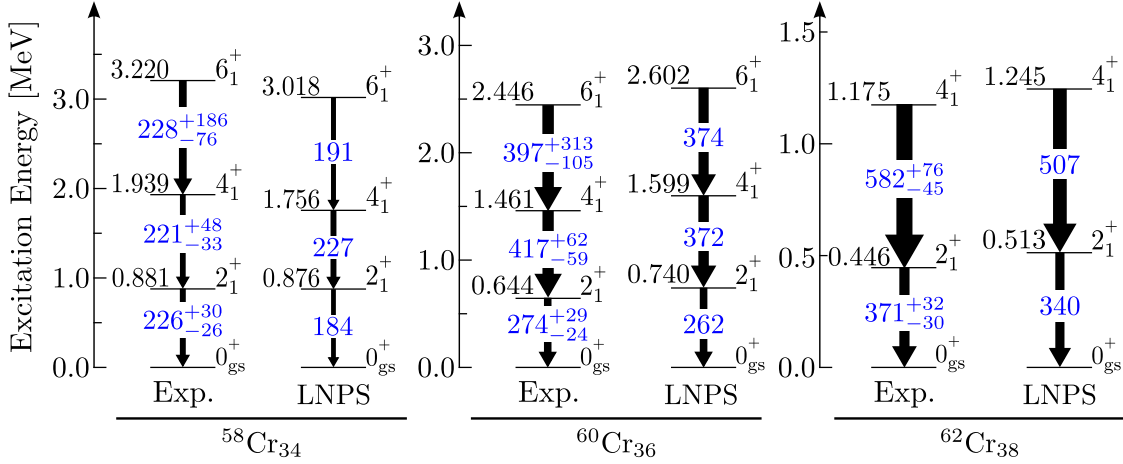


Figure 6.8.: Comparison of level energies (in MeV) and  $B(E2)$  values (blue, in  $e^2\text{fm}^4$ ) for even  $^{58-62}\text{Cr}$  isotopes with shell-model calculations using the interaction LNPS [Len10].

value are reproduced by the LNPS interaction.

Compared to  $^{58}\text{Cr}$ , experimental data of  $^{60}\text{Cr}$  reveal an enhancement of collective behavior which is reflected in decreasing level energies and increasing  $B(E2)$  values. All present experimental  $B(E2)$  values are reproduced by the LNPS calculation, although the increase of the experimental  $B(E2)$  values is slightly larger. The agreement with respect to the level energies in  $^{60}\text{Cr}$  is good, the LNPS interaction overestimates the given experimental level energies by  $\sim 100 - 150$  keV.

In  $^{62}\text{Cr}$ , the experimental  $B(E2)$  values exceed the LNPS predictions by  $\sim 10\%$ . Similar to  $^{60}\text{Cr}$ , the LNPS interaction overestimates the level energy slightly, but the agreement is still reasonable.

### Structural Predictions by LNPS

LNPS calculations predict rotor-like behaviour with large deformation parameters  $\beta \sim 0.3 - 0.35$  for the neutron-rich chromium isotopes ( $N \geq 38$ ), which agrees with the present results listed in Table 6.1.

The LNPS interactions forecasts the emergence of an island of inversion around  $^{64}\text{Cr}$  [Len10]. Toward  $^{64}\text{Cr}$ , the LNPS interaction concludes that multi-particle multi-hole configurations become dominant already in the ground-state configuration. For  $^{64}\text{Cr}$ , it is expected that  $4p - 4h$  excitations across the  $N = 40$  gap contribute to the ground state configuration by almost 75% [Len10].

To follow the evolution along the  $^{58,60,62}\text{Cr}$  isotopes, the mean orbital occupation numbers as calculated by the LNPS calculation are a helpful quantity, see Fig. 6.9.

In  $^{58}\text{Cr}$ , less than 0.4(0.1) neutrons on average occupy the  $g_{9/2}(d_{5/2})$  orbital in the ground state. Here, these numbers decrease with increasing spin.

From  $^{58}\text{Cr}$  to  $^{60}\text{Cr}$ , the mean occupation of the  $g_{9/2}$  orbital more than triples (1.5 neutrons), while the occupation of the  $d_{5/2}$  becomes sizeable (0.3). In contrast to  $^{58}\text{Cr}$ , these

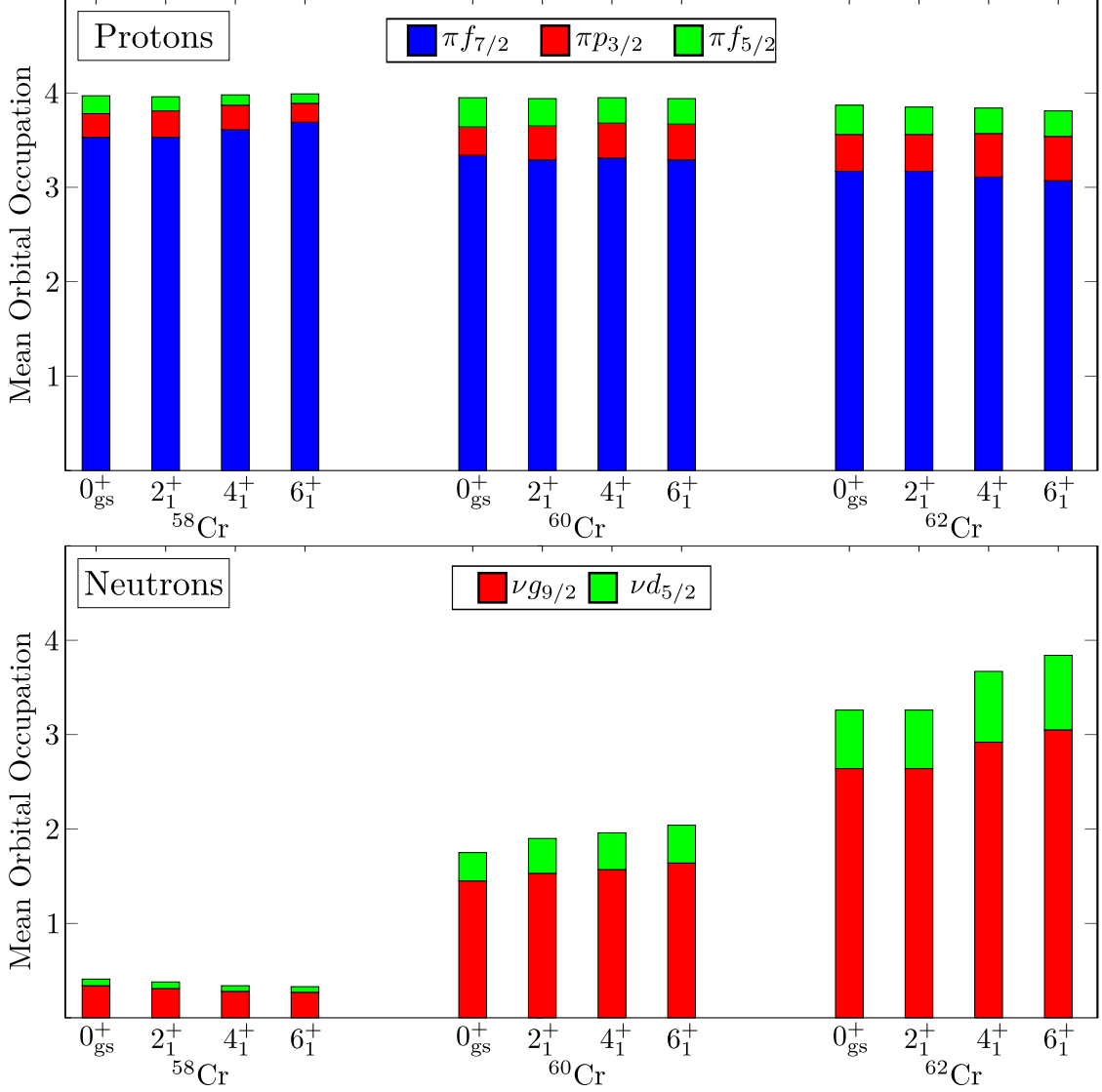


Figure 6.9.: Orbital occupation numbers for excitations across  $Z = 28$  (*top*) and  $N = 40$  (*bottom*) for yrast states in  $^{58,60,62}\text{Cr}$ . See Appendix E.1 for precise values.

occupation numbers show a weak increase with increasing spin.

In  $^{62}\text{Cr}$ , more than three neutrons on average are excited across the  $N = 40$  gap (2.6 in  $g_{9/2}$  and 0.6 in  $d_{5/2}$ , respectively). Comparable to  $^{60}\text{Cr}$ , the occupation numbers rise with increasing spin.

Although the occupation of  $d_{5/2}$  appears marginal, calculations highlight that its contribution to the increasing quadrupole collectivity is sizeable.

In comparison to the neutron occupation numbers, the mean proton occupation numbers behave rather stable. However, it is evident that the mean occupation number related to the  $f_{7/2}$  orbital is significantly less than four: On average, 0.5 protons are excited into the  $p_{3/2}$  and  $f_{5/2}$  orbitals for  $^{58}\text{Cr}$ . Toward  $^{62}\text{Cr}$ , this number increases to 0.8 protons.

In conclusion, the LNPS interaction is able to describe the enhancement of collectivity toward  $N = 40$  as observed in the chromium isotopes in qualitative and quantitative terms. Still, the experimental  $B(E2)$  values indicate a trend toward a more collective behavior compared to the LNPS interactions. This is also reflected in experimental level energies which in  $^{60,62}\text{Cr}$  are overestimated by the LNPS calculations.

As already mentioned, a modified version of the LNPS interaction (LNPS- $m$ ) was introduced in Ref. [San15]. Unfortunately, no systematic LNPS- $m$  calculations are available for  $^{58,60,62}\text{Cr}$ , although few calculated values for  $^{62}\text{Cr}$  are quoted in Ref. [San15]. With respect to the level energies of the  $2_1^+$  and  $4_1^+$  states in  $^{62}\text{Cr}$ , the LNPS- $m$  calculations (430 and 1130 keV) improve the agreement with experimental values (446.1(9) and 1175.1(68) keV).

In addition, the present experimental  $B(E2)$  values are reproduced almost perfectly: LNPS- $m$  predicts  $B(E2; 2_1^+ \rightarrow 0_{\text{gs}}^+) = 378 e^2\text{fm}^4$  and  $B(E2; 4_1^+ \rightarrow 2_1^+) = 562 e^2\text{fm}^4$  which agree nicely with the present experimental values of  $371_{-30}^{+32} e^2\text{fm}^4$  and  $582_{-46}^{+76} e^2\text{fm}^4$ .

### 6.3.2. Comparison of $^{59,61,63}\text{Mn}$ with the KB3G and LNPS- $m$ Interactions

Recently, a laser spectroscopy experiment performed on odd-mass  $^{55-63}\text{Mn}$  revealed information on charge radii [Hey16], spins and magnetic moments [Bab15] as well as quadrupole moments [Bab16]. The authors discussed their results in the shell-model framework which can be summarized as follows:

- The established  $fp$  interaction GXFP1a reproduces the experimental data up to  $N = 34$ .
- Good agreement was achieved with shell-model calculations using the LNPS [Len10] interaction as well as with Monte Carlo shell-model (MCSM) calculations using the modified A3DA interaction [Shi12; Tsu14]. Both interactions benefit from an extended valence space that allows neutron scattering into the  $g_{9/2}$  and  $d_{5/2}$  orbitals.
- MCSM calculations predict an evolution from a spherical shape ( $N = 28$ ) toward a well deformed prolate shape maximized at  $N = 40$ . Here, the prolate minimum of the potential energy surface shows triaxial contributions and considerable shape fluctuations.

This section discusses the experimental signatures in  $^{59,61,63}\text{Mn}$  within the shell-model framework. For the latter, calculations were performed with the  $fp$ -shell interaction KB3G [Pov01] and the state-of-the-art interaction LNPS- $m$  [Len17].

For both interactions, modified effective charges  $e_\pi = 1.31e$  and  $e_\nu = 0.46e$  [Duf96] were used to calculate  $B(E2)$  values. Using such effective charges, the spectroscopic quadrupole moments [Bab16] are described quite nicely by both LNPS and LNPS- $m$  interactions (see Fig. 6.10), although the agreement improves slightly for the latter.

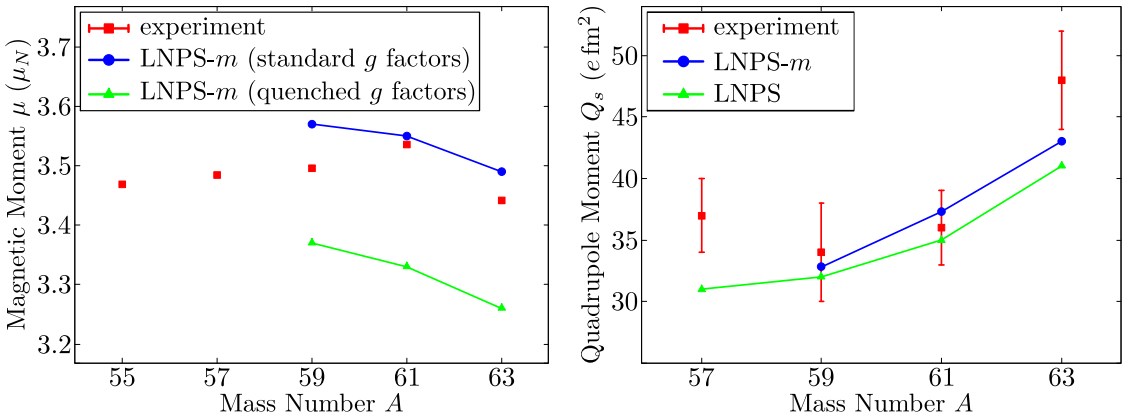


Figure 6.10.: *Left Figure:* Experimental and shell-model calculated magnetic moments  $\mu$  for the ground states in neutron-rich Mn isotopes. *Right Figure:* Experimental and shell-model calculated spectroscopic quadrupole moments  $Q_s$  for the ground states in neutron-rich Mn isotopes. See text for details.

$B(M1)$  values and magnetic moments  $\mu$  were calculated for two sets of  $g$  factors using the LNPS- $m$  interaction:

- Free  $g$  factors:  $g_p^s = 5.586$ ,  $g_n^s = -3.826$ ,  $g_p^l = 1.0$  and  $g_n^l = 0.0$
- Effective  $g$  factors:  $g_p^s = 4.189$ ,  $g_n^s = -2.869$ ,  $g_p^l = 1.1$  and  $g_n^l = -0.1$

Calculated magnetic moments  $\mu$  using the LNPS- $m$  interactions are compared to experimental values for both sets of  $g$  factors in Fig. 6.10. As can be seen, quenched effective  $g$  factors underestimate the experimental magnetic moments  $\mu$  of the ground states in neutron-rich Mn isotopes. A better agreement is found for free  $g$  factors. Hence, magnetic transition strengths are calculated using free  $g$  factors.

Figs. 6.11, 6.12 and 6.13 illustrate the comparison of experimental with shell-model calculated spectra for  $^{59,61,63}\text{Mn}$ . Precise values are listed in Appendix E.2.

### General Remarks

Within the present work, level lifetimes in  $^{59,61,63}\text{Mn}$  were determined for (candidates of) the  $7/2_1^-$ ,  $9/2_1^-$  states and – in case of  $^{59,61}\text{Mn}$  – the  $11/2_1^-$  states. The level lifetimes of the  $7/2_1^-$  and  $9/2_1^-$  states were analysed based on decay transitions with  $\Delta I = 1$ , which in the present case are expected to have mixed E2/M1 character. The corresponding mixing ratios  $\delta_{E2/M1}$  were unknown prior to this work. No transition strengths could therefore be evaluated for such transitions and, hence, the discussion is to some extent limited to the comparison of level lifetimes. For this purpose, the shell-model level lifetimes were recalculated using the experimental transition energies to remove the effect of shell-model energies. Such a recalculation affects level lifetimes, mixing ratios as well as branching ratios. Two cases can be distinguished:

- **Single decay branch with mixed E1/M2 character**

The mixing ratio is recalculated using the experimental transition energy according to Eq. 4.7 while the lifetime is re-evaluated using Eq. 4.8.

- **M1/E2 transition in competition with a pure E2 transition**

First, the mixing ratio is recalculated to the given experimental  $\Delta I = 1$   $\gamma$ -ray energy according to Eq. 4.7.

Second, the branching ratio is recalculated in terms of  $\lambda = I_\gamma(I \rightarrow I - 2)/I_\gamma(I \rightarrow I - 1)$ , which depends on the transition energy, the transition strength as well as the mixing ratio [Byr92] according to:

$$\lambda = 0.6967 \cdot \frac{B(E2; \Delta I = 2)[e^2b^2]}{B(M1; \Delta I = 1)[\mu_N^2]} \cdot \frac{E_\gamma^5(I \rightarrow I - 2)}{E_\gamma^3(I \rightarrow I - 1)} \cdot \frac{1}{1 + \delta^2} \quad (6.6)$$

The level lifetime is then recalculated using Eq. 4.8.

If lifetimes are compared to shell-model calculations in the following, such recalculated values are quoted.

### Comparison of $^{59}\text{Mn}$ to Shell-Model Calculations

Calculated level energies using the LNPS- $m$  interaction are in pleasant agreement with experimental values, although the calculated level structure appears mildly expanded. The KB3G interaction reproduces the level energies of the  $7/2_1^-$  and  $11/2_1^-$  with good precision, but the ordering of the  $9/2_1^-$  and  $11/2_1^-$  states is permuted. Both interactions predict that both  $9/2_1^-$  and  $11/2_1^-$  states decay predominantly into the  $7/2_1^-$  state, which is in good agreement with the given experimental branching ratios.

From the present experimental lifetime, the  $B(E2; 11/2_1^- \rightarrow 7/2_1^-)$  value is given by  $145_{-50}^{+94} e^2\text{fm}^4$ , which is in very good agreement with the KB3G ( $163 e^2\text{fm}^4$ ) and the LNPS- $m$  ( $152 e^2\text{fm}^4$ ) predictions.

A good agreement is also found for the level lifetime of the  $11/2_1^-$  state. The experimental level lifetime of the  $9/2_1^-$  state exceeds the calculated values for both interactions, and also the experimental  $B(E2; 9/2_1^- \rightarrow 5/2_{\text{gs}}^-)$  is in significant disagreement with both calculations. The experimental lifetime of the  $7/2^-$  state,  $\tau(7/2^-) = 525_{-50}^{+125}$  ps, is overestimated by both KB3G (762 ps) and LNPS- $m$  (877 ps).

Apart from the almost degenerate  $9/2_1^-$  and  $11/2_1^-$  states predicted by KB3G, the present observables show no clear preference with respect to the chosen interaction.

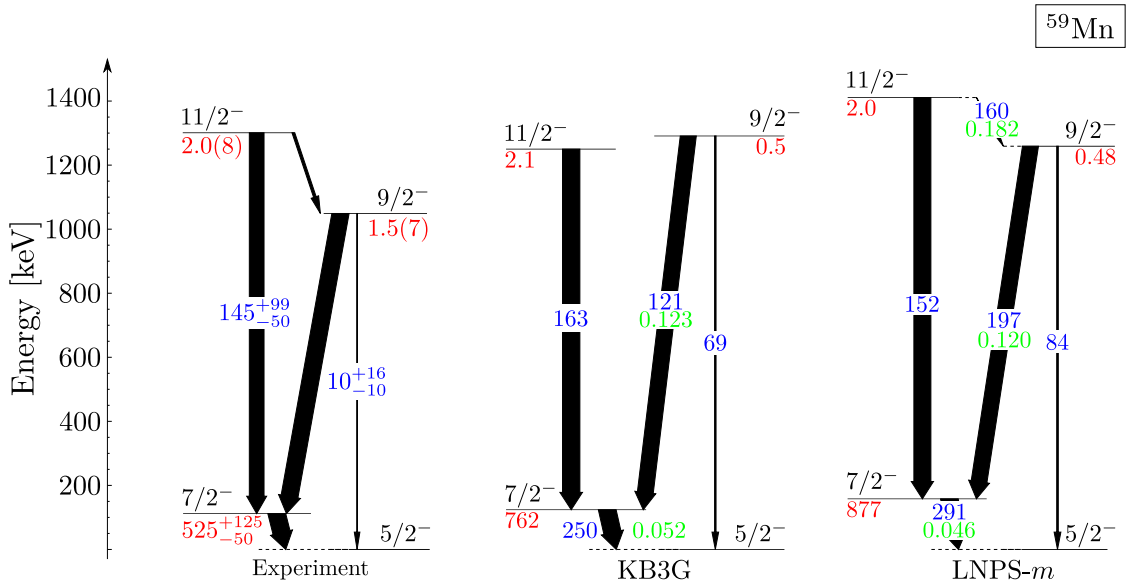


Figure 6.11.: Comparison of experimental low-lying structures in  $^{59}\text{Mn}$  (left) and shell-model counterparts using the KB3G (middle) and LNPS- $m$  (right) interaction. Level lifetimes are written in red,  $B(E2)$  values (in  $e^2\text{fm}^4$ ) in blue and  $B(M1)$  values (in  $\mu_N^2$ ) in green. The width of the arrows indicate the branching ratios. If applicable, shell-model lifetimes are adjusted to experimental  $\gamma$ -ray energies. See text for details

### Comparison of $^{61}\text{Mn}$ to Shell-Model Calculations

The spin assignment of excited states in  $^{61}\text{Mn}$  is only tentative. Assuming that the preliminary assignment is correct, one observes an agreement between experimental and shell-model level energies as well as branching ratios which is comparable to  $^{59}\text{Mn}$ . Again, the LNPS- $m$  predicts the right order and a slightly expanded level structure, while the KB3G interaction predicts almost degenerate  $9/2_1^-$  and  $11/2_1^-$  states although the level ordering is correct.

Compared to  $^{59}\text{Mn}$ , KB3G predicts a decrease with respect to the quadrupole transition strength while the LNPS- $m$  interaction predicts enhanced  $B(E2)$  values, which highlights the role of the different (neutron) valence spaces.

The experimental level lifetime of the  $11/2_1^-$  ( $3.2(10)$  ps) is reproduced by KB3G (2.5 ps) and is in slight disagreement with LNPS- $m$  (1.7 ps). Hence, the  $B(E2; 11/2_1^- \rightarrow 7/2_1^-)$  value agrees only with the KB3G prediction within the error.

Both interactions predict for the  $9/2_1^-$  state a level lifetime which is in agreement with the experimental value, although it is obvious that the experimental value suffers from a comparably large uncertainty.

Most interesting for the present discussion is the  $7/2_1^-$  state due to the known experimental  $B(E2; 7/2_1^- \rightarrow 5/2_{\text{gs}}^-)$  value [VdW09]. This  $B(E2)$  value is in significant disagreement with the KB3G calculation and in pleasant agreement with the LNPS- $m$  interaction. Combining experimental lifetime and  $B(E2)$  value, the corresponding experimental  $B(M1)$  value is determined to  $0.104(23) \mu_N^2$  which is in good agreement with the KB3G

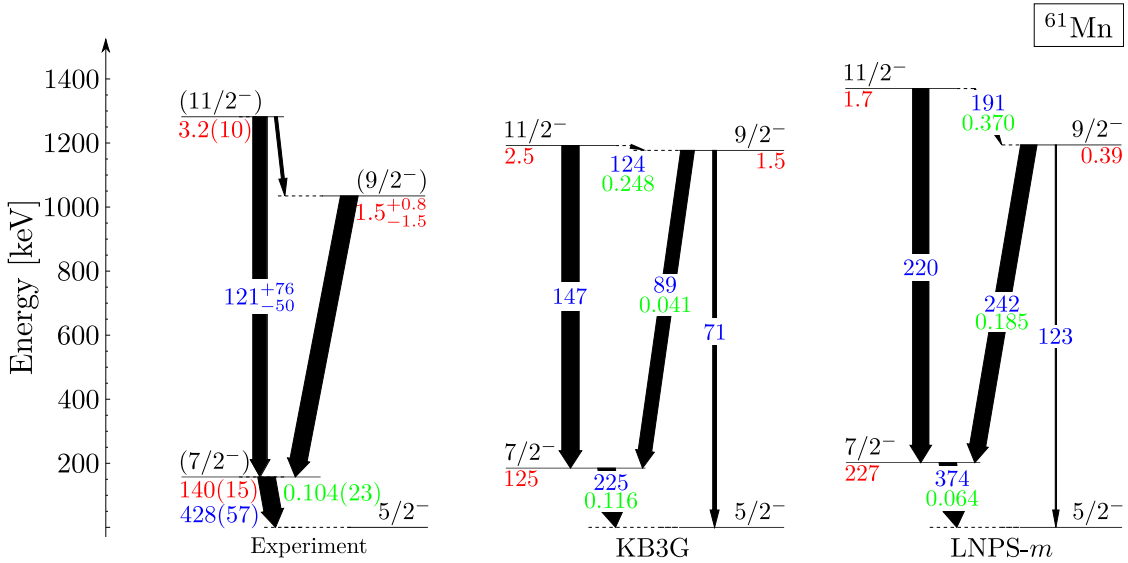


Figure 6.12.: Comparison of experimental low-lying structures in  $^{61}\text{Mn}$  (left) and shell-model counterparts using the KB3G (middle) and LNPS- $m$  (right) interaction. Level lifetimes are written in red,  $B(E2)$  values (in  $e^2\text{fm}^4$ ) in blue and  $B(M1)$  values (in  $\mu_N^2$ ) in green. The width of the arrows indicate the branching ratios. If applicable, shell-model lifetimes are adjusted to experimental  $\gamma$ -ray energies. See text for details.

( $0.116 \mu_N^2$ ) interaction but exceeds the LNPS- $m$  value by a factor of  $\sim 1.6$  ( $0.064 \mu_N^2$ ). As a consequence, the level lifetime calculated with LNPS- $m$  exceeds the experimental value. It is worth to note, that the disagreement increases when quenched  $g$  factors are used.

### Comparison of $^{63}\text{Mn}$ to Shell-Model Calculations

Also in  $^{63}\text{Mn}$  the spin assignment for levels above the ground state is only tentative. For the present discussion, it is assumed that this assignment is valid.

The KB3G interactions predicts a level scheme which appears compressed compared to the experimental level scheme. Again, KB3G predicts that the  $9/2_1^-$  and  $11/2_1^-$  states are almost degenerate and, comparable to  $^{59}\text{Mn}$ , the ordering is reversed. In comparison, the LNPS- $m$  prediction offers a remarkable agreement with the experimental level energies. The experimental lifetimes are significantly overestimated by the KB3G interaction which can be well understood in terms of underestimated transition strengths due to the limited valence space. Unfortunately, only an upper limit of the ( $9/2_1^-$ )-state lifetime was determined which agrees with the LNPS- $m$  prediction. The experimental lifetime of the ( $7/2_1^-$ ) state is reproduced by LNPS- $m$  within  $2\sigma$ .

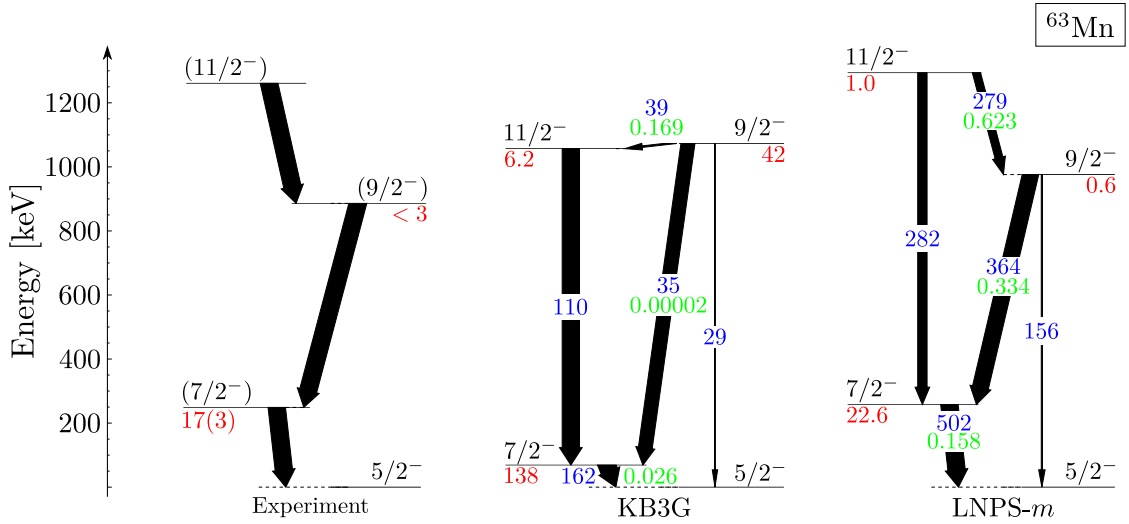


Figure 6.13.: Comparison of experimental low-lying structures in  $^{63}\text{Mn}$  (*left*) and shell-model counterparts using the KB3G (*middle*) and LNPS- $m$  (*right*) interaction. Level lifetimes are written in red,  $B(E2)$  values (in  $e^2\text{fm}^4$ ) in blue and  $B(M1)$  values (in  $\mu_N^2$ ) in green. The width of the arrows indicate the branching ratios. If applicable, shell-model lifetimes are adjusted to experimental  $\gamma$ -ray energies. See text for details

## General Discussion

The experimental level lifetimes of the  $9/2_1^-$  and  $11/2_1^-$  states are comparably small and, hence, the chosen foil separations were not optimal to determine their lifetimes. In fact, it may be easier to investigate the corresponding lifetimes of at least some of the states by DSAM measurements. In addition, the one-proton knockout reactions favoured the population of the  $7/2_1^-$  state. As a consequence, the lifetimes of the  $9/2_1^-$  and  $11/2_1^-$  states could only be determined with large uncertainties which complicated a quantitative discussion.

The significantly larger level lifetimes of the  $7/2_1^-$  state in combination with the significantly larger  $\gamma$ -ray yield provide a solid benchmark.

In  $^{59}\text{Mn}$ , the agreement of KB3G and LNPS- $m$  calculations with available experimental transition strengths and level lifetimes are comparable.

On the one hand, the  $B(\text{E}2; 11/2_1^- \rightarrow 7/2_1^-)$  in  $^{61}\text{Mn}$  shows a better agreement with the KB3G interaction. On the other hand, the experimental  $B(\text{E}2; (7/2_1^-) \rightarrow 5/2_{\text{gs}}^-)$  value in  $^{61}\text{Mn}$  clearly requires to expand the shell-model valence space beyond the neutron  $N = 40$  closure. The present data may indicate that the structural change happens in  $^{61}\text{Mn}$ , for which some observables require the inclusion of neutron orbitals beyond the  $fp$  shell. Interestingly, the  $B(\text{M}1; 7/2_1^- \rightarrow 5/2_{\text{gs}}^-)$  value in  $^{61}\text{Mn}$  as determined from the level lifetime and the known  $B(\text{E}2)$  value [VdW09], exceeds the LNPS- $m$  calculated  $B(\text{M}1)$  value significantly.

In  $^{63}\text{Mn}$  ( $N = 38$ ) the structural change is evident for all known observables and the KB3G interactions completely fails to reproduce the experimental lifetime of the  $(7/2^-)$  state, while the LNPS- $m$  interaction offers reasonable agreement.

At this point, one can only suspect that at least part of the deviations in  $^{59,63}\text{Mn}$  between experimental and LNPS- $m$  calculated  $\tau(7/2_1^-)$  is due to an underestimated  $B(\text{M}1)$  strength. To discuss this aspect in more detail, direct measurements of mixing ratios or  $B(\text{E}2)$  values are needed.

In conclusion, the present data for the neutron-rich Mn isotopes agrees with a structural change between  $N = 36$  and  $N = 38$ .

---

## 7. Summary

Level lifetimes in  $^{58,60,62}\text{Cr}$  were determined and enabled the calculation of model independent transition strengths. The  $B(\text{E}2; 2_1^+ \rightarrow 0_{\text{gs}}^+)$  values in  $^{58,60,62}\text{Cr}$  are in agreement with previous results from Coulomb-excitation experiments performed at intermediate energies, although the present results indicate slightly enhanced collectivity toward  $N = 40$ . The experimental  $B(\text{E}2)$  values for the yrast transitions in  $^{58}\text{Cr}$  show no significant transition dependence. This changes toward  $^{60,62}\text{Cr}$ , for which the measured  $B_{42}$  values are in agreement with rotor-like behaviour.

Shell-model calculations using the effective state-of-the-art interaction LNPS reproduce this rapid onset of collectivity toward  $N = 40$ . However, LNPS slightly underestimates (overestimates) the reduced transition strengths (level energies).

The LNPS interaction predicts that this increase of collectivity is associated with quadrupole deformation driven by  $np - nh$  excitations across  $N = 40$  into the intruding  $g_{9/2}$  and  $d_{5/2}$  orbitals.

Within the Interacting Boson Model available experimental signatures can be reproduced, while the rapid onset of quadrupole deformation is not reproduced. The E(5) assumption to describe the transitional nucleus  $^{58}\text{Cr}$  is not supported by experimental  $B(\text{E}2)$  ratios. A better agreement is found for  $^{60}\text{Cr}$ , although more experimental signatures are mandatory before a solid conclusion on the transitional nature can be drawn.

In addition, level lifetimes in  $^{55}\text{V}$ ,  $^{57}\text{Cr}$ ,  $^{64}\text{Fe}$  and  $^{59,61,63}\text{Mn}$  were determined, some of them for the first time. With respect to the manganese isotopes, lifetimes of (candidates for) the  $7/2_1^-$ ,  $9/2_1^-$ ,  $11/2_1^-$  states ( $^{59,61}\text{Mn}$ ) and of the  $(7/2_1^-)$ ,  $(9/2_1^-)$  states ( $^{63}\text{Mn}$ ) were determined. The results are compared to shell-model calculations using the established  $fp$  interaction KB3G and the state-of-the-art interaction LNPS- $m$ , a modified offspring of LNPS. An interpretation of the present data is aggravated due to missing information on E2/M1 mixing ratios, but the experimental data is in agreement with the onset of a structural change close to  $N = 36$ . This behaviour is comparable to the neighbouring iron isotopes. In  $^{63}\text{Mn}$ , only LNPS- $m$  calculations are in agreement with experimental observables.

Which steps will follow? The predicted island of inversion around  $N = 40$  has been further established. Another island of inversion is predicted to emerge around  $N = 50$  and first theoretical works expect both islands to merge [Now16]. The next logical step is therefore the investigation of neutron-rich iron and chromium isotopes beyond  $N = 40$ , with first steps already been made [San15]. Further investigations will be enabled by progresses in instrumentation and the advent of next generation radioactive ion beam facilities such as FRIB and FAIR. In addition, further efforts will be spent on mapping the  $N = 40$  island of inversion, e.g. with respect to the neutron-rich titanium isotopes.



Part II.

Development of a Simulation  
Tool for RDDS Spectra

---

## 8. Motivation

Ambitious state-of-the art lifetime experiments using the RDDS technique are usually characterized by low  $\gamma$ -ray yields. As a consequence, the analysis is often limited to  $\gamma$ -single data or particle-gated  $\gamma$ -single data. One can therefore not profit from the advantages of  $\gamma\gamma$  coincidences, such as the possibility to select specific  $\gamma$ -ray cascades by which the contribution of unobserved level feeding may be drastically reduced. An imprecise description of the feeding scheme increases the vulnerability to systematic errors. The impact on the lifetime analysis is muted for reactions characterized by low  $\gamma$ -ray multiplicities (e.g. Coulomb excitation or knockout reactions) which are often the tool of choice in such experiments.

In addition, often only data for few foil separations can be recorded due to the limited beam-on-target time in such ambitious experiments. This limits the advantages of the Differential Decay-Curve Method [Dew12] with respect to the lifetime analysis and in such cases lifetimes are often determined by fitting the decay curves.

This part of the thesis reports on the development and first applications of a tool which is applicable to various scenarios in the field of Recoil-Distance Method experiments as well as problems commonly occurring in RDDS measurements. Numerous tools already exist and the need for additional tools has to be illustrated. For this purpose, it is instructive to compare the two major approaches to analyse lifetime data from RDDS measurements characterized by low statistics and low  $\gamma$ -ray multiplicity.

- **Monte Carlo simulations using frameworks such as GEANT4**

These tools offer a *realistic* description of the experiment. Realistic in this sense should be understood in terms of an accurate description of elementary physical processes (e.g. with respect to the interaction of radiation and matter as well as with respect to the description of stopping powers) and a reasonable description of the experimental geometry. Such tools commonly define the standard for experiments using fast radioactive ion beams (see the first part of this thesis) and are often available for experiments using advanced  $\gamma$ -ray detector systems such as AGATA. On the one hand this approach benefits from the realistic description, but it requires comparably strong processing powers on the other hand. In addition, such toolkits are often tailored to specific experimental places and even small modifications often demand time-consuming changes to the code. Some experimental conditions are challenging to simulate (e.g. electronic signal processing and dead-time related issues) and, hence, are often omitted.

- **Lifetime analysis based on experimental decay curves**

This approach is often applied to stable-beam experiments, in which states of interest are populated by direct reactions (low  $\gamma$ -ray multiplicity) induced in thin (few  $\text{mg}/\text{cm}^2$ ) foils. One typical scenario is given in terms of multi-nucleon transfer experiments performed at GANIL with VAMOS (see, e.g., Ref. [Kli17]) or at LNL

---

with PRISMA. This approach suffers from limitations originating from the simplified picture (e.g. with respect to velocity distributions or position dependent effects). In this approach, the fast and slow components in the  $\gamma$ -ray spectra are considered as integrated quantities which neglects the properties of individual recoils, such as broad distributions of the recoil angles as well as of the angle-dependent momentum transfer. One may be reminded on typical features of multi-nucleon transfer reactions which are not only characterized by a broad distribution in the angles of recoils but also show a momentum transfer that strongly correlates with the recoil angle.

A considerable number of co-existing tools allow to investigate higher-order effects such as slowing-down processes of recoils in matter. This, in particular, is relevant in case of short lifetime and/or DSAM experiments.

The present tool follows an approach which to some extent takes ingredients from all of the above mentioned approaches. The development was driven by the following guidelines:

- **Use of experimental observables and modelled distributions**

In practice, a complete and realistic simulation of the experiment is often not needed for reasonable results. One may think of (relative) full energy-peak efficiencies that are evaluated for almost all experiments by using standard sources (e.g.  $^{152}\text{Eu}$  or  $^{226}\text{Ra}$ ). Such measurements offer experimental results after signal processing. Hence, there is no strong argument favouring simulated over experimental efficiencies. State-of-the art spectrometers at facilities like NSCL or GANIL allow to reconstruct the momentum vector of recoils at the experimental place. If experimental distributions are known with reasonable quality, there is no need to assume a priori specific distributions.

- **Monte Carlo approach**

For simplicity, the simulation should follow a Monte Carlo approach based on pre-defined standard distributions as well as specific distributions defined by the user.

- **High flexibility**

The tool should not be limited to specific scenarios, e.g. with respect to geometries or energies. Instead, it should be able to account for line-shape effects caused by slowing-down processes (DSAM) or changing solid angles in case of long level lifetimes. In addition, the simulation of RDDS experiments should not be limited to only two foils. The desired flexibility implies a reasonable description of the underlying physics (e.g. in terms of stopping powers, lateral straggling and relativistic effects) to provide reasonable and realistic results.

- **Simple application and event tracking**

The tool should be fed using input files which cover all necessary parameters. These input files can be created (semi-)automatically with script files. This enables the possibility to produce multiple simulations based on slightly varying parameters, which is helpful when investigating systematic effects. The results should be stored event-by-event using ROOT. This enables the possibility to create user-defined spectra for which – based on the available event properties – strict correlation conditions can be assumed.

---

## 9. Basic Properties

The present tool is written in C++. The ROOT framework is used for the event tracking, which enables the possibility to create user-defined histograms assuming arbitrary correlations based on stored event properties. In addition, the library EIGEN is used to solve mathematical problems related to linear algebra efficiently.

With respect to the detection of  $\gamma$  rays, most experimental setups in nuclear  $\gamma$ -ray spectroscopy follow an approximate cylindrical symmetry. The spectroscopic foils, i.e. target and degrader foils, are usually placed perpendicular to the beam axis and/or the recoil axis, while the HPGe detectors are placed in rings around the beam-/recoil-axis at specific polar angles  $\theta$  with detectors facing a fixed pivot point. In addition, scattering angles are often quite small. This motivates a reduction of the geometry to two dimensions: Within the simulation tool, the coordinates  $z, x$  refer to the laboratory frame. Here, the  $z$ -axis ( $x$ -axis) can be considered as the (non-)dispersive axis.

Input parameters needed to perform a simulation with the present tool can be grouped as follows:

- **Basic properties**

This class of input parameters relates to general aspects concerning the number of iterations within the simulation, the information to be stored in the output file as well as properties of the Doppler-reconstruction method.

- **Beam properties**

The incoming beam is characterized by mass  $m$ , mass number  $A$ , atomic number  $Z$ , position distribution  $\varrho(x, z)$ , energy distribution  $\varrho(E)$  and angular distribution  $\varrho(\alpha)$ , where the latter describes the direction of the beam. Information on stopping powers and lateral straggling are defined to describe the energy loss and the angular straggling in matter.

- **Foil properties**

A user-defined number of foils can be placed arbitrarily in space. Each foil  $i$  is characterized by its mass number  $A_i$ , its atomic number  $Z_i$  its density  $\varrho_i$ , its width  $\Delta w_i$  (along the  $x$  axis) and its thickness  $\Delta T$ . To handle energy losses and straggling of beam particles as well as of recoils, the foils are divided into a user-defined number of segments.

- **Reaction properties**

The presented tool allows the handling of an arbitrary number of reactions. Each reaction is characterized by its total probability as well as relative probabilities describing the chance of a reaction to take place in specific foils. The reaction itself is described with respect to the number of exchanged nucleons  $\Delta A$  and protons  $\Delta Z$ , the induced reaction angle with respect to the beam trajectory as well as the induced

momentum transfer which is allowed to depend on the reaction angle. The reaction angle and the transferred momentum may either follow Gaussian distributions or user-defined distributions.

The probabilities to excite specific states are read from a user-defined file.

- **Recoil properties**

Recoils are identified by mass  $m_r$ , mass number  $A_r$  and atomic number  $Z_r$ . Information on stopping powers and lateral straggling are needed to describe the interaction of recoils with the experimental foils.

The level scheme and the possible  $\gamma$ -ray transitions are given in a user-defined file.

- **Detector properties**

A user-defined number of detectors can be placed arbitrarily in space. Each detector is characterized by four coordinate tuples  $(z_i, x_i)$ . The active volume is then given by the inner space related to lines connecting adjacent coordinates. The detector efficiencies are treated in global terms using one parametrization or in terms of position dependent efficiency parametrizations. The energy dependence of the efficiency can either be neglected or be accounted for using the parametrizations introduced in Refs. [Gra85; Deb84]. In addition, lower and upper limits with respect to the detectable (Doppler-shifted)  $\gamma$ -ray energies can be set. The efficiencies are taken with respect to a reference position. In the simulations, efficiencies are corrected based on the change of the solid angle at the point of emission compared to a given reference position. Parameters describing energy and angular resolutions complete the needed detector information.

A detailed list of input parameters and commands can be found in Appendix F.

## 9.1. Sketch of an Iteration

Each iteration begins with the creation of a beam particle with randomly assigned properties (total kinetic energy, position and direction) according to the user-defined distributions and/or parameters.

This is followed by a first determination of basic properties related to the reaction. Based on their probabilities, it is randomly determined which reaction is used for the considered event. When this is done, foil (*reaction foil*) and segment (*reaction segment*) in which the reaction takes place are defined. This is followed by a determination of the initially populated state  $i$  and its *actual* lifetime  $\tilde{\tau}_i$  within this event. Information on the probabilities for initial populations is defined by the user, while the actual lifetime is randomly determined based on the probability distribution  $\varrho(t, \tau_i)$ ,

$$\varrho(t, \tau_i) = \frac{1}{\tau_i} \exp(-t/\tau_i), \quad (9.1)$$

with  $\tau_i$  being the level lifetime of the excited state  $i$ .

The beam is guided through the foils in the following. When it hits the (next) foil and/or segment, the energy loss and the lateral straggling for the next segment are calculated based on the given input parameters.

The reaction is initiated if the beam impinges on the reaction segment within the reaction foil. First, the kinematics of the recoil are determined according to the given distributions with respect to the momentum transfer as well as the reaction angle. A timer  $t_r$  (initially set to 0) is started which is used to measure the proper time of the recoil after its production. Within a foil, the value of  $t_r$  is updated after every segment by adding the flight time (particle frame) of the recoil through the segment.

As soon as the condition  $t_r \geq \tilde{\tau}_i$  is fulfilled, the decay of the state is initiated. If the recoil is between two foils, the position of the recoil at the time of de-excitation is calculated. If this position is upstream of the next foil, the de-excitation takes place precisely at this position. A similar approach is followed if the recoil is downstream of the last foil. If a de-excitation takes place, it is first determined to which state it decays based on the user-defined branching ratios. This decay defines the next state  $j$  for which an actual lifetime  $\tilde{\tau}_j$  is determined following the above mentioned approach and the timer  $t_r$  is reset to zero. With respect to the  $\gamma$ -ray, the emission angle in the laboratory frame is determined assuming isotropy in the particle reference frame. It is then checked if a.) this angle is within the solid angle of a detector and b.) if the  $\gamma$ -ray is also detected based on the user-defined efficiency. These steps are repeated until the recoil is in its ground state.

## 9.2. Tracking of Events

The present simulation tool allows to track information in five different events which are explained in the following.

- **Primary beam events**

This event tracks properties of the primary beam when it is created. For each iteration, information on the position, the emission angle, the beam energy and the beam  $\beta$  velocity are recorded.

- **Reaction events**

The reaction event tracks information related to the reaction and the thereby created recoils. This event records the reaction mechanism, the position where the reaction took place (in absolute  $x,z$  coordinates and in relative coordinates related to foil and segment), the kinematics (reaction angle and absolute momentum transfer), the excited state as well as its lifetime. With respect to the recoil, the event stores information on the energy, the momentum and the  $\beta$  velocity instantaneously after the reaction took place.

- **Beam Properties behind each foil**

This event tracks the beam kinematics behind each foil and stores  $\beta$  velocity, energy, trajectory angle and position.

- **Recoil Properties behind each foil**

This event tracks the recoil kinematics behind each foil and stores  $\beta$  velocity, energy, trajectory angle and position.

- **$\gamma$ -ray events**

This event keeps track of all  $\gamma$ -ray emissions. Here, basic properties of the underlying reaction mechanism are stored: The coordinates of the reaction ( $(z, x)$  coordinates as well as corresponding foil and segment), properties of the recoil at the time the reaction took place (energy,  $\beta$  velocity, angle) and the initially populated state.

With respect to the  $\gamma$ -ray emission, recoil properties (position,  $\beta$  velocity, energy and direction), properties of the decaying state (actual lifetime  $\tilde{\tau}$ , absolute  $\gamma$ -ray energy) and properties related to the  $\gamma$ -ray detection (Doppler-shifted and Doppler-corrected energy as well as a flag to distinguish detected and undetected  $\gamma$  rays, the corresponding detector and the angle under which the  $\gamma$  ray was observed) are recorded.

This event enriches the possibility to manipulate the  $\gamma$ -ray spectrum by forcing specific correlations. E.g., it is possible to select a specific initially populated state which essentially mimics a  $Q$ -value gate which is a helpful and often used tool to minimize unknown feeding contributions.

### 9.3. Limitations

The strength of the present tool is its high versatility. However, certain factors limit the applicability and the most important aspects shall be discussed here.

- **Rudimentary description of full-energy peak efficiencies**

Within the simulation, the efficiency is empirically corrected to account for changes in the solid angle due to variable  $\gamma$ -ray emission points. In first order this is a reasonable approach. However, corrections due to changing effective detector thicknesses may be necessary in particular for  $\gamma$ -ray emission coordinates far away from the reference point. This is relevant for long lifetimes in combination with fast beams. This problem can be circumvented if the experimental efficiency for different efficiencies is incorporated.

- **No direct treatment of reaction cross sections**

Within the simulation it is *explicitly* assumed that the reaction cross section is independent of the recoil energy. Such a dependence can be included *implicitly* in terms of the relative reaction probabilities for foils or by splitting foils into multiple foils which mimics an energy-dependent reaction cross section.

- **Simplified  $\gamma$ -ray response signal**

At the current state, the simulation only describes full photo-peak absorptions. In particular for detectors without Compton suppression this may be problematic when simulations are to be compared to experimental results.

- **Reduction to two dimensions**

For simplicity, the present tool is limited to two dimensions. This is a reasonable simplification for many experimental setups, in particular those with near-cylindrical symmetry.

---

## 10. Proof of Principles

This chapter reports on the application of the simulation tool to real experimental cases and the results are discussed in the light of different guiding questions.

In Sec. 10.1, the simulation is applied to the experimental case of  $^{58}\text{Cr}$  taken from the present NSCL experiment as it was discussed in the first part of this thesis. The discussion focuses on the question, to which extent the simulation is able to reproduce the experimental spectra assuming input parameters equivalent to the simulations performed with G4LIFETIMEG.

In Sec. 10.2, the isotope of interest is  $^{50}\text{Ti}$ . In this experiment, excited states in  $^{50}\text{Ti}$  were populated by inelastic scattering of a  $^{238}\text{U}$  beam on a  $^{50}\text{Ti}$  plunger target. The experiment suffered from severe problems related to the plunger target which were caused by microscopic damages induced by the impinging uranium beam. This led to comparably large wrinkles on the target surface which were of the order of at least 100  $\mu\text{m}$ . Hence, these problems make the determination of absolute foil separations using the capacitance method highly questionable. In  $^{50}\text{Ti}$ , level lifetimes of low-lying yrast states are known with good precision. Using these level lifetimes as fixed ingredients, the simulation was applied to estimate effective absolute target-to-degrader separations used in this experiment.

In Sec. 10.3, the influence of velocity distributions on the lifetime analysis is discussed in the context of three distinct and realistic cases.

### 10.1. Simulation of $^{58}\text{Cr}$

For a first benchmark, experimental data of  $^{58}\text{Cr}$  taken from the MSU experiment is considered. The following assumptions were made:

- The energy distribution of the  $^{59}\text{Mn}$  beam is deduced from the experimental energy spectrum as measured with S800 using beam-only data. Also the angular distribution with respect to the dispersive  $x$ -direction was deduced from experimental data.
- Excited states in  $^{58}\text{Cr}$  are produced by one-proton knockout reactions for which a Gaussian distribution with  $\Delta\bar{p} = -600 \text{ MeV}/c$  and  $\sigma_p = 90 \text{ MeV}/c$  is assumed. The reaction angle is centered around  $0^\circ$  assuming standard deviations of  $0.8^\circ$  and  $1.3^\circ$  for reactions in the target and degrader.
- The stopping powers to describe the energy loss of beam and recoils are taken from SRIM [Zie10] calculations.
- Two experimental efficiency parametrizations are used to describe  $\gamma$ -ray emissions between target and degrader as well as behind the degrader.

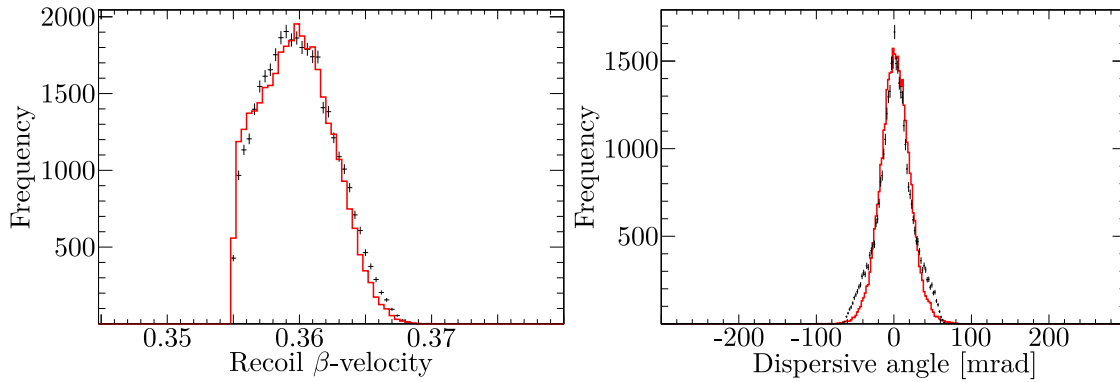


Figure 10.1.: Comparison of experimental (red) and simulated (black) spectra showing the  $\beta$  distribution (*left*) and the distribution of the dispersive recoil angle (*right*).

- Foil thicknesses, the decay scheme and level lifetimes were taken from the first part of this thesis.

Experimental and simulated distributions with respect to the velocity as well as the scattering angle (behind the plunger foils) are shown in Fig. 10.2. While the velocity distribution is reproduced quite nicely by the simulation, the tails in the experimental recoil-angle spectra were unreproducible. An improvement was achieved by assuming a larger standard deviation with respect to the reaction angle for reactions in the degrader. The tails were not observed using target-only data, which makes it likely that this shape originates from reactions taking place in the degrader. The assumption of a Gaussian distribution with respect to transversal momentum transfer is apparently too simplistic.

Doppler-reconstructed  $\gamma$ -ray spectra related to the downstream detector ring are shown for three different separations in Fig. 10.2. A reasonable agreement between experimental and simulated spectra is found.

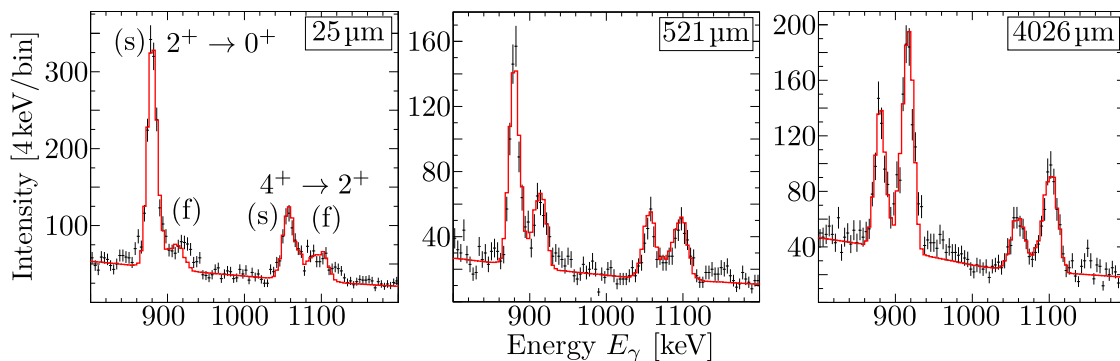


Figure 10.2.: Comparison of experimental (black) and simulated (red) Doppler-corrected  $\gamma$ -ray spectra of  $^{58}\text{Cr}$ . The spectra show the statistics of the downstream detector ring for three different foil separations (see inlet) assuming level lifetimes as determined in the first part of the present thesis.

## 10.2. Determination of Absolute Foil Separations in a Multi-Nucleon Transfer Experiment

An experiment was performed at GANIL in 2016 to investigate transition strengths in neutron-rich titanium isotopes around  $A = 54$  by employing multi-nucleon transfer reactions of a  $^{238}\text{U}$  beam in a  $^{50}\text{Ti}$  target at  $E = 1609$  MeV.

The experiment suffered from severe problems with the plunger target due to wrinkles on the surface of the plunger target which were caused by interactions with the heavy uranium beam. As a consequence, the absolute foil separations as determined by extrapolation of the capacitance signal can only be considered as a first guess. This motivates the determination of effective absolute foil separations by analysing states whose lifetimes are already known with sufficient precision.

A good candidate for this approach is given in terms of  $^{50}\text{Ti}$  which was populated by inelastic scattering/Coulomb excitation. Assuming reported level lifetimes in combination with the experimentally observed decay scheme, the simulation was used to estimate the absolute foil separations. The following assumptions were made:

- The  $^{238}\text{U}$  beam impinged with an energy of 1609 MeV on the plunger target.
- The grazing angle of the reaction channel was  $46^\circ$  with an estimated width of  $\pm 5^\circ$  and corresponding recoil energies were calculated with LISE++ [Tar08]. Precise experimental distributions with respect to recoil angles and energies can be used instead. Unfortunately, this information was not available when this thesis was written.
- The plunger target was made of  $1.5 \text{ mg/cm}^2$   $^{50}\text{Ti}$  with a  $0.4 \text{ mg/cm}^2$  fronting made of copper. The degrader was made of  $3.0 \text{ mg/cm}^2$  natural magnesium.
- The geometry of the highly-segmented  $\gamma$ -ray spectrometer AGATA was given in compact configuration [Cle17].
- The experimental efficiencies were taken from a previous RDDS experiment on  $^{106,108}\text{Sn}$  [Sic17] to fix the decay scheme as well as the initial populations. The latter were determined to be  $n_0(6^+) = 4.5\%$ ,  $n_0(4^+) = 18.4\%$  and  $n_0(2^+) = 77.1\%$ .
- The Doppler-reconstruction is performed using the recoil velocity behind the degrader and the effective  $\gamma$ -ray emission angle with respect to the recoil trajectory. The effective angular resolution is assumed to be  $2^\circ$ .

A comparison of experimental and simulated Doppler-reconstructed  $\gamma$ -ray spectra for various foil separations is depicted in Fig. 10.3. Due to the very short (long) lifetime of the  $2_1^+$  ( $6_1^+$ ) state ( $\tau(2_1^+) = 1.53(5)$  ps and  $\tau(6_1^+) = 603(25)$  ps), only the lifetime of the  $4_1^+$  state ( $\tau(4_1^+) = 7.6(16)$  ps) offers a reasonable sensitivity to distance changes.

For all spectra one can see that the determined absolute foil separations exceeds the extrapolated foil separation. The latter includes nominative foil separation and zero offset as determined by the capacitance method.

It is recommended to repeat the procedure when the experimental full-energy peak efficiencies of this particular experiment are evaluated and velocity as well as angular distributions are known.

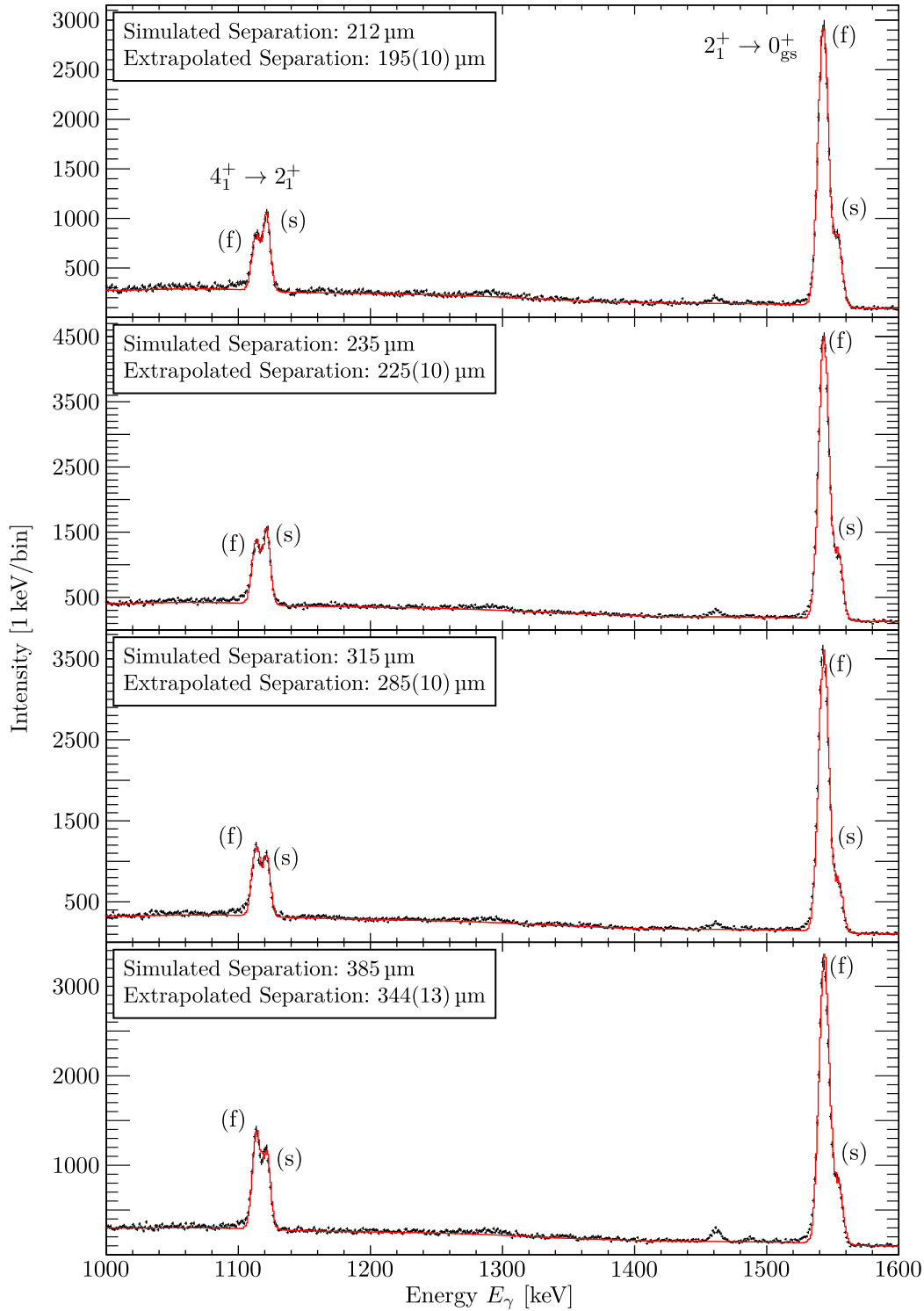


Figure 10.3.: Comparison of experimental (black) and simulated (red) Doppler-reconstructed  $\gamma$ -ray spectra correlated to  $^{50}\text{Ti}$ . The assumed separations (in the simulation) and the extrapolated separations (including the zero offset) based on the capacitance signals are listed in the inlets. See text for details.

### 10.3. The Impact of Velocity Distributions on RDDS Spectra

In the analysis of RDDS data, the foil separation is translated from the position frame ( $d_i$ ) into the time frame ( $t_i$ ) for which assumptions on the recoil velocities have to be made. In practical cases, the velocity distribution for recoils leaving the plunger target, labelled  $\beta^{\text{distr}}$ , may deviate from the velocity distribution limited to decays before the stopper/degrader (labelled  $\beta_{\text{T}}^{\text{distr}}$  with mean value  $\bar{\beta}_{\text{T}}^{\text{distr}}$  and width  $\Delta\beta_{\text{T}}^{\text{distr}}$ ). The effect of the velocity distribution on the lifetime analysis has been studied in the past (see e.g. Ref. [Dew12; Hac14] and references therein), concluding that the impact of  $\beta^{\text{distr}}$  on the determined lifetime is in most cases small but becomes measurable for broad distributions, i.e.  $\Delta\beta^{\text{distr}} > 30\%$ . In standard experiments with narrow velocity distributions, the assumption of a mean velocity  $\bar{\beta}$  as determined from the experimental energy shift between shifted and stopped component is sufficient.

The velocity distribution  $\beta^{\text{distr}}$  for recoils (reaction products) leaving the plunger target is predominately determined by the following factors:

- **The energy distribution of the projectiles**

The energy distribution affects the mean reaction cross section (e.g. in fusion-evaporation reactions) as well as the energy distribution of the reaction products. In stable-beam RDDS experiment the projectiles can be considered in good approximation as mono-energetic.

- **Properties of the reaction**

The momentum of the reaction product,  $p_r$ , depends on the momentum of the projectile ( $p_p$ ) and a momentum change  $\Delta p_r$  according to:

$$p_r = p_p + \Delta p_r \quad (10.1)$$

The additional term  $\Delta p_r$  depends on the reaction mechanism and most often is given in terms of a distribution.

- **The thickness of the plunger target**

Even in cases of constant reaction cross sections, the target thickness increases the width of  $\beta^{\text{distr}}$  due to different energy losses of projectiles and reaction products.

The following discussion is restricted to fusion-evaporation reactions. In this case,  $\Delta p_r$  depends on the  $Q$  value of the reaction as well as the momenta carried away by the evaporated nucleons/clusters. Within the rest-frame of the compound nucleus, the angular distribution of evaporated nucleons is in first order isotropic. For neutrons, the corresponding kinetic energies follow Maxwellian distributions, while for charged particles the additional influence of the Coulomb interaction has to be taken into account. As a consequence,  $\Delta p_r$  follows a characteristic distribution. Standard reaction codes for fusion evaporation reaction such as PACE4 [Gav80] calculate the energies and angular distributions of evaporated nucleons/clusters and, hence, are useful to estimate  $\Delta p_r$ .

$\beta$ (%)	$\Delta\beta$ (%)	$\Delta E_{\gamma, \Delta\theta}$ (keV)	$\Delta E_{\gamma, \Delta\beta}$ (keV)	$\Delta E_{\gamma, \text{intr}}$ (keV)	$\Delta E_{\gamma, \text{tot}}$ (keV)
1.0	0.2	1.37	1.40	1.0	2.2
1.0	0.5	1.37	3.51	1.0	3.9
1.0	0.7	1.37	4.91	1.0	5.2

Table 10.1.: Influences of the detector resolution  $\Delta\theta$ , the width of the velocity distribution  $\Delta\beta$  as well as the intrinsic detector resolution on the total energy resolution for different velocity distributions. See text for details.

### Experimental Signatures of Velocity Distributions

In first order, the energy resolution  $\Delta E_{\gamma}$  of a Doppler-shifted component depends on the angular detector resolution  $\Delta\theta$ , the width of the velocity distribution  $\Delta\beta$  and the intrinsic detector resolution:

$$\left(\frac{\Delta E_{\gamma}}{E_{\gamma}}\right)^2 = \left(\frac{\beta \sin \theta \Delta\theta}{1 - \beta \cos \theta}\right)^2 + \left(\frac{(\beta - \cos \theta) \Delta\beta}{(1 - \beta^2)(1 - \beta \cos \theta)}\right)^2 + \left(\frac{\Delta E_{\text{intr}}^{\text{lab}}}{E_{\gamma}}\right)^2 \quad (10.2)$$

Table 10.1 lists for an exemplary case (assuming  $E_{\gamma} = 1000$  keV,  $\theta = 45^{\circ}$  (width  $11^{\circ}$ ) and  $E_{\gamma}^{\text{intr}} = 1$  keV) the contributions for different velocity distributions on the energy resolution. With respect to RDDS experiments it is therefore evident, that the velocity distribution  $\beta^{\text{distr}}$  contributes not only to the centroid energy of the Doppler-shifted component,  $\bar{E}_{\gamma}$ , but also broadens the shifted component. Changes in  $\Delta\beta_{\text{T}}^{\text{distr}}$  may also alter the resolution of the Doppler-shifted component.

### Exemplary Case Studies

To investigate the effect of the recoil velocity distribution on the lifetime analysis, the present simulation tool was applied to describe three realistic experiments which were performed in the past.

- $^{48}\text{Cr}$  was investigated using the reaction  $^{40}\text{Ca}(^{10}\text{B}, np)^{48}\text{Cr}$  at 26 MeV. The target material was  $^{48}\text{Ca}$  with a nominative thickness of  $0.5$  mg/cm<sup>2</sup> sandwiched by a gold fronting ( $2$  mg/cm<sup>2</sup>) and a gold backing ( $0.1$  mg/cm<sup>2</sup>). According to PACE4 calculations the momentum change  $\Delta p_z$  is given by  $-20(90)$  MeV/c. The total width of the recoil velocity distribution is estimated to  $31\%$ . The experimental results were already published [Arn17]. The authors observed a positive correlation between absolute peak separation,  $|\bar{E}_{\gamma, sh} - E_{\gamma}|$ , and foil separation  $d_i$ . Hence, the authors used distance-dependent recoil velocities  $\beta_i$  in their lifetime analysis.
- $^{112}\text{Te}$  was investigated using the reaction  $^{92}\text{Mo}(^{23}\text{Na}, p2n)^{112}\text{Te}$  at 81 MeV. The target thickness was chosen to be  $1.0$  mg/cm<sup>2</sup>. In this case, a width of  $13\%$  is expected for the recoil velocity distribution.
- $^{184}\text{Hg}$  was investigated using the reaction  $^{148}\text{Sm}(^{40}\text{Ar}, 4n)^{184}\text{Hg}$  at 200 MeV. Here, the width of the recoil velocity distribution is expected to be  $5\%$ . The aspect of the

velocity distribution in this particular case was already discussed [Hac14] and the authors concluded that the velocity distribution in this specific case has negligible effects on the lifetime analysis.

For simplicity, the  $\gamma$ -ray detection is restricted to a detector placed at  $\theta = 45^\circ$  with  $\Delta\theta = 11^\circ$ . This resembles the properties of the downstream detector ring at the plunger setup at the Cologne FN tandem facility. The beam properties and foil configurations assumed in the simulation are adopted to the nominative values of the corresponding experiment. Energy losses are taken from SRIM calculations. PACE4 was used to estimate the momentum change  $\Delta p_z$ , while - for simplicity - the momentum spread perpendicular to the beam axis is neglected. Details are summarized in Table 10.2.

Simulated spectra were generated assuming simplified decay schemes covering yrast states up to  $J = 6^+$  which receives 100 % of the initial population. Level energies and lifetimes were adopted from the ENSDF database [ENSDF]. The discussion is limited to the  $2^+$  states.

Some of the generated  $\gamma$ -ray spectra, including the corresponding distributions  $\beta_T^{\text{distr}}$  are depicted in Fig. 10.4. Additional and more detailed signatures illustrating the influence of the velocity distribution on the lifetime analysis are depicted in Fig. 10.5. For the  $2^+ \rightarrow 0^+$  transition in  $^{48}\text{Cr}$  an increasing energy gap between shifted and stopped component as a function of the foil separation  $d_i$  is observed. This is caused by the evolving  $\beta_T^{\text{distr}}$  which, in particular, is manifested in increasing  $\bar{\beta}_T^{\text{distr}}$  values as a function of  $d_i$ . A similar observation, although significantly weaker, is made for the  $2^+ \rightarrow 0^+$  in  $^{112}\text{Te}$ . Responsible for the less pronounced effect is given in terms of the narrower distribution  $\beta_T^{\text{distr}}$ . For  $^{184}\text{Hg}$ , the centroid of the shifted component shows no significant shift due to an almost stationary velocity distribution  $\beta_T^{\text{distr}}$ .

It is interesting to note that for all three cases the width of the shifted component (illustrated in Fig. 10.5 in terms of the FWHM) shows no significant changes as a function of foil separation. This can be understood in terms of  $\Delta\beta_T^{\text{distr}}$  which shows only marginal correlations to the foil separation.

	$^{48}\text{Cr}$	$^{112}\text{Te}$	$^{184}\text{Hg}$
Reaction	$^{40}\text{Ca}(^{10}\text{B},np)^{48}\text{Cr}$	$^{92}\text{Mo}(^{23}\text{Na},p2n)^{112}\text{Te}$	$^{148}\text{Sm}(^{40}\text{Ar},4n)^{184}\text{Hg}$
Beam energy	26 MeV	81 MeV	200 MeV
Target thickness	0.5 mg/cm <sup>2</sup>	1.0 mg/cm <sup>2</sup>	0.6 mg/cm <sup>2</sup>
Momentum change $\Delta p_z$	-20(90) MeV/c	9(94) MeV/c	48(103) MeV/c
<b>Estimated properties of recoil-velocity distribution behind the target</b>			
Mean $\beta$ -velocity $\bar{\beta}^{\text{distr}}$	1.07 %	1.49 %	2.15 %
$\Delta\beta_{\text{tot}}^{\text{distr}}$	0.33 %	0.19 %	0.10 %
$\Delta\beta_{\text{reaction}}^{\text{distr}}$	0.22 %	0.08 %	0.06 %
$\Delta\beta_{\text{foil thickness}}^{\text{distr}}$	0.24 %	0.17 %	0.08 %
$\Delta\beta_{\text{tot}}^{\text{distr}}/\bar{\beta}^{\text{distr}}$	31 %	13 %	5 %

Table 10.2.: Information on key signatures related to the experiment on  $^{48}\text{Cr}$ ,  $^{112}\text{Te}$  and  $^{184}\text{Hg}$ . See text for details.

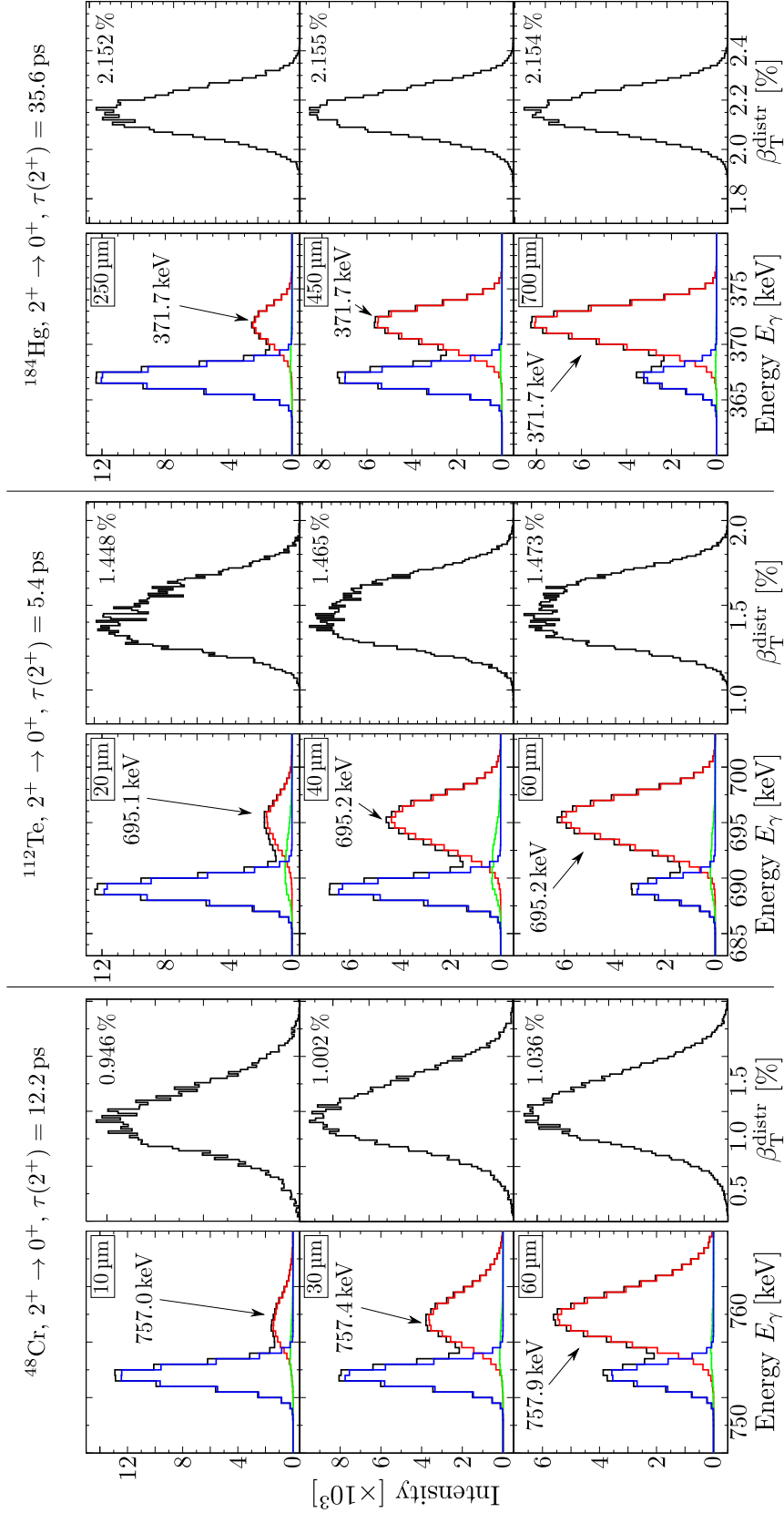


Figure 10.4.: Simulated  $\gamma$ -ray spectra for the  $2^+ \rightarrow 0^+$  transition in  $^{48}\text{Cr}$  (*left*),  $^{112}\text{Te}$  (*centre*) and  $^{184}\text{Hg}$  (*right*) and corresponding distributions  $\beta_{\Gamma}^{\text{distr}}$  showing the yields of different foil separations. The total spectra are drawn in black, the stopped component in blue and the shifted component in red. The contributions of decays within the stopper characterized by  $\beta > 0$  are depicted in green. Quoted values indicate mean values. See text for details.

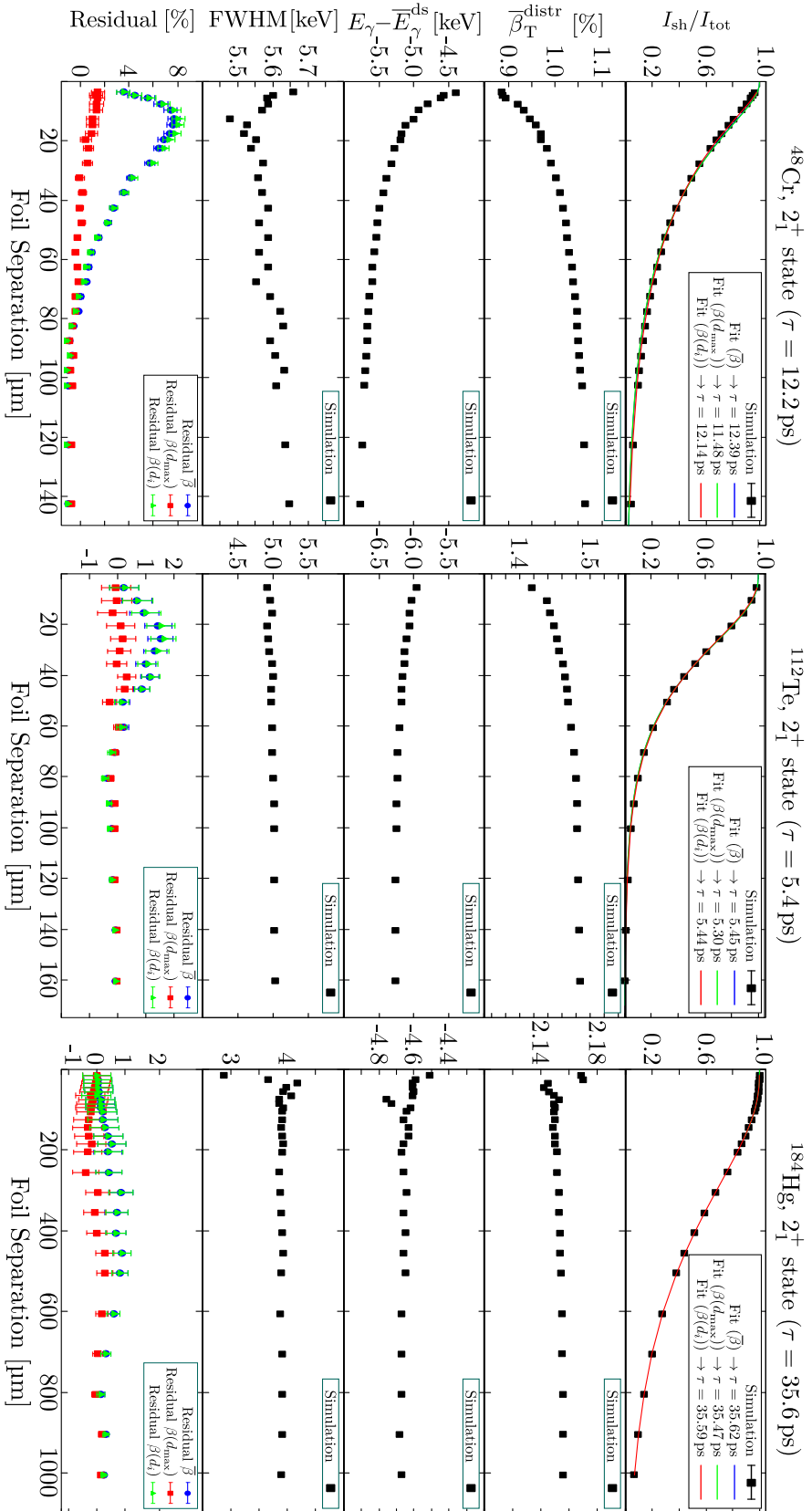


Figure 10.5.: Distance-dependent information related to de-excitations of the  $2^+$  states in  $^{48}\text{Cr}$  (left),  $^{112}\text{Te}$  (centre) and  $^{184}\text{Hg}$  (right). The fitted decay curves for different assumptions on the  $\beta$  velocity are depicted in the top row. The second row illustrates the evolution of mean velocities corresponding to de-excitations before the stopper and the third row shows the (mean) energy gap between stopped and shifted component. The fourth row shows the energy resolution of the Doppler-shifted component. The bottom row shows the residuals for different  $\beta$  assumptions between fitted decay curve and experimental data. See text for details.

	$\beta(\mathbf{d}_i)$	$\bar{\beta}$	$\beta_{\max}$
$\Delta\tau_{\text{rel}}(2^+)$ in $^{48}\text{Cr}$	0.5 %	1.6 %	6.0 %
$\Delta\tau_{\text{rel}}(2^+)$ in $^{112}\text{Te}$	0.7 %	0.9 %	1.9 %
$\Delta\tau_{\text{rel}}(2^+)$ in $^{184}\text{Hg}$	0.03 %	0.06 %	0.37 %

Table 10.3.: Relative errors of the  $2^+$  lifetime in  $^{48}\text{Cr}$ ,  $^{112}\text{Te}$  and  $^{184}\text{Hg}$  for three distinct assumption on the recoil velocities. See text for details.

Lifetimes are determined by fitting the Bateman equations to the experimental data, using three different assumptions to transform from the position frame ( $d_i$ ) to the time frame ( $t_i$ ):

- Assume a mean recoil velocity  $\bar{\beta}$  as deduced from the energy gap between shifted and stopped component,  $t_i = d_i/\bar{\beta}$  (based on summed spectra).
- Assume a maximum recoil velocity  $\beta_{\max}$  determined from the *largest* separation,  $t_i = d_i/\beta_{\max}$ .
- Assume distance-dependent recoil velocities  $\beta(d_i)$  and calculate  $t_i$  via  $t_i = d_i/\beta(d_i)$ .

The results are shown in Fig. 10.5. The top figure depict the fitted decay curves, while the bottom figures show the corresponding residuals. The relative deviations between fitted and real lifetime,  $\Delta\tau_{\text{rel}} = (\tau_{\text{fit}} - \tau_{\text{lit}})/\tau_{\text{lit}}$ , are listed in Table 10.3.

In all three cases, the level lifetime is best reproduced assuming distance-dependent recoil velocities  $\beta_i$ , although only for  $\tau(2^+)$  in  $^{48}\text{Cr}$  the agreement is significantly better compared to the assumption of  $\bar{\beta}$ . The worst agreement is found if  $\beta_{\max}$  is assumed for the lifetime analysis.

---

## 11. Summary

A Monte Carlo simulation tool based on C++ was developed. It can be applied to RDDS experiments and works in close proximity to experimental observables. The treatment of relativistic effects known to affect the line shapes is incorporated. This is in particular relevant for RDDS experiments using fast radioactive ion beams.

The tool is extraordinary flexible and can handle distinctively different experimental setups varying from single foil experiments (DSAM and line-shape analysis) to standard RDDS experiments up to multi-foil RDDS experiments. Due to the simple handling of arbitrary level schemes, the tool can be applied to RDDS experiments using fusion evaporation reactions. The tool is also helpful in the preparation of experiments: It can be used to illustrate the expected peak separability as well as to visualize  $\gamma$ -ray yields. This was already done to motivate experiments at the HIE ISOLDE facility.

Its functionality was shown for selected cases. In particular, it was applied to investigate the influence of velocity distributions on line shapes and level lifetimes for selected and realistic cases. First applications show that the assumption of a mean recoil velocity leads to reasonable results even for distributions with  $\Delta\beta \sim 30\%$ . However, the systematic deviations are reduced if distance-dependent recoil velocities are used. This, however, requires a certain minimum of statistics.

## A. Considered Transitions in $^{152}\text{Eu}$ Data

Energy (keV)	Absolute Intensities (%)	Nucleus
121.7817(3)	28.507(169)	$^{152}\text{Sm}$
244.6974(8)	7.542(44)	$^{152}\text{Sm}$
344.2785(12)	26.591(199)	$^{152}\text{Gd}$
411.1165(12)	2.237(12)	$^{152}\text{Gd}$
443.9606(16)	2.824(15)	$^{152}\text{Sm}$
444.01(17)	0.298(11)	$^{152}\text{Sm}$
563.9860(50)	0.493(5)	$^{152}\text{Sm}$
566.4380(60)	0.131(3)	$^{152}\text{Sm}$
686.6(5)	0.020(1)	$^{152}\text{Sm}$
688.670(5)	0.856(6)	$^{152}\text{Sm}$
778.9045(24)	12.929(83)	$^{152}\text{Gd}$
867.3800(300)	4.224(31)	$^{152}\text{Sm}$
963.367(7)	0.140(6)	$^{152}\text{Sm}$
964.0570(50)	14.498(75)	$^{152}\text{Sm}$
1085.837(10)	10.106(54)	$^{152}\text{Sm}$
1089.7370(50)	1.734(11)	$^{152}\text{Gd}$
1112.0760(30)	13.656(88)	$^{152}\text{Sm}$
1212.9480(110)	1.413(9)	$^{152}\text{Sm}$
1299.1420(80)	1.633(11)	$^{152}\text{Gd}$
1408.0130(30)	20.850(102)	$^{152}\text{Sm}$
1528.100(40)	0.279(3)	$^{152}\text{Sm}$

Table A.1.: Transitions in  $^{152}\text{Eu}$ . Energies are taken from Ref. [NDS152]. Relative intensities from in Ref. [NDS152] are translated into absolute intensities by normalizing to specifically known absolute intensities given in Ref. [IAEA07].

---

## B. Decay Curves in $^{58,60,62}\text{Cr}$

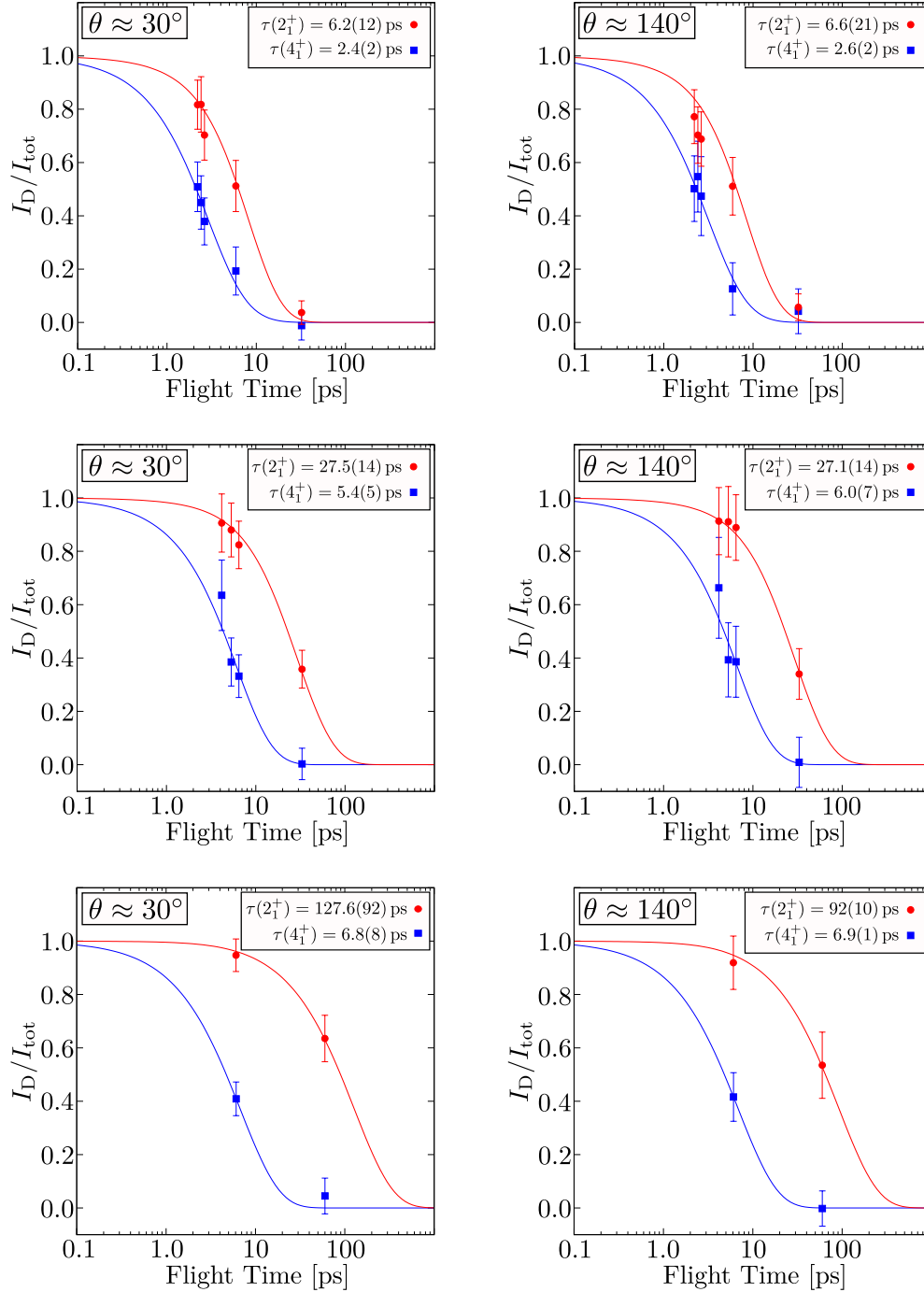


Figure B.1.: Investigation of the lifetimes for the  $2_1^+$  and  $4_1^+$  states in  $^{58}\text{Cr}$  (*top*),  $^{60}\text{Cr}$  (*centre*) and  $^{62}\text{Cr}$  (*bottom*) by means of their decay curves. Results are shown for the independent data sets of the downstream (*left*) and upstream (*right*) detector ring. The quoted errors include only statistical effects.

---

## C. Reacted Beam Cuts

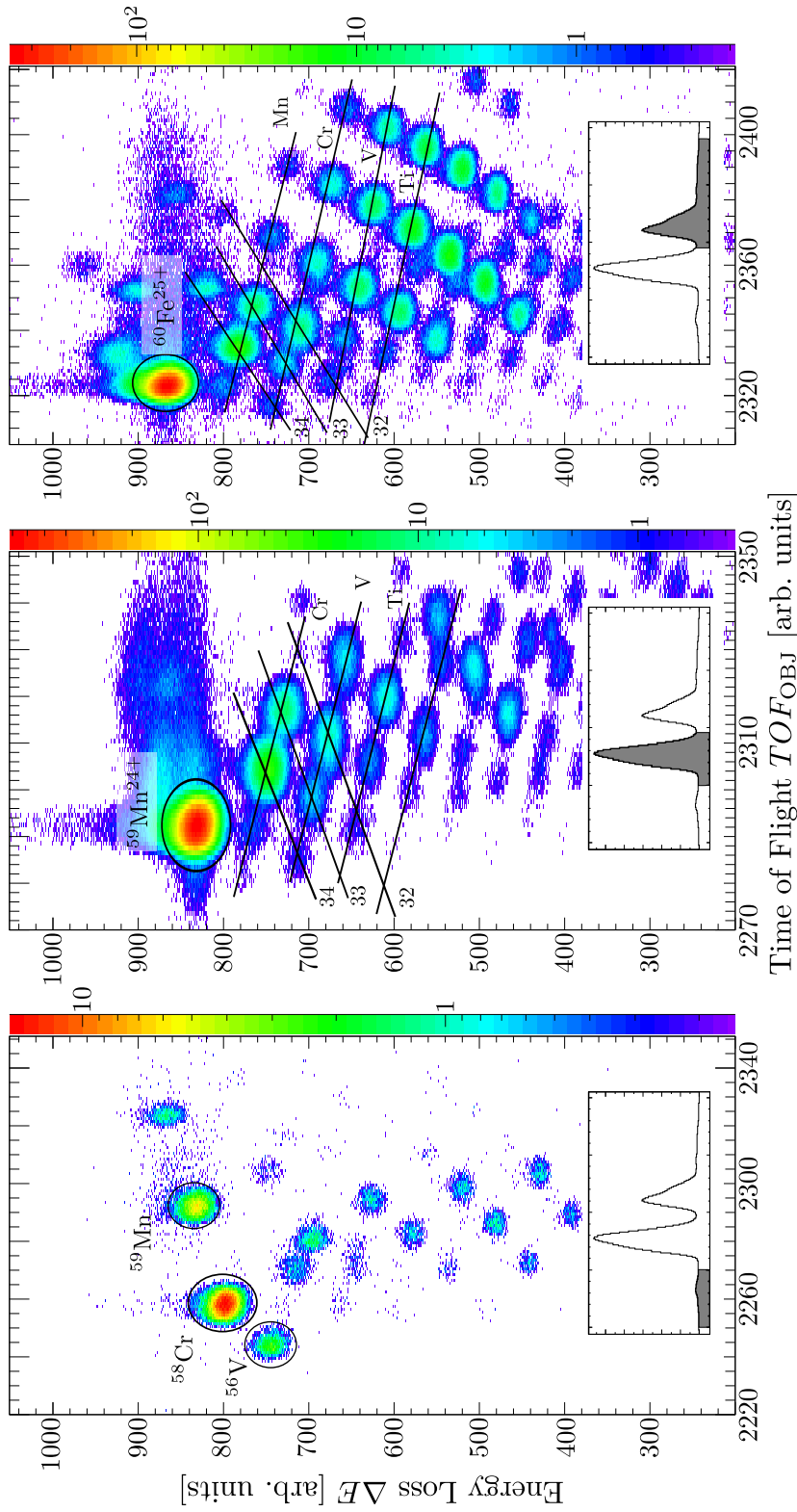


Figure C.1.: (First setup) Beam and recoil identification based on  $\Delta E - TOF$  correlations for different incoming beam gases as depicted in the inlet (see Fig. 5.1). The secondary beams in the correlation plots are circled and identified. For some cases, the identification of isotopes (element and neutron number) is sketched with lines.

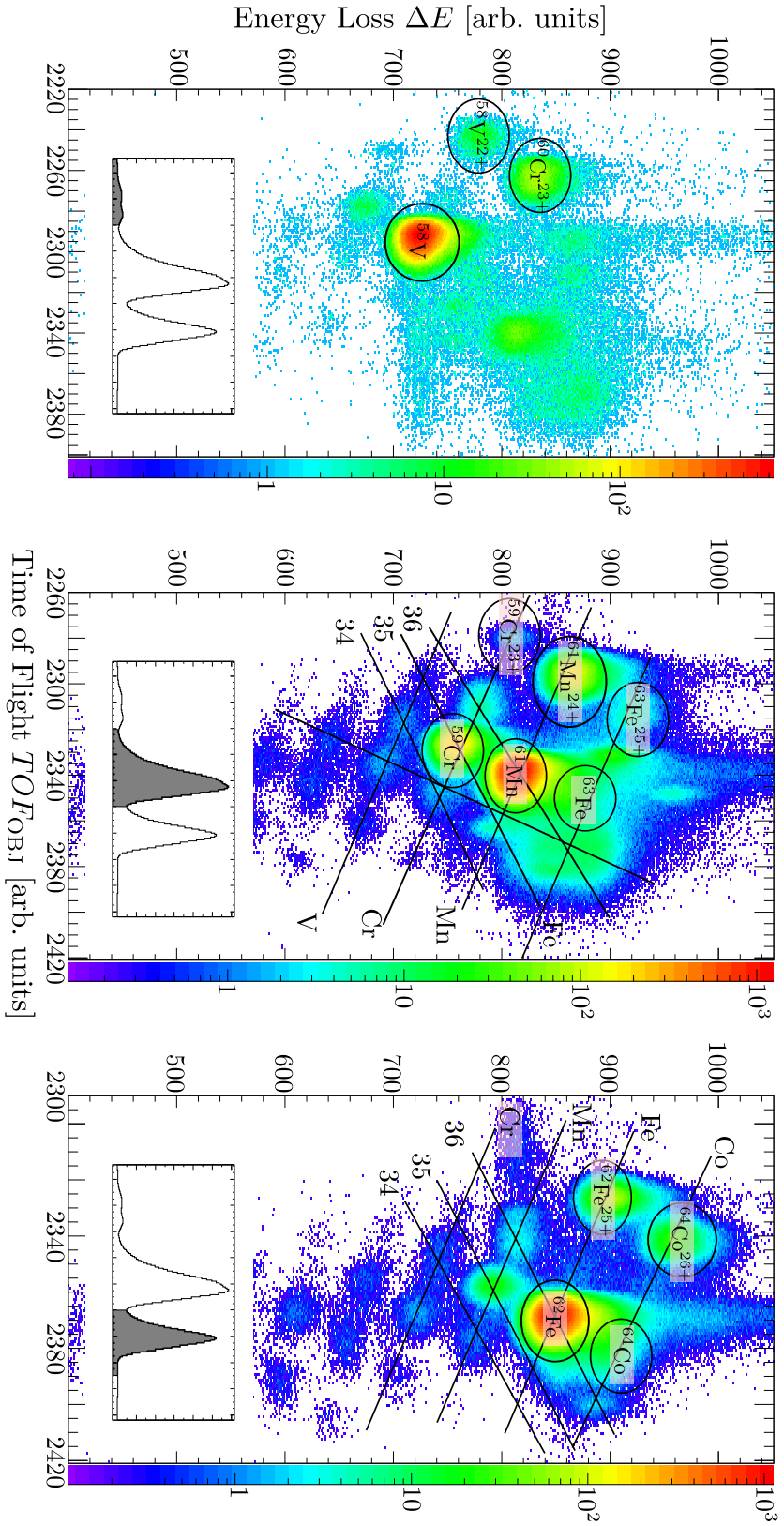


Figure C.2.: (Second setup) Beam and recoil identification based on  $\Delta E - TOF$  correlations for different incoming beam gates as depicted in the inlet (see Fig. 5.1). The secondary beams in the correlation plots are circled and identified. For some cases, the identification of isotopes (element and neutron number) is sketched with lines.



## D. Experimental Data - Systematics

Particle	$E(2_1^+)$ (keV)	$E(4_1^+)$ (keV)
$^{40}_{20}\text{Ca}_{20}$	3904.38(3) [NDS40]	5278.80(6) [NDS40]
$^{42}_{20}\text{Ca}_{22}$	1524.71(3) [NDS42]	2752.40(4) [NDS42]
$^{44}_{20}\text{Ca}_{24}$	1157.019(4) [NDS44]	2283.114(10) [NDS44]
$^{46}_{20}\text{Ca}_{26}$	1346.0(3) [NDS46]	2574.7(5) [NDS46]
$^{48}_{20}\text{Ca}_{28}$	3381.72(6) [NDS48]	4503.14(8) [NDS48]
$^{50}_{20}\text{Ca}_{30}$	1026.72(10) [NDS50]	4515.02(14) [NDS50]
$^{52}_{20}\text{Ca}_{32}$	2563(1) [NDS50]	-
$^{54}_{20}\text{Ca}_{32}$	2043(19) [Ste13]	-
$^{42}_{22}\text{Ti}_{20}$	1554.6(3) [NDS42]	2676.6(8) [NDS42]
$^{44}_{22}\text{Ti}_{22}$	1083.06(9) [NDS44]	2554.33(12) [NDS44]
$^{46}_{22}\text{Ti}_{24}$	889.286(3) [NDS46]	2009.846(5) [NDS46]
$^{48}_{22}\text{Ti}_{26}$	983.5390(24) [NDS48]	2295.654(5) [NDS48]
$^{50}_{22}\text{Ti}_{28}$	1553.778(7) [NDS50]	2674.910(8) [NDS50]
$^{52}_{22}\text{Ti}_{30}$	1050.06(9) [NDS52]	2318.19(11) [NDS52]
$^{54}_{22}\text{Ti}_{32}$	1494.8(8) [NDS54]	2496.0(10) [NDS54]
$^{56}_{22}\text{Ti}_{34}$	1128.2(4) [NDS56]	2288.2(7) [NDS56]
$^{58}_{22}\text{Ti}_{36}$	1047(4) [Gad14]	2038(6) [Gad14]
$^{60}_{22}\text{Ti}_{38}$	850(5) [Gad14]	1716(7) [Gad14]
$^{46}_{24}\text{Cr}_{22}$	892.5(5) [Gar07]	1987.7(7) [Gar07]
$^{48}_{24}\text{Cr}_{24}$	752.19(11) [NDS48]	1858.47(17) [NDS48]
$^{50}_{24}\text{Cr}_{26}$	783.32(3) [NDS50]	1881.31(9) [NDS50]
$^{52}_{24}\text{Cr}_{28}$	1434.091(14) [NDS52]	2369.630(18) [NDS52]
$^{54}_{24}\text{Cr}_{30}$	834.855(3) [NDS54]	1823.93(7) [NDS54]
$^{56}_{24}\text{Cr}_{32}$	1006.61(20) [NDS56]	2076.6(3) [NDS56]
$^{58}_{24}\text{Cr}_{34}$	880.7(2) [NDS58]	1938.6(4) [NDS58]
$^{60}_{24}\text{Cr}_{36}$	643.9(2) [NDS60]	1460.7(5) [NDS60]
$^{62}_{24}\text{Cr}_{38}$	446.1(9) <sup>1</sup>	1175.1(68) <sup>2</sup>
$^{64}_{24}\text{Cr}_{40}$	422.7(63) <sup>3</sup>	1133.7(11) [Gad10]
$^{66}_{24}\text{Cr}_{42}$	386(10) [San15]	1069(13) [San15]

*Continued on next page ...*

<sup>1</sup>Weighted mean of 449(4) [Aoi09], 440(7) [Gad10], 447(6) [Bau12] and 446(1) [Sor03].

<sup>2</sup>Weighted mean using  $E_\gamma(4_1^+ \rightarrow 2_1^+)$  of 725(9) [Gad10] and 734(10) [Aoi09].

<sup>3</sup>Weighted mean of 420(7) [Gad10] and 435(15) [Cra13].

... continued..

Particle	$E(2_1^+)$ (keV)	$E(4_1^+)$ (keV)
$^{48}_{26}\text{Fe}_{22}$	969.5(5) [Dos07]	-
$^{50}_{26}\text{Fe}_{24}$	764.9(3) [NDS50]	1851.5(5) [NDS50]
$^{52}_{26}\text{Fe}_{26}$	849.45(10) [NDS52]	2384.55(17) [NDS52]
$^{54}_{26}\text{Fe}_{28}$	1408.19(19) [NDS54]	2538.1(3) [NDS54]
$^{56}_{26}\text{Fe}_{30}$	846.7778(19) [NDS56]	2085.1045(25) [NDS56]
$^{58}_{26}\text{Fe}_{32}$	810.7662(2) [NDS58]	2076.52(3) [NDS58]
$^{60}_{26}\text{Fe}_{34}$	823.83(9) [NDS60]	2114.6(12) [NDS60]
$^{62}_{26}\text{Fe}_{36}$	877.31(10) [NDS62]	2176.47(14) [NDS62]
$^{64}_{26}\text{Fe}_{38}$	746.4(1) [NDS64]	1763.12(14) [NDS64]
$^{66}_{26}\text{Fe}_{40}$	573.44(10) [Lid13]	1407.34(22) [Lid13]
$^{68}_{26}\text{Fe}_{42}$	522(1) [Dau11]	1389.0(14) [Dau11]
$^{70}_{26}\text{Fe}_{44}$	480(13) [San15]	1346(16) [San15]
$^{72}_{26}\text{Fe}_{46}$	520(16) [San15]	1334(20) [San15]
$^{52}_{28}\text{Ni}_{24}$	1397(6) [NDS52]	2385(10) [NDS52]
$^{54}_{28}\text{Ni}_{26}$	1392.3(4) [NDS54]	2619.7(6) [NDS54]
$^{56}_{28}\text{Ni}_{28}$	2700.6(7) [NDS56]	3923.6(13) [NDS56]
$^{58}_{28}\text{Ni}_{30}$	1454.21(9) [NDS58]	2459.21(14) [NDS58]
$^{60}_{28}\text{Ni}_{32}$	1332.514(4) [NDS60]	2505.753(4) [NDS60]
$^{62}_{28}\text{Ni}_{34}$	1172.98(10) [NDS62]	2336.52(14) [NDS62]
$^{64}_{28}\text{Ni}_{36}$	1345.75(5) [NDS64]	2610.1(1) [NDS64]
$^{66}_{28}\text{Ni}_{38}$	1425.12(10) [Bro12]	3185.33(14) [Bro12]
$^{68}_{28}\text{Ni}_{40}$	2032.93(20) [Bro12]	3147.45(22) [Bro12]
$^{70}_{28}\text{Ni}_{42}$	1259.55(5) [NDS70]	2229.44(6) [NDS70]
$^{72}_{28}\text{Ni}_{44}$	1095.2(5) [Chi11]	1938.2(11) [Chi11]
$^{74}_{28}\text{Ni}_{46}$	1024(1) [Maz05]	1763(1) [Maz05]

Table D.1.: Experimental level energies  $E(2_1^+)$ ,  $E(4_1^+)$  for even-even nuclei characterized by  $20 \leq Z \leq 28$  and  $20 \leq N \leq 46$ .

Particle	$B(E2; 2_1^+ \rightarrow 0_{\text{gs}}^+) \text{ (e}^2\text{fm}^4)$	$B(E2; 4_1^+ \rightarrow 2_1^+) \text{ (e}^2\text{fm}^4)$
$^{40}_{20}\text{Ca}_{20}$	$17.9^{+4.5}_{-3.0}$ [NDS40] <sup>D</sup>	$551.6^{+192.8}_{-88.3}$ [NDS40] <sup>D</sup>
$^{42}_{20}\text{Ca}_{22}$	$83.1^{+3.1}_{-2.9}$ [NDS42] <sup>R,D,C</sup>	$72.9^{+12.1}_{-9.1}$ [NDS42] <sup>R</sup>
$^{44}_{20}\text{Ca}_{24}$	$101.1^{+5.9}_{-5.3}$ [NDS44] <sup>R,D,C</sup>	$165.1^{+96.3}_{-44.5}$ [NDS44] <sup>R,D</sup>
$^{46}_{20}\text{Ca}_{26}$	$33.7^{+2.3}_{-2.1}$ <sup>4</sup>	-
$^{48}_{20}\text{Ca}_{28}$	$17.8^{+0.9}_{-0.8}$ [NDS48] <sup>D</sup>	2.7(1) [NDS48] <sup>R</sup>

Continued on next page ...

<sup>4</sup>Weighted mean of  $35.6(26) \text{ e}^2\text{fm}^4$  [NDS46]<sup>C</sup>,  $39.8^{+22.1}_{-9.6}$  [Men09]<sup>R</sup> and  $25.4^{+5.5}_{-3.8}$  [Mon12]<sup>R</sup>.

... continued..

Particle	$B(E2; 2_1^+ \rightarrow 0_{gs}^+) (e^2\text{fm}^4)$	$B(E2; 4_1^+ \rightarrow 2_1^+) (e^2\text{fm}^4)$
$^{50}_{20}\text{Ca}_{30}$	$7.5(2)^5$	-
$^{52}_{20}\text{Ca}_{32}$	-	-
$^{54}_{20}\text{Ca}_{32}$	-	-
$^{42}_{22}\text{Ti}_{20}$	$144.2^{+47.4}_{-28.4}$ [NDS42] <sup>D</sup>	$< 228$ [NDS42] <sup>D</sup>
$^{44}_{22}\text{Ti}_{22}$	$123.0^{+42.8}_{-25.2}$ [NDS44] <sup>D</sup>	$279^{+55.8}_{-39.9}$ [NDS44] <sup>D</sup>
$^{46}_{22}\text{Ti}_{24}$	$192.0(53)$ [NDS46] <sup>C,D,O</sup>	$198.5^{+13.6}_{-11.5}$ [NDS46] <sup>C,D,O</sup>
$^{48}_{22}\text{Ti}_{26}$	$152.8^{+3.9}_{-3.7}$ [NDS48] <sup>C,D,O</sup>	$191.7^{+19.4}_{-16.1}$ [NDS48] <sup>D</sup>
$^{50}_{22}\text{Ti}_{28}$	$59.1^{+2.0}_{-1.9}$ [NDS50] <sup>C,D,O</sup>	$60.5^{+15.9}_{-10.4}$ [NDS50] <sup>R</sup>
$^{52}_{22}\text{Ti}_{30}$	$123.6^{+5.0}_{-4.6}$ [NDS52] <sup>D</sup>	$52.5^{+7.2}_{-5.7}$ [NDS52] <sup>D</sup>
$^{54}_{22}\text{Ti}_{32}$	$71.4(126)$ [Din05] <sup>IC</sup>	-
$^{56}_{22}\text{Ti}_{34}$	$119.8(394)$ [Din05] <sup>IC</sup>	-
$^{58}_{22}\text{Ti}_{36}$	-	-
$^{60}_{22}\text{Ti}_{38}$	-	-
$^{46}_{24}\text{Cr}_{22}$	$186(40)$ [Yam05] <sup>IC</sup>	-
$^{48}_{24}\text{Cr}_{24}$	$323.2^{+39.8}_{-31.9}$ [NDS48] <sup>R</sup>	$278.8^{+30.1}_{-24.8}$ [NDS48] <sup>D,O</sup>
$^{50}_{24}\text{Cr}_{26}$	$212.2^{+6.8}_{-6.4}$ [NDS50] <sup>C,D,R,O</sup>	$160.4^{+19.4}_{-15.7}$ [NDS50] <sup>C,R,D</sup>
$^{52}_{24}\text{Cr}_{28}$	$112(6)$ [NDS52] <sup>C</sup>	$118.3^{+40.2}_{-40.6}$ [NDS52] <sup>D</sup>
$^{54}_{24}\text{Cr}_{30}$	$174(8)$ [NDS54] <sup>C</sup>	$315.9^{+145.8}_{-75.8}$ [NDS54] <sup>D</sup>
$^{56}_{24}\text{Cr}_{32}$	$143.5(38)^6$	$185.8(64)$ [Sei11] <sup>R</sup>
$^{58}_{24}\text{Cr}_{34}$	$192.1^{17.7}_{-16.1}$ <sup>7</sup>	$221^{+36}_{-28}$ [Bra15] <sup>R</sup>
$^{60}_{24}\text{Cr}_{36}$	$242^{+23}_{-21}$ <sup>8</sup>	$433^{+90}_{-64}$ [Bra15] <sup>R</sup>
$^{62}_{24}\text{Cr}_{38}$	$342.8^{+27.4}_{-23.9}$ <sup>9</sup>	$589^{+79}_{-62}$ [Bra15] <sup>R</sup>
$^{64}_{24}\text{Cr}_{40}$	$312(79)$ [Cra13] <sup>IC</sup>	-
$^{66}_{24}\text{Cr}_{42}$	-	-
$^{48}_{26}\text{Fe}_{22}$	-	-
$^{50}_{26}\text{Fe}_{24}$	$280(60)$ [Yam05] <sup>IC</sup>	-
$^{52}_{26}\text{Fe}_{26}$	$164(20)$ [Yur04] <sup>IC</sup>	$302.9^{+89.1}_{-56.1}$ [NDS52] <sup>D</sup>
$^{54}_{26}\text{Fe}_{28}$	$135.0^{+3.7}_{-3.5}$ [NDS54] <sup>C</sup>	$77.1^{+19.3}_{-12.9}$ [NDS54] <sup>R</sup>
$^{56}_{26}\text{Fe}_{30}$	$215^{+8.5}_{-7.9}$ [NDS56] <sup>C</sup>	$304.9^{+70.4}_{-48.1}$ [NDS56] <sup>D</sup>
$^{58}_{26}\text{Fe}_{32}$	$246.8(72)$ [NDS58] <sup>C</sup>	$624.5^{+104.1}_{-78.1}$ [NDS58] <sup>D</sup>
$^{60}_{26}\text{Fe}_{34}$	$198.5^{+21.4}_{-17.4}$ [Lju10] <sup>R</sup>	$191.1^{+64.7}_{-38.6}$ [NDS60] <sup>R</sup>

Continued on next page ...

<sup>5</sup>Weighted mean of  $7.5(2) e^2\text{fm}^4$  [Val06]<sup>R</sup> and  $7.3^{+0.6}_{-0.5} e^2\text{fm}^4$  [Ril14]<sup>D</sup>.

<sup>6</sup>Weighted mean of  $110(38) e^2\text{fm}^4$  [Bür05]<sup>IC</sup> and  $143.8(38) e^2\text{fm}^4$  [Sei11]<sup>R</sup>.

<sup>7</sup>Weighted mean of  $197(36) e^2\text{fm}^4$  [Bür05]<sup>IC</sup>,  $172(25) e^2\text{fm}^4$  [Bau12]<sup>IC</sup> and  $227^{+35}_{-26}$  [Bra15]<sup>R</sup>.

<sup>8</sup>Weighted mean of  $221(29) e^2\text{fm}^4$  [Bau12]<sup>IC</sup> and  $279^{+38}_{-30} e^2\text{fm}^4$  [Bra15]<sup>R</sup>.

<sup>9</sup>Weighted mean of  $325(44)$  [Bau12]<sup>IC</sup>,  $321^{+60}_{-49}$  [Bau12]<sup>O</sup> and  $371^{+43}_{-35} e^2\text{fm}^4$  [Bra15]<sup>R</sup>.

... continued.

Particle	$B(E2; 2_1^+ \rightarrow 0_{gs}^+) (e^2\text{fm}^4)$	$B(E2; 4_1^+ \rightarrow 2_1^+) (e^2\text{fm}^4)$
$^{62}_{26}\text{Fe}_{36}$	204(17) <sup>10</sup>	$279^{+89}_{-54}$ [Kli17] <sup>R</sup>
$^{64}_{26}\text{Fe}_{38}$	$347.0^{+32.6}_{-31.6}$ <sup>11</sup>	>470 [Kli17] <sup>R</sup>
$^{66}_{26}\text{Fe}_{40}$	304(20) <sup>12</sup>	-
$^{68}_{26}\text{Fe}_{42}$	356(44) [Cra13] <sup>IC</sup>	-
$^{70}_{26}\text{Fe}_{44}$	-	-
$^{72}_{26}\text{Fe}_{46}$	-	-
$^{52}_{28}\text{Ni}_{24}$	-	-
$^{54}_{28}\text{Ni}_{26}$	122(24) [NDS54]	-
$^{56}_{28}\text{Ni}_{28}$	$75^{+34}_{-30}$ [NDS56]	< 296.6 [NDS56]
$^{58}_{28}\text{Ni}_{30}$	$134.0^{+4.5}_{-4.2}$ [NDS58] <sup>C,D,O</sup>	$149.8^{+18.2}_{-14.6}$ [NDS58] <sup>C</sup>
$^{60}_{28}\text{Ni}_{32}$	$104.0^{+18.9}_{-19.5}$ [NDS60] <sup>D,O</sup>	$77.5^{+33.7}_{-18}$ [NDS60] <sup>C</sup>
$^{62}_{28}\text{Ni}_{34}$	$176.5^{+5.0}_{-4.7}$ [NDS62] <sup>C,D,O</sup>	$309.8^{+55.2}_{-67.6}$ [NDS62] <sup>D</sup>
$^{64}_{28}\text{Ni}_{36}$	$118.3^{+3.9}_{-3.7}$ [NDS64] <sup>D</sup>	$101.6^{+19.6}_{-14.2}$ [NDS64] <sup>D</sup>
$^{66}_{28}\text{Ni}_{38}$	120(40) [Sor02] <sup>IC</sup>	-
$^{68}_{28}\text{Ni}_{40}$	52(8) [NDS68] <sup>IC,C</sup>	-
$^{70}_{28}\text{Ni}_{42}$	172(28) [Per06] <sup>IC</sup>	-
$^{72}_{28}\text{Ni}_{44}$	74(10) [Kol16] <sup>R</sup>	50(9) [Kol16] <sup>R</sup>
$^{74}_{28}\text{Ni}_{46}$	$128.4^{+43.2}_{-45.2}$ [Mar14] <sup>IC</sup>	-

Table D.2.: Experimental data for even-even nuclei with  $20 \leq Z \leq 28$  and  $20 \leq N \leq 46$ . The type of measurements that led to the quoted  $B(E2)$  values are distinguished and marked with R (RDDS), D (DSAM), C (Coulomb excitation at safe energies), IC (Coulomb excitation at intermediate energies) and O (others), respectively.

<sup>10</sup>Weighted mean of 214(26) [Lju10]<sup>R</sup>, 198(25) [Rot11]<sup>R</sup> and 190(58) [Gaf15]<sup>C</sup>.

<sup>11</sup>Weighted mean of  $470^{+210}_{-110} e^2\text{fm}^4$  [Lju10]<sup>R</sup> and 198(25)  $e^2\text{fm}^4$  [Rot11]<sup>R</sup>.

<sup>12</sup>Weighted mean of 332(34) [Rot11]<sup>R</sup> and 290(24) [Cra13]<sup>IC</sup>.

## E. Theoretical Calculations

### E.1. Shell-Model Calculations for $^{56,58,60,62}\text{Cr}$

Signature	$^{56}\text{Cr}$	$^{58}\text{Cr}$	$^{60}\text{Cr}$	$^{62}\text{Cr}$
$E(2_1^+)$ (keV)	920	879	773	770
$E(4_1^+)$ (keV)	1841	1771	1623	1524
$E(6_1^+)$ (keV)	3007	2991	2549	2392
$E_\gamma(2_1^+ \rightarrow 0_{\text{gs}}^+)$ (keV)	920	879	773	770
$E_\gamma(4_1^+ \rightarrow 2_1^+)$ (keV)	920	892	850	754
$E_\gamma(6_1^+ \rightarrow 4_1^+)$ (keV)	1166	1220	926	868
$B(E2; 2_1^+ \rightarrow 0_{\text{gs}}^+)$ ( $e^2\text{fm}^4$ )	166	157	141	109
$B(E2; 4_1^+ \rightarrow 2_1^+)$ ( $e^2\text{fm}^4$ )	228	178	178	130
$B(E2; 6_1^+ \rightarrow 4_1^+)$ ( $e^2\text{fm}^4$ )	211	176	176	120

Table E.1.: Key signatures deduced from shell-model calculations for  $^{56,58,60,62}\text{Cr}$  using the KB3G interaction [Pov01] within the full  $fp$  space.  $B(E2)$  values are calculated using modified effective charges  $e_\pi = 1.31e$  and  $e_\nu = 0.46e$ .

Orbital	$^{58}\text{Cr}$				$^{60}\text{Cr}$				$^{62}\text{Cr}$			
	$0_{\text{gs}}^+$	$2_1^+$	$4_1^+$	$6_1^+$	$0_{\text{gs}}^+$	$2_1^+$	$4_1^+$	$6_1^+$	$0_{\text{gs}}^+$	$2_1^+$	$4_1^+$	$6_1^+$
$\nu g_{9/2}$	0.34	0.31	0.28	0.27	1.45	1.53	1.57	1.64	2.64	2.80	2.92	3.05
$\nu d_{5/2}$	0.07	0.07	0.06	0.06	0.30	0.37	0.39	0.40	0.62	0.72	0.75	0.79
$\pi f_{7/2}$	3.53	3.53	3.61	3.69	3.34	3.29	3.31	3.29	3.17	3.14	3.11	3.07
$\pi p_{3/2}$	0.25	0.28	0.26	0.20	0.30	0.36	0.37	0.38	0.39	0.45	0.46	0.47
$\pi f_{5/2}$	0.19	0.15	0.11	0.10	0.31	0.29	0.27	0.27	0.39	0.38	0.38	0.38

Table E.2.: Calculated occupation numbers [Len15] in the wave function of low-lying yrast states in  $^{58,60,62}\text{Cr}$  using the LNPS interaction.

Signature	$^{58}\text{Cr}$	$^{60}\text{Cr}$	$^{62}\text{Cr}$		$^{64}\text{Cr}$
	LNPS	LNPS	LNPS	LNPS- $m$	LNPS- $m$
$E(2_1^+)$ (keV)	876	740	513	460	430
$E(4_1^+)$ (keV)	1756	1599	1245	1180	1130
$E(6_1^+)$ (keV)	3018	2602	-	-	-
$E_\gamma(2_1^+ \rightarrow 0_{\text{gs}}^+)$ (keV)	876	740	513	460	430
$E_\gamma(4_1^+ \rightarrow 2_1^+)$ (keV)	880	859	732	720	700
$E_\gamma(6_1^+ \rightarrow 4_1^+)$ (keV)	1262	1003	-	-	-
$B(\text{E}2; 2_1^+ \rightarrow 0_{\text{gs}}^+)$ ( $e^2\text{fm}^4$ )	184	262	340	378	388
$B(\text{E}2; 4_1^+ \rightarrow 2_1^+)$ ( $e^2\text{fm}^4$ )	227	372	507	562	534
$B(\text{E}2; 6_1^+ \rightarrow 4_1^+)$ ( $e^2\text{fm}^4$ )	191	374	-	-	-

Table E.3.: Key signatures deduced from shell-model calculations for  $^{56,58,60,62}\text{Cr}$  using the LNPS [Len10; Len15] and modified LNPS- $m$  [San15] interaction. The valence space was spanned by the  $fp$  orbitals and the neutron  $g_{9/2}$  and  $d_{5/2}$  orbitals.  $B(\text{E}2)$  values are calculated using modified effective charges  $e_\pi = 1.31e$  and  $e_\nu = 0.46e$ .

## E.2. Shell-Model Calculations for $^{59,61,63}\text{Mn}$

Signature	LNPS- <i>m</i>		
	$^{59}\text{Mn}$	$^{61}\text{Mn}$	$^{63}\text{Mn}$
<b>Level energies in keV</b>			
$E(7/2_1^-)$	157.6	201.9	258.2
$E(9/2_1^-)$	1258.9	1193.9	975.5
$E(11/2_1^-)$	1410.5	1369.7	1293.9
<b>Level lifetimes in ps</b>			
$\tau(7/2_1^-)$	319 [877]	107 [227]	20.6 [22.6]
$\tau(9/2_1^-)$	0.28 [0.48]	0.26 [0.39]	0.41 [0.59]
$\tau(11/2_1^-)$	1.7 [2.0]	1.6 [1.7]	1.3 [1.0]
<b><math>B(\text{E}2)</math> values in <math>e^2\text{fm}^4</math></b>			
$B(\text{E}2; 7/2_1^- \rightarrow 5/2_1^-)$	291	374	502
$B(\text{E}2; 9/2_1^- \rightarrow 7/2_1^-)$	197	242	364
$B(\text{E}2; 9/2_1^- \rightarrow 5/2_1^-)$	84	123	156
$B(\text{E}2; 11/2_1^- \rightarrow 9/2_1^-)$	160	191	279
$B(\text{E}2; 11/2_1^- \rightarrow 7/2_1^-)$	152	220	282
<b><math>B(\text{M}1)</math> values in <math>\mu_N^2</math></b>			
$B(\text{M}1; 7/2_1^- \rightarrow 5/2_1^-)$	0.0458	0.0636	0.1584
$B(\text{M}1; 9/2_1^- \rightarrow 7/2_1^-)$	0.1201	0.1853	0.3338
$B(\text{M}1; 11/2_1^- \rightarrow 9/2_1^-)$	0.1815	0.3696	0.6225
<b>Branching ratios in %</b>			
$BR(7/2_1^- \rightarrow 5/2_1^-)$	100	100	100
$BR(9/2_1^- \rightarrow 7/2_1^-)$	90.8 [93.6]	90.5 [93.0]	93.0 [93.7]
$BR(9/2_1^- \rightarrow 5/2_1^-)$	9.2 [6.4]	9.5 [7.0]	7.0 [6.3]
$BR(11/2_1^- \rightarrow 9/2_1^-)$	1.9 [10.4]	5.7 [16.7]	46.3 [61.3]
$BR(11/2_1^- \rightarrow 7/2_1^-)$	98.1 [89.6]	94.3 [83.3]	53.7 [38.7]
<b>Magnetic moments in <math>\mu_N</math></b>			
$\mu(5/2^-)$	3.57	3.55	3.49
$\mu(7/2^-)$	4.61	4.48	4.13
$\mu(9/2^-)$	4.90	4.15	3.70
$\mu(11/2^-)$	6.07	5.09	4.36
<b>Quadrupole moments in <math>e^2\text{fm}</math></b>			
$Q_s(5/2^-)$	32.8	37.3	43.0
$Q_s(7/2^-)$	7.7	9.4	9.8
$Q_s(9/2^-)$	-8.5	-4.9	-8.4
$Q_s(11/2^-)$	-8.9	-3.3	-11.6

Table E.4.: Shell-model results for neutron-rich  $^{59,61,63}\text{Mn}$  isotopes using the LNPS-*m* interaction with modified effective charges ( $e_\pi = 1.31e$ ,  $e_\nu = 0.46e$ ) and standard  $g$ -factors ( $g_p^s = 5.586$ ,  $g_n^s = -3.826$ ,  $g_p^l = 1.0$ ,  $g_n^l = 0.0$ ).

Signature	$^{59}\text{Mn}$	KB3G $^{61}\text{Mn}$	$^{63}\text{Mn}$
<b>Level energies in keV</b>			
$E(7/2_1^-)$	124	185	69
$E(9/2_1^-)$	1291	1177	1073
$E(11/2_1^-)$	1250	1192	1057
<b>Level lifetimes in ps</b>			
$\tau(7/2_1^-)$	564 [762]	76.7 [125]	6744 [138]
$\tau(9/2_1^-)$	0.24 [0.50]	1.0 [1.5]	18.2 [41.6]
$\tau(11/2_1^-)$	2.8 [2.1]	5.4 [2.5]	7.9 [6.2]
<b><math>B(\text{E}2)</math> values in <math>e^2\text{fm}^4</math></b>			
$B(\text{E}2; 7/2_1^- \rightarrow 5/2_1^-)$	250	225	162
$B(\text{E}2; 9/2_1^- \rightarrow 7/2_1^-)$	121	89	34.5
$B(\text{E}2; 9/2_1^- \rightarrow 5/2_1^-)$	69	71	28.9
$B(\text{E}2; 11/2_1^- \rightarrow 9/2_1^-)$	-	124	-
$B(\text{E}2; 11/2_1^- \rightarrow 7/2_1^-)$	163	147	110
<b><math>B(\text{M}1)</math> values in <math>\mu_N^2</math></b>			
$B(\text{M}1; 7/2_1^- \rightarrow 5/2_1^-)$	0.052	0.1164	0.0256
$B(\text{M}1; 9/2_1^- \rightarrow 7/2_1^-)$	0.1225	0.0406	0.000002
$B(\text{M}1; 11/2_1^- \rightarrow 9/2_1^-)$	-	0.2477	-
<b>Branching ratios in %</b>			
$BR(7/2_1^- \rightarrow 5/2_1^-)$	100	100	100
$BR(9/2_1^- \rightarrow 7/2_1^-)$	92.5 [94.6]	80.3 [83.9]	8.5 [18.8]
$BR(9/2_1^- \rightarrow 5/2_1^-)$	7.5 [5.4]	19.7 [16.1]	91.5 [81.2]
$BR(11/2_1^- \rightarrow 9/2_1^-)$	- [-]	0.01 [16.8]	- [81.8]
$BR(11/2_1^- \rightarrow 7/2_1^-)$	100 [100]	99.99 [83.2]	100 [18.2]

Table E.5.: Shell-model results for neutron-rich  $^{59,61,63}\text{Mn}$  isotopes using the KB3G interaction with modified effective charges ( $e_\pi = 1.31e, e_\nu = 0.46e$ ) and standard  $g$ -factors ( $g_p^s = 5.586, g_n^s = -3.826, g_p^l = 1.0, g_n^l = 0.0$ ).

---

## F. Input Parameters for the Monte Carlo Simulation

### General attributes

- **ITERATIONS:**  $\langle N_{IT} \rangle$   
Sets the number of iterations in the Monte Carlo simulation.
- **OUTPUTFILE:**  $\langle \text{FILENAME} \rangle$   
Sets the name of the output file to which the events are written.
- **WRITEINBEAMEVENTS:**  $\langle \text{FLAG} \rangle$   
If  $\langle \text{FLAG} \rangle = 1(0)$  the incoming beam events are (not) written to the output file.
- **WRITEREACTIONEVENTS:**  $\langle \text{FLAG} \rangle$   
If  $\langle \text{FLAG} \rangle = 1(0)$  the reaction events are (not) written to the output file.
- **WRITEBEAMEVENTS:**  $\langle \text{FLAG} \rangle$   
If  $\langle \text{FLAG} \rangle = 1(0)$  the beam events related to information behind foils are (not) written to the output file.
- **WRITERECOILSBEHINDFOILS:**  $\langle \text{FLAG} \rangle$   
If  $\langle \text{FLAG} \rangle = 1(0)$  the recoil events related to information behind foils are (not) written to the output file.
- **WRITEGAMMAEVENTS:**  $\langle \text{FLAG} \rangle$   
If  $\langle \text{FLAG} \rangle = 1(0)$  the gamma events are (not) written to the output file.
- **DCBETAMETHOD:**  $\langle \text{METHOD} \rangle \langle \text{PAR} \rangle$   
This command controls the choice of the  $\beta$  velocity used for the Doppler reconstruction. If  $\langle \text{METHOD} \rangle = 0$ , a fixed  $\beta$  velocity equal to  $\langle \text{PAR} \rangle$  is used. If  $\langle \text{METHOD} \rangle = 1$ , the  $\beta$  velocity behind Foil  $\langle \text{PAR} \rangle$  is used. If  $\langle \text{METHOD} \rangle = 2$ , the precise  $\beta$  velocity of the recoil at the time of the  $\gamma$ -ray emission is used.
- **DCTHETAMETHOD:**  $\langle \text{METHOD} \rangle \langle \text{PAR} \rangle$   
This command controls the choice of the angle used in the Doppler reconstruction. If  $\langle \text{METHOD} \rangle = 0$ , a fixed angle equal to  $\langle \text{PAR} \rangle$  is used. If  $\langle \text{METHOD} \rangle = 1$ , the angle behind foil  $\langle \text{PAR} \rangle$  is used. If  $\langle \text{METHOD} \rangle = 2$ , the precise emission angle is used.

---

## Beam attributes

- **BEAM:** <LABEL> <A<sub>B</sub>> <Z<sub>B</sub>>  
The beam is labelled and its mass number  $A_B$  and atomic number  $Z_B$  are set.
- **BEAMMASS:** <MASS>  
The beam mass  $m_B$  is set in atomic mass units.
- **BEAMPOXPROFILE:** <METHOD> <PAR1> <PAR2>  
This command controls the  $x$  coordinate profile of the incoming beam given in mm. If <METHOD> = 0, a Gaussian distribution  $\varrho_G(\bar{x}, \sigma_x)$  with mean  $\bar{x} = \langle \text{PAR1} \rangle$  and standard deviation  $\sigma_x = \langle \text{PAR1} \rangle$  is taken. If <METHOD> = 1, a user defined distribution of the  $x$  coordinate is taken which is defined in the file <PAR1> (<PAR2> is not needed in this case). The input file consists of three columns and in each line the probability (third column) of a  $x$ -coordinate between  $x_{\min}$  (second column) and  $x_{\max}$  (third column) is stored.
- **BEAMPOZ:** <POSZ>  
This command sets the initial  $z$ -coordinate of the beam given in cm.
- **BEAMENERGYPROFILE:** <METHOD> <PAR1> <PAR2>  
This command controls the total kinetic energy profile (in MeV) of the incoming beam. If <METHOD> = 0, a Gaussian distribution  $\varrho_G(\bar{E}, \sigma_E)$  with mean  $\bar{E} = \langle \text{PAR1} \rangle$  and standard deviation  $\sigma_E = \langle \text{PAR1} \rangle$  is taken. If <METHOD> = 1, a user defined energy distribution given in the file <PAR1> is taken (<PAR2> is not needed in this case). The input file consists of three columns and in each line the probability (third column) of a beam energy between  $E_{\min}$  (second column) and  $E_{\max}$  (third column) is stored.
- **BEAMANGLEPROFILE:** <METHOD> <PAR1> <PAR2>  
This command controls the direction of the incoming beam in term of an emission angle  $\alpha$  given in degree. If <METHOD> = 0, a Gaussian distribution  $\varrho_G(\bar{\alpha}, \sigma_\alpha)$  with mean  $\bar{\alpha} = \langle \text{PAR1} \rangle$  and standard deviation  $\sigma_\alpha = \langle \text{PAR1} \rangle$  is taken. If <METHOD> = 1, a user-defined distribution given in the file <PAR1> is taken. The input file consists of three columns and in each line the probability (third column) of an angle  $\alpha$  between  $\alpha_{\min}$  (second column) and  $\alpha_{\max}$  (third column) are stored.
- **ENERGYLOSSBEAM:** <FOIL> <METHOD> <PAR>  
This command controls for each foil the energy loss (in MeV/(mg/cm<sup>2</sup>)) of the beam. If <METHOD> = 0, a constant energy loss equal to <PAR> is taken. If <METHOD> = 1, user-defined stopping powers to calculate the energy loss are taken from the file <PAR>. The input file consists of five columns. The electronic and nuclear stopping powers at specific beam energies (first column) are listed in the second and third column, with corresponding relative uncertainties listed in the fourth and fifth column. Precise estimates of the stopping powers may be calculated using tools such as SRIM [Zie10]. Within the simulation, specific stopping powers are calculated by interpolation of the tabulated values.

- STRAGGLINGBEAM: <FOIL> <METHOD> <PAR>  
This command controls for each foil the lateral straggling of the beam given in  $\mu\text{m}/\text{mm}$ . If <METHOD>=0, a constant lateral straggling equal to <PAR> is taken. If <METHOD>=1, user-defined lateral straggling information is taken from the file <PAR>. The input file consists of three columns. The projected range (second column) and lateral straggling parameters (third column) at specific energies (first column) are listed. Precise estimates of the lateral straggling may be calculated using tools such as SRIM [Zie10]. Within the simulation, specific lateral straggling parameters for given energies are calculated by interpolation of the tabulated values.

## Foil attributes

- PLUNGERFOILS: <NRFOILS>  
This command sets the number of foils.
- ADDPLUNGERFOIL: <FOIL> <LABEL> <A> <Z> <DENS.> <THICKN.>  
Each foil  $i$  is identified by a label, its mass number  $A_{F,i}$ , its atomic number  $Z_{F,i}$ , its density  $\rho_{F,i}$  (in  $\text{g}/\text{cm}^3$ ) and its thickness  $\Delta T$  (in  $\mu\text{m}$ ).
- PLACEPLUNGERFOIL: <FOIL> <OPTIONZ> < $\bar{x}$ > <z> < $\Delta X$ > <ANGLE>  
Each foil  $i$  is placed in space based on its mean  $x$ -coordinate  $\bar{x}$  (in mm) assuming a width < $\Delta X$ > along the  $x$ -axis. With respect to the  $z$  coordinate three options are available. If <OPTIONZ>=0 (1,2), the left side (centre, right side) of the foil is placed at the  $z$ -coordinate <z> (in mm). The foil  $i$  is then rotated by an angle  $\alpha_{F,i}$ .
- DIVIDEPLUNGERFOIL: <FOIL> <SEGMENTS>  
Each foil is divided into segments.

## Reaction attributes

- DECAYScheme: <FILEDECAYScheme>  
This command sets the name of the file in which information on the decay scheme is stored. This file contains information on excited states in terms of level energies and level lifetimes. In addition, allowed transitions characterized by their branching ratios are listed in this file.
- RECOILMASS: <MASS>  
This command sets the mass  $m_r$  (in atomic mass units) of the considered recoil.
- REACTIONS: <NRREACTIONS>  
This commands sets the number of reactions that are considered in the simulation.
- REACTIONPROBABILITY: <REACTION> <PAR>  
For each reaction  $r$  the relative probability is set with this command.

- 
- **REACTIONFOILPROBABILITY:**  $\langle \text{REACTION} \rangle \langle \text{PFOIL1} \rangle \dots \langle \text{PLASTFOIL} \rangle$   
This command sets for each reaction  $r$  the probability of this reaction to happen in the available foils.
  - **REACTIONEXCScheme:**  $\langle \text{REACTION} \rangle \langle \text{FILENAME} \rangle$   
This command sets for each reaction  $r$  the name of the file which contains information on the probabilities to excite specific states by this reaction.
  - **REACTIONNUCLEONEXCHANGE:**  $\langle \text{REACTION} \rangle \langle \text{DELTA A} \rangle \langle \text{DELTA Z} \rangle$   
This command sets the number of transferred nucleons  $\Delta A$  and protons  $\Delta Z$  with respect to the beam.
  - **REACTIONANGULARDISTRIBUTION:**  $\langle \text{REACTION} \rangle \langle \text{METH} \rangle \langle \text{P1} \rangle \langle \text{P2} \rangle$   
This command defines for each reaction the change of the recoil angle  $\Delta\alpha$  with respect to the beam direction given in degree. If  $\langle \text{METH} \rangle = 0$ , a Gaussian distribution  $\varrho(\overline{\Delta\alpha}, \sigma_{\Delta\alpha})$  is assumed with mean  $\overline{\Delta\alpha} = \langle \text{P1} \rangle$  and standard deviation  $\sigma_{\Delta\alpha} = \langle \text{P2} \rangle$ . If  $\langle \text{METH} \rangle = 1$ , a user-defined distribution stored in the file  $\langle \text{P1} \rangle$  is taken. The input file consists of three columns and in each line the probability (third column) of a reaction angle  $\Delta\alpha$  between  $\Delta\alpha_{\min}$  and  $\Delta\alpha_{\max}$  (second and third column) is stored.
  - **REACTIONMOMTRANSFER:**  $\langle \text{REACTION} \rangle \langle \text{METHOD} \rangle \langle \text{PAR1} \rangle \langle \text{PAR2} \rangle$   
This command defines for each reaction  $r$  the momentum transfer  $\Delta p$  given in MeV/c. If  $\langle \text{METHOD} \rangle = 0$ , a Gaussian distribution  $\varrho(\overline{\Delta p}, \sigma_{\Delta p})$  is assumed with mean  $\overline{\Delta p} = \langle \text{PAR1} \rangle$  and standard deviation  $\sigma_{\Delta p} = \langle \text{PAR2} \rangle$ . If  $\langle \text{METHOD} \rangle = 1$ , a user-defined distribution stored in the file  $\langle \text{PAR1} \rangle$  is taken. This file contains information related to the mean momentum transfer (second column) and its standard deviation (third column) for specific recoil angles (first column).

## Recoil attributes

- **RECOILLOSSBEAM:**  $\langle \text{FOIL} \rangle \langle \text{METHOD} \rangle \langle \text{PAR} \rangle$   
This command controls for each foil the energy loss (in MeV/(mg/cm<sup>2</sup>)) of the recoil. If  $\langle \text{METHOD} \rangle = 0$ , a constant energy loss equal to  $\langle \text{PAR} \rangle$  is taken. If  $\langle \text{METHOD} \rangle = 1$ , user-defined stopping powers to calculate the energy loss are taken from the file  $\langle \text{PAR} \rangle$ . The input file consists of five columns. The electronic and nuclear stopping powers at specific beam energies (first column) are listed in the second and third column, with corresponding relative uncertainties listed in the fourth and fifth column. Precise estimates of the stopping powers may be calculated using tools such as SRIM [Zie10]. Within the simulation, specific stopping powers are calculated by interpolation of the tabulated values.
- **STRAGGLINGRECOIL:**  $\langle \text{FOIL} \rangle \langle \text{METHOD} \rangle \langle \text{PAR} \rangle$   
This command controls for each foil the lateral straggling of the recoil given in  $\mu\text{m}/\text{mm}$ . If  $\langle \text{METHOD} \rangle = 0$ , a constant lateral straggling equal to  $\langle \text{PAR} \rangle$  is taken. If  $\langle \text{METHOD} \rangle = 1$ , user-defined lateral straggling information are taken from the file  $\langle \text{PAR} \rangle$ . The input file consists of three columns. The projected

range (second column) and lateral straggling parameters (third column) at specific energies (first column) are listed. Precise estimates of the lateral straggling may be calculated using tools such as SRIM [Zie10]. Within the simulation, specific lateral straggling parameters for given energies are calculated by interpolation of the tabulated values.

## Detector attributes

- DETECTOR: <NRDETS>  
This command defines the number of detectors.
- PLACEDETECTOR: <DET> <X1> <Z1> .. <X4> <Z4> <ANGLE> This command sets the coordinates (in mm) of the four edges of each detector, which is followed by a rotation by the given angle in degree.
- DETENERGYRES: <DET> <PAR1> <PAR2> <PAR3>  
This command defines the energy resolution  $\Delta E_{\text{res}}$  in MeV assuming the function  $\Delta E_{\text{res}} = \sqrt{\langle \text{PAR1} \rangle + \langle \text{PAR2} \rangle \cdot E + \langle \text{PAR3} \rangle \cdot E^2}$ .
- DETANGLERES: <DET> <PAR>  
This command defines the angular resolution in degree of the detector which is relevant for the Doppler reconstruction.
- EFFICIENCYMETHOD: <DET> <METHOD>  
This command defines for each detector how full photo peak-efficiencies are handled. If <METHOD> = 0, a global parametrization is used independent of the recoil position. In this case the efficiency is only corrected with respect to changes in the solid angles. If <METHOD> = 1, in total  $n = \langle \text{NRFOILS} \rangle$  efficiency parametrizations are considered, which are valid to describe efficiencies for decays taking place behind a specific foil (but before the following foil).
- EFFICIENCYFUNCTION: <DET> <I> <FUNCTION>  
This command defines for each detector the function to describe the efficiency. If <FUNCTION> = 0, a constant efficiency is taken for decays behind foil <I>. If <FUNCTION> = 1(2), the parametrization introduced in Ref [Gra85]([Deb84]) is taken.
- EFFICIENCYPAR: <DET> <RANGE> <PAR1> <PAR2> ...  
This command sets the efficiency parameters.
- SOLIDAPOS: <DET> <REFPOSX> <REFPOSZ>  
This command sets the reference coordinates for the efficiency parametrization.
- EFFICIENCYEMIN: <DET> <RANGE> <EMIN>  
This command sets for each detector the lower limit for the detection of  $\gamma$  rays.
- EFFICIENCYEMAX: <DET> <RANGE> <EMAX>  
This command sets for each detector the upper limit for the detection of  $\gamma$  rays.

---

## Glossary

A list of acronyms abbreviations and short notations commonly used in this work.

**Beam-only data** Data taken with no target material at the experimental place.

**$\beta$  velocity** Velocity of a particle with respect to the speed of light,  $\beta = v/c$ .

**CCF** Coupled Cyclotron Facility

**DAQ** Data Acquisition

**Fast component** Describes the peak related to  $\gamma$ -ray emissions before the degrader, characterized by a fast recoil  $\beta$  velocity.

**FRIB** Facility for Rare Isotope Beams

**FT** Fragmentation Target

**FWHM** Full Width at Half Maximum

**HPGe** High Purity Germanium

**NSCL** National Superconducting Cyclotron Laboratory

**MSU** Michigan State University

**RDDS** Recoil Distance Doppler-Shift. A technique to analyse lifetimes in the ps range.

**RIB** Radioactive Ion Beam

**SeGA** Segmented Germanium Array

**Slow component** Describes the peak related to  $\gamma$ -ray emissions behind the degrader, characterized by a slow recoil  $\beta$  velocity.

**Target-only data** Data taken with only the target material placed at the experimental place and with S800 optimized on the isotope of interest.

**TRIPLEX** Triple Plunger for Exotic beams.

**Zero Offset** The offset between electrical contact and extrapolated vanishing foil separation.

---

## Bibliography

- [Adr09] P. Adrich, D. Enderich, D. Miller, V. Moeller, R.P. Norris, K. Starosta, C. Vaman, P. Voss, and A. Dewald. “A simulation tool for Recoil Distance Method lifetime measurements at NSCL”. In: *Nuclear Instruments and Methods in Physics Research Section A: Accelerators, Spectrometers, Detectors and Associated Equipment* **598** (2009), pp. 454–464. DOI: 10.1016/j.nima.2008.09.055.
- [Ago03] S. Agostinelli et al. “Geant4 – a simulation toolkit”. In: *Nuclear Instruments and Methods in Physics Research Section A: Accelerators, Spectrometers, Detectors and Associated Equipment* **506** (2003), pp. 250–303. DOI: 10.1016/S0168-9002(03)01368-8.
- [Ale70] T.K. Alexander and A. Bell. “A target chamber for recoil-distance lifetime measurements”. In: *Nuclear Instruments and Methods* **81** (1970), pp. 22–26. DOI: 10.1016/0029-554X(70)90604-X.
- [Aoi09] N. Aoi et al. “Development of Large Deformation in  $^{62}\text{Cr}$ ”. In: *Physical Review Letters* **102**, 012502 (2009). DOI: 10.1103/PhysRevLett.102.012502.
- [Arn17] K. Arnsward et al. “Enhanced collectivity along the  $N=Z$  line: Lifetime measurements in  $^{44}\text{Ti}$ ,  $^{48}\text{Cr}$ , and  $^{52}\text{Fe}$ ”. In: *Physics Letters B* **772** (2017), pp. 599–606. DOI: <http://dx.doi.org/10.1016/j.physletb.2017.07.032>.
- [Ati] *ATIMA*. URL: <https://web-docs.gsi.de/~weick/atima/>.
- [Bab15] C. Babcock et al. “Evidence for Increased neutron and proton excitations between  $^{51-63}\text{Mn}$ ”. In: *Physics Letters B* **750** (2015), pp. 176–180. DOI: 10.1016/j.physletb.2015.09.012.
- [Bab16] C. Babcock et al. “Quadrupole moments of odd- $A$   $^{53-63}\text{Mn}$ : Onset of collectivity towards  $N = 40$ ”. In: *Physics Letters B* **760** (2016), pp. 387–392. DOI: 10.1016/j.physletb.2016.07.016.
- [Bas07] B. Bastin et al. “Collapse of the  $N = 28$  Shell Closure in  $^{42}\text{Si}$ ”. In: *Physical Review Letters* **99**, 022503 (2007), p. 022503. DOI: 10.1103/PhysRevLett.99.022503.
- [Bat10] H. Bateman. “Solution of a system of differential equations occurring in the theory of radioactive transformation”. In: *Proceedings of the Cambridge Philosophical Society, Mathematical and Physical Sciences* **15** (1910), pp. 423–427.
- [Bau12] T. Baugher et al. “Intermediate-energy Coulomb excitation of  $^{58,60,62}\text{Cr}$ : The onset of collectivity toward  $N = 40$ ”. In: *Physical Review C* **86**, 011305(R) (2012). DOI: 10.1103/PhysRevC.86.011305.
- [Bau16] T. Baugher et al. “In-beam  $\gamma$ -ray spectroscopy of  $^{63}\text{Mn}$ ”. In: *Physical Review C* **93**, 014313 (2016). DOI: 10.1103/PhysRevC.93.014313.

- [Baz03] D. Bazin, J.A. Caggiano, B.M. Sherrill, J. Yurkon, and A. Zeller. “The S800 spectrograph”. In: *Nuclear Instruments and Methods in Physics Research Section B: Beam Interactions with Materials and Atoms* **204** (2003), pp. 629–633. DOI: 10.1016/S0168-583X(02)02142-0.
- [Bla79] J. M. Blatt and V. F. Weisskopf. *Theoretical Nuclear Physics*. Springer-Verlag New York, 1979. DOI: 10.1007/978-1-4612-9959-2.
- [Boh52] A. Bohr. In: *Mat. Fys. Medd. K. Dan. Vidensk Selsk.* **26**.14 (1952).
- [Bra15] T. Braunroth et al. “Reduced transition strengths of low-lying yrast states in chromium isotopes in the vicinity of  $N = 40$ ”. In: *Physical Review C* **92**, 034306 (2015). DOI: 10.1103/PhysRevC.92.034306.
- [Bre08] N. Bree et al. “Coulomb excitation of  $^{68}\text{Ni}_{40}$  at “safe” energies”. In: *Physical Review C* **78**, 047301 (2008). DOI: 10.1103/PhysRevC.78.047301.
- [Bro12] R. Broda et al. “Spectroscopic study of the  $^{64,66,68}\text{Ni}$  isotopes populated in  $^{64}\text{Ni} + ^{238}\text{U}$  collisions”. In: *Physical Review C* **86**, 064312 (2012). DOI: 10.1103/PhysRevC.86.064312.
- [Bro14] B.A. Brown and W.D.M. Rae. “The Shell-Model Code NuShellX@MSU”. In: *Nuclear Data Sheets* **120** (2014), pp. 115–118. DOI: 10.1016/j.nds.2014.07.022.
- [Bro95] R. Broda et al. “ $N = 40$  Neutron Subshell Closure in the  $^{68}\text{Ni}$  Nucleus”. In: *Physical Review Letters* **74** (1995), pp. 868–871. DOI: 10.1103/PhysRevLett.74.868.
- [Bru97] R. Brun and F. Rademakers. “ROOT – An object oriented data analysis framework”. In: *Nuclear Instruments and Methods in Physics Research Section A: Accelerators, Spectrometers, Detectors and Associated Equipment* **389** (1997), pp. 81–86. DOI: 10.1016/S0168-9002(97)00048-X.
- [Bür05] A. Bürger et al. “Relativistic Coulomb excitation of neutron-rich  $^{54,56,58}\text{Cr}$ : On the pathway of magicity from  $N = 40$  to  $N = 32$ ”. In: *Physics Letters B* **622** (2005), pp. 29–34. DOI: 10.1016/j.physletb.2005.07.004.
- [Byr92] A.P. Byrne, K. Schiffer, G.D. Dracoulis, B. Fabricius, T. Kibédi, A.E. Stuchbery, and K.P. Lieb. “High-spin bandcrossing in  $^{129}\text{Ba}$ ”. In: *Nuclear Physics A* **548**.1 (1992), pp. 131–158. ISSN: 0375-9474. DOI: 10.1016/0375-9474(92)90080-4.
- [Cas00] R.F. Casten and N.V. Zamfir. “Evidence for a Possible E(5) Symmetry in  $^{134}\text{Ba}$ ”. In: *Physical Review Letters* **85** (2000), pp. 3584–3586. DOI: 10.1103/PhysRevLett.85.3584.
- [Cas07] R F Casten and E A McCutchan. “Quantum phase transitions and structural evolution in nuclei”. In: *Journal of Physics G: Nuclear and Particle Physics* **34**.7 (2007), R285. DOI: 10.1088/0954-3899/34/7/R01.
- [Cau02] E. Caurier, F. Nowacki, and A. Poves. “Large-scale shell model calculations for exotic nuclei”. In: *The European Physical Journal A - Hadrons and Nuclei* **15** (2002), pp. 145–150. DOI: 10.1140/epja/i2001-10243-7.

- [Cau99] E. Caurier and F. Nowacki. “Present Status of Shell Model Techniques”. In: *Acta Physica Polonica B* **30** (1999), pp. 705–714.
- [Chi10] C.J. Chiara et al. “Influence of the  $\nu g_{9/2}$  orbital on level structures of neutron-rich  $^{61,62}\text{Mn}_{36,37}$ ”. In: *Physical Review C* **82**, 054313 (2010). DOI: 10.1103/PhysRevC.82.054313.
- [Chi11] C.J. Chiara et al. “Seniority, collectivity, and  $B(E2)$  enhancement in  $^{72}\text{Ni}$ ”. In: *Physical Review C* **84**, 037304 (2011). DOI: 10.1103/PhysRevC.84.037304.
- [Cle17] E. Clement et al. “Conceptual design of the AGATA  $1\pi$  array at GANIL”. In: *Nuclear Instruments and Methods in Physics Research Section A: Accelerators, Spectrometers, Detectors and Associated Equipment* **855** (2017), pp. 1–12. DOI: <http://dx.doi.org/10.1016/j.nima.2017.02.063>.
- [Cra09] H.L. Crawford et al. “Low-energy structure of  $^{61}\text{Mn}$  populated following  $\beta$  decay of  $^{61}\text{Cr}$ ”. In: *Physical Review C* **79**, 054320 (2009). DOI: 10.1103/PhysRevC.79.054320.
- [Cra10b] H.L. Crawford. “Evolution of nuclear shell structure:  $\beta$ -decay and isomeric properties of nuclei in and near the  $fp$  shell”. PhD thesis. Michigan State University, 2010.
- [Cra13] H.L. Crawford et al. “Quadrupole Collectivity in Neutron-Rich Fe and Cr Isotopes”. In: *Physical Review Letters* **110**, 242701 (2013). DOI: 10.1103/PhysRevLett.110.242701.
- [Dau11] J.M. Daugas et al. “ $\beta$ -decay measurements for  $N > 40$  Mn nuclei and inference of collectivity for neutron-rich Fe isotopes”. In: *Physical Review C* **83**, 054312 (2011). DOI: 10.1103/PhysRevC.83.054312.
- [Dav58] A.S. Davydov and G.F. Filippov. “Rotational states in even atomic nuclei”. In: *Nuclear Physics* **8** (1958), pp. 237–249. DOI: 10.1016/0029-5582(58)90153-6.
- [Dea05] A.N. Deacon et al. “Changes in  $\nu g_{9/2}$  shape polarisation across the odd neutron-rich Cr isotopes”. In: *Physics Letters B* **622** (2005), pp. 151–158. DOI: 10.1016/j.physletb.2005.07.005.
- [Dea11] A.N. Deacon et al. “Single-particle and collective structures in  $^{55}\text{Cr}$  and  $^{55}\text{V}$ ”. In: *Physical Review C* **83**, 064305 (2011). DOI: 10.1103/PhysRevC.83.064305.
- [Deb84] K. Debertin. “The effect of correlations in the efficiency calibration of germanium detectors”. In: *Nuclear Instruments and Methods in Physics Research Section A: Accelerators, Spectrometers, Detectors and Associated Equipment* **226** (1984), pp. 566–568. DOI: 10.1016/0168-9002(84)90084-6.
- [Dét79] C. Détraz, D. Guillemaud, G. Huber, R. Klapisch, M. Langevin, F. Naulin, C. Thibault, L.C. Carraz, and F. Touchard. “Beta decay of  $^{27-32}\text{Na}$  and their descendants”. In: *Physical Review C* **19** (1979), pp. 164–176. DOI: 10.1103/PhysRevC.19.164.

- [Dew06] A. Dewald, B. Melon, O. Möller, J. Jolie, C. Fransen, K. Jessen, K.O.Zell, and K. Starosta. “A Plunger Apparatus for Relativistic Radioactive Beams”. In: *GSI Scientific Report 2005*. Gesellschaft für Schwerionenforschung mbH (GSI), 2006, p. 38.
- [Dew12] A. Dewald, O. Möller, and P. Petkov. “Developing the Recoil Distance Doppler-Shift technique towards a versatile tool for lifetime measurements of excited nuclear states”. In: *Progress in Particle and Nuclear Physics* **67** (2012), pp. 786–839. DOI: 10.1016/j.pnpnp.2012.03.003.
- [Die80] A.E.L. Dieperink, O. Scholten, and F. Iachello. “Classical Limit of the Interacting-Boson Model”. In: *Physical Review Letters* **44** (1980), pp. 1747–1750. DOI: 10.1103/PhysRevLett.44.1747.
- [Din05] D.-C. Dinca et al. “Reduced transition probabilities to the first  $2^+$  state in  $^{52,54,56}\text{Ti}$  and development of shell closures at  $N = 32, 34$ ”. In: *Physical Review C* **71**, 041302(R) (2005). DOI: 10.1103/PhysRevC.71.041302.
- [Dos07] C. Dossat et al. “The decay of proton-rich nuclei in the mass  $A = 36 - 56$  region”. In: *Nuclear Physics A* **792** (2007), pp. 18–86. DOI: 10.1016/j.nuclphysa.2007.05.004.
- [Duf96] M. Dufour and A.P. Zuker. “Realistic collective nuclear Hamiltonian”. In: *Physical Review C* **54** (1996), pp. 1641–1660. DOI: 10.1103/PhysRevC.54.1641.
- [ENSDF] ENSDF Database. URL: <http://www.nndc.bnl.gov/ensdf/>.
- [Fuc92] Y. Fuchi, M.H. Tanaka, S. Kubono, H. Kawashima, U. Takaku, and T. Ichihara. “High-resolution, two-dimensional focal-plane detectors for inter-mediate-energy heavy ions”. In: *Nuclear Science Symposium and Medical Imaging Conference, 1992., Conference Record of the 1992 IEEE*. 1992, pp. 172–174. DOI: 10.1109/NSSMIC.1992.301113.
- [Gad10] A. Gade et al. “Collectivity at  $N = 40$  in neutron-rich  $^{64}\text{Cr}$ ”. In: *Physical Review C* **81**, 051304(R) (2010). DOI: 10.1103/PhysRevC.81.051304.
- [Gad14] A. Gade et al. “Nuclear Structure Towards  $N = 40$   $^{60}\text{Ca}$ : In-Beam  $\gamma$ -Ray Spectroscopy of  $^{58,60}\text{Ti}$ ”. In: *Physical Review Letters* **112**, 112503 (2014). DOI: 10.1103/PhysRevLett.112.112503.
- [Gaf15] L. P. Gaffney et al. “Low-energy Coulomb excitation of  $^{62}\text{Fe}$  and  $^{62}\text{Mn}$  following in-beam decay of  $^{62}\text{Mn}$ ”. In: *The European Physical Journal A* **51** (2015), p. 136. DOI: 10.1140/epja/i2015-15136-6.
- [Gar07] P. E. Garrett et al. “Spectroscopy of the  $N = Z - 2$  nucleus  $^{46}\text{Cr}$  and mirror energy differences”. In: *Physical Review C* **75**, 014307 (2007). DOI: 10.1103/PhysRevC.75.014307.
- [Gau05] L. Gaudefroy et al. “Beta-decay studies of neutron-rich Sc-Cr nuclei”. In: *The European Physical Journal A* **23** (2005), pp. 41–48. DOI: 10.1140/epja/i2004-10068-x.
- [Gav80] A. Gavron. “Statistical model calculations in heavy ion reactions”. In: *Physical Review C* **21** (1980), pp. 230–236. DOI: 10.1103/PhysRevC.21.230.

- [Gin80] J.N. Ginocchio and M.W. Kirson. “Relationship between the Bohr Collective Hamiltonian and the Interacting-Boson Model”. In: *Physical Review Letters* **44** (1980), pp. 1744–1747. DOI: 10.1103/PhysRevLett.44.1744.
- [Gra85] P.W. Gray and A. Ahmad. “Linear classes of Ge(Li) detector efficiency functions”. In: *Nuclear Instruments and Methods in Physics Research Section A: Accelerators, Spectrometers, Detectors and Associated Equipment* **237** (1985), pp. 577–589. DOI: 10.1016/0168-9002(85)91069-1.
- [Grz98] R. Grzywacz et al. “New Island of  $\mu$ s Isomers in Neutron-Rich Nuclei around the  $Z = 28$  and  $N = 40$  Shell Closures”. In: *Physical Review Letters* **81** (1998), pp. 766–769. DOI: 10.1103/PhysRevLett.81.766.
- [Gué07] C. Guénaut et al. “High-precision mass measurements of nickel, copper, and gallium isotopes and the purported shell closure at  $N = 40$ ”. In: *Physical Review C* **75**, 044303 (2007). DOI: 10.1103/PhysRevC.75.044303.
- [Hac14] M. Hackstein and A. Dewald. “Velocity distribution in Recoil-Distance Doppler-Shift experiments”. In: *Nuclear Instruments and Methods in Physics Research Section A: Accelerators, Spectrometers, Detectors and Associated Equipment* **738** (2014), pp. 93–98. URL: <http://www.sciencedirect.com/science/article/pii/S0168900213015866>.
- [Hei08] S. Heinze. “Eine Methode zur Lösung beliebiger bosonischer und fermionischer Vielteilchensysteme”. PhD thesis. Universität zu Köln, 2008.
- [Hey16] H. Heylen et al. “Changes in nuclear structure along the Mn isotopic chain studied via charge radii”. In: *Physical Review C* **94**, 054321 (2016). DOI: 10.1103/physrevc.94.054321.
- [Hof09] C.R. Hoffman et al. “Evidence for a doubly magic  $^{24}\text{O}$ ”. In: *Physics Letters B* **672** (2009), pp. 17–21. DOI: 10.1016/j.physletb.2008.12.066.
- [Hon02] M. Honma, T. Otsuka, B.A. Brown, and T. Mizusaki. “Effective interaction for  $pf$ -shell nuclei”. In: *Physical Review C* **65**, 061301(R) (2002). DOI: 10.1103/PhysRevC.65.061301.
- [Hon05] M. Honma, T. Otsuka, B.A. Brown, and T. Mizusaki. “Shell-model description of neutron-rich  $pf$ -shell nuclei with a new effective interaction GXPF1”. In: *The European Physical Journal A - Hadrons and Nuclei* **25** (2005), pp. 499–502. DOI: 10.1140/epjad/i2005-06-032-2.
- [Hot06] N. Hotelling et al. “Yrast structure of  $^{64}\text{Fe}$ ”. In: *Physical Review C* **74**, 064313 (2006). DOI: 10.1103/PhysRevC.74.064313.
- [Iac00] F. Iachello. “Dynamic Symmetries at the Critical Point”. In: *Physical Review Letters* **85** (2000), pp. 3580–3583. DOI: 10.1103/PhysRevLett.85.3580.
- [Iac87] F. Iachello and A. Arima. *The Interacting Boson Model*. Cambridge Books Online. Cambridge University Press, 1987. ISBN: 9780511895517. DOI: 10.1017/CB09780511895517.
- [IAEA07] International Atomic Energy Agency. *Update of X Ray and Gamma Ray Decay Data Standards for Detector Calibration and Other Applications*. International Atomic Energy Agency, 2007.

- [Iwa16] H. Iwasaki, A. Dewald, T. Braunroth, C. Fransen, D. Smalley, A. Lemasson, C. Morse, K. Whitmore, and C. Loelius. “The TRIPLE PLunger for EXotic beams (TRIPLEX) for excited-state lifetime measurement studies on rare isotopes”. In: *Nuclear Instruments and Methods in Physics Research Section A: Accelerators, Spectrometers, Detectors and Associated Equipment* **806** (2016), pp. 123–131. DOI: 10.1016/j.nima.2015.09.091.
- [Kan09] R. Kanungo et al. “One-Neutron Removal Measurement Reveals  $^{24}\text{O}$  as a New Doubly Magic Nucleus”. In: *Physical Review Letters* **102**, 152501 (2009). DOI: 10.1103/PhysRevLett.102.152501.
- [Kli16] M. Klintefjord et al. “Structure of low-lying states in  $^{140}\text{Sm}$  studied by Coulomb excitation”. In: *Physical Review C* **93**, 054303 (2016). DOI: 10.1103/PhysRevC.93.054303.
- [Kli17] M. Klintefjord et al. “Measurement of lifetimes in  $^{62,64}\text{Fe}$ ,  $^{61,63}\text{Co}$ , and  $^{59}\text{Mn}$ ”. In: *Physical Review C* **95**, 024312 (2017). DOI: 10.1103/PhysRevC.95.024312.
- [Koi00] H. Koivisto, P. Heikkinen, V. Hänninen, A. Lassila, H. Leinonen, V. Nieminen, J. Pakarinen, K. Ranttila, J. Ärje, and E. Liukkonen. “The first results from the new JYFL 14 GHz ECRIS”. In: *Proceedings of the Workshop on Production of Intense Beams of Highly Charged Ions*. Vol. **72**. 2000, pp. 83–88.
- [Kol16] K. Kolos et al. “Direct Lifetime Measurements of the Excited States in  $^{72}\text{Ni}$ ”. In: *Physical Review Letters* **116**, 122502 (2016). DOI: 10.1103/PhysRevLett.116.122502.
- [Kot14] J. Kotila and S. M. Lenzi. “Collective features of Cr and Fe isotopes”. In: *Physical Review C* **89**, 064304 (2014). DOI: 10.1103/PhysRevC.89.064304.
- [Lan03] K. Langanke, J. Terasaki, F. Nowacki, D. J. Dean, and W. Nazarewicz. “How magic is the magic  $^{68}\text{Ni}$  nucleus?” In: *Physical Review C* **67**, 044314 (2003). DOI: 10.1103/PhysRevC.67.044314.
- [Lem12] A. Lemasson et al. “Observation of mutually enhanced collectivity in self-conjugate  $^{76}_{38}\text{Sr}_{38}$ ”. In: *Physical Review C* **85**, 041303(R) (2012). DOI: 10.1103/PhysRevC.85.041303.
- [Len10] S.M. Lenzi, F. Nowacki, A. Poves, and K. Sieja. “Island of inversion around  $^{64}\text{Cr}$ ”. In: *Physical Review C* **82**, 054301 (2010). DOI: 10.1103/PhysRevC.82.054301.
- [Len15] S.M. Lenzi. “Private Communication”. 2015.
- [Len17] S.M. Lenzi. “Private Communication”. 2017.
- [Lid04] S.N. Liddick. “Beta-decay studies of neutron-rich nuclides and the possibility of an  $N = 34$  subshell closure”. PhD thesis. Michigan State University, 2004.
- [Lid05] S.N. Liddick et al. “ $\beta$ -decay of odd- $A$   $^{57}\text{Ti}$  and  $^{59}\text{V}$ ”. In: *Physical Review C* **72**, 054321 (2005). DOI: 10.1103/PhysRevC.72.054321.

- [Lid13] S.N. Liddick et al. “Low-energy level schemes of  $^{66,68}\text{Fe}$  and inferred proton and neutron excitations across  $Z = 28$  and  $N = 40$ ”. In: *Physical Review C* **87**, 014325 (2013). DOI: 10.1103/PhysRevC.87.014325.
- [Lju10] J. Ljungvall et al. “Onset of collectivity in neutron-rich Fe isotopes: Toward a new island of inversion?” In: *Physical Review C* **81**, 061301(R) (2010). DOI: 10.1103/PhysRevC.81.061301.
- [Lou13] C. Louchart et al. “Collective nature of low-lying excitations in  $^{70,72,74}\text{Zn}$  from lifetime measurements using the AGATA spectrometer demonstrator”. In: *Physical Review C* **87**, 054302 (2013). DOI: 10.1103/PhysRevC.87.054302.
- [Lun07] S. Lunardi et al. “Spectroscopy of neutron-rich Fe isotopes populated in the  $^{64}\text{Ni}+^{238}\text{U}$  reaction”. In: *Physical Review C* **76**, 034303 (2007). DOI: 10.1103/PhysRevC.76.034303.
- [Mak06] K. Makino and M. Berz. “COSY INFINITY Version 9”. In: *Nuclear Instruments and Methods in Physics Research Section A: Accelerators, Spectrometers, Detectors and Associated Equipment* **558** (2006), pp. 346–350. DOI: 10.1016/j.nima.2005.11.109.
- [Man03] P.F. Mantica et al. “ $\beta$  decay studies of the neutron-rich  $^{56-58}\text{V}$  isotopes”. In: *Physical Review C* **67**, 014311 (2003). DOI: 10.1103/PhysRevC.67.014311.
- [Man03b] P. F. Mantica et al. “ $\beta$ -decay properties of  $^{55,56}\text{Ti}$ ”. In: *Physical Review C* **68**, 044311 (2003). DOI: 10.1103/PhysRevC.68.044311.
- [Mar06] N. Mărginean et al. “Shape transitions far from stability: The nucleus  $^{58}\text{Cr}$ ”. In: *Physics Letters B* **633** (2006), pp. 696–700. DOI: 10.1016/j.physletb.2005.12.047.
- [Mar14] T. Marchi et al. “Quadrupole Transition Strength in the  $^{74}\text{Ni}$  Nucleus and Core Polarization Effects in the Neutron-Rich Ni Isotopes”. In: *Physical Review Letters* **113**, 182501 (2014). DOI: 10.1103/PhysRevLett.113.182501.
- [Maz05] C. Mazzocchi et al. “Low energy structure of even-even Ni isotopes close to  $^{78}\text{Ni}$ ”. In: *Physics Letters B* **622** (2005), pp. 45–54. DOI: 10.1016/j.physletb.2005.07.006.
- [Men09] D. Mengoni, J. J. Valiente-Dobón, E. Farnea, A. Gadea, A. Dewald, and A. Latina. “Lifetime measurements of neutron-rich nuclei around  $^{48}\text{Ca}$  with the CLARA-PRISMA setup”. In: *The European Physical Journal A* **42** (2009), p. 387. DOI: 10.1140/epja/i2008-10775-2.
- [Mil01] P. Miller, F. Marti, D. Poe, M. Steiner, J. Stetson, and X.Y. Wu. “Commissioning of the Coupled Cyclotron Facility at NSCL”. In: *Proceedings of the 2001 Particle Accelerator Conference*. IEEE, 2001, pp. 2557–2559. DOI: 10.1109/PAC.2001.987829.
- [Mon12] D. Montanari et al. “ $\gamma$  spectroscopy of calcium nuclei around doubly magic  $^{48}\text{Ca}$  using heavy-ion transfer reactions”. In: *Physical Review C* **85**, 044301 (2012). DOI: 10.1103/PhysRevC.85.044301.

- [Mor03] D.J. Morrissey, B.M. Sherrill, M. Steiner, A. Stolz, and I. Wiedenhoever. “Commissioning the A1900 projectile fragment separator”. In: *Nuclear Instruments and Methods in Physics Research Section B: Beam Interactions with Materials and Atoms* **204** (2003), pp. 90–96. DOI: 10.1016/S0168-583X(02)01895-5.
- [Mor04] D.J. Morrissey and B. M. Sherrill. “In-Flight Separation of Projectile Fragments”. In: *The Euroschool Lectures on Physics with Exotic Beams, Volume I*. Ed. by Jim Al-Khalili and Ernst Roeckl. Berlin, Heidelberg: Springer Berlin Heidelberg, 2004, pp. 113–135. DOI: 10.1007/978-3-540-44490-9\_4.
- [Mor76] H. Morinaga and T. Yamazaki. *In-Beam Gamma-Ray Spectroscopy*. North-Holland Publishing Company, 1976.
- [Mot95] T. Motobayashi et al. “Large deformation of the very neutron-rich nucleus  $^{32}\text{Mg}$  from intermediate-energy Coulomb excitation”. In: *Physics Letters B* **346** (1995), pp. 9–14. DOI: 10.1016/0370-2693(95)00012-A.
- [Mue01] W.F. Mueller, J.A. Church, T. Glasmacher, D. Gutknecht, G. Hackman, P.G. Hansen, Z. Hu, K.L. Miller, and P. Quirin. “Thirty-two-fold segmented germanium detectors to identify  $\gamma$ -rays from intermediate-energy exotic beams”. In: *Nuclear Instruments and Methods in Physics Research Section A: Accelerators, Spectrometers, Detectors and Associated Equipment* **466** (2001), pp. 492–498. DOI: 10.1016/S0168-9002(01)00257-1.
- [NDS152] M.J. Martin. “Nuclear Data Sheets for  $A = 152$ ”. In: *Nuclear Data Sheets* **114** (2013), pp. 1497–1847. ISSN: 0090-3752. DOI: 10.1016/j.nds.2013.11.001.
- [NDS40] J.A. Cameron and B. Singh. “Nuclear Data Sheets for  $A = 40$ ”. In: *Nuclear Data Sheets* **102** (2004), pp. 293–513. DOI: 10.1016/j.nds.2004.06.001.
- [NDS42] J. Chen and B. Singh. “Nuclear Data Sheets for  $A = 42$ ”. In: *Nuclear Data Sheets* **135** (2016), pp. 1–192. DOI: 10.1016/j.nds.2016.06.001.
- [NDS44] J. Chen, B. Singh, and J.A. Cameron. “Nuclear Data Sheets for  $A = 44$ ”. In: *Nuclear Data Sheets* **112** (2011), pp. 2357–2495. DOI: 10.1016/j.nds.2011.08.005.
- [NDS46] S.C. Wu. “Nuclear Data Sheets for  $A = 46$ ”. In: *Nuclear Data Sheets* **91** (2000), pp. 1–116. DOI: 10.1006/ndsh.2000.0014.
- [NDS48] T.W. Burrows. “Nuclear Data Sheets for  $A = 48$ ”. In: *Nuclear Data Sheets* **107** (2006), pp. 1747–1922. DOI: 10.1016/j.nds.2006.05.005.
- [NDS50] Z. Elekes, J. Timar, and B. Singh. “Nuclear Data Sheets for  $A = 50$ ”. In: *Nuclear Data Sheets* **112** (2011), pp. 1–131. DOI: 10.1016/j.nds.2010.12.001.
- [NDS52] Y. Dong and H. Junde. “Nuclear Data Sheets for  $A = 52$ ”. In: *Nuclear Data Sheets* **128** (2015), pp. 185–314. DOI: 10.1016/j.nds.2015.08.003.
- [NDS54] Y. Dong and H. Junde. “Nuclear Data Sheets for  $A = 54$ ”. In: *Nuclear Data Sheets* **121** (2014), pp. 1–142. DOI: 10.1016/j.nds.2014.09.001.

- [NDS56] H. Junde, H. Su, and Y. Dong. “Nuclear Data Sheets for  $A = 56$ ”. In: *Nuclear Data Sheets* **112** (2011), pp. 1513–1645. DOI: <http://dx.doi.org/10.1016/j.nds.2011.04.004>.
- [NDS58] C.D. Nesaraja, S.D. Geraedts, and B. Singh. “Nuclear Data Sheets for  $A = 58$ ”. In: *Nuclear Data Sheets* **111** (2010), pp. 897–1092. DOI: [10.1016/j.nds.2010.03.003](https://doi.org/10.1016/j.nds.2010.03.003).
- [NDS60] E. Browne and J.K. Tuli. “Nuclear Data Sheets for  $A = 60$ ”. In: *Nuclear Data Sheets* **114** (2013), pp. 1849–2022. DOI: [10.1016/j.nds.2013.11.002](https://doi.org/10.1016/j.nds.2013.11.002).
- [NDS62] A.L. Nichols, B. Singh, and J.K. Tuli. “Nuclear Data Sheets for  $A = 62$ ”. In: *Nuclear Data Sheets* **113** (2012), pp. 973–1114. DOI: [10.1016/j.nds.2012.04.002](https://doi.org/10.1016/j.nds.2012.04.002).
- [NDS64] B. Singh. “Nuclear Data Sheets for  $A = 64$ ”. In: *Nuclear Data Sheets* **108** (2007), pp. 197–364. DOI: [10.1016/j.nds.2007.01.003](https://doi.org/10.1016/j.nds.2007.01.003).
- [NDS68] E.A. McCutchan. “Nuclear Data Sheets for  $A = 68$ ”. In: *Nuclear Data Sheets* **113** (2012), pp. 1735–1870. DOI: [10.1016/j.nds.2012.06.002](https://doi.org/10.1016/j.nds.2012.06.002).
- [NDS70] G. Gürdal and E.A. McCutchan. “Nuclear Data Sheets for  $A = 70$ ”. In: *Nuclear Data Sheets* **136** (2016), pp. 1–162. DOI: [10.1016/j.nds.2016.08.001](https://doi.org/10.1016/j.nds.2016.08.001).
- [Nic14] A.J. Nichols et al. “Collectivity in  $A \sim 70$  nuclei studied via lifetime measurements in  $^{70}\text{Br}$  and  $^{68,70}\text{Se}$ ”. In: *Physics Letters B* **733** (2014), pp. 52–57. DOI: [10.1016/j.physletb.2014.04.016](https://doi.org/10.1016/j.physletb.2014.04.016).
- [Nic15] A. J. Nichols et al. “Spectroscopy and lifetime measurements in  $^{66}\text{Ge}$ ,  $^{69}\text{Se}$ , and  $^{65}\text{Ga}$  using fragmentation reactions”. In: *Physical Review C* **91**, 014319 (2015). DOI: [10.1103/PhysRevC.91.014319](https://doi.org/10.1103/PhysRevC.91.014319).
- [Now16] F. Nowacki, A. Poves, E. Caurier, and B. Bounthong. “Shape Coexistence in  $^{78}\text{Ni}$  as the Portal to the Fifth Island of Inversion”. In: *Physical Review Letters* **117**, 272501 (2016). DOI: [10.1103/PhysRevLett.117.272501](https://doi.org/10.1103/PhysRevLett.117.272501).
- [Ots01] Takaharu Otsuka, Rintaro Fujimoto, Yutaka Utsuno, B. Alex Brown, Michio Honma, and Takahiro Mizusaki. “Magic Numbers in Exotic Nuclei and Spin-Isospin Properties of the  $NN$  Interaction”. In: *Physical Review Letters* **87** (2001), p. 082502. DOI: [10.1103/PhysRevLett.87.082502](https://doi.org/10.1103/PhysRevLett.87.082502).
- [Ots05] T. Otsuka, T. Suzuki, R. Fujimoto, H. Grawe, and Y. Akaishi. “Evolution of Nuclear Shells due to the Tensor Force”. In: *Physical Review Letters* **95**, 232502 (2005). DOI: [10.1103/PhysRevLett.95.232502](https://doi.org/10.1103/PhysRevLett.95.232502).
- [Ots10] Takaharu Otsuka, Toshio Suzuki, Michio Honma, Yutaka Utsuno, Naofumi Tsunoda, Koshiroh Tsukiyama, and Morten Hjorth-Jensen. “Novel Features of Nuclear Forces and Shell Evolution in Exotic Nuclei”. In: *Physical Review Letters* **104** (2010), p. 012501. DOI: [10.1103/PhysRevLett.104.012501](https://doi.org/10.1103/PhysRevLett.104.012501).
- [Per06] O. Perru et al. “Enhanced Core Polarization in  $^{70}\text{Ni}$  and  $^{74}\text{Zn}$ ”. In: *Physical Review Letters* **96**, 232501 (2006). DOI: [10.1103/PhysRevLett.96.232501](https://doi.org/10.1103/PhysRevLett.96.232501).
- [Pov01] A. Poves, J. Sánchez-Solano, E. Caurier, and F. Nowacki. “Shell model study of the isobaric chains  $A = 50$ ,  $A = 51$  and  $A = 52$ ”. In: *Nuclear Physics A* **694** (2001), pp. 157–198. DOI: [10.1016/S0375-9474\(01\)00967-8](https://doi.org/10.1016/S0375-9474(01)00967-8).

- [Pri01] J.I. Prisciandaro et al. “New evidence for a subshell gap at  $N = 32$ ”. In: *Physics Letters B* **510** (2001), pp. 17–23. DOI: 10.1016/S0370-2693(01)00565-2.
- [Rec12] F. Recchia et al. “Spectroscopy of odd-mass cobalt isotopes toward the  $N = 40$  subshell closure and shell-model description of spherical and deformed states”. In: *Physical Review C* **85**, 064305 (2012). DOI: 10.1103/PhysRevC.85.064305.
- [Rec13] F. Recchia et al. “Configuration mixing and relative transition rates between low-spin states in  $^{68}\text{Ni}$ ”. In: *Physical Review C* **88**, 041302(R) (2013). DOI: 10.1103/PhysRevC.88.041302.
- [Res04] J.J. Ressler et al. “Transition from the seniority regime to collective motion”. In: *Physical Review C* **69**, 034317 (2004). DOI: 10.1103/PhysRevC.69.034317.
- [Ril14] L.A. Riley et al. “Inverse-kinematics proton scattering on  $^{50}\text{Ca}$ : Determining effective charges using complementary probes”. In: *Physical Review C* **90**, 011305(R) (2014). DOI: 10.1103/PhysRevC.90.011305.
- [Rot11] W. Rother et al. “Enhanced Quadrupole Collectivity at  $N = 40$ : The Case of Neutron-Rich Fe Isotopes”. In: *Physical Review Letters* **106**, 022502 (2011). DOI: 10.1103/PhysRevLett.106.022502.
- [San15] C. Santamaria et al. “Extension of the  $N = 40$  Island of Inversion towards  $N = 50$ : Spectroscopy of  $^{66}\text{Cr}$ ,  $^{70,72}\text{Fe}$ ”. In: *Physical Review Letters* **115**, 192501 (2015). DOI: 10.1103/PhysRevLett.115.192501.
- [Sei11] M. Seidlitz et al. “Precision lifetime measurements of the first  $2^+$  and  $4^+$  states in  $^{56}\text{Cr}$  at the  $N = 32$  subshell closure”. In: *Physical Review C* **84**, 034318 (2011). DOI: 10.1103/PhysRevC.84.034318.
- [Shi12] N. Shimizu, T. Abe, Y. Tsunoda, Y. Utsuno, T. Yoshida, T. Mizusaki, M. Honma, and T. Otsuka. “New-generation Monte Carlo shell model for the K computer era”. In: *Progress of Theoretical and Experimental Physics* **2012**, 01A205 (2012). DOI: 10.1093/ptep/pts012.
- [Sic17] M. Siciliano et al. “Study of Quadrupole Correlations in  $N = Z = 50$  Region via Lifetime Measurements”. In: *Acta Physica Polonica B* **48** (2017), pp. 331–336.
- [Sor02] O. Sorlin et al. “ $^{68}_{28}\text{Ni}_{40}$ : Magicity versus Superfluidity”. In: *Physical Review Letters* **88**, 092501 (2002). DOI: 10.1103/PhysRevLett.88.092501.
- [Sor03] O. Sorlin et al. “New region of deformation in the neutron-rich  $^{60}_{24}\text{Cr}_{36}$  and  $^{62}_{24}\text{Cr}_{38}$ ”. In: *The European Physical Journal A - Hadrons and Nuclei* **16** (2003), pp. 55–61. DOI: 10.1140/epja/i2002-10069-9.
- [Ste10] D. Steppenbeck et al. “High-spin structures in the neutron-rich isotopes  $^{57-60}\text{Mn}$ ”. In: *Physical Review C* **81**, 014305 (2010). DOI: 10.1103/PhysRevC.81.014305.

- [Ste13] D. Steppenbeck et al. “Evidence for a new nuclear ‘magic number’ magic number from the level structure of  $^{54}\text{Ca}$ ”. In: *Nature* **502** (2013), pp. 207–210. DOI: doi:10.1038/nature12522.
- [Tar08] O.B. Tarasov and D. Bazin. “LISE++: Radioactive beam production with in-flight separators”. In: *Nuclear Instruments and Methods in Physics Research Section B: Beam Interactions with Materials and Atoms* **266** (2008), pp. 4657–4664. DOI: <http://dx.doi.org/10.1016/j.nimb.2008.05.110>.
- [Tar09] O. B. Tarasov et al. “Production of very neutron-rich nuclei with a  $^{76}\text{Ge}$  beam”. In: *Physical Review C* **80** (2009), p. 034609. DOI: 10.1103/PhysRevC.80.034609.
- [Tar13] O.B. Tarasov et al. “Production cross sections from  $^{82}\text{Se}$  fragmentation as indications of shell effects in neutron-rich isotopes close to the drip-line”. In: *Physical Review C* **87**, 054612 (2013). DOI: 10.1103/PhysRevC.87.054612.
- [Tos01] J.A. Tostevin. “Single-nucleon knockout reactions at fragmentation beam energies”. In: *Nuclear Physics A* **682** (2001), pp. 320–331. DOI: 10.1016/S0375-9474(00)00656-4.
- [Tsu14] Y. Tsunoda, T. Otsuka, N. Shimizu, M. Honma, and Y. Utsuno. “Novel shape evolution in exotic Ni isotopes and configuration-dependent shell structure”. In: *Physical Review C* **89**, 031301(R) (2014). DOI: 10.1103/PhysRevC.89.031301.
- [Val06] J.J. Valiente-Dobón et al. “Lifetime Measurements of the Neutron-Rich  $N = 30$  Isotones  $^{50}\text{Ca}$  and  $^{51}\text{Sc}$ : Orbital Dependence of Effective Charges in the  $fp$  Shell”. In: *Physical Review Letters* **102**, 242502 (2009). DOI: 10.1103/PhysRevLett.102.242502.
- [Val08] J.J. Valiente-Dobón et al. “Spectroscopy of neutron-rich  $^{59-63}\text{Mn}$  isotopes”. In: *Physical Review C* **78**, 024302 (2008). DOI: 10.1103/PhysRevC.78.024302.
- [VdW09] J. Van de Walle et al. “In-trap decay of  $^{61}\text{Mn}$  and Coulomb excitation of  $^{61}\text{Mn}/^{61}\text{Fe}$ ”. In: *The European Physical Journal A* **42** (2009), pp. 401–406. DOI: 10.1140/epja/i2009-10814-6.
- [Wan12] M. Wang, G. Audi, A.H. Wapstra, F.G. Kondev, M. MacCormick, X. Xu, and B. Pfeiffer. “The Ame2012 atomic mass evaluation–(II). Tables, graphs and references”. In: *Chinese Physics C* **36** (2012), pp. 1603–2014. DOI: 10.1088/1674-1137/36/12/003.
- [War82] D.D. Warner and R.F. Casten. “Revised Formulation of the Phenomenological Interacting Boson Approximation”. In: *Physical Review Letters* **48** (1982), pp. 1385–1389. DOI: 10.1103/PhysRevLett.48.1385.
- [Yam05] K. Yamada et al. “Reduced transition probabilities for the first  $2^+$  excited state in  $^{46}\text{Cr}$ ,  $^{50}\text{Fe}$ , and  $^{54}\text{Ni}$ ”. In: *The European Physical Journal A - Hadrons and Nuclei* **25** (2005), pp. 409–413. DOI: 10.1140/epjad/i2005-06-094-0.
- [Yur04] K.L. Yurkewicz et al. “Intermediate-energy Coulomb excitation of  $^{52}\text{Fe}$ ”. In: *Physical Review C* **70**, 034301 (2004). DOI: 10.1103/PhysRevC.70.034301.

- [Yur99] J. Yurkon, D. Bazin, W. Benenson, D.J. Morrissey, B.M. Sherrill, D. Swan, and R. Swanson. “Focal plane detector for the S800 high-resolution spectrometer”. In: *Nuclear Instruments and Methods in Physics Research Section A: Accelerators, Spectrometers, Detectors and Associated Equipmen* **422** (1999), pp. 291–295. DOI: 10.1016/S0168-9002(98)00960-7.
- [Zhu06] S. Zhu et al. “Level structure of the neutron-rich  $^{56,58,60}\text{Cr}$  isotopes: Single-particle and collective aspects”. In: *Physical Review C* **74**, 064315 (2006). DOI: 10.1103/PhysRevC.74.064315.
- [Zhu07] S. Zhu et al. “One-particle excitations outside the  $^{54}\text{Ti}$  semi-magic core: The  $^{55}\text{V}$  and  $^{55}\text{Ti}$  yrast structures”. In: *Physics Letters B* **650** (2007), pp. 135–140. DOI: 10.1016/j.physletb.2007.05.014.
- [Zie10] James F. Ziegler, M.D. Ziegler, and J.P. Biersack. “{SRIM} – The stopping and range of ions in matter (2010)”. In: *Nuclear Instruments and Methods in Physics Research Section B: Beam Interactions with Materials and Atoms* **268** (2010), pp. 1818–1823. DOI: 10.1016/j.nimb.2010.02.091.
- [Zuk94] A.P. Zuker, J. Retamosa, A. Poves, and E. Caurier. “Spherical shell model description of rotational motion”. In: *Physical Review C* **52**, 1741(R) (1995). DOI: 10.1103/PhysRevC.52.R1741.

---

## Dank

An dieser Stelle möchte ich all jenen meinen Dank aussprechen, die mir in der Zeit der Promotion auf jedwede Art Unterstützung zugesprochen haben. Insbesondere gilt mein Dank:

- Prof. Dr. Alfred Dewald, zuvorderst für die Vergabe und Betreuung dieser Arbeit. Bereits im Rahmen meiner Diplomarbeit konnte ich nahe an der Entwicklung der Plunger Apparatur TRIPLEX arbeiten, was naturgemäß die Bindung zu diesem Projekt deutlich erhöht hat. Prof. Dr. Dewald hat mich in meiner Selbständigkeit fortwährend unterstützt und mir die Möglichkeit geboten, frei zu arbeiten. Ermöglicht wurde dies durch seine stets offene Tür. Dafür gebührt ihm mein aufrichtiger Dank.
- Prof Dr. Jan Jolie, für sein aufrichtiges Interesse und die Diskussionen offener Fragen, insbesondere im Hinblick auf die IBA Rechnungen.
- Dr. Christoph Fransen, für seine nahezu grenzenlose Hilfsbereitschaft, für die vielen Gespräche und für die vielen kleinen Dingen die zum Erfolg dieser Arbeit beigetragen haben.
- Prof. Dr. Hironori Iwasaki, für seine Betreuung am NSCL und der zielgerichteten Atmosphäre bei der Planung und Durchführung der Experimente am NSCL.
- Prof Dr. S. M. Lenzi, für die Bereitstellung der Schalenmodellergebnisse auf Basis der LNPS Wechselwirkung und Diskussionen.
- Dr. Andrej Blazhev, für Diskussion der Schalenmodellrechnungen.
- Den Kollegen aus der Plunger Arbeitsgruppe, insbesondere den treuen Weggefährten Claus Müller-Gatermann und Julia Litzinger.
- Den Bewohnern des Büro 209, für die stets entspannte Atmosphäre und der geteilten Affinität zu Kaffee.
- Konrad Arnswald, für die zahlreichen Anmerkungen in der Korrekturphase und den zahlreichen Diskussion im Rahmen der vergangenen Jahre.

Zum Abschluss gilt mein Dank meiner Familie, die mich immer wieder und auf vielfältige Art und Weise unterstützt hat. Nicht zuletzt gilt mein persönlicher Dank meiner Lebensgefährtin Nora, die mit bemerkenswerter Geduld die Phasen meiner – meist geistigen – Abwesenheit ertragen hat.

---

## Erklärung

Ich versichere, dass ich die von mir vorgelegte Dissertation selbständig angefertigt, die benutzten Quellen und Hilfsmittel vollständig angegeben und die Stellen der Arbeit – einschließlich Tabellen, Karten und Abbildungen –, die anderen Werken im Wortlaut oder dem Sinn nach entnommen sind, in jedem Einzelfall als Entlehnung kenntlich gemacht habe; dass diese Dissertation noch keiner anderen Fakultät oder Universität zur Prüfung vorgelegen hat; dass sie – abgesehen von unten angegebenen Teilpublikationen – noch nicht veröffentlicht worden ist, sowie, dass ich eine solche Veröffentlichung vor Abschluss des Promotionsverfahrens nicht vornehmen werde. Die Bestimmungen der Promotionsordnung sind mir bekannt. Die von mir vorgelegte Dissertation ist von Prof. Dr. Alfred Dewald betreut worden.

Teilveröffentlichungen:

- Thomas Braunroth et al. “Reduced transition strengths of low-lying yrast states in chromium isotopes in the vicinity of  $N = 40$ ”. In: *Physical Review C* **92**, 034306 (2015).

Hürth, den 15. Dezember 2017

---

(Thomas Braunroth)